Addressing Efficiency in Enzyme Biofuel Cells

A thesis submitted to The University of Manchester for the degree of

Doctor of Philosophy

In the Faculty of Engineering and Physical Sciences

2011

Michael Adrian Roberts

School of Materials

Table of Contents

Abstract....6
Declaration....7
Copyright....7
Acknowledgements....8
Abbreviations....9
Standard constants....10
Nomenclature....10
1 Introduction and Aims....11
2 Literature Review....13
2.1 Introduction to Enzyme Biofuel Cells....13
2.1.1 Enzymes as Catalysts....16
2.1.2 Fuel Cell Performance....19
2.1.3 Current Limitations....23
2.1.4 Cell Design....26
2.1.5 The Role of Nanostructure....28
2.1.6 Examples of Enzyme Biofuel Cells and Potential Applications....32
2.2 Carbon Nanotubes....36
2.2.1 Introduction to Carbon Nanotubes....36
2.2.1.1 Morphology....37
2.2.1.2 Electronic Properties....40
2.2.1.3 Spectroscopic Properties....44
2.2.1.4 Electrochemical Properties....48
2.2.2 Production Routes and Growth Mechanisms....52
2.2.2.1 Introduction....52
2.2.2.2 Catalytic Vapour Deposition (CVD)....53
2.2.2.3 Catalytic Synthesis of Multi-Walled Nanotubes....54
2.2.2.4 Growth Mechanisms of Catalytically Produced Multi-walled Nanotubes....56
2.2.3 Multi-walled Nanotube Purification and Functionalisation....57
2.2.3.1 Purification of Multi-walled Nanotubes....58
2.2.3.2 Functionalisation of Carbon Nanotubes....60
2.3 Enzymes....62
2.3.1 Introduction to ***Trametes versicolor*** laccase....62
2.3.1.1 Occurrence, Physiological Function and Localisation in Cell....63
2.3.1.2 Production and Purification....64
2.3.1.3 Structure and Catalytic Mechanism....67
2.3.1.4 Redox Potentials....69
2.3.2 Laccase Electrochemistry....72
2.3.2.1 Direct Electron Transfer....73
2.3.2.2 Immobilisation of Enzymes by Direct Electron Transfer....74
2.3.2.2.1 Adsorbed and Coadsorbed Enzyme Monolayers....75
2.3.2.2.2 Diazonium Coupling....76
2.3.2.2.3 Self-Assembled Monolayers....77
2.3.2.2.4 Enzymes on Nanostructures....78
2.3.2.2.4.1 Carbon Nanotubes....79
2.3.2.2.4.2 Gold Nanoparticles....79
2.3.3 Biocathode....80
3 Theory and Experimental....82
3.1 Electrochemistry....82

3.1.1 Experimental Methodology 82
3.1.2 Equilibrium Measurements 85
3.1.2.1 Reference Electrodes 86
3.1.2.2 Nernst Equation 87
3.1.3 Dynamic Measurements 88
3.1.3.1 Diffusion Controlled Cyclic Voltammetry 90
3.1.3.2 Diffusion Controlled Chronoamperometry 92
3.1.3.3 Convective Control: Hydrodynamic Techniques 94
3.1.4 Electrode Kinetics 96
3.1.4.1 Tafel Kinetics 96
3.1.4.2 Butler-Volmer Kinetics 97
3.1.4.3 Koutecky-Levich Kinetics 98
3.1.4.4 The Marcus Theory 98
3.1.5 Faradaic and Non-Faradaic Charge 103
3.1.5.1 Electrode Double Layer and Capacitance 103
3.1.6 Effect of Electrode Porosity: Thin-Layer Behaviour 106
3.1.7 Voltammetry of Adsorbed Enzymes: Protein-Film Voltammetry 108
3.1.7.1 Non-Catalytic Voltammetry 109
3.1.7.2 Catalytic Voltammetry 112
3.1.7.3 Catalytic Chronoamperometry 117
3.1.8 Equipment 117
3.2 Physical Analysis 118
3.2.1 Raman Spectroscopy 118
3.2.2. Scanning Electron Microscopy/Energy Dispersive X-ray Analysis (EDX) 120
3.2.3 Transmission Electron Microscopy 120
3.2.4 Ultraviolet-Visible Light Spectroscopy (UV-Vis) 120
3.2.5 Contact Angle Measurements 121
3.2.6 Epifluorescence Microscopy 123
3.3 Experimental 123
3.3.1 Chemicals and Samples 123
3.3.2 Laccase voltammetry 124
3.3.3 Enzyme Purification - Purification of laccase from *Trametes versicolor* 125
3.3.3.1 Moderately purified laccase (produced in The University of Manchester) 125
3.3.3.2 Highly purified laccase (produced in The University of Oxford) 126
3.3.4 Enzyme Purity and Concentration 127
3.3.4.1 Enzyme Assays 127
3.3.4.2 ABTS Assay Method (Diammonium 2,2′ -azino-bis(3-ethylbenzothiazoline-6-sulfonate) 127
3.3.4.3 Protein Assays 128
3.3.4.4 Kinetic Constants of Trametes versicolor laccase 128
3.3.5 Epifluorescence Measurements 131
3.3.6 Effect of pH 131
3.3.7 Aligned Carbon Nanotube Electrodes 132
3.3.7.1 Aligned Carbon Nanotube Growth 132
3.3.7.2 Surface Functionalisation 133
3.3.8. Patterned CNT Electrodes 133
3.3.8.1 Patterned CNT Growth 133

3.3.9 Electrode Preparation 134
3.3.9.1 Working Electrodes 134
3.3.9.1.1 Aligned Carbon Nanotube Electrodes 134
3.3.9.1.2 Patterned Carbon Nanotube Electrodes 134
3.3.9.1.3 Glassy Carbon Electrodes 135
3.3.9.1.4 Edge-Plane Highly Orientated Pyrolytic Graphite (Edge-HOPG) 135
3.3.9.1.5 Rotating Disc Electrode 135
3.3.9.2 Reference Electrodes 136
3.3.9.3 Counter Electrodes 136
4 Laccase Purification, Kinetics and Preliminary Electrochemistry 137
4.1 Introduction to Laccase Purification, Kinetics and Electrochemistry 137
4.2 Kinetics and Electrochemistry 138
4.2.1 Results - Comparing Laccase Purification Procedures 138
4.2.2 Physical Characterisation 139
4.2.2.1 UV-Vis Absorption Spectrum 139
4.2.2.2 Bradford Assay 141
4.2.2.3 Laccase Voltammetry 143
4.3 Highly Purified Laccase 146
4.3.1 Enzyme Kinetics 147
4.3.2 Effect of pH on Laccase Activity 150
4.4 TvL Electrocatalytic Response - Effect of Topology 153
4.4.1 Glassy Carbon, Edge-HOPG and aCNTs 153
4.5 Aligned Carbon Nanotube Electrodes (aCNTs) 157
4.5.1 Preliminary CVD Experiments 157
4.5.2 Electrode Surface Area and Mass Calculations 159
4.5.3 Preliminary Electrochemistry 160
4.5.3.1 Cyclic Voltammetry 160
4.5.3.2 Enzyme Adsorption onto the Electrodes 164
4.6 Carbon Nanotubes- Laccase Electrochemistry 166
4.6.1 Effect of Carbon Nanotube Electrode Area 166
4.6.2 Effect of CNT Length 169
4.6.3 Effect of Laccase Loading and Thin-Layer Behaviour 173
4.7 Conclusion 177
5 Laccase Electrocatalytic Response on Functionalised CNT Surfaces 179
5.1 Introduction to CNT Functionalisation and Enzyme Electrochemistry on Functionalised Surfaces 179
5.2 Results 181
5.2.1 Physical Properties of Short aCNT-arrays (2 hour Grown) 181
5.2.1.1 Contact Angle Measurements of as-grown aCNT arrays 181
5.2.1.2 Thermal Treatment 183
5.2.2 Physical Characterisation 185
5.2.2.1 SEM Analysis 185
5.2.2.2 TEM Analysis 190
5.2.2.3 Raman Spectroscopy 192
5.2.3 Physical Properties of Long aCNT-arrays (4 hour Grown) 197
5.2.3.1 SEM Analysis 197
5.2.3.2 TEM Analysis 202
5.2.3.3 Raman Spectroscopy 204
5.2.4 Electrochemical Characterisation of Long aCNT Arrays 205

5.2.4.1 Effect of Surface Chemistry on Capacitance....205
5.2.4.2 Laccase Electrochemistry....208
5.3 Conclusion....211
6 Laccase Electrochemistry on Patterned CNT Electrodes with Increased Pore Size for Efficient O_2 Diffusion....213
6.1 Introduction....213
6.2 Results....214
6.2.1 Growth of Patterned Electrodes....214
6.2.2 Electrode Characterisation....215
6.2.3 Laccase Electrochemistry....219
6.2.3.1 As-Grown aCNT Micro-patterned Electrodes....219
6.2.3.2 Oxidised aCNT Micro-patterned Electrodes....222
6.2.3.2.1 Capacitance Measurements....222
6.2.3.2.2 Laccase Electrochemistry....228
6.3 Comparison of electrodes and future work....230
6.4 Conclusion....231
7 Future Work....232
7.1 Thermal Treatment....232
7.2 Microarrays....233
7.3 Genetically Engineered Enzymes....234
8 Overall Thesis Conclusions....235
9 References....239

Thesis Total Word Count = 64,616

Abstract

Biofuel cells (BFCs) use either enzymes or bacteria to catalyse a fuel to generate power. Their advantages over conventional fuels is that they do not use precious metals and the high selectivity of biocatalysts mean that no separation membranes are required between the electrodes. However, the application of BFCs is limited by their low power output and poor enzyme lifetimes. This thesis addresses these limitations by investigating aligned carbon nanotubes (aCNTs) as potential electrode materials. These aCNT electrodes offer high surface areas to increase enzyme coverage and hence power output and their surface topology can stabilise the enzymes to ensure maximum lifetime and current density.

A novel BFC half cell was developed using aCNTs and the fungal enzyme, *Trametes versicolor* laccase which catalyses the four-electron reduction of oxygen to water. Laccase was shown to communicate directly with the nanotubes enabling the oxidant reduction reaction to be monitored without the need for mediators.

Initial investigations compared aCNTs with other commonly reported carbon electrodes and found that the current densities were ~30-fold higher on the aCNTs than at pyrolytic graphite edge electrodes. The high surface area of these electrodes contributed to greater electroactive coverage of enzyme and minimal loss of enzyme upon deposition. Cathodic currents increased linearly with geometric electrode area; however they did not scale with actual electrode surface area and the current density was limited to the order of $\mu A\ cm^{-2}$ due to O_2-transport limitations.

It was also discovered that the porous contribution of these aCNT electrodes could lead to misleading interpretations on nanotube electrochemistry. This effect was observed when increments in electrode area resulted in apparently significantly faster kinetics. This improvement in catalytic behaviour was proposed to be due to a transition from mass diffusion limited to thin layer cell behaviour exhibited by porous materials.

Thermal pretreatment of the aCNT electrodes in oxidative and reductive atmospheres were found to improve their performance. These treatments worked by changing the nanotube surface chemistry and purifying the nanotubes, as evidenced by various physical characterisation methods. Furthermore, laccase activity was enhanced significantly after electrodes had been treated under both atmospheres, where it was believed that the removal of contaminant material and higher defect densities increased electrochemical performance.

Finally, mass transport limitations were addressed by developing micro-patterned aCNT electrodes which possessed channels in the arrays, allowing better oxygen diffusion. Fundamental studies showed higher current densities per surface area and thus represent a promising electrode for future BFC research.

Declaration

I, the author, declare that no portion of the work referred to in the thesis has been submitted in support of an application for another degree or qualification of this or any other university or other institute of learning.

Copyright

Acknowledgements

The author would like to thank Dr. Ian Kinloch for his guidance and support throughout and Prof. Robert Dryfe who taught the author a great deal about electrochemistry. Further thanks go to Dr. Chris Blanford who enabled the collaboration and has offered guidance and encouragement at times of need. In addition, Prof. Brian Derby for kindly lending the potentiostat for all the electrochemical studies conducted.

Thanks also go to Yanning Li for providing the TEM images and being a helping hand around the laboratory, Dr. Jeffrey Martin for additional help with electrochemistry problems and finally Kulveer Singh who provided the images of *Trametes versicolor* laccase.

Most of all, the author is indebted to his family for all their support and much needed funding to complete the degree and his girlfriend Dr. Jennifer Marion whose encouragement, love and support cannot be overstated. The PhD survival boxes were very much appreciated.

Abbreviations

aCNT	Aligned carbon nanotube
ABTS	2, 2′-azino-bis(3-ethylbenzothiazoline-6-sulfonate)
BFCs	Biofuel cells
BOD	Bilirubin oxidase
CNT	Carbon nanotube
CV	Cyclic voltammetry
CVD	Chemical vapour deposition
DC	Direct current
DET	Direct electron transfer
DOS	Density of states
EDX	Energy dispersive x-ray analysis
HOPG	Highly orientated pyrolytic graphite
MET	Mediated electron transfer
MWNTs	Multi-walled nanotubes
NHE	Normal hydrogen electrode
OCV	Open circuit voltage
PEM	Proton exchange membrane
RBM	Radial breathing mode
RDE	Rotating disk electrode
RHE	Reversible hydrogen electrode
SAM	Self-assembled monolayer
SEM	Scanning electron microscopy
SWNTs	Single-walled nanotubes
TEM	Transmission electron microscopy
UV-Vis	Ultraviolet-visible light spectroscopy

Standard constants

e	Elementary charge	1.602×10^{-19} C
F	Faraday constant	96485.339 C mol^{-1}
N_A (or K)	Avogadro constant	6.022×10^{23} mol^{-1}
R	Ideal Gas constant	8.314 J K^{-1} mol^{-1}

Nomenclature

A	Area
C	Capacitance
D	Diffusion coefficient
ε	Absorption (molar extinction) coefficient
E	Electrode potential
$E^{0'}$	Formal Redox potential
E^{θ}	Potential for the redox couple under standard conditions
emf	Electromotive force or cell potential
E_{pc}	Cathodic Peak Potential
ΔG	Gibbs energy
ΔH	Heat of the reaction
I_{lim}	Limiting current
I_P	Peak current
K	Kelvin
k	Rate constant
k_{cat}	Turnover rate
k_{et}	Electron transfer rate constant
n	Number of electrons
η	Overpotential
Γ	Surface coverage of enzyme
T	Temperature
t	Time
V	Voltage
V_{max}	Maximum catalytic rate

1 Introduction and Aims

Biofuel cells (BFCs) utilise enzymes as electrocatalysts for the conversion of chemical energy into electrical energy, producing a novel energy-conversion device that is distinct from conventional fuel cells. Not only are enzymes capable of high catalytic activity, but they also offer other interesting advantages over conventional fuel cell catalysts (e.g. platinum, Pt), in that they are optimised to work under ambient temperatures and are highly selective for their fuel or oxidant (substrate). This inherent selectivity removes the need for an expensive ion-conducting membrane, typically found in conventional fuel cells, thus providing great potential for miniaturisation.

Nevertheless, BFCs are still limited by their low power density and short enzyme lifetimes. Enzymes are large molecules, therefore their catalytic density per volume is low and the active site is usually buried, limiting substrate turnover (i.e. current output). Furthermore, long-term enzyme stability is difficult to achieve outside ambient conditions and when immobilised on an electrode surface.

This project describes efforts to address these limitations, through direct attachment of a fungal laccase enzyme, a highly efficient oxygen (O_2) reduction electrocatalyst, to aligned carbon nanotube (aCNT) electrode materials. Research was focussed at one electrode, the cathode, where performance is currently restricted by the sluggish kinetics of the O_2 reduction. It is well known that laccases have high specificity towards this reaction and are able to reduce oxygen to water at high (electrode) potentials. The high electrical conductivity and small size of CNTs was used to gain close proximity to the enzyme active site and enhance electron transfer kinetics, since the extent of catalysis (i.e. power output) is dependant on the efficacy of this communication. In addition, the absence of electron transfer mediators offered improved understanding of nanotube-enzyme interactions (inc. CNT functionalisation effects) and facilitates a simple electrode system. The CNT growth method chosen was highly controlled; enabling the growth of vertically aligned arrays of nanotubes with large surface areas and controlled architectures (lengths and diameters). These nanotube arrays provide an excellent ‘3D’ conducting network, significantly increasing the current by

engaging a greater number of enzyme molecules. Therefore, through using innovative materials science approaches to increase the power and operational lifetime of enzyme BFCs, the following objectives of the thesis were proposed:

1. To develop a purification method to obtain high purity and concentrated laccase enzyme extract from contaminated commercial samples:
    a. Using the laboratory equipment available.
    b. Assessing the purity and kinetics of the newly-purified enzyme using Ultraviolet-Visible (UV-Vis) spectroscopic techniques.

2. To develop a novel BFC half cell comprising of the fungal enzyme laccase combined to aCNTs and investigate its performance:
    a. Using electrochemical and physical characterisation methods.
    b. Examining the effect of varying the topology, area, length and enzyme loading on catalytic activity.

3. To investigate how changes in nanotube surface chemistry affect enzyme activity and stability:
    a. Using gas-phase oxidative and reductive thermal treatments to chemically functionalise the nanotubes.
    b. Using cyclic voltammetry and chronoamperometry techniques to directly measure activity and stability.

4. To identify limitations in measurements and consider further improvements to be made to the electrode:
    a. Optimising experimental conditions and cell design for improved enzyme activity.
    b. Determine the best electrode and measure long-term stability.
    c. Assess overall electrode performance and compare to literature.
    d. Use the results from the aims above to discuss the efficiency of the enzyme biofuel cell.

5. To evaluate the current use of CNTs as electrode materials for BFCs and identify possible future advances for their market application.

2 Literature Review

2.1 Introduction to Enzyme Biofuel Cells

Today most energy-conversion methods rely on the combustion of fuels to generate electrical energy or mechanical energy and these processes are thwarted with thermal and fuel inefficiencies. Internal combustion engines found in automotives are only 20 to 25 % efficient[1] and added concerns over health and environmental well-being have since increased the demand for viable alternatives.

Fuel cells which create electricity chemically, rather than by combustion represent one promising and viable alternative. These energy-conversion devices were first introduced by Grove and Schoenbein back in 1839[2, 3] and were found to be far more efficient due to their isothermal nature and thus not subject to Carnot-cycle limitations[4]. However, it took until the 1960's before NASA found an application for them, as a source of electricity and water on space voyages.

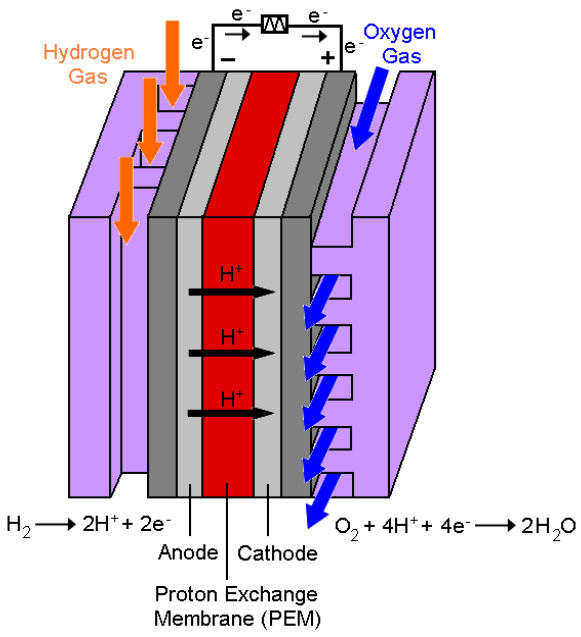

Figure 1: Schematic of hydrogen-oxygen proton exchange membrane fuel cell (PEMFC) with corresponding half cell reactions.

Fuel cells function in a similar manner to batteries, converting chemical energy into electrical energy. However fuel cells, unlike batteries, introduce an external and continuous source of chemicals to the electrodes, while batteries have a limited enclosed source of reacting chemicals. As a result, fuel cells produce power continuously as long as the fuel supply is maintained. An example of a fuel cell is shown in Figure 1.

An individual fuel cell consists of two electrodes, a cathode (positive) and an anode (negative), separated by an electrolyte which carries ions from one electrode to another. In Figure 1, this electrolyte consists of a proton exchange membrane (PEM). The fuel cell system operates when the reductant or 'fuel' is fed to the anode and reacts in the presence of a catalyst and electrolyte to form electrons and hydrogen ions (protons). The electrons travel through the external circuit while the protons diffuse through the electrolyte towards the cathode. Both electrons and hydrogen ions then complete the circuit by participating in a reaction with the oxidant (typically oxygen) at the cathode, generating electricity.

Fuel cells are usually 'stacked' (placed on top of each other) to achieve the required power level for the desired application. Typical fuels exploited are hydrogen and methanol due to their high energy densities, providing enough energy to power building-integrated systems or even small electronic devices.

The market interest for fuel cells has since grown due to environmental pressures, depletion of fossil resources and growing energy demands for niche applications. However, a whole range of issues continue to delay global implementation, these include the high cost of precious-metal catalysts (e.g. platinum (Pt)), generation and storage issues of hydrogen, slow technological developments, limited manufacturing infrastructures and overcoming business strongholds.

This thesis is based on improving BFCs which are slightly different to conventional fuel cells in that they use enzymes as catalysts at either, or both of the electrodes, as shown in Figure 2.

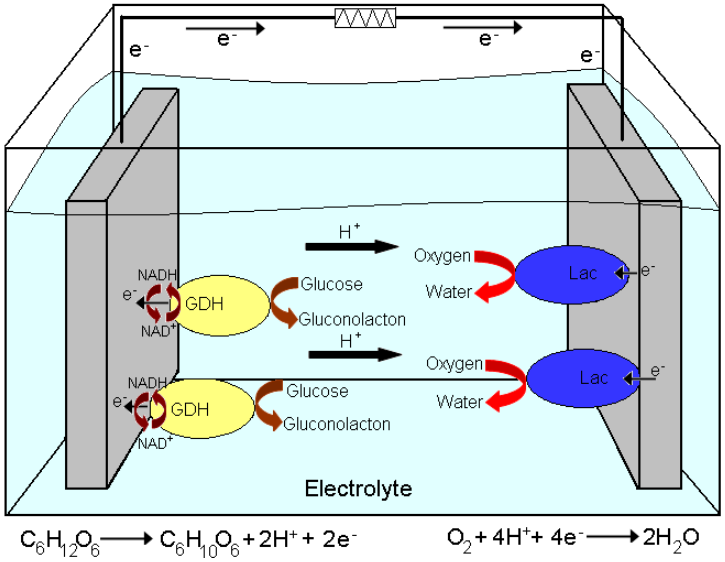

Figure 2: Schematic representation of glucose-oxygen BFC with corresponding half cell reactions. The cell is based on work by Yan *et al.*[5], who used glucose dehydrogenase (GDH) and laccase (Lac) enzymes to catalyse glucose oxidation and oxygen reduction respectively. The cofactor (nicotinamide adenine dinucleotide with hydrogen) was employed to help shuttle the electrons. Note: Electrodes shown are non-representative.

In 1964, Yahiro *et al.*[6] reported the first BFC based on membrane separated Pt foil electrodes in phosphate buffer. Utilising glucose and glucose oxidase enzyme at the anode and oxygen fed to the cathode, the cell produced a tiny current density of 30 nA cm^{-2} at 0.6-0.7 V. The poor performance was probably due to the absence of mediators, a usual requirement for glucose oxidase (GOx) with a deeply buried active site.

Over the last decade, research into the use of enzymes as fuel cell catalysts has gathered momentum due to the search for alternative low cost electrocatalysts, the envisagement of biorenewable fuels, and recent advances in biological science and technology[7]. Enzymes are not only excellent catalysts, with higher activities per mole than their precious-metal counterparts, but also highly selective for their substrates, essentially removing the need for expensive ion-conducting membranes (PEMs). This authorises the use of reactant mixtures in enzyme biofuel cells which not only simplifies the fuel cell but allows fabrication on a small scale. Moreover, nature has already optimised enzymes to function at ambient conditions of temperature and pH, while conventional fuel cells generally operate at higher temperatures.

Nature's design of enzymes has essentially provided a "tool kit" to facilitate our understanding of the important structural aspects and catalytic mechanisms of these special proteins. Recent efforts have been made to design novel synthetic enzymes, while further advances in structural genomics and protein electrochemistry might enhance our understanding of how to engineer or perfectly implement these enzymes at an electrode surface for outstanding catalytic performance.

2.1.1 Enzymes as Catalysts

Enzyme catalysis occurs when the enzyme binds the transition state more strongly than the ground state reactants[8], and this decrease in energy is responsible for the acceleration in reaction rate. Ever since the first enzymatic studies in the 1830's, investigators have been fascinated by the phenomenal rate accelerations and specificities of enzymes[9]. These remarkable properties, along with the diverse range of fuels available, offer interesting advantages over other catalysts used for fuel cell applications.

The performance of a catalyst is determined by the turnover rate (k_{cat}), the maximum rate at which a catalyst can convert the fuel or oxidant, and the potential required to achieve catalysis. Recently, Barton[7] compared the performance of laccase and Pt based on their turnover rates at comparable potentials (0.8 V vs. reversible hydrogen electrode (RHE)). The turnover numbers were estimated at 200 s^{-1} and 25 s^{-1} respectively, thus laccase was deemed to be competitive with Pt (noting: 650 s^{-1} for Pt at 0.7 V vs. RHE). Given that many enzymes achieve these high turnover rates with minimal potential, these catalysts are extremely efficient and highly promising for fuel cell applications.

In addition to their high catalytic power, enzymes can be extremely selective when used as biocatalysts. The active site of the enzyme is naturally designed to be precisely complimentary to the reactants in their transition-state geometry, thus avoiding interferences with other reactants. This is an important property for fuel cell catalysis since many traditional metal catalysts suffer from catalyst poisoning

and fuel crossover effects. The specificity of an enzyme for its substrate is given by its Michaelis constant value (K_M), which is derived in section 3.3.4.4. In fuel cells, substrate concentrations are often higher than the K_M value, so enzymes are working at their maximum catalytic rate (i.e. the rate of catalysis is equal to the k_{cat}). However, at the cathode this is not always the case. The maximum concentration of O_2 in aqueous solution is 0.27 mM (25 °C) [10], about the same as the K_M value for reaction of O_2 with laccase. The low concentration and diffusion coefficient of O_2 in solution (1.97×10^{-5} cm^2 s^{-1} at 20 °C)[11] results in the sluggish kinetics usually found at the cathode. Many scientists look to enhance the diffusional transport of O_2 (i.e. mass transport) through using a rotating disk electrode (RDE) or magnetic stirrer, although the power requirements of these systems often outweighs the power produced by the fuel cell. A more sensible approach would be to improve the electrode design, in order to generate a high performance gas diffusion electrode that reduces oxygen effectively at the cathode.

The two main disadvantages of employing enzymes for fuel cell catalysis are that they are inherently large and often unstable when removed from their natural environment. The bulk of the enzyme consists of a 'protein coat' which encapsulates the catalytic active site and has various important roles such as producing the substrate selectivity, stabilising the active site and providing the internal electron relay system. However, when enzymes are considered on the basis of their catalytic density per unit volume they are greatly disadvantaged compared to their metal catalyst counterparts. Barton demonstrated the challenges that must be overcome before BFCs can be considered for high power applications[7]. With reference to his previous calculations above, laccase with a diameter of 5 nm was calculated to achieve a 40-fold lower turnover rate per volume than Pt, yielding a volumetric oxygen reduction current density of 260 A cm^{-3}. On the basis that the majority of the catalytic volume is reserved for water, mediators and the porous electrode, Barton implied that the actual volumetric current density value would only be 26 A cm^{-3} (10 % of its ideal). This was well below the estimated target value of 130 A cm^{-3} determined for high power density automotive applications[12]. As a result, near-term applications of BFCs are currently limited to low power density implantable devices. Future improvements

in designing 3D electrodes with high surface areas will enhance enzyme loadings and power density, hence BFC performance.

It is also necessary to improve the stability of the enzyme, since they are relatively unstable outside their natural environment and typically only last for 1-2 days in electrolyte solutions. Immobilising the enzyme to an electrode surface has been shown to extend enzyme lifetime. For example, Blanford *et al.* demonstrated that laccase interacts favourably on an anthracene-modified graphite electrode and is stable over a 60 day period[13]. In addition, a miniature BFC with bilirubin oxidase (BOD) and glucose oxidase (GOx) immobilised in osmium (Os) redox hydrogels lasted 20 days at 37 °C[14, 15]. In both these cases, however, the electrode(s) lost over 40% of initial power after one week. Unfortunately, nature's structural design of enzymes is not ideally suited for immobilisation on electrode surfaces or polymer entrapment and therefore the immobilisation method must be carefully selected to avoid denaturing the enzyme and reducing its activity through loss of structural freedom. It is necessary that enzymes are correctly orientated on electrodes not only for improved stability but also for efficient electron transport from or to the electrode. The small size and large surface areas of nanostructures have been shown to improve the power density of BFCs through "wiring" to the active site, and have also extended enzyme lifetimes.

Finally, enzymes used in fuel cell applications are easily obtainable but often come in low yields and low purities. The properties of enzymes for fuel cells can be improved by purification which removes any contaminants that may affect activity. Conversely, a more powerful approach which enables high level expression and efficient biocatalysis is protein engineering. Naturally derived enzymes may eventually be replaced by synthetic enzymes that contain properties which are finely tuned for target applications and can be produced on an industrial-scale. This work is still at a fundamental stage and depends strongly on increased understanding of the structure and function relationships of enzymes. Although, it is certain that if robust and highly efficient industrial enzymes are ever realised, then many of the hurdles already mentioned will be eradicated.

2.1.2 Fuel Cell Performance

For any fuel cell system, the performance is characterised in terms of power output, W_{cell}. The W_{cell} of a fuel cell corresponds to:

$$W_{cell} = (V_{cell})(I_{cell}) \qquad \textbf{Equation 1}$$

where V_{cell} and I_{cell} represent cell voltage and cell current respectively. This equation corresponds to a cell running at constant current which represents performance in an ideal case, since current can change over time due to rate limitations, the following relationship is usually used:

$$W_{cell} = V_{cell} \int I \, dt \qquad \textbf{Equation 2}$$

According to the equations above, the best fuel cells will be those operating at high voltages and able to maintain high currents. However, this is not so readily attained since high cell voltages are difficult to achieve as will be explained.

The maximum voltage associated with a fuel cell is known as the open circuit voltage (OCV) and is obtained when there is no current flow; the cell is understood to be at equilibrium. For a "perfect" fuel cell system, the OCV corresponds to the difference between the thermodynamic (equilibrium) potentials of the redox couples at the respective electrodes (anode and cathode), E_{eq}, adjusted for nonstandard conditions. As represented by the difference between the ideal voltage current responses, blue curves in Figure 3. This maximum voltage is given by:

$$E_{eq} = -\frac{\Delta G_{rxn}}{n\mathrm{F}} \qquad \textbf{Equation 3}$$

Where *n* is the number of electrons and F is the Faraday constant (96500 C mol^{-1}).

The Gibbs energy, ΔG_{rxn}, is an important thermodynamic function which defines the maximum amount of energy that can be derived from the cell reaction at a given temperature, T, as shown below:

$$\Delta G = \Delta H - T\Delta S \qquad \textbf{Equation 4}$$

$$\Delta G_{rxn} = \Sigma \Delta G_{products} - \Sigma \Delta G_{reac\,tan\,ts} \qquad \textbf{Equation 5}$$

where ΔH is the heat of the reaction (i.e. equal to calorific value of the fuel) and ΔS is the entropy change. Furthermore, the maximum thermal efficiency of a fuel cell, η_{thFC}, is often compared against Carnot's efficiency, $\eta_{thCarnot}$, for internal combustion engines, as shown below:

$$\eta_{thFC} = \frac{\Delta G}{\Delta H} \qquad \textbf{Equation 6}$$

$$\eta_{thCarnot} = 1 - \frac{T_2}{T_1} \qquad \textbf{Equation 7}$$

where T_1 is the temperature of the hot fuel state and T_2 is the temperature of the cooled fuel state (i.e. leaving the system via exhaust). The only way to increase the Carnot efficiency of a heat engine is to increase T_1, since T_2 is fixed. These theoretical efficiency values are expressed as percentages and are often higher than actual measured values because additional efficiency losses are disregarded, such as friction and heat losses for heat engines and voltage losses due to cell resistances in fuel cells, as will be explained.

For a BFC under open circuit conditions, the cell voltage is often lower than E_{eq} due to the redox potentials of enzymes (see Figure 3). Some enzymes operate near E_{eq}, while others require larger potentials to drive their chemical reactions. In addition, if electron mediators are used to shuttle electrons then these can further lower the potential, along with the temperature and substrate concentration.

When current flows, the loss in cell voltage from E_{eq} is described as polarisation, and the magnitude of this polarisation with respect to E_{eq} is defined as the overpotential, η, as shown below:

$$\eta = E_{measured} - E_{equilibrium} \qquad \textbf{Equation 8}$$

where η is always positive for the anode and negative for the cathode.

Therefore, the OCV for a fuel cell is determined by the difference between the onset potential for catalysis at both electrodes (Red line), as shown in Figure 3.

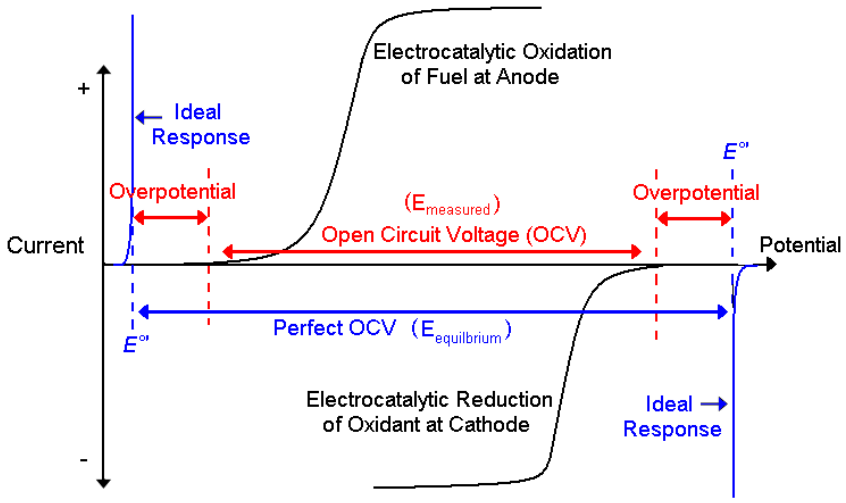

Figure 3: Representative current-voltage curves for a pair of electrodes tested sepearately. The redox potential of the cathodic enzyme is lower than the thermodynamic potential of the oxidant/reduced product redox couple, E_{eq}, thus a small overpotential is required to initiate the reaction.

Conventionally, this overpotential is considered as the sum of three rate determining steps: activation overpotential (η_{act}), ohmic overpotential (η_{iR}) and concentration overpotential (η_{conc})[16]. Each type of overpotential contributes to the overall shape of a current-voltage curve (or polarisation curve) for a fuel cell, as illustrated in Figure 4. Therefore, Equation 8 can be re-written as:

$$\eta_{total} = E_{measured} - E_{equilibrium} = \eta_{act} + \eta_{iR} + \eta_{conc} \qquad \textbf{Equation 9}$$

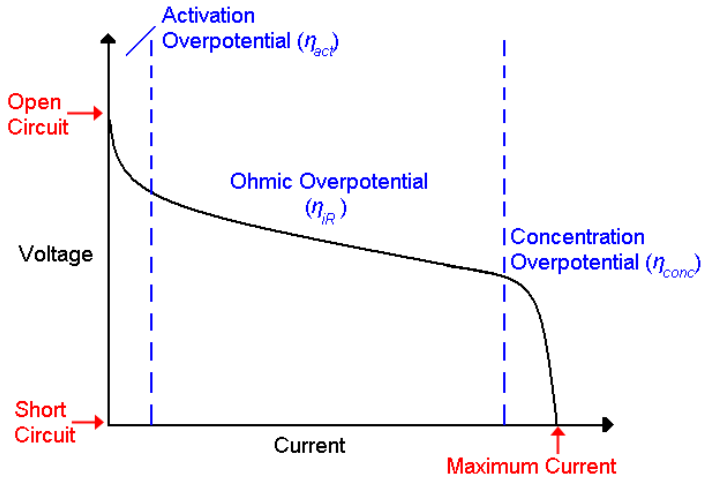

Figure 4: Representative polarisation curve showing the contribution of activation, ohmic and concentration overpotential on the shape of the current-voltage curve, respectively.

These irreversible potential losses can be described as follows:

-Activation losses occur at low currents and results from slow interfacial electron transfer. This first potential drop can be a result of poor electronic coupling of enzymes to the electrode, electrolyte double layer or imperfect cell conditions. Losses can be reduced by increasing enzyme loading, temperature, electrode surface area[17].

-Ohmic overpotential, or 'ohmic drop', is the result of various resistances in the electrochemical cell associated with the electrolyte, electrical connections and ion-conducting membrane (if used). Ohmic resistance losses can be addressed by minimising the inter-electrode gap or operating at lower current density, hence maximising the driving force (cell voltage) but limiting power density[18].

-Concentration overpotential describes the limitations due to mass transport. At large currents and especially at small overpotentials, the rate at which reactants and products move in bulk towards or away from the reaction sites becomes dominant[19]. This results in a maximum current, known as the limiting current, when the concentration of reactants approaches zero at the reaction sites.

The aim of all fuel cell research is to maximise cell voltage at any given current by minimising the value of these overpotential contributions. Fuel cells that operate at low cell voltages produce less power for a given current, however, depending on the required application (i.e. small low power devices) the fuel cell can still be fit for purpose. Often fuel cells operate at low cell voltages because the highest fuel cell currents are at low cell voltages, as shown in Figure 5. Furthermore, individual fuel cells are rarely used to power a single device and are therefore 'stacked' to achieve the required power level and minimise ohmic losses. In the extreme case, sometimes the fuel cell voltage is so low that when the anode and cathode are electrically connected, no useful work is done because there is no driving force for the catalytic reactions. This is generally termed as short circuit. Therefore, 'steady' fuel cells operate between open circuit and short circuit (see Figure 5).

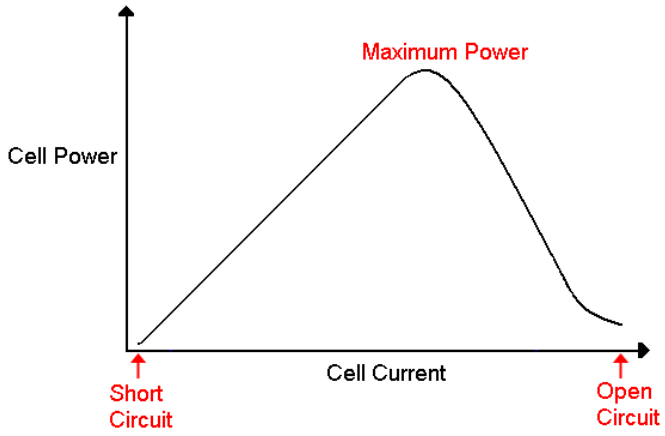

Figure 5: Representative power-voltage performance curve for a fuel cell detailing overpotential contributions to the overall voltage and power possible.

2.1.3 Current Limitations

Currently, BFCs are limited by their poor power density and short enzyme lifetimes, related to problems with electron transfer, enzyme stability and enzyme loading. Enzyme catalysis requires fast and efficient electron transfer across the enzyme-electrode interface. The efficiency of this interfacial reaction is dependant on the two sites having low reorganisation energies[20, 21] and being separated by a short distance. For example, the surface of the enzyme laccase and the primary

electron acceptor site (T1-Cu site) are separated by a distance of about 8 Å[22]. If correctly orientated on the electrode surface, such a distance would allow for efficient electron transfer with high turnover rates[23]. However, the fact that nature did not evolve enzymes for bioelectrocatalytic applications makes orientating the enzyme for effective electrical communication, as well as achieving long-term stability at the enzyme-electrode interface, two of the most difficult challenges in energy-related science.

In order to overcome these challenges, various immobilisation strategies directed at controlling enzyme orientation, stability and activity have been investigated; these are described in more detail in section 2.3.2.2. The most attractive method of immobilisation, as mentioned above, comes from engaging the direct electron transfer pathway through non-covalent adsorption or directed covalent attachment, so that no mediators are required. This method is only possible for enzymes with active sites or primary electron acceptor sites located near the protein surface (e.g. laccase, bilirubin oxidase). Only within the last few years has direct electrical communication been reported in biofuel cell systems using biocathodes containing laccase[5, 24] and bilirubin oxidase[25] and bioanodes employing glucose oxidase[26]. In all cases, the electrodes consisted of carbon networks, with the majority composed of 2D-CNT films, in which the small size, curvature and high surface areas, increased the chances of effective communication. In addition, CNTs have shown direct communication with glucose oxidase which has a buried active site[27].

Electrical communication can be further improved through the use of electron transfer mediators which help to shuttle electrons between the electrode surface and enzyme. Mediators are typically small organic dyes or organometallic complexes, which are either free in solution (i.e. diffusive) or attached along with the enzyme to the electrode (i.e. non-diffusive). Although mediators are useful for improving the electrical communication, especially for enzymes with buried active sites (which includes the vast majority), they also increase the complexity of the fuel cell system. There are many problems associated with mediators which are often overlooked including poor lifetimes and performance as well as handling and toxicity problems. Generally, immobilisation methods are often combined to

enhance performance and reduce component effects. For example, Heller and co-workers developed a method to co-immobilise the enzyme and mediator through using a redox hydrogel[28].

Essential for future application of BFCs is improving the long-term stability from days to months and then eventually years (for long-term implantable in-vivo devices). Hydrogels and sol-gels have shown improved stabilities with enzymes lasting 1-2 weeks with minimal loss of activity[14]. Currently, these miniature BFC systems are being considered for in-vivo devices since they meet the low power density requirements, however significant improvements in enzyme lifetime, enzyme stability and biocompatibility of redox hydrogels still remain to be addressed.

In order to maximise power density, it is essential that electrodes possess high surface area 3D-porous networks which support high enzyme loadings and mass-transfer of reactants. Carbon aerogels[29] and CNT-modified porous chitosan scaffolds[30] have shown potential in terms of the characteristics mentioned. Power densities around 1 mW cm^{-2} have been reported for the aerogel system, although this was measured under stirring and is still far from target figures of around 100 mW[31]. Deeper understanding of the complex enzyme reactions and incomplete oxidation of high density fuels (ethanol and glycerol) should further increase power densities. Recent work has shown that the immobilisation of enzyme cascades at anode surfaces could solve this problem[32, 33]. Finally, improvements in electrochemical characterisation procedures, such as combining spectroscopic methods with electrochemical testing, and using standardised test models are important steps in further developing BFCs.

2.1.4 Cell Design

Optimising the cell design of BFCs may greatly improve their performance and reproducibility, while also improving their commercial applicability. Most of the research to date utilises the traditional electrochemical H-cell design (Figure 6), which was designed to separate the two electrochemical reactions (half cell reactions) at the respective electrodes. These electrodes are usually separated by a Nafion® (ion-exchange) membrane which completes the circuit. However, this cell is often limited by mass transport resistances due to the cell geometry (i.e. large electrode separation) and low concentration and diffusion coefficient of O_2 in cathodic solutions. Commercial fuel cells incorporate the electrodes directly onto the membrane to avoid these limitations, however, this is impractical in research laboratories because electrodes and cell solutions are frequently changed.

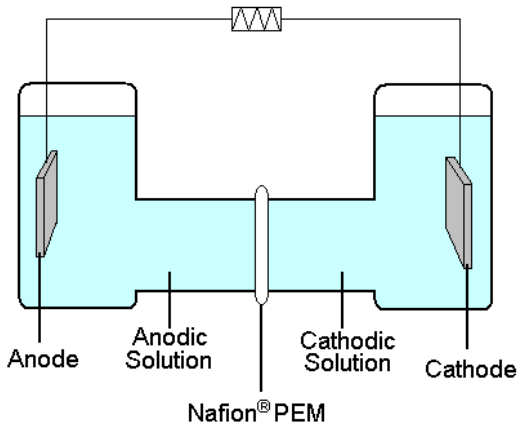

Figure 6: Schematic diagram of the most common electrochemical test cell used in the development of BFCs.

Using enzymes essentially removes the requirement for physical separation of anodic and cathodic solutions and provides the possibility for miniaturisation. Therefore, recent improvements have since been made to the traditional H-cell design and in terms of scale-up and cost, the concept of a single compartment BFC is very attractive.

Teodorescu *et al.*[34, 35] designed a miniature-stacked BFC to overcome the resistances mentioned above and reported an OCV of 1.57 V and power density of 0.35 mW cm^{-2} (six stacked cells). The cell performance was limited by diffusion of O_2 to the cathode due to its compact size and poor material selection. An intriguingly different BFC design involved implanting bioelectrodes directly within a grape, although due to its extremely small size it only produced a maximum power density of 240 µW cm^{-2}[36].

Recent work using microfluidic BFCs has produced promising results, despite the limited amount of research on these systems. Palmore *et al.* recently designed a microfluidic BFC using laminar flow boundary layers to provide cathodic (containing laccase) and anodic solutions (containing ABTS) to gold electrodes[37]. The device had a maximum power density of 26 µW cm^{-2} and OCV of 0.4V, the schematic of the design is shown below.

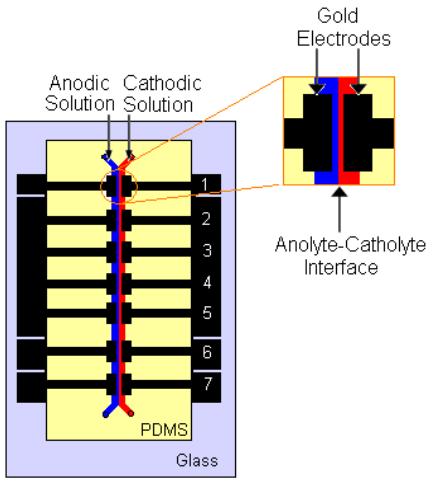

Figure 7: Schematic design of the microfluidic cell based on the work by Palmore *et al.*[37].

This design has many advantages, including a low production cost, small size and stacking capability, absence of resistive membranes and adequate capacity for fast and controlled transport of reactant mixtures. Further improvements to the design of this platform may eventually lead to commercially competitive BFCs.

It is also important to consider the design of the electrodes used in BFC systems in order to address the problems of power density and enzyme stability. Recent developments have moved from the conventional flat 2D-electrodes to the novel

highly organised nano-assembled 3D-electrodes resulting in higher enzyme loadings, higher currents and improved stability. These nanostructures have shown great promise but a few issues still impede their application such as quality, purity, conductive properties and adverse electrode kinetics. Thus further improvements in design and understanding are still required. The most important challenge is achieving effective electrical communication with the active site, which has been accomplished but not optimised through direct adsorption on nanomaterials.

Alternative immobilisations have been attempted through the use of mediators, covalent attachment methods or entrapment in redox polymers or gels. This removes enzyme orientation requirements, thus increasing the number of active enzymes. However, recent problems with long-term gel stability and leaching of components when in solution have hampered progress. Furthermore, it is important to consider the reproducibility of such designs (e.g. hydrogels are often unstable), the scalability and durability of these systems, as well as the associated production costs. These practicalities should be considered when investigating and developing such BFC electrode systems.

The simplest approach would be to use genetically engineered enzymes that would function optimally at the electrode surface, thereby eliminating the need for redox mediators. However, this still remains a long-term and challenging goal that is yet to be accomplished.

2.1.5 The Role of Nanostructure

Currently, the performance of BFCs is limited by their poor power density and short enzyme lifetimes. However, recent advances in nanoscale science and technology has introduced new levels of BFC performance and revitalised the field of bioelectrochemistry. Since many of the controlling aspects of performance are size-dependant there has been great interest in the development of novel nanostructured materials owing to their high surface area, enhanced kinetics and novel size-effects[38]. This section will focus on the benefits of such materials and

highlight some of the recent developments made in the field of nano-biotechnology. Some of the following reviews were drawn upon due to their relevance to this topic[38-43].

For a BFC, the maximum electrocatalytic current achievable at either electrode is dependant on the electroactive coverage of enzyme and rate of catalysis per active site[44]. High enzyme loading is difficult on flat 2D electrode surfaces with typical monolayer coverage in the range of 10^{-9}-10^{-12} mol/cm^2[44]; even if the entire enzyme monolayer is active the maximum power output would only be in the low mA/cm^2 range. Nanostructured electrodes such as mesoporous materials, nanoparticles, nanotubes or nanocomposites offer significant improvements in performance due to the increased surface area to volume ratios, resulting in greater enzyme coverage. Power densities can be increased by up to an order of magnitude using such supports, which has brought BFCs into the power range of conventional low temperature alcohol fuel cells[35]. The small size of these structures also allows for effective electrical communication between enzymes and electrodes[45], while the nanomaterial properties can also enhance protein stability and influence the activity of proteins[46]. The nanoarchitecture of these electrodes is also critical in further improving the performance. A positive approach for energy conversion devices is the development of 3D electrodes based on appropriate nanoscale building blocks[39]. Achieving the correct 3D orientation of the nanostructures is necessary to coordinate mass and charge transport and facilitate electron transfer kinetics.

Various nanostructures have been investigated as potential electrode materials for BFCs, such as mesoporous materials, nanoparticles, nanofibres and nanotubes. In all these materials, the performance will depend on a combination of the size, shape and characteristics of the material, the nanoarchitecture and hierarchical organisation, and the electronic properties (or 'true-size' effects)[39]. The relative complexity of this problem, coupled with understanding enzyme behaviour on these supports continues to hamper BFC performance.

Much interest has been given to mesoporous materials because of their controlled porosity, high pore volume and high surface areas. In fact, there have been

encouraging results with regards to enzyme stabilisation due to the development of novel structured scaffolds combined with established enzyme immobilisation methods. Recent work by Kwon *et al.* demonstrated the stabilisation of glucose oxidase in mesoporous carbon by enzyme adsorption and then enzyme crosslinking[47]. The 'bottle-neck' structure (i.e. small outer pores and large inner pores) of the mesoporous scaffold along with cross-linking prevented enzyme leaching and allowed for high enzyme loadings. However, the maximum power density output was only 14μWcm^{-2} under stirring and with addition of mediators. Recent experiments using mesoporous electrodes are still at a fundamental stage and further improvements are required, especially in improving the conductivity of the mesoporous electrodes.

Enzyme immobilisation onto conductive nanoparticles such as carbon black and graphite powder has recently gathered interest. Carbon black is often used as a support for Pt nanoparticles in PEM fuel cells, providing high dispersion of the Pt nanoparticles while maintaining conductivity. Habrioux *et al.* used a similar approach to construct a BFC with Au-Pt nanoparticles supported in a Nafion/carbon black mix, together with the oxygen reducing enzyme bilirubin oxidase and its mediator 2,2'-azinobis(3-ethylbenzothiazoline-6-sulphonic acid) (ABTS)[48]. This BFC combined the high stability and good catalytic activity of the platinum inorganic catalyst with the superior O_2 kinetics and low operational temperature of biological catalysts to produce a maximum power density of 0.19mWcm^{-2} at 0.52 V (37 °C and pH 7.4). Recently, silicon nanoparticles have also been used as electrocatalysts with great effect, for the electrooxidation of glucose[49]. The advantage is that each particle provides a large surface area per unit mass; however, the high surface energy of these nanoparticles can result in agglomerates which are difficult to disperse. Therefore, the implementation of 3D nanoparticle assemblies is not practical due to particle agglomeration and poor electron conduction pathways in comparison to assembled CNTs, as shown in Figure 8. Deng *et al.* recently compared the response of a flat electrode, with an electrode containing an increasing number of Au nanoparticle-bilayers[50]. Maximum current and power output was reached after the addition of five bilayers due to mass transfer resistances, and the lower cell voltage, compared to the flat electrode, was attributed to the higher electrical resistance due to particle build-up.

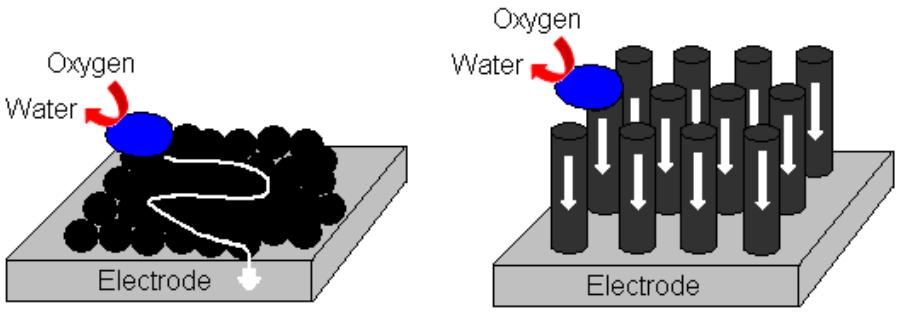

Figure 8: Schematic model of the differences in electron path between thin films composed of carbon black nanoparticles and nanostructured aligned carbon nanotubes (aCNTs).

The majority of the nano electrode materials reported comprise of CNTs. These CNT electrodes include 'buckypapers' (i.e. random entangled network of CNTs), self-assembled monolayers through chemical functionalisation, and vertically aligned CNT arrays. The latter structure has gathered most interest for energy conversion due to the longer and uninterrupted paths for electron transport compared to nanoparticle assemblies (see Figure 8), larger surface areas and uniform mesopores for high enzyme loadings and fast mass transport. CNTs have shown superior performance compared to other carbon materials. Their high-surface area-to-volume ratio increases current by engaging more enzyme molecules and their small size enables close proximity to the active site, thus allowing direct communication with the enzyme. However, the reported 'electrocatalytic' properties of CNTs are somewhat controversial due to the influence of impurities (i.e. residual metal catalyst and carbon contaminants) and defects such as surface defects edge-plane sites which behave as catalytic sites improving electrocatalytic performance. Further improvements are still required, such as understanding the electrocatalytic behaviour of CNTs, enzyme stability and development of structures for mass and charge transport.

It is evident that nanomaterials have shown great promise in overcoming the problems concurrent to BFCs as result of their favourable properties such as their high surface areas, small size and good electrical conductivity. However, there are important aspects which still need to be addressed, these include: i) long-term enzyme stability on electrodes ii) optimisation of nanostructures and surface modifications, iii) scalable, reproducible, durable and cost effective materials.

Recent developments in the synthesis of 3D electrodes and high controllability of the processes allows for the production of structures with optimally organised nanostructures. Furthermore, the scalability of these production methods already adds one step towards commercial realisation.

2.1.6 Examples of Enzyme Biofuel Cells and Potential Applications

The nature of employed catalysts in BFCs allows the utilisation of numerous fuels including various sugars and alcohols[43]. Many oxidants are also possible, although O_2 is often favoured due to its high potential and abundance. Given that BFCs generally only differ in the fuel employed, this section will describe the different types of BFCs on this basis. These cell systems will also be described in terms of their performance and improvements necessary for their target applications. Although, directly comparing the performance of these BFCs is often difficult due to the variety of experimental conditions, such as fuel concentration, mass transport conditions etc.

Currently, the majority of BFCs are based on glucose and oxygen due to their intended *in-vivo* applications. Glucose oxidation is often catalysed by glucose oxidase (GOx) and oxygen reduction catalysed by laccase or BOD. Systems employing GOx are typically mediated, although, some studies have claimed direct electrical communication using carbon nanomaterials[26]. Heller's group first introduced osmium (Os)-based redox hydrogels as mediators and immobilisation matrices to improve enzyme electron transfer and stability[28]. Subsequently, his group has published a series of papers employing glucose oxidase (GOx) as the anodic catalyst and either laccase or BOD as the cathodic catalysts supported on Os-polymer modified carbon fibers (7 μm diameter and 2 cm length)[14, 51-53]. These reports have shown that replacing laccase at the cathode with BOD allows the cell to function in physiological buffer and without chlorine inhibition. An interesting paper implanted these electrodes in the centre of a living organism (a grape), where it produced a maximum power density of 47 μW cm^{-2} and 240 μW cm^{-2} when located near the skin, due to the higher O_2 concentration[36].

In addition to GOx-based BFCs, other common enzymes that catalyse glucose oxidation include glucose dehydrogenase (GDH) and cellobiose dehydrogense (CDH)[43]. The advantage of these enzymes is that the natural electron acceptor is not O_2, as such these systems are not limited by low anodic currents and hydrogen peroxide accumulation like GOx-based BFCs. This approach also permits membrane-less configurations, although GDH requires a soluble cofactor nicotinamide adenine dinucleotide ($NADH/NAD^+$), as such these enzymes are not considered for implantable applications and will not be discussed further. In regard to CDH, Gorton and collaborators recently reported a membrane-, mediator-, cofactor-less glucose-O_2 BFC with CDH and laccase adsorbed on graphite electrodes[54]. Unfortunately, the cell performance was better in the presence of its natural sugar substrate cellobiose compared to glucose. However, CDH has shown great promise as an alternative to GOx for future BFC applications, displaying direct electron transfer properties, low O_2 sensitivity and flexibility towards oxidising different sugars for in-vitro devices.

In summary, glucose-O_2 BFCs based on electrodes containing osmium-based redox hydrogels have demonstrated superior performance, however, their focal purpose as implantable BFC devices is still long-term due to their short lifetimes and possible toxicity from the osmium.

Aside from glucose and other sugars, fuels such as alcohols (methanol and ethanol) and glycerol have been used in BFCs. These fuels are readily available from biomass and have shown great promise for portable electronic devices due to their high energy densities. Palmore *et al.* developed the first BFC to completely oxidise methanol to carbon dioxide using a multi-enzyme cascade reaction involving dehydrogenase and diaphorase enzymes in solution[55]. This anode was combined with a platinum cathode which catalysed oxygen reduction to water. The methanol-O_2 BFC produced a power density of 680 $\mu W\ cm^{-2}$ and an OCV of 0.8 V. Unfortunately the cell required a membrane to separate both electrode compartments due to the presence of soluble cofactors and the platinum cathode.

Another enzyme cascade reaction has been reported by Minteer's group in the development of an ethanol-O_2 BFC. The fuel cell used a Nafion matrix to

immobilise the enzymes on the carbon electrodes and coupled the reduction of O_2 by mediated BOD with the oxidation of ethanol to acetate by dehydrogenases[56, 57]. In a membrane-less setup, the ethanol-O_2 BFC had an OCV of 0.51 V and power density of 390 μW cm^{-2}, with a membrane, a higher voltage and power density was achieved (0.68 V, 830 μW cm^{-2}). More recent work by Yan *et al.* demonstrated ethanol oxidation through the immobilisation of alcohol dehydrogenase to NAD^+-SWNTs on a glassy carbon electrode[58]. The anode combined with a cathode containing a Pt-BOD crosslinked composite achieved a maximum power density of 200 μW cm^{-2} at 0.55 V.

Recently, glycerol has attracted increasing interest as a novel fuel for BFCs due to its high energy density (> alcohols) and abundance (by-product of biodiesel). Using a similar multi-enzyme system for glycerol oxidation, Minteer and coworkers immobilised dehydogenase enzymes in a neutralised Nafion membane for the complete oxidation of glycerol to carbon dioxide[59]. A maximum power density of 445 μW cm^{-2} was achieved. This work, along with others previously discussed, highlights the importance of immobilising enzyme cascades at the electrode surface, to decrease mass transport limitations and allow for complete oxidation of fuels.

Finally, there have been recent reports of H_2-O_2 BFCs using hydrogenases to catalyse the oxidation of hydrogen. Armstrong and coworkers employed the membrane-bound hydrogenase from *R. eutropha* HI6 coupled with a laccase cathode to produce a membrane-less BFC[60]. The cell gave an OCV of 0.95 V and a power density of 7 μW cm^{-2}, but decreased when O_2 was brought near the anode, possibly due to hydrogenase inhibition and/or O_2 reduction. In contrast to conventional Pt-based catalysts, these systems can operate solely on air mixtures and with high tolerance to carbon monoxide (CO)[61]. The performance can be further improved through adopting 3D porous nanomaterials and using hydrogenases with high O_2 tolerance.

In summary, the market-use of BFCs is currently limited to low power niche applications, the most obvious ones being self-powered sensors, temporary implantable devices, and miniature membrane-less fuel cells for portable

electronic devices. Enzymes are highly suitable for implantable systems due to their unique properties (high catalytic activity and selectivity) and the demand for miniaturisation of biomedical devices makes BFCs ideal candidates. Currently, the highest powered glucose-O_2 BFC generates ~1 $mWcm^{-2}$[31] which is already more than enough power for a cardiac pacemaker. Before these systems become viable, however, significant improvements need to be made in enzyme stability and many *in-vivo* trials need to be conducted. In regard to general power, the emergence of BFCs will never threaten the current high-energy power systems of today in terms of power output and stability. The long-term goal for BFCs is to produce small portable electronic devices. Sony have already demonstrated the possibility of powering small electronic devices, such as MP3s, using sugars from Coca-Cola (based on Sakai's work[31]) and further developments in these systems could make them commercially available.

2.2 Carbon Nanotubes

2.2.1 Introduction to Carbon Nanotubes

Since their discovery, carbon nanotubes have been one of the most intensively studied materials in science. However, it is not absolutely clear who deserves the credit for their discovery and this uncertainty probably explains why no Nobel prizes have yet been awarded in this area. To this date, the most credited and recognised scientist is Sumio Iijima, an electron microscopist working in Japan, who first published images of perfectly structured carbon nanotubes produced by arc-evaporation. Interest in carbon nanotubes exploded following this publication of Ijima's paper in Nature in 1991[62]. CNTs have since been reported to possess extraordinary properties, with mechanical stiffness' greater than steel[63, 64] and very high conductivities within metallic or semiconducting states[65]. Over this period, a wealth of information has been gathered on not only their outstanding physicochemical properties, but also on how to attach things to the outside of tubes, put things inside, manipulating the tubes into defined arrangements or even incorporate them into varied matrices (polymers, ceramics, metals etc.)[66].

The synthesis of multi-walled nanotubes (MWNTs) has proven to be significantly easier than the single-walled nanotubes (SWNTs), with a world-wide capacity for ~ 4000 tonnes/year of MWNTs. This recent commercial scale-up of the production of MWNTs, means that commercial products are beginning to be realised, initially in specialised areas. Presently, the highest demand for nanotubes comes from their use as components in lithium ion batteries[38]. MWNTs have also found use as fillers in composites for anti-static applications for clean room and fuel line applications. The associated cost of high quality SWNTs is currently around $100 per gram, compared with $30 per gram for gold[66]. Therefore, their applications are still limited to research and development.

2.2.1.1 Morphology

The allotropes of carbon include diamond, graphite, glassy carbon, fullerenes and nanotubes. These carbons tend to be classified into two groups containing, either saturated sp^3 hybridised bonds (e.g. diamond) or unsaturated sp^2 hybridised bonds (e.g. graphite).

The structure of graphite consists of individual two-dimensional layers ("graphene") of carbon atoms hexagonally arranged with sp^2 bonds, which are the strongest bonds known. The most crystalline form of graphite is highly oriented pyrolytic graphite (HOPG). The HOPG lattice consists of individual two-dimensional layers of hexagonally arranged carbon atoms stacked on top of each other, with an interlayer spacing of 3.35 Å (Figure 9).

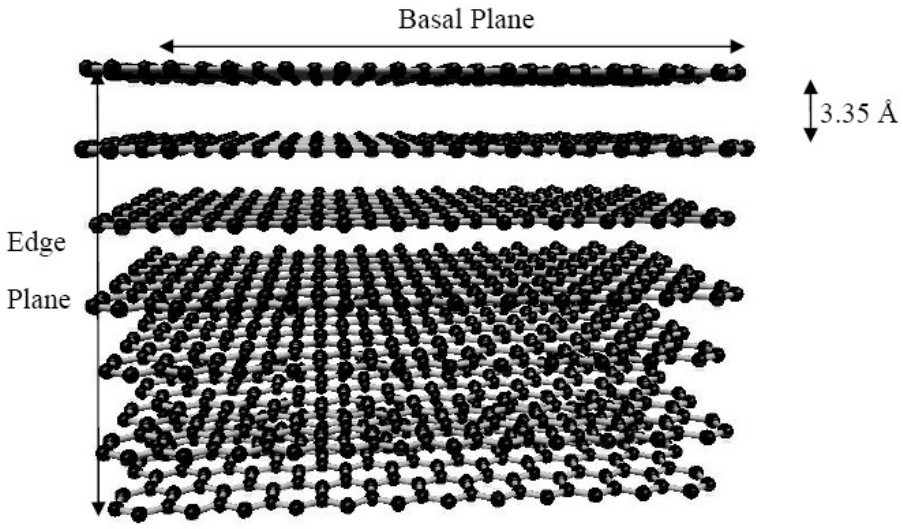

Figure 9: Representative image of HOPG consisting of several individual graphene layers which are stacked to from bulk graphite[1].

[1] All molecular model images were created using Nanotube Modeler Software version 1.7.0, www.jcrystal.com

In the graphene layers each carbon atom is trigonally bonded to the three nearest neighbours by means of sp^2 hybridised orbitals which form the strong covalent C-C (σ) bonds. The overlap of the un-hybridised p-orbitals from each carbon atom forms the delocalised π-bonds. The overlapping orbitals produce a fully conjugated system, providing fast electron transfer between the layers. This delocalisation gives graphite its anisotropic nature; attributed to slow electron transfer perpendicular to the basal plane (one reason why electrochemical studies are conducted on graphite edges rather than basal planes). Each individual layer interacts with its neighbouring layers by weak van der Waals forces. This weak bonding allows the layers to slide across each other easily; this is routinely demonstrated by writing using graphite pencils. Mechanical cleavage of single atomic layers of graphite, known as graphene, has recently been achieved by Geim and co-workers[67]. These graphene layers have received huge interest, mainly due to their extremely small dimensions and unique electronic properties.

A carbon nanotube consists of one of more tubes of graphene with nanoscale dimensions and lengths. The ends of the tubes are ideally 'capped' by hemispheres of fullerene molecules.

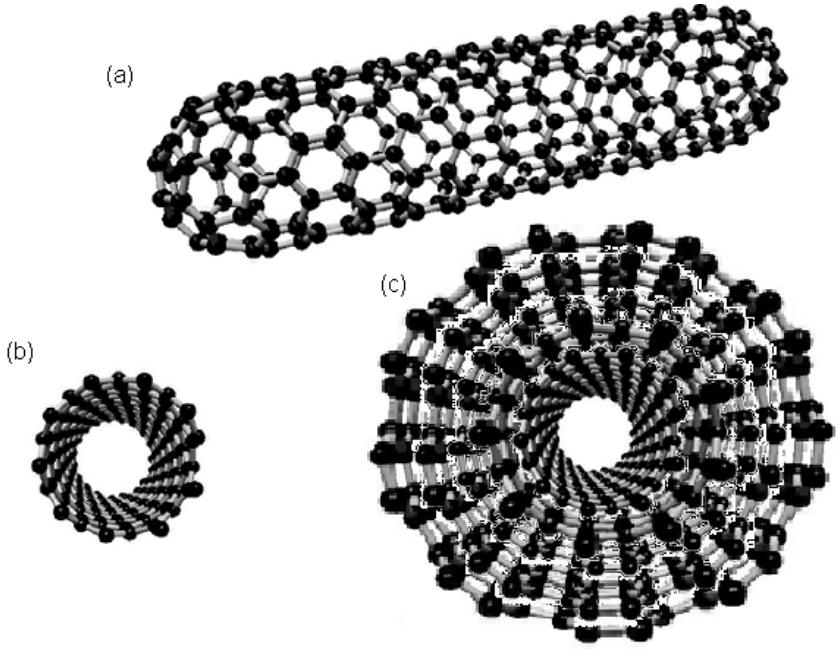

Figure 10: Images of (a) Hemispherically capped SWNT (b) Cross-section of SWNT (c) Cross-section of MWNT consisting of five concentric walls.

Two main types of nanotubes exist: single-walled carbon nanotubes (SWNTs) which are composed of a monolayered cylindrical sheet of carbon and multi-walled carbon nanotubes (MWNTs) that have several layers (2-50) of cylindrical sheets of graphitic carbon usually separated by distance of 0.34 nm, similar to the interlayer spacing in HOPG. Both of which are displayed in Figure 10. SWNTs have diameters between 1 to 2 nm, with the smallest observed at 0.5 nm, and MWNTs from 1.4 to 100 nm. The lengths of SWNTs and MWNTs are usually on the order of microns to tens of microns. However, catalytic vapour techniques have significantly increased nanotube lengths, with 4 cm lengths recently reported for SWNTs[68] and >18.5 cm for MWNTs[69].

The symmetry of a nanotube's wall is referred to as the nanotube's chirality. These structures are defined by the vector (n,m) which characterises the nanotube from the way the graphene layer is conceptually rolled up to form it. A typical nanotube is specified by the chiral vector:

$$C_h = na_1 + ma_2 = (n,m) \qquad \textbf{Equation 10}$$

where C_h is the chiral vector, a_1 and a_2 are the graphene lattice vectors and n and m are integers.

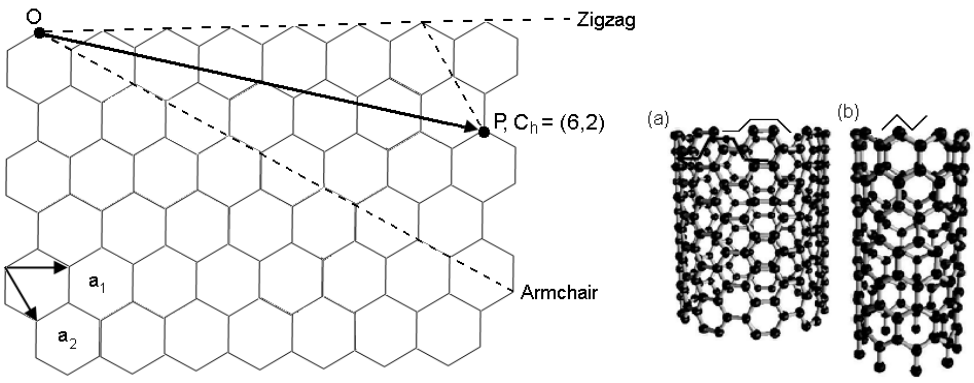

Figure 11: (Left) Determination of carbon nanotube chirality based on the folding of an imaginary graphene sheet using the chiral vector nomenclature. (Right) (a) Armchair and (b) zig-zag nanotubes.

Using the chiral nomenclature (Equation 10) and Figure 11, the different tube chiralities can be described. Through joining points O and P together, the C_h can be calculated. The length of the C_h determines the tube diameter and the angle between C_h and the (n,0) lattice vector, the chiral angle θ, determines the helicity. The three structures are known as 'armchair', 'zig-zag' and 'chiral'. When m=0 and θ = 0°, the nanotube is 'zig-zag', and when n = m and θ = 30°, the nanotube is 'armchair'. Both 'armchair' and 'zig-zag' have a high degree of symmetry and the terms refer to the way the hexagons are arranged around the circumference of the nanotube, as shown in Figure 11, all other tubes are determined to be 'chiral'.

The chiral angle dictates the diameter and the electronic structure of the layer. All 'armchair' single-walled tubes are metallic and 'zig-zag' and 'chiral' are metallic when n is divisable by 3 and n – m = 3 or a multiple of 3. Thin MWNTs have multiple layers of differing chiralities and are therefore more complex due to the overlapping contributions of each individual layer. However, it is known that only one concentric tube needs to be metallic for the overall electronic properties to be essentially metallic[70]. Whereas, large diameter MWNTs lose their quantum confinement effect and behave as graphite. This will be further discussed in the following section.

2.2.1.2 Electronic Properties

An electric current arises from the flow of electrons within a solid material and the magnitude of this current is strongly dependant on the number of electrons available in the conduction process. Solid materials form a diverse range of structures, crystal structure and chemical bonding that affects the number of electrons available for conduction. For each individual atom within the solid there exist electrons arranged in certain states or levels with respect to energy, and the manner in which these states are occupied by electrons influences the electronic properties of the material[71]. Understanding the concepts behind the behaviour of electrons in atoms and crystalline solids involves the discussion of quantum-mechanical concepts which is beyond the scope of thesis. However, the fundamentals of these concepts will be discussed below.

The electronic properties of solids are dependant on the arrangement of electrons in these outermost electron bands and the way in which these are filled. This is usually best described in terms of the band model[16]. Simple band structure diagrams allow the broad distinction between conductors, semiconductors and insulators to be understood, as highlighted in Figure 12.

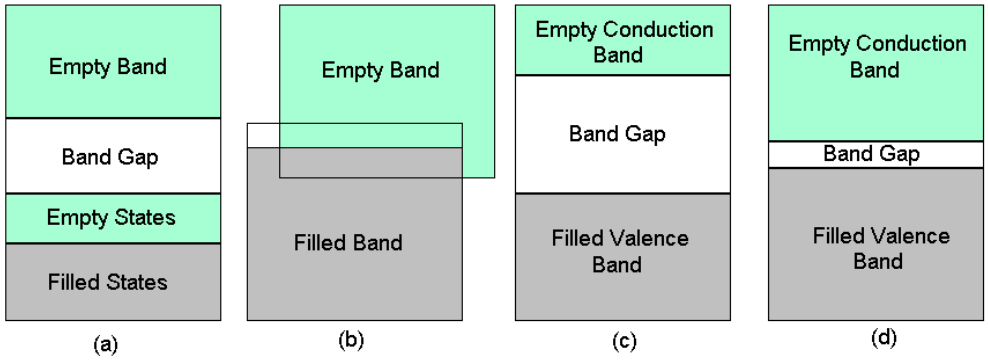

Figure 12: Various possible energy band structures for solids at 0 K, where (a) metals (e.g. copper) with empty electron states adjacent to filled states in same band, (b) metals (e.g. magnesium) where filled and outer empty bands overlap, (c) insulators where large band gap (>2 eV) separates the filled valence and empty conduction bands, and (d) semiconductors which is similar to insulators but wth smaller band gap (<2 eV).

It can be noticed that four different types of band structures are possible at 0 K (i.e. temperature where electrons have minimal energy). For metals having the band structures shown in Figures (a) and (b), the promotion of an electron from the highest filled state to the vacant energy state requires little energy, both occupied and vacant states are present at energies near the Fermi energy or Fermi level, E_f, which is the energy corresponding to the highest filled state at 0 K. It is understood that electrons can only be promoted with energies greater than Fermi energy, therefore metals only require the presence of an electric field to excite large numbers of electrons into these conducting states due to the small energy requirements or overlapping of the orbitals (energy states).

For insulators and semiconductors, there exists an energy gap between adjacent states, as shown in Figures (c) and (d). In order to promote an electron into the conduction band the energy difference between these states needs to be met, hence the larger the band gap the more difficult it is for a valence electron to be promoted. Thus the distinction between insulators and semiconductors lies in the

width of the band gap; for semiconductors it is narrow, whereas for insulators it is wide. Furthermore, the atomic bonding between atoms in insulators and semi-conductors also contributes to the conductivity. The bonding in insulators is ionic or strongly covalent, thus the electrons are highly localised because they are ionically bound or covalently shared with the nearest atoms. While in semiconductors the bonding is mainly covalent and relatively weak, these electrons can be promoted more easily since it requires less energy. For an intrinsic semiconductor, the Fermi level usually lies halfway between the conduction and valence bands.

In the context of heterogeneous electron transfer, (i.e. from an electrode to an electroactive species), similar principles are applied to those stated above. In a reduction reaction, the electron transfer process only takes place once the occupied energy state of the electrode is matched in energy with the unoccupied receiving state on the reactant. For a metal there is a range of electron energies available for electron transfer over the electrode area. Metallic electrodes are known to have a high density of states and therefore electrons are readily available for electron transfer to the electroreactant.

Semiconductors are the opposite extreme to metals, since the presence of the band gap region leaves zero density of states for electron conduction and hence transfer to the electroreactant. This means that any reactant with a formal potential in the band gap region will not undergo a reaction.

Various techniques have been used to determine the electronic properties of nanotubes, such as scanning tunnelling microscopy and scanning tunnelling spectroscopy. Work by Wilder[72] and Odom[73] confirmed that the electronic nature of the nanotubes depended on their structure. Furthermore, the conducting nature of the nanotubes has been demonstrated to vary along the length of nanotube due to the presence of structural defects[65]. It was also found that the curvature of single-walled nanotubes can have a small but significant effect on the electronic properties[74]. For non-armchair metallic nanotubes with diameters (d) larger than 20 nm, the band gap becomes negligible and the magnitude has shown to be proportional to $1/d^2$. While, for most single-walled nanotubes a band gap on

the order of 10 meV can occur because of displacement of the Fermi point. However, using these nanotubes electrochemically, Heller *et al.* found that even if the redox potential of the electroactive species falls within the band gap, and the Fermi energy also falls within the gap (although it can be increased to higher energies when applying external negative potentials), electron transfer is still apparent due to electron tunnelling occurring at energies not equal to the Fermi energy[75].

Electron transport behaviour in metallic carbon nanotubes is akin to a quantum wire due to limitations on the allowed electronic states as a consequence of the helicity and diameter of the tube, which results in conduction through well separated discrete electron states. The transport along the tube can also be ballistic in nature meaning that electrons pass along the full length of the nanotube without experiencing any scattering from impurities or phonons, effectively there is no resistance to the current. This quantum wire behaviour has been observed in both single-walled and multi-walled nanotubes[76, 77]. Electron transport in semiconducting single-walled nanotubes is more complicated, with scattering processes still not fully understood and therefore are not considered as being ballistic but diffusive in nature.

2.2.1.3 Spectroscopic Properties

In a spectroscopy experiment, radiation is used as a probe of the properties of a system. The source (probe) can be X-rays, laser light (visible and infrared radiations), neutrons, electrons etc. Infrared absorption and Raman spectroscopy (or Raman Scattering) are popular spectroscopic techniques which provide information on phonons in condensed matter. However, light absorption techniques such as infrared are rarely conducted on black carbon materials due to their ability to absorb light across a wide range of wavelengths. By contrast, Raman spectroscopy has been used as a powerful tool for the analysis of carbon materials providing a deep insight into the vibrational properties, electronic states and elastic states of a system. In this section, the fundamentals of Raman scattering in carbon nanotubes will be discussed. For in depth discussion of Raman spectroscopy of nanotubes the reader is directed to a review by Dresselhaus[78].

Raman spectroscopy is a light scattering technique, which is based on the presence of a small fraction of photons in laser light which are inelastically scattered upon interaction with a sample. This Raman effect is known as inelastic scattering, the scattered photons either lose or gain energy depending on whether phonons are created or absorbed in the material. Usually, the scattered photon will have a lower energy (longer wavelength) than the incident photon and the energy difference between them is termed the Raman shift (cm^{-1}). In essence, the Raman Spectrum is a plot of intensity of scattered light versus the change in wavenumber difference, the latter of which is proportional to the energy of the phonon. This is further explained in section 3.2.1.

In carbon based materials, there are two main lattice vibrational modes (or phonons), which can be observed as peaks in the Raman spectra. The G peak is a first-order phonon mode, observed at 1580 cm^{-1} and is associated with the in-plane vibrations of the graphene sheet (i.e. stretching of the C-C bond), as shown in Figure 13 (a). The D peak is a second order two phonon scattering peak, observed at 1350 cm^{-1}, and relates to the defects in the structure. Carbons containing sp^2 hybridised atoms present the G peak and G and D peak positions

are known to vary slightly between them. Ratios of the D peak to the G peak are often used to assess the 'quality' of structures (crystallinity). For example, the smaller the D:G intensity ratio (I_D/I_G) the fewer structural defects present and vice versa. Carbon materials such as HOPG and graphene typically contain no D peaks due to their high structural crystallinity, while glassy carbon, a typically disordered graphitic material, contains high I_D/I_G ratios. The effectiveness of CNT purification treatments is usually determined by changes in these ratios.

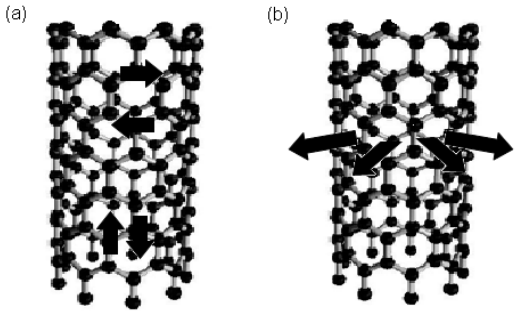

Figure 13: Schematic picture showing the atomic vibrations for (a) the G-band and (b) RBM modes. (RBM is a unique phonon mode appearing only in spectra from SWNTs).

Other second-order peaks are also present in the Raman spectrum of carbon materials. The maxima are positioned around 2600 cm^{-1}, which is assigned to the second order harmonic of the D mode, known as G'or 2nd D. This G' peak can be present in all carbon materials and independently of any structural defects present in the material. Further second order modes can be found between 1700 and 1800 cm^{-1}; these are not of great value when characterising nanotubes[66].

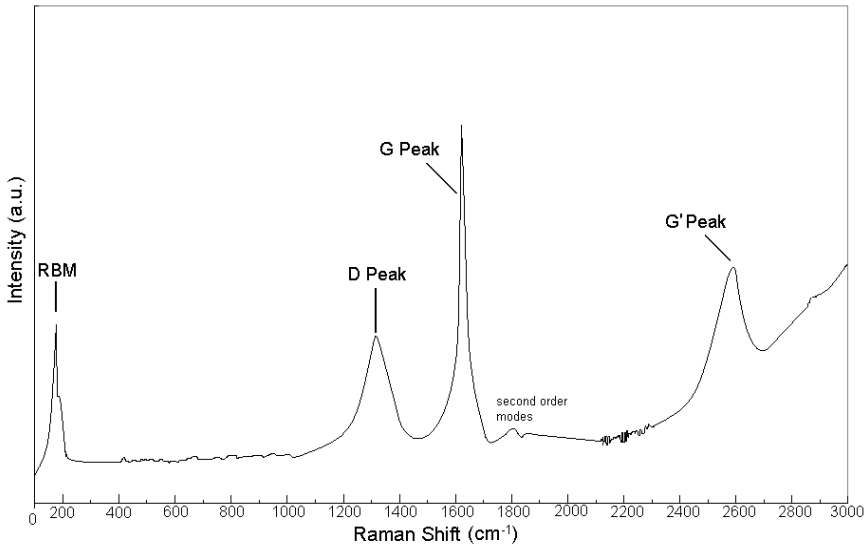

Figure 14: Example Raman spectrum for a SWNT sample.

Usually the Raman scattering signal is weak due to the spectra only involving phonons explicitly; this results in small spectra peak intensities. However, single-walled nanotubes have shown to improve the scattering efficiency and produce stronger spectra through resonance enhancement (see Figure 14). The one-dimensional nature of SWNTs can be characterised by their density of states displaying sharp spikes with large intensities, known as van Hove singularities (vHss), see Figure 15 (a-c). If the energy difference between these vHss , known as the optical transition energy (ΔE_{ii}) (see also Figure 15 (d)), matches the laser energy to approximately ± 0.05 eV, an enhanced Raman signal can be achieved.

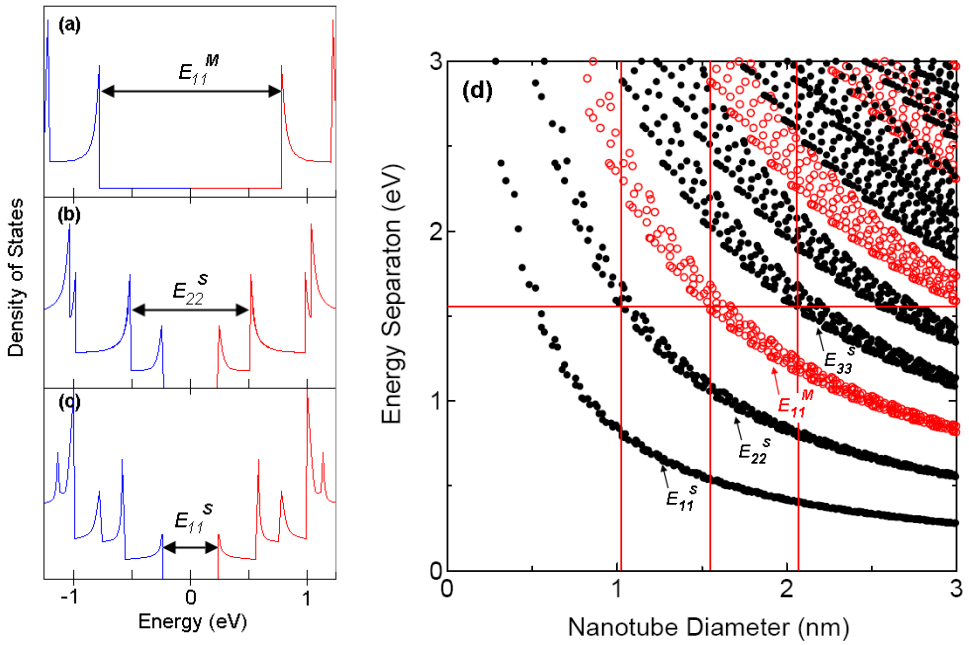

Figure 15: Example of DOS for SWNTs corresponding to (a) armchair (10, 10), (b) chiral (11,9) and (c) zigzag (22,0). (d) Kataura plot of electronic transition energy for all the (n, m) SWNTs as a function of nanotube diameter (data for plot obtained from S. Murayama[79]).

SWNTs also display an additional unique phonon mode which is useful in characterising its presence within a bulk sample. Rao *et al.*[80] discovered that this phonon mode is observed as a low frequency peak (<200 cm^{-1}). The peak in this region is known as the radial breathing mode (RBM) and corresponds to the expansion and contraction of the SWNT structure in the radial direction, hence "radial breathing" (see Figure 13 (b) and 14). The frequency of the peak depends on the diameter of the nanotube. Usually, the Raman spectrum contains more than one peak assigned to tubes with different diameters due to difficulties associated

in isolating individual SWNTs. Although, Dresselhaus *et al.* recorded the RBMs for three different isolated tubes[81] and subsequently calculated their diameters using Equation 11 below. The relationship highlights that the frequency of the RBM, ω_{RBM}, varies inversely with tube diameter, d_t, (for nanotubes within 1 nm < d_t < 2 nm)[82, 83]:

$$\omega_{RBM} = \frac{248}{d_t} \quad \textbf{Equation 11}$$

where the constant 248 has units nm cm^{-1} and corresponds to isolated SWNTs, an offset value of 12.5 is included when the nanotubes are present in bundles[84, 85].

Once the tube diameter has been deduced it is possible to determine the chirality of the tubes using the Kataura plot[86] (Figure 15 (d)). The plot details the calculated optical transition energies for a large number of (n, m) tube structures. Since the observable Raman spectra come from tubes in resonance with the laser excitation energy, the plot can be used to determine the tube chirality for a given diameter (or RBM), as shown by the lines in Figure 15 (d). In addition, the electronic states can be determined because each energy band gap corresponds to either semi-conducting or metallic tubes over a range of diameters.

Raman spectroscopy has proven to be an extremely valuable tool for the study of nanotubes, although this refers mainly to single-walled nanotubes. For reasons being that the Raman spectra of bulk graphite and MWNTs are practically indistinguishable and provide limited structural information such as crystallinity. The large diameter of MWNTs means that the RBM signal is usually too weak to be observable[66]. Whilst, a spectrum at the single nanotube level is distinguishable from other carbons and more importantly provides information concerning tube chirality, tube diameter and electronic state.

2.2.1.4 Electrochemical Properties

CNTs have emerged as attractive electrode materials, hence show promise in a wide range of electrochemical applications. Much of the collected interest resulted from the reported "electrocatalytic" properties of these materials which are inherently unique to CNTs. Some of these properties include fast electron transfer kinetics and increased voltammetric currents. However, these claims are often made without any fundamental understanding behind the electrochemical and "electrocatalytic" activity of CNTs. As a result, there have been numerous conflicting reports and this review aims to bring together the most relevant and recent literature to explain the key developments in CNT electrochemistry and identify any potential gaps in our understanding. The following reviews were referred to[40, 70, 87-89] and related topics were referenced where necessary.

CNTs are analogous to rolled-up graphene sheets comprising of two distinct regions: the sidewalls and the tube ends. This planar configuration has been likened to HOPG, as such CNTs are assumed to have similar anisotropic electrochemical behaviours. The sidewalls are thought to resemble basal-plane HOPG and display slow electron transfer kinetics, while the nanotube ends resemble edge-plane HOPG and should therefore display high electrochemical activity. However, there exist many discrepancies in the literature over the electrochemical contribution of the sidewalls and tube ends of CNTs, as such this will initially be discussed.

Evidence that the CNT sidewall is electrochemically inert was first conveyed by Compton *et al.*[90], who studied the oxidation of NADH, epinephrine and norepinephrine using MWNTs- and graphite powder- modified basal plane pyrolytic graphite (either prepared by abrasive attachment or pipetted as a film). They found that both electrodes displayed almost identical electrochemical responses, suggesting an inherent relationship between surface structure and electrochemical activity. Comparing the responses of basal plane and edge plane graphite electrodes with those modified with MWNTs, they found that both edge-plane and MWNT electrodes had equivalent voltammetric responses[91, 92]. These results strongly suggested that edge-plane-like sites, defects that occur at the

nanotube ends or along the walls resemble the behaviour and fast electron transfer of edge-plane graphite. In other words, the electrochemical reactivity of MWNTs resides solely in these defects. Note that defects relate to any alteration in the CNT structure from its pristine condition. Common defects are sp^3 hybridised sites, which are the edge sites prone to oxidation, impurities (metal catalysts and amorphous carbon), Stone-Wales defects (rotated bonds), point defects (atomic vacancies) and open ends created from oxidative treatments. Further reports have supported these claims[93-95] and enhanced activities have been displayed by increasing the amount of originally defective tubes on an electrode surface[96] or by inducing defects with treatments such as acid, thermal or electrochemical oxidations[94, 97-99].

Given that analogies have been drawn on the electrochemistry between MWNTs and HOPG, similar assumptions have been made on SWNTs without consideration of differences in physicochemical properties. In the case of SWNTs, the increased curvature suggests increased chemical reactivity, due to the reduction in overlap between the p-orbitals on neighbouring carbon atoms involved in π-bonding[100]. Therefore, both the tube ends and sidewalls of SWNTs could be electrochemically active. Recent compelling evidence that the SWNT sidewall is in fact electrochemically active comes from studies by Heller *et al.*[101]. This study utilised SWNTs grown by catalytic CVD (cCVD) which generally contain fewer defects and impurities, thus assumed to be almost pristine-like. The group investigated ferrocene voltammetry on a single, pristine metallic SWNT connected at both ends, leaving only the sidewalls exposed to the electrolyte[101]. The electrochemical response of the sidewalls followed Butler-Volmer kinetics with electron transfer rates similar to typical metal electrodes. The experiment was also conducted on semi-conducting SWNTs and subsequently found to be similar, possibly due to the fast redox response of the couple employed given the potential range of the oxidation reaction. Further evidence of CNT intrinsic activity was demonstrated by Day and co-workers[102]. Electrodeposition of metal nanoparticles onto SWNTs from solution resulted in random and continuous distribution over the nanotube surface. This work highlighted that deposition was not localised to defect sites on the tubes and hence the entirety of the SWNTs are

active, as has been further confirmed using scanning electrochemical analysis[103]. Although, it must be noted in both reported cases the SWNTs were not fully characterised, therefore minor defects, could have played some part in the electroactivities observed. Improvements in sample characterisation was shown by Dumitrescu *et al.*[104], who compared the electroactivity and conductivity of 2D connected networks of pristine and chemically treated cCVD SWNTs. The nanotubes were treated by acid oxidation and oxygen plasma resulting in defects and opening of tube ends which become functionalised with oxygen-containing groups. Both oxidative treatments resulted in a reduction in network conductivity, probably due to the cutting of the tubes by acid oxidation and functionalisation of the sidewalls, however, an enhancement in dopamine oxidation was achieved over the pristine tubes. The improvements in electron transfer and adsorption were believed to occur at the oxygenated-surface functionalities[87]. Interestingly, Holloway *et al.* investigated the sidewall activity of high temperature annealed SWNTs and MWNTs. This treatment had the effect of healing any existing structural defects and thereby restoring the pristine structure, as characterised by high-resolution TEM and Raman spectroscopy[93, 100]. In both cases, the measurements displayed no sidewall activity. This highlights the complexity of carbon nanotube electrochemistry since different CNT sources, preparations, qualities, and processing techniques provide conflicting results. Furthermore, incomplete characterisations can convey false conclusions.

An important consideration not to be overlooked in CNT electrochemistry is the influence of metallic impurities. Since different CNT synthesis methods contain different grades of purity and even batch to batch variations in impurity, the user often applies a purification method prior to application. Typical established purification procedures involve oxidation in nitric acid or as a mixture with sulphuric acid, followed by washing in hydrochloric acid. However, even after extensive treatment the CNTs have still been shown to contain metallic nanoparticles. In fact, the most effective catalyst removal treatments involve high temperature annealing treatments at temperatures above 1000 °C, as employed by Holloway *et al.* [93, 100]. Recent studies have shown that the electrocatalyic properties can be attributed to the presence of metallic catalysts. Compton *et al.* illustrated that localised iron catalyst particles were responsible for the

electrocatalytic oxidation of hydrazine[89]. Furthermore, reports have suggested that different catalysts used in the growth and present in the material could induce different electrocatalytic responses to different redox couples[105, 106]. Recently, it has been shown that only iron-containing CNTs are responsible for the reduction of hydrogen peroxide when multi-component impurities are present, while all components were found to contribute in the oxidation of hydrazine[89, 107]. The catalyst contribution is further complicated when it was discovered that catalyst redox activity also varies with supporting electrolyte[108].

Finally, among other things often overlooked is the arrangement of the electrode material which can affect CNT 'electrocatalytic' behaviour. Work by Gooding and coworkers found that the oxidation of ferrocyanide was more effective at vertically aligned SWNTs compared to randomly dispersed 2D network[97]. Using acid shortened SWNTs, the peak separations were 59 mV (aligned) and 99 mV (dispersed) and hence electrochemical reversibility was claimed for the aligned electrode. Gooding concluded that the electrochemical properties were governed by the concentration of surface oxides presented on the open end sites and sidewalls, which was in higher amounts at the aligned electrode. McCreery and coworkers illustrated that ferrocyanide is surface sensitive but not oxide sensitive and therefore surface adsorption and differing CNT oxide concentrations can be ignored[87, 109]. Although, other studies have demonstrated that electron transfer properties are dependant on the amount of defects not concentration of surface oxides[110].

In summary, the field of CNT electrochemistry is vast and complex. The wide variance in sample purities, properties (electronic and physical) have led to many conflicting opinions in the literature. However, considering the detailed studies carried out by Compton *et al.*[93, 100] and Pumera *et al.*[88, 105, 106] it does appear that the electrochemical activity observed is strongly influenced by the presence of defect sites and impurities and thus these should always be accounted for when conducting nanotube electrochemical experiments.

2.2.2 Production Routes and Growth Mechanisms

2.2.2.1 Introduction

There are three main methods used to synthesise carbon nanotubes: arc-evaporation, laser-vaporisation and catalytic vapour deposition. All production methods have in common the breaking down (pyrolysis) of a carbon source and then reforming the carbon into carbon nanotubes. Catalysts are employed for the growth of single-walled nanotubes. However, multi-walled nanotubes can be produced with or without a catalyst. The production route can be optimised depending on the catalyst employed [111], with catalysts being used from Group VIII and Lanthanide series in the periodic table.

Commercial realisation of carbon nanotubes relies upon the bulk synthesis of high-quality carbon nanotubes with defined structures and controllable size and length distributions. Presently, only some of these criteria have been met due to the poor understanding of the nanotube growth mechanisms in these production processes.
Some of the advances made already include:

- Carbon nanotubes produced by the arc and laser methods produce tubes of high quality with controlled diameters.
- Catalytically produced nanotubes are grown under milder conditions giving more control over the growth process. Nanotube arrays can be grown with controlled lengths, diameters and in complex patterns.
- The bulk synthesis of catalytic nanotubes is already commercially known, with companies producing around 100 tons of multi-walled nanotubes per year.

These production processes are still limited by the following:

- Despite the arc and laser methods producing high quality nanotubes these techniques are limited by their scalability.

- High quality catalytic single-walled nanotubes can be produced in bulk, but the production volumes are inevitably rather lower compared to multi-walled produced nanotubes.
- These catalytically produced multi-walled nanotubes contain a large number of defects
- Although scaling of the reactors can improve quantity levels, the quality of the nanotubes can be compromised.

The nanotube quality can be described in terms of 'the amount of nanomaterial produced that is 'nanotubes'. The quality is usually determined using microscopic techniques such as transmission and scanning electron microscopy. The images can detail unreacted carbon or metallic catalyst impurities around or inside the nanotubes, structural damage to the nanotube walls, and also detail the diameters and lengths of the nanotubes. Spectroscopic techniques such as Raman spectroscopy has also become a powerful tool, especially for analysing single-walled nanotubes, where the relative intensities of peaks can be used to determine the structural and electronic nature of the tubes.

The following sections will detail the catalytic chemical vapour deposition technique for the production of multi-walled nanotubes and the proposed growth mechanisms of the process. The other nanotube production techniques will not be mentioned since these techniques were not experimentally applied in the thesis.

2.2.2.2 Catalytic Vapour Deposition (CVD)

Catalytic techniques are highly amenable to scale-up contributing to large-scale synthesis of both multi and single-walled carbon nanotubes. The nanotubes are grown from carbon containing gaseous compounds (i.e. hydrocarbon) which are reacted with a metal catalyst at moderate temperatures (≤ 1000 °C). The catalyst is present either in-situ from a precursor or pre-produced on a substrate. The latter is used to make aligned arrays of nanotubes.

2.2.2.3 Catalytic Synthesis of Multi-Walled Nanotubes

Two experimental approaches are used for the catalytic vapour method depending on the catalyst and carbon compound employed. The first involves a single-zone furnace, where the carbon compound is gaseous at room temperature and reacts across a catalytically treated substrate surface. The second approach involves a two-zone furnace. This involves using a catalyst in the vapour phase (e.g. metallocene) or pre-vaporising the hydrocarbon which is present in liquid or solid form in the first heating zone. This allows for nanotube growth on a two dimensional substrate and/or the surrounding three-dimensional reactor space in the second furnace zone. Introducing the catalyst into the furnace as a vapour is known as the 'floating catalyst technique' and was introduced in the late 1980's by Endo and Dresselhaus *et al.*[112]. Catalytic synthesis typically occurs over temperatures between 600 – 900 °C, using hydrocarbons (e.g. benzene, toluene) which are diluted by a carrier gas such as argon, nitrogen or hydrogen.

Extensive research on the catalytic production of multi-walled nanotubes has resulted in significant improvements in nanotube quality. Influencing factors such as the catalyst adopted, catalyst preparation and reaction temperature has shown to influence the overall quality of the nanotube. The use of metallocenes (e.g. ferrocene, cobaltocene), where the carbon source and catalyst are in the same phase have shown improved structural properties[113]. These compounds are typically used in the production of aligned arrays and nanotube yarns. Metallocene and hydrocarbon mixtures are also used to improve nanotube yield and quality. Typical catalysts used are Fe, Co and Ni[114] , since these have shown to be most active for multi-walled nanotube production, where successful catalysts showed good carbon solubility limits (0.5-1.5 wt %)[115]. Catalysts such as chromium, manganese and zinc have shown to produce multi-walled nanotubes at lower purities due to their low carbon solubility. Impurities found on nanotubes are amorphous carbon deposits and metal catalyst particles coated in amorphous or graphitic carbon.

The catalytic synthesis of aligned nanotubes on substrates has shown great promise for applications such as field emitters for flat screen displays, super-

capacitors for high energy and storage, energy-conversion devices, sensors, photonics and many other applications. Methods for growing these aligned structures involves the catalyst either being in a floating state or substrate-bound. The former involves, as described earlier, decomposition of a metallocene with the carbon source, which contributes to aligned growth on a metal oxide substrate surface (e.g. silica). This is the simplest technique since the nanotubes self-assemble on the surface and the density of catalytic particles deposited on the substrate controls the growth direction. If the density is high the nanotubes grow vertically due to van der Waals interactions between the nanotubes, whereas low densities results in entangled highly curved nanotubes. Depending on the strength of interaction between the catalyst and substrate, the catalyst particles either remain attached to the substrate or follow the growth of the nanotube, this will be further explained in the following section. Furthermore, the aligned nanotubes grow both parallel and perpendicular to the substrate surface which is not achieved using the substrate-bound technique.

In the substrate bound technique, numerous methods have been used to attach the catalytic particles to substrates, these include:

- Physical techniques such as ion beam sputtering and electron gun evaporation, enabling defined patterns of nanotubes with precise separations suited for field emission applications.
- Coating the substrates with solutions containing salts of the catalytic metals, which are then dried and reduced to leave particles on the surface.
- Laser etching a catalytically coated surface.

Typically silica and silicon are used as substrates and porous substrates are preferable due to their high surface areas[116]. The alignment and straightness of the nanotubes in this technique is also dependant on the density of the catalytic particles on the substrate. However, various groups have also demonstrated aligned arrays of tubes being formed by effect of plasmas[117-119], which is an excited/ionised gas. The plasmas are generated using DC, RF or microwave excitation and it is believed the alignment is due to the presence of the electric

field[118]. Also, aligned nanotubes can be produced by growing the tubes from embedded catalytic particles in porous substrates, as stated above.

2.2.2.4 Growth Mechanisms of Catalytically Produced Multi-walled Nanotubes

The growth mechanism for multi-walled carbon nanotubes was first proposed by Baker *et al.*[120] in the 1970s, even today the mechanism is still widely accepted and reported in numerous literatures. Baker *et al.* theorised that catalytic growth of carbon filaments involved the diffusion of carbon into the catalyst. Further detailed work resulted in him proposing two possible mechanisms in which the filament nucleates from the catalyst, known as tip growth and base growth[121] (see Figure 16 below).

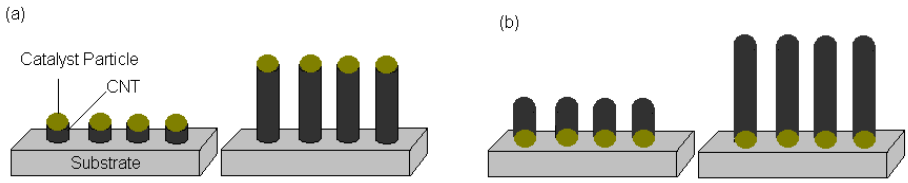

Figure 16: Schematic representation of proposed (a) tip and (b) base-growth mechanisms for CNTs by Baker *et al.*[121].

Tip growth involves the decomposition of the hydrocarbon upon the catalyst surface, producing carbon, which then dissolves through the particle. The growth of the filament occurs when carbon is deposited between the particle and substrate; the metal particle advances as carbon deposition and diffusion continues (Figure16 (a)). If there is strong interaction between the particle and substrate, then the carbon grows away from the substrate and base growth occurs (Figure 16 (b)). It is known that nickel on silica favours tip-growth[122], while cobalt or Fe on silica seems to favour base growth[123]. This theory is supported by transmission electron microscopy (TEM) and scanning electron microscopy (SEM), where the majority of metal particles are found at the base or tips of the nanotubes. The diameter of the nanotube is also known to depend on the size of the catalyst particle[124] and the particles spherical nature contributes to the tubular growth[125].

There have been conflicting reports on the state of catalytic particle during the growth, although evidence suggests that the particle remains in its solid state. The melting temperature of individual metals and even eutectic mixtures with carbon are higher than those used to produce multi-walled nanotubes. This is further supported by Baker's conclusion that the activation energy for growth correlates with the diffusion rate of carbon through the solid metal[126].

The effectiveness of the catalytic growth mechanism has shown to be dependant on the temperature and concentration gradients of carbon. At higher temperatures, the rate of carbon deposition increases resulting in build up on the catalyst surface; consequently amorphous carbon is formed. This is a problem typically experienced during catalytic growth of single-walled nanotubes due to the higher synthesis temperatures involved (900-1200 °C). Furthermore, different nanotube structures can be formed as consequence of graphitic build-up on the catalyst, such as herringbone fibres, bamboo and platelet fibres.

2.2.3 Multi-walled Nanotube Purification and Functionalisation

The catalytic vapour route is the most widely-used for carbon nanotube synthesis. However, catalytically produced samples inevitably contain catalyst and amorphous carbon impurities. In order to obtain optimal performance of carbon nanotubes in various applications, it is often important that these impurities are removed. Currently, a number of different purification strategies are available providing the opportunity to produce high purity carbon nanotubes, as well as introducing various surface chemistries. This section will begin with a summary of the strategies available for purifying nanotubes, followed by reviewing the techniques for functionalising them.

2.2.3.1 Purification of Multi-walled Nanotubes

Acid treatments are often used to purify CVD-synthesised MWNTs. Many researchers adopt this approach since it is highly effective and has the capability of purifying nanotubes on a large scale. In addition, this technique often introduces oxygenated functional groups, such as carboxylic acids onto the nanotubes surface which can serve as a template for further surface chemistry. As such, acid treatments are often termed as oxidative treatments due to this behaviour.

The first acid treatment on carbon nanotubes was published in 1998 by Rinzler *et al*.[127], who treated raw single-walled nanotubes in nitric acid to oxidise the metals and impurities. Since, Liu *et al.*[128] have demonstrated an alternative purification procedure using a mixture of concentrated sulphuric and nitric acid, H_2SO_4/HNO_3 (3:1). Reaction with sulphuric acid shortens the nanotubes and functionalises the tube ends and defects on the sidewalls. Further work has shown that using acid mixtures, results in better effectiveness of catalyst dissolution than nitric acid[129]. Despite the relatively high purities of CNTs gained through acid treatment, the structure of the nanotubes is sacrificed. Furthermore, acid oxidation is not always preferable because it opens up the tubes and functionalises the surface, which can also influence the performance of nanotubes in certain niche applications.

Purification of multi-walled nanotubes by oxidative gas treatments has also been investigated. Initial experiments using nanotubes heated in air or oxygen at 500-750 °C for ~30 minutes proved to be highly destructive, with only 1 wt% of the initial material remaining. In the presence of oxidising gases, the catalyst impurities effectively lowered the carbon oxidation temperature resulting in high loss of nanotube material. Recently, Tran *et al.* demonstrated a fast and efficient method of purifying and functionalising MWNTs[130]. The process involved short thermal oxidation treatments in air at 600 °C for 5 mins and then annealing the nanotubes in nitrogen at 950 °C to remove the surface oxygen, then subsequent cooling of the nanotubes in air to room temperature. The attractiveness of the method was the ability to reverse the character of the surface oxides from acidic to

basic using a simple thermal treatment. This is useful for enhancing compatibility in polymer applications and has shown to substantially improve the materials wettability[131]. The short oxidation and subsequent annealing method has been highly effective at removing amorphous carbon, however, much higher temperatures are required for catalyst removal. Perhaps the most successful method of purifying nanotubes involves annealing at 'graphitisation' temperatures (1600-3000 °C). Research by Andrews *et al.* showed that annealing was not only effective at removing catalyst impurities but also improved the structural quality of the tubes[132]. However, the high temperatures required and associated equipment costs have limited the application of this technique. Instead, many researchers employ less expensive methods such as oxidative acid treatments or oxidative gaseous treatment followed by an acid wash, usually HCl, to remove the catalyst particles.

Non-destructive techniques have also been developed to reduce structural damage and functionalisation to the nanotubes. Smalley and co-workers used cationic surfactants to disperse the nanotubes and then adopted filtration steps to purify the nanotubes[133]. However, the procedure often required multiple filtration steps, making it slow and inefficient with only small improvements in purification. This method was later improved by adopting ultrasonication to improve dispersability of the nanotubes and prevent the filter pores from becoming blocked[134]. However, the severity of the ultrasonication treatment (2.5-6 hrs) most probably damaged the tubes and the procedure can no longer be classed as 'non-destructive'. Alternative techniques such as centrifugation and size-exclusion chromatography have been used to purify nanotubes, with the latter effective at separating the nanotubes by length and diameter.

Often combinations of two or more methods are employed by researchers. It is often important to achieve a fine balance between the requirements of impurity removal with that of conservation of nanotube structure and yield. In addition, the technique chosen usually depends on the type of the nanotube and its intended application. For example, substrate-bound arrays of CNTs have shown promise for electronic devices. Therefore, the gaseous purification approaches would be required to ensure that the aligned morphology of the nanotubes was preserved.

2.2.3.2 Functionalisation of Carbon Nanotubes

Carbon nanotubes are usually functionalised by purification in acid oxidants, as already mentioned above. Such treatment introduces hydrophilic groups (-COOH, -OH, -C=O) on the surface of the nanotubes which can facilitate in solubilisation. Many studies implement the following acid and acid mixtures, HNO_3, H_2SO_4 + $KMnO_4$ and HNO_3 + H_2SO_4. The latter mixture was developed to shorten or 'chop-up' nanotube aggregates as well as oxidise their surfaces. Indeed, it is believed the edge-plane sites of nanotubes such as the tube ends and defects are highly reactive towards functionalisation[93]. In many studies the aim of the functionalisation is to solubilise the nanotubes. However, the nanotubes can be further functionalised by reaction with these hydrophilic groups. For example, various silyl moieties have been chemically grafted to these groups[135] and polymers, such as poly(vinyl acetate-co-vinyl alcohol), (PVA-VA)[136]. These respective chemical modifications showed promise for composite and optical applications.

Other covalent and non-covalent methods involve direct treatment on 'pristine' tube walls, termed as sidewall-targeted functionalisation, and have shown promise in wide areas ranging from composites to sensors. Studies of small diameter nanotubes displayed higher reactivity and susceptibility to functionalisation compared to their larger counterparts[137]. The increased curvature present in small diameter SWNTs introduces structural distortion and an increased tendency to undergo functionalisation, as previously observed in studies of different fullerenes[138]. Fluorine was first functionalised onto the sidewalls of SWNTs by workers from Rice[139]. Elemental fluorine can be a useful precursor for further functionalisation with applications for use in lithium-ion batteries, supercapacitors and as lubricants. Alternatives to fluorine include additions of other reactive compounds such as carbenes, nitrenes, silylenes[135, 140, 141] and even ozone[142] which also purifies the nanotube samples. The electrochemical functionalisation of nanotubes has proven to be a highly effective and valuable method. This method is highly controlled since the extent of reaction can be directly adjusted by an applied potential. Many studies have attached a variety of aryl diazonium salts for improved interaction with redox molecules/enzymes at the nanotube surface[13,

[143, 144]. Furthermore, the application of extreme potentials in aqueous and acidic solutions can effectively purify and functionalise the nanotubes [108, 145].

Non-covalent approaches have been shown to enhance the solubility of nanotubes. Ionic surfacants such as sodium dodecyl sulphate (SDS)[146] and sodium dodecyl benzene sulphonate (SDBS)[147] are frequently used to facilitate dispersions. The electrostatic forces between the nanotube and surfactant create the dispersion, while the dispersion behaviour will depend on the solution pH. Non-ionic surfactants are also employed, such as triton X-100[148], and these work by hydrogen bonding and/or steric effects. Other approaches involve the adsorption of planar groups to the nanotube surface using π-stacking or helically wrapping the tubes with a polymer. Non-covalently attaching biological molecules to nanotubes, such as proteins (e.g. enzymes), DNA and other nucleic acids has also found applications in nanoscale sensing and energy-conversion devices.

2.3 Enzymes

2.3.1 Introduction to ***Trametes versicolor*** laccase

The need for efficient fuel cell catalysts is greatest at the oxygen cathode, where the reaction kinetics for the conversion of oxygen to water are sluggish and catalyst loadings are high. A key class of enzymes, known as laccases, have shown to be excellent catalysts for this reaction, converting oxygen to water efficiently, with minimal overpotential and peroxide generation[149].

Laccases are multicopper oxidases that catalyse the four-electron reduction of oxygen to water, accompanied by the simultaneous oxidation, typically, of an organic substrate. Enzymes which catalyse oxidation-reduction reactions are known as oxidoreductases, and are classified into several groups. Laccases are part of a group known as oxidases, as stated above, meaning they catalyse oxidation reactions using oxygen as the natural electron acceptor[7]. The simultaneous oxidation-reduction mechanism of the enzyme suggests that catalysis occurs at two active sites and based on structural[150] and spectroscopic data[151] made available, this notion still remains. The two active sites typically contain a total four copper atoms (hence the term multicopper), allowing laccases to perform electron transfer reactions in the above mentioned processes. This electron transfer mechanism will be explained in more detail in section 2.3.1.3 and 2.3.2.1.

Currently, more than a hundred laccases have been isolated and characterised from plants and fungi[152]. Different laccase strains were shown to have different physiological roles and as such it was discovered that fungal laccases held higher potentials than other species, possessed excellent substrate turnover rates and held highly accessible sites due to the outer surface proximity. Therefore, the laccase chosen for this thesis was from the fungus Trametes versicolor, these laccases have shown great potential as cathode catalysts for biosensor and biofuel cell technologies. *Trametes versicolor* laccase will be discussed in more detail in the following sections.

2.3.1.1 Occurrence, Physiological Function and Localisation in Cell

Since their discovery more than a century ago in the Japanese laquer tree *Rhus vernicifera*[153], laccases have been widely found in fungi as well as in some bacteria and insects. The majority of laccases characterised so far have been derived from fungi, especially from wood-destroying white-rot fungi responsible for decomposition of lignin. Lignin provides the structural component of the plant cell wall and is one of the most widely-distrubuted natural polymers[152]. Well-known laccase producers include fungi such as *Trametes versicolor, T. hirsuta, T. ochracea, Cerrana maxima, Pycnoporous cinnabarinusm, T. villosa,* etc.

The physiological roles of laccases in plants and fungi are diverse. Plant laccases are involved in the synthesis of lignin and catalyse the polymerisation of lignin structural units[152]. In fungal physiology, laccases are involved in plant pathogenesis, pigmentation, detoxification and lignin degradation[154]. Of more interest to the reader are the fungal laccases from wood-destroying white-rot fungi such as *Trametes versicolor* and *Pycnoporus cinnabarinus.* These laccases play a major role in lignin degradation, where they mainly oxidise phenolic compounds using oxygen as the electron acceptor[155].

The diverse range of physiological functions of laccases comes from their ability to oxidise a wide variety of organic and inorganic substrates by means of oxygen, such as monophenols, polyphenols, aromatic amines, and considerable range of other compounds. The localisation of laccase in the cell is believed to be associated with its physiological function. Therefore, enzymes involved in lignin degradation, such as laccases produced from *Trametes versicolor* should be exclusively extracellular[152]. However, while most laccases are of extracellular origin, the laccases of wood-rotting fungi such as *Trametes versicolor* exist both intracellularly and extracellularly[156], although a substantial part is present in the extracellular cell wall[157].

2.3.1.2 Production and Purification

Fungal enzyme production is mainly through the use of submerged fermentation strategies. This essentially involves producing laccases through cultivation in a sterile culture medium, containing the appropriate nutrients and aerobic environment. On a laboratory scale, this cultivation is carried out usually in small flasks, while on an industrial scale large tanks are used.

The most efficient laccase producers are known to be white-rot fungi[158]. However, these fungal laccases are generally produced in low concentrations when cultivated in submerged culture or on wood. Cultivation in submerged culture, or submerged fermentation, is the main method used for fungal enzyme production. This involves producing laccases through cultivation of the fungal strain in a sterile culture medium, containing the appropriate nutrients and aerobic environment.

Much research has been carried out to improve and develop these production strategies, since successful application of laccases requires production of high amounts at reduced costs. Higher laccase concentrations can be achieved by optimising the culture conditions, such as the carbon and nitrogen source, initial pH and concentration of Cu^{II}[159]. In fact, mimicking laccases natural environment with the addition of lignin resembling compounds, such as 2, 5-xylidine and veratryl alcohol has also shown to increase laccase production[159, 160]. However, these additives can considerably increase the overall cost when developed on an industrial scale. Furthermore, implementation of novel fermentation methods can also cause undesirable increases to cost due to modifications to pre-existing facilities[161].

Other production methods include the heterologous expression of laccases, which involves transferring laccase genes from the native host into other fungal strains or bacteria enabling high-level protein production. Since laccase genes are expressed at very low levels in the native hosts, this has shown to be an effective method to improve laccase production. Research by Lopez et al.[162] found that high expression of heterologous proteins could be achieved by transforming

laccase genes from *Trametes versicolor* into methyltropic yeast *Pichia pastoris*, carried out in minimal media and over a short time period.

Despite these above mentioned methods improving laccase production, the reported production levels are still rather low for industrial applications, with overall yields in the region of milligrams per litre. Therefore, in order to produce inexpensive enzyme sources which can be commercially implemented for potential applications, further research and developments in laccase production methods still need to be made.

Laccases, such as those from *Trametes versicolor*, can be purchased commercially but only in low quantities, (1 to 10 g), with only 10 % of the mass being laccase. The high impurity content of these commercial samples and low yields obtained, increase overall costs and the required purification protocol, thus time.

Typically after production and removal of the biomass, the laccases are isolated and purified to high concentration. Purification simply involves a series of processes used to isolate the desired protein from a complex mixture of other soluble undesired proteins and membrane material. The ease of the purification process is usually dependant on the starting material, such as its cellular location and concentration. The majority of laccases characterised so far have been derived from fungi, especially from the wood-destroying white-rot fungi. For reasons being that these laccases are mainly extracellular, meaning they are easier to obtain, with higher concentrations and are often more stable[163]. Plant laccases are often difficult to detect and purify because they contain a large number of oxidative enzymes with broad substrate specificity[164], which explains why the first isolated plant laccase, Rhus vernicifera, has been well researched[165, 166]. The difficulties found with purifying intracellular proteins compared to extracellular proteins can be seen in Figure 17.

Proteins vary tremendously in a number of physical and chemical properties. By exploiting the differences in properties between the protein of interest and other proteins in the mixture, a rational series of fractionation steps can be designed.

Separation steps may exploit differences in size, shape, charge, hydrophobicity, solubility, ligand binding and many more.

The most commonly used protein purification technique in biochemistry is column chromatography. The basic concept is to flow the protein through a column material which contains various adsorbents for proteins to interact with differently. This protocol can contain one or more steps depending on the difficulty of extraction or required purity level.

This technique frequently results in purification steps that give the greatest increase in protein purity, and, in terms of enzyme isolation, the greatest increase in specific activity[163]. There are several types of column chromatography with each containing different protein adsorbants such as hydrophobic materials, ion exchangers, inorganics, chemically synthesised ligand adsorbents or biological compounds such as substrates. Further detail on the basic principles will not be discussed here, but detailed explanations on the adsorbents used for purification of laccase in this thesis can be found[163, 167].

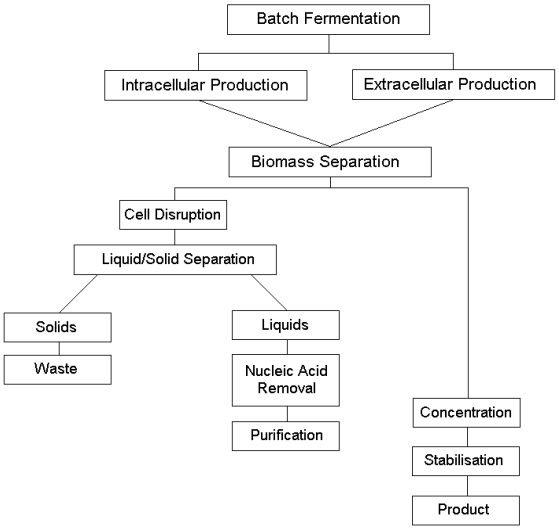

Figure 17: Flow diagram of fungal enzyme production[168].

2.3.1.3 Structure and Catalytic Mechanism

Fungal laccases are glycoproteins, consisting of a small amount of glycans (i.e. carbohydrate portions) attached to the polypeptide chain (protein). The carbohydrate portion of laccases typically consists of 10-20 % and is believed to protect the enzyme molecule against proteolysis and inactivation from free radicals[152, 155] or even provide a chemical attachment site to the electrode[169]. Despite some localised structural differences between laccases (e.g. in the chains organising and forming the substrate binding pocket), the majority of laccase structures determined to date, from fungi and bacteria, have shown a significant degree of overall structural homology[170].

The structure of *Trametes versicolor* laccase consists of a single glycosylated polypeptide chain (monomer) organised into three sequentially arranged domains, with dimensions 65 x 55 x 45 Å[150]. Each of the three domains has a similar β-barrel type structure. Incorporated within these domains are copper atoms which allow the proteins to perform electron transfer reactions for their respective biological redox processes, because copper atoms can switch their oxidation states between Cu^{I} and Cu^{II}. It is now generally accepted that laccases contain four copper atoms in the protein structure allowing the enzyme to catalyse reactions that involve several electrons at a time. The active site for oxygen reduction comprises of three copper atoms (the type 2/3 tri-nuclear cluster), while the fourth copper site at which organic substrates are bound and oxidised is known as the type-1 site or mononuclear 'blue' copper centre[152]. The structure of Trametes versicolor laccase is shown in Figure 18. The type-2/3 (or T2/T3) sites of the enzyme are buried about 12 Å deep within the structure and positioned about 4 Å apart, while the type-1 (T1) site is more surface bound, lying 6.5 Å below the surface of the enzyme and located 12 Å from the T2/T3 site[150, 171]. Furthermore, the different coppers can be classified by their spectroscopic characteristics. The T1 site of laccases imparts a deep blue colour to the enzyme solutions, hence the name mononuclear 'blue' copper centre, and is characterised by a strong adsorption around 600 nm[151] . The T1 site and T2 site can also be determined by electron paramagnetic resonance (EPR). While, the T3 site cannot be EPR

detected, but identified by the presence of shoulder at 330 nm in the UV region of the spectrum[151].

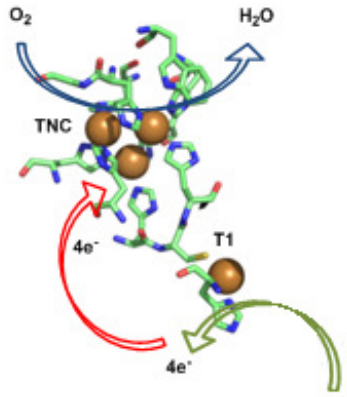

Figure 18: Stick and ball model representation of the structure of *Trametes versicolor* laccase. Copper sites are represented by the balls[172].

Naturally, laccases oxidise a broad range of substrates such as phenols, aromatic amines, inorganic compounds and many others. When oxidised by laccase, the substrate donates an electron to the T1 copper site. In fact, it is believed the substrate binds in a small negatively charged binding pocket near the copper T1 site, which lies about 7 Å below the surface of the enzyme[150, 173]. The T1 copper is the primary electron acceptor site and behaves like an electron relay centre, shuttling the electrons to the T2/T3 site via a His-Cys-His tripeptide[150, 173], where the reduction of oxygen to water takes place. The catalytic process is only complete once four electrons have been transferred, thus requiring four substrates per catalytic cycle as shown in the reaction schematic in Figure18. It must also not be forgotten that the protons necessary for the reduction of oxygen to water are taken from the surrounding solution. Laccase activity has shown to be dependant on the solution pH (i.e. concentration of hydrogen ions/protons in solution), usually at high pH values laccase inhibition by OH^- ions occurs and stability losses of laccases occurs at low pH values[174].

The reaction mechanism of laccases has been studied intensively by monitoring the coordination states of the coppers during the reaction cycle using various spectroscopic techniques[151, 175, 176]; however the mechanism behind the shuttling

of electrons and particularly the reduction of oxygen to water in the tri-nuclear centre still remain unclear.

The catalytic efficiency of the reaction mechanism has been shown to be influenced by the suitability of the substrate for different laccases. Though, laccases natural co-substrates are phenols, the enzyme is only moderately selective and displays activity with a wide range of substrates[7]. First of all, the structural nature of the substrate strongly affects its interaction with the T1 substrate binding pocket, especially those with those bulky side chains[173]. Furthermore, the reaction rate depends on the difference between the redox potentials (E°) of the substrate and T1 copper site. The redox potential of the substrate must be low enough for the $1e^-$ transfer from the substrate to the protein, so not to be rate limiting. The redox potential of the substrate is mainly determined by its chemical structure and likewise the redox potential of the T1 site varies in relation to its catalytic structure. The different T1 site redox potentials will be discussed in the following section.

2.3.1.4 Redox Potentials

The redox potentials of laccases vary between 0.4 and 0.8 V. due to the structural differences in Cu^I coordination at the T1 copper site[150]. As a result, laccases are subdivided into three groups in accordance with the redox potential of the T1 site: low, middle, and high potential laccases. Laccases with the lowest potentials are derived from trees, e.g. *Rhus vernicefera* with a T1 site potential of about 430 mV versus NHE[177], while the high potential laccases are those of fungal origin, e.g. *Trametes*, such as *Trametes versicolor* used in this thesis, which has a T1 site potential of 780 mV versus NHE[177].

Based on redox titration and structural studies, the redox potentials and subsequences between laccases from different sources can be compared, as shown in Table 1. However, it must be noted that most laccase species produce several isoenzymes, therefore it has been suggested that the gathered redox potentials may actually be of single or multiple laccases and therefore may not be accurately

represented[178]. Currently, it is unclear whether the presence of laccase isoenzymes is due to varied genes encoding laccases, posttranslational modifications and/or proteolysis during cultivation and purification, which cause variation in the physicochemical properties between isoenzymes from one origin/within same species[150, 178, 179]. Furthermore, these titration studies consider laccases in their inactive reduced states and sometimes without consideration of pH influences on redox potentials, resulting in laccases with a wide range of potentials, which requires intricate understanding[177, 180].

Laccases	Subsequence	E°′, T1 (mV)	Type
Trametes hirsuta	H…H C H I D F H L E A G F	780	High
Trametes versicolor	H…H C H I D F H L E A G F	780	High
Coprinus cinereus	H…H C H I D F H L M N G L	550	Middle
Myceliophthora thermophila	H…H C H I D F H V S G G L	470	Middle
Rhus vernicefera	H…H C H F E R H T T E G M	430	Low

Table 1: Comparison of the redox ptoetnial of the T1 site and the subsequences between laccases from different sources[177, 181, 182]. Note: Underline-ligand to T1 copper. All potentials vs. NHE.

It was previously suggested that the redox potential of the T1 site depends on the axial ligands and the amino acids around the T1 binding pocket. Figure 19 highlights the typical copper geometries found in laccases.

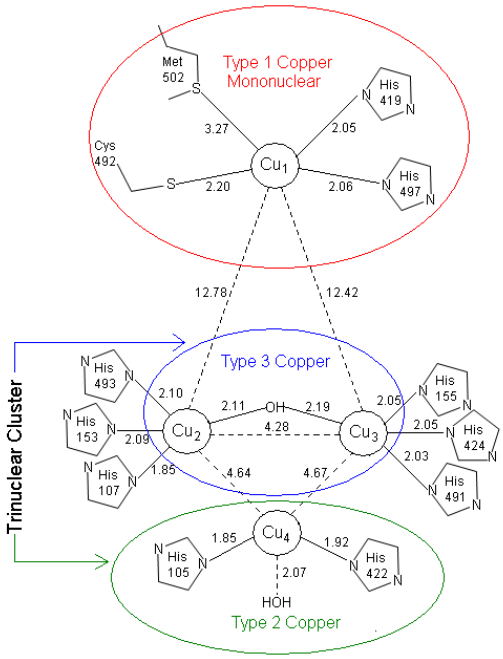

Figure 19: Schematic representation of T1 and T2/T3 copper sites of laccase CotA from *Bacillus subtilis*, including interatomic distances among relevant ligands[183, 184].

Two histidines (2x H) and one cysteine (C) are arranged trigonally around the T1 copper, and two axial ligands that are usually non-coordinating sit within 0.4 nm in the axial positions[150, 171, 173]. One of the axial ligands usually consists of isoleucine (I), while the other has shown to differ between laccases. This variation is illustrated in Table 1. Where low redox potential enzymes (340-490 mV) have methionine (M) as an axial ligand, the middle (470-710 mV) have leucine (L) and the high (730-780 mV) have phenylalanine (F). This T1 site redox potential dependence on the non-coordinating nature of the axial ligand was further investigated by mutating the corresponding phenylalanine axial ligand to methionine in *Trametes villosa* laccase. The results showed that the redox potential of the T1 copper was indeed lowered by as much as 110mV[185]. However, these mutations were ineffective when changing leucine to phenylalanine in other low potential and high potential laccases[185, 186] On the basis of these results and structural data obtained from the high redox potential laccase *Trametes versicolor*, Pointek *et al.* proposed an alternative mechanism by which laccases or other redox metalloenzymes can increase their redox potentials[150]. According to Pointek *et al*., hydrogen bonds around the T1 copper site have shown to affect the bond length between the T1 copper and one of the trigonally arranged histidine molecules. As a result, an increase in the bond length could decrease the electron density of the T1 copper atom, thus making it more electron deficient and highly oxidising. The distance between the copper and histidine in high potential laccases is longer compared to those in the middle potential group, thus making them highly oxidising (i.e. more susceptible towards accepting electrons from reducing substrates)[150]. Although, some exceptions were found to this theory[187], with measured potentials hugely different to the reported values. The nature of the axial ligand and its affect on the redox potential of the T1 site was not so misjudged[185, 186] and found not to exceed 150 mV when measured and compared to reported values[179].

Furthermore, it must be recognised that factors such as solvent accessibility and charge distribution may contribute to the redox potential of laccases[181], and therefore further understanding between the big differences between the redox potentials of the T1 site is still required.

2.3.2 Laccase Electrochemistry

The ability of laccases to oxidise phenolic and various other non-phenolic aromatic compounds is well-known but still not fully understood. It is believed that laccases can either directly oxidise these substrates and/or indirectly through the use of other enzymes and non-enzymatic components such as mediators. In order to improve understanding of laccase redox chemistry there has been increased research in the area of laccase electrochemistry (i.e. combining laccase and electrodes). Electrochemical techniques have been recognised as powerful means for characterising the electron transfer properties of redox enzymes on various electrodes. The major driving force behind these studies was the emergence of electrochemical enzyme biosensors and further development of other novel technological applications such as biofuel cells.

Since the mid 1960s, numerous methods have been proposed and investigated in the field of enzyme electrochemistry in an effort to establish efficient electrical communication between redox enzymes and electrodes[188-192]. As a result, the electron transfer between enzymes and electrodes has been generalised into two different mechanisms: direct electron transfer (DET) and mediated electron transfer (MET), with DET covering direct electron exchange between the enzyme active site and electrode, and MET involving a mediator, in order to shuttle electrons between the enzyme active site and electrode.

The following sections will only be concentrating on reported DET techniques, since this technique was adopted in the thesis.

2.3.2.1 Direct Electron Transfer

The first publication on the DET for laccases with enzymatic activity was in the late 1970s[193], where the electrocatalytic reduction of oxygen was demonstrated, using *Trametes versicolor* laccase adsorbed at a carbon electrode. In this case, the electrode surface is considered as the 'substrate' of the enzyme, with the reaction kinetics controlled by the electrode potential and the proximity of the laccase T1 active site to the electrode surface. Laccases along with other blue copper oxidases have shown to be effective electrode communicators, believed to be partly due to the redox centre being located near the periphery of the protein shell and also the aromatic binding pocket situated nearby. It is believed that this pocket behaves as a substrate docking site usually for the oxidation of phenolic substrates but instead has been shown to interact favourably with electrode surfaces[192], enabling electron shuttling from the redox centre for oxygen reduction.

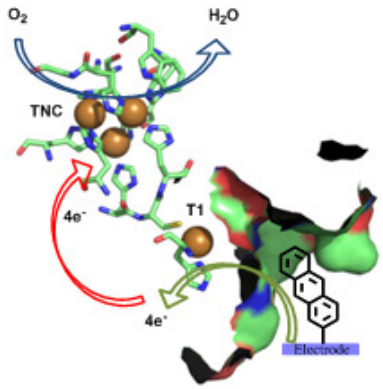

Figure 20: DET Mechanism showing laccasse interacting with electrode with 2-aminoanthracene tether[172].

The DET mechanism between the electrode and laccase, as well as other 'blue' multi-copper oxidases, has been proposed by Shleev *et al.*[174] and is illustrated in Figure 20. As shown, the electrons are transferred from the electrode to the T1 site of the adsorbed enzyme and then shuttled to the T2/T3 cluster using the tri-peptide (His-Cys-His), where oxygen is reduced to water. This proposed mechanism was based on investigations showing the potentials at which laccase catalyses the electroreduction of oxygen were close to the potentials measured for the T1 sites of different laccase sources. Furthermore, these potentials and

observed electrocatalytic currents are known to be dependent on pH for both homogeneous and heterogeneous catalysis, which suggests the T1 site dictates these properties and has been determined to be the first electron acceptor[151, 181, 194].

The DET mechanism is the simplest and most attractive interaction between an enzyme and electrode surface, due to the minimal amount of electron transfer steps and active species involved[7]. Furthermore, the intimacy of this interaction can help probe the mechanisms and kinetics of biological electron transfer. However, attaining efficient DET is not always possible due to the various challenges that need to be overcome, these include:

1. Obtaining the correct orientation of the enzyme active site to within electron tunnelling distance of the electrode surface, assumed to be 8 Å[151].
2. Strong adsorption of the enzyme to the electrode to facilitate electron transfer while preventing denaturing effects
3. Achieving effective heterogenous electron transfer which is thermodynamically favourable between electrode and enzyme, thus with minimal overpotential.

In summary, these limitations essentially reveal the importance of the "electrode environment", this is further highlighted in the Marcus theory which effectively explains the distance dependence of electron transfer[21] (see section 3.1.4.4.).

2.3.2.2 Immobilisation of Enzymes by Direct Electron Transfer

Numerous electrochemical studies have explored ways to successfully immobilise enzymes to achieve direct electron exchange with the underlying electrode. Some of the different methods investigated include direct adsorption or co-adsorption of enzymes onto electrodes[195], adsorption onto self-assembled monolayers[196], covalent attachment onto electrodes[197], and the use of nanostructured electrodes[198, 199].

The earliest studies of direct electrochemistry involved enzymes in solution (i.e. not immobilised) and were often hindered by adsorption and denaturation of enzymes on electrode surfaces[200, 201]. In fact, initial experiments often involved the application of redox proteins rather than enzymes, such as cytochrome c, which contains a Fe active centre capable of undergoing oxidation and reduction. In 1977, Eddowes and Hill first reported reversible voltammetry for cytochrome c on gold electrodes coated with 4,4'-bipyridyl[202]. These electrodes contained chemical functionalities capable of interacting specifically and reversibly with the protein surface. This work first highlighted the importance of the electrode surface structure for DET between electrodes and redox proteins and enzymes.

Concurrent work explored ways of controlling the electrode surface structure through using metal oxide, organic-monolayer-coated and pyrolytic edge electrodes. Armstrong *et al.* discovered that using the edge of pyrolytic graphite gave more reversible voltammograms than using the basal plane for cytochrome c[203]. The edge sites of the pyrolytic graphite have been shown to be rich in C-O functionalities[204] facilitating electrostatic interactions and hydrogen bonds with redox proteins and enzymes. This research demonstrated that enzymes could be immobilised in thin-films, using favoured chemical interactions in order to orientate and improve the electroactivity of redox proteins. Fraser Armstrong termed this technique as 'protein-film voltammetry', this has since transpired to be the method of choice for fundamental electrochemical studies of enzyme redox chemistry.

2.3.2.2.1 Adsorbed and Coadsorbed Enzyme Monolayers

Enzyme adsorption on electrode surfaces in a favourable configuration, referred to as 'protein-film voltammetry', often facilitates DET and removes any limitations due to, the slow diffusion of the large biomolecules and adsorption of macromolecular impurities. Armstrong demonstrated this through achieving reversible CV scans of adsorbed proteins at scan rates of 3000 Vs^{-1} and above[205], which is impossible for proteins moving freely in solution due to diffusion limitations (and without mediators). Coadsorption of enzymes with positively

charged species, such as aminocyclitols, has also produced stable films at negatively charged pyrolytic edge electrodes[195]. The concept of controlling the electrode surface structure to study DET at electrode surfaces has been extended over the years. Further developments in electrode structural configurations are discussed below.

2.3.2.2.2 Diazonium Coupling

A common method used for the functionalisation of carbon surfaces with a wide variety of organic species was recently developed by Pinson *et al.*[206]. The technique involves the grafting of functionalised aryl groups onto electrode surfaces via the electrochemical reduction of diazonium salts, the schematic of the reaction is shown below (see Figure 21). This technique has been widely adopted by researchers due to the relative ease with which diazonium salts can be tailored with a diverse range of functional groups, as well as the overall structure and stability of the resulting layer[207].

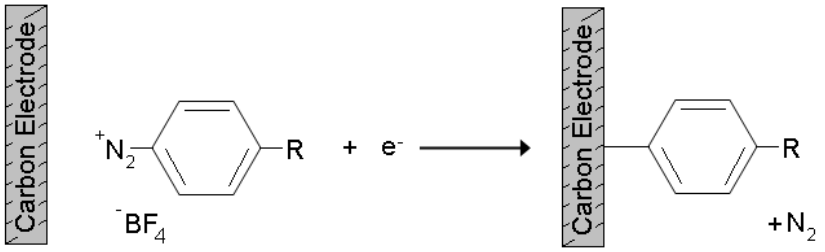

Figure 21: Schematic illustration of the proposed mechanism for diazonium surface modification. Diazonium salt ArN_2^+ dissolved in aprotic medium with supporting electrolyte (acetonitrile ACN + 0.1 M NBu_4BF_4), (or acid aqueous medium), is reduced onto the electrode surface at the potential of the voltammetric peak of the diazonium or more negative potentials (for seconds or minutes).

Recently Blanford *et al.* functionalised pyrolytic graphite edge electrodes with diazonium compounds derived from 2-aminoanthracene[13, 143] to produce surfaces that orient and bind laccase. The anthracene group was rationally chosen to mimic natural organic substrates in order to bind to the T1 hydrophobic pocket of laccase and provide efficient electron transfer. The electrode demonstrated higher electrochemical activity and long-term stability compared to the unmodified

electrode. Conversely, Sosna *et al.* demonstrated that their best electrode, a smooth glassy carbon electrode modified with anthraquinone monolayer gave current densities 10^3 times smaller[144]. Taking into account different experimental conditions and procedures, the difference is still large and for the most part could be accounted for the difference in electrode roughness (abraded edge vs. smooth) and also the formation of the film (multilayer vs. monolayer).

2.3.2.2.3 Self-Assembled Monolayers

These are organised layers, normally formed from alkanethiols, and usually attached to metal surfaces by chemisorption, as shown in Figure 22.

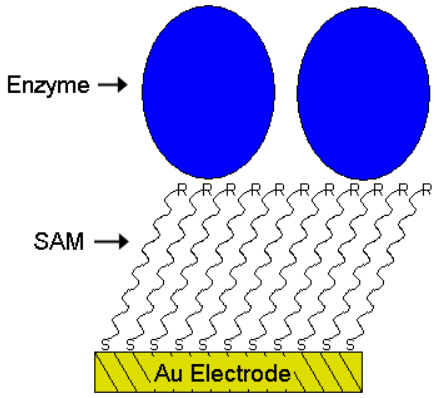

Figure 22: Schematic illustration of gold electrode coated with SAM suitable for binding enzymes through interaction with terminal R groups (which may be $-COO^-$, $-CH_2-OH$).

The alkanethiol consists of an alkyl chain (C-C), as the backbone, with a terminal end group (-R) which may be functionalised to bind the enzyme and head group (–S-H), thiol, which forms the semi-covalent bond to the electrode surface. These self-assembled monolayers (SAMs) are usually present on noble metal surfaces such as gold and silver due the strong affinity for these metals, and are reasonably stable outside of extremes of pH and potential, hence their reversible nature. Given these characteristics, SAMs are usually formed by spontaneous adsorption from solution but can be formed using other methods such as physical vapour deposition, and electrodeposition. There are only a few studies reporting on the electrochemical behaviour of laccase on SAMs and the most relevant of these will be discussed.

Recent detailed reports by Shleev *et al.* have highlighted the complexity of DET of high redox potential laccases and BOD on thiol-modified and bare gold electrodes[208, 209]. Their studies have suggested that enzymes are often poorly orientated at these electrodes, resulting in poor catalytic activity and low reduction potentials (ca. 0.4 V vs. NHE) which can even promote the reduction of oxygen to hydrogen peroxide instead of water. The highest catalytic activities were observed for gold electrodes modified with 4-aminothiophenol[208, 210] and those containing thiols with shorter alkyl chains[211], the latter is also in agreement with diazonium modified electrodes[144].

Conversely, fresh work has shown laccase to directly reduce O_2 at low overpotentials on roughened gold electrodes modified with anthracene-2-methanethiol (AMT). Interestingly, this was accomplished using a roughened electrode surface and mixed monolayer of AMT and ethanethiol (ET) which disrupted the self-assembled anthracene monolayer and increased the number of isolated anthracene moieties accessible to the enzyme. A reduction potential of 1.13.V vs. RHE and current density of 25 μA cm^{-2} was achieved.

2.3.2.2.4 Enzymes on Nanostructures

An alternative approach to producing highly conductive linkages to the enzyme and achieving higher turnover rates is to combine highly conducting nanomaterials and enzymes. This approach is known as 'bionanoelectronics', a term which is often misconstrued. Many of the controlling aspects that limit the performance of current electrodes are size-dependant such as optimising charge transport, electron-transfer kinetics, mass transport and electroactive surface area. Nanostructured electrodes have shown promise in overcoming current limits, improving immobilisation and adding a new level of performance to the enzyme electrode. Some of the nanomaterials used for enzyme electrochemistry include CNTs, gold nanoparticles, and carbon black. Some of the most pertinent and recent reports covering these materials will be mentioned.

2.3.2.2.4.1 Carbon Nanotubes

CNTs have recently received a lot of attention due to their excellent electrical conductivity and their ability to address many of the above limiting factors. Typically, CNT electrodes are created by randomly depositing nanotubes on conventional electrode surfaces or grown directly on metal electrodes as aligned assemblies, 'carbon nanotube forests'. Enzymes are adsorbed or covalently linked to the nanotube surface, similar to the immobilisation techniques already discussed.

Thus far, the majority of studies have used electrodes where the nanotubes are randomly deposited on the surface and either held without any binders, with binders, dispersed as carbon pastes which can be screen printed or forming nanotube composites. However, recent studies have highlighted that superior electrochemical performance can be achieved when nanotubes are vertically aligned as opposed to randomly dispersed[212, 213]. The improved catalytic performance could be due to a number of reasons, such as better electron conduction paths and contact with electrode, higher surface areas and higher amount of defects exposed (CNT tips). Novel electrodes with advanced 3D nanoarchitectures have emerged. These electrodes consist of highly aligned nanotubes orientated perpendicular to the electrode surface, thus offering a highly directional pathway along the nanotube length to the enzyme, and allowing for faster mass transport and electron-transfer kinetics.

2.3.2.2.4.2 Gold Nanoparticles

Contrary to earlier reports by Shleev and co-workers[208, 209], the same group recently discovered that efficient DET of laccase can be achieved on gold surfaces[214]. This study was conducted by simply dispersing gold-nanoparticles (50 nm) on gold or glassy carbon electrodes (formerly these electrodes displayed poor DET to laccase) and then adsorbing laccase on the electrode and recording the voltammetric response. The nanometer-size of the gold particles improved accessibility to the T1 copper site and efficient DET transfer was observed, confirmed by the high midpoint potentials (710 mV vs. NHE) and current

densities (5-30 μAcm^{-2}) in quiescent buffer solution. In truth the most striking example of using gold-nanoparticles to 'wire' into the enzyme active site has been demonstrated by Willner and co-workers[197]. Although, it has been observed in this thesis that gold nanoparticles have displayed poor biocompatibility with laccase.

2.3.3 Biocathode

Oxygen is usually chosen as the oxidant for most BFCs because it is widely available and has a high reduction potential. The oxygen reduction reaction is catalysed typically by laccase or BOD and the mechanism can either be DET or MET. This is significant because of the vast number of enzymes available, only a select few are capable of DET.

Laccases derived from white-rot fungi, such as *Trametes versicolor*, are often chosen at the biocathode because they reduce O_2 to water at high potentials and can be obtained more easily. These enzymes function between pH 3-5, making them unsuitable for implantable applications and are also inhibited by halide ions, such as chlorides and fluorides. For implantable applications, BOD has been studied as an alternative to laccase, because it is active at neutral pH and insensitive to Cl^-. The cathodic catalysts, laccase and BOD, have similar structures and comparable electrocatalytic properties to Pt.

Despite the DET properties of these enzymes, mediators are often employed to increase current density. ABTS is a mediator most commonly used in conjunction with laccase and BOD at the cathode. Palmore and Kim described a membrane-based BFC containing a diffusive solution of laccase/ABTS at the carbon cathode[215]. The BFC operated at a higher OCV and power density compared to laccase immobilised on different types of electrodes. Futhermore, the reduction potential of ABTS was found to be similar to that of laccase's T1 site and thus allowing for fast electron transfer under a small driving force. However, since the mediators are present in solution, a membrane is required to prevent electrons from passing from anode to cathode.

An alternative approach developed by Heller involves wiring laccase or BOD to an Os based-redox hydrogel. The redox polymer confines a large amount of enzyme, improving O_2 reduction activity and allows construction of membraneless configurations[216].

In regard to DET, both laccase and BOD have displayed good O_2 reduction activity when adsorbed on carbon electrodes. Although, this DET mechanism has shown to be dependent on the electrode material employed. A high potential laccase and BOD were adsorbed on graphite and gold electrodes and their electrochemical responses determined[174, 209]. On the graphite electrode, both enzymes displayed O_2 reduction at potentials close to the T1 site. While on the gold electrode, a redox process at a much lower potential was displayed for laccase[174, 217] and for BOD catalytic action was only observed in the presence of mediators[209]. These results suggest that enzyme orientation on the two electrode materials is different. Blanford *et al.* recently demonstrated this orientation dependence using an anthracene-modified graphite electrode. The anthracene linker was used to target the hydrophobic pocket near the T1 site in order to bind laccase tightly and allow fast electron transfer. A significant improvement in current density and enzyme stability was observed when compared to the unmodified electrode, indicating the ability of the modified electrode to correctly orientate and stabilise the enzyme at a high level of activity.

3 Theory and Experimental

3.1 Electrochemistry

Electrochemistry is the branch of chemistry concerned with chemical reactions that occur due to, or are driven by, a change in electrical potential. These chemical reactions often involve heterogeneous electron transfer between two phases, an electronic conductor (electrode) and ionic conductor (electrolyte), defined as the electrode|electrolyte interface. This charge transfer has resulted in the science being used for a wide range of devices, including batteries, fuel cells, supercapacitors, and sensors, whilst electrochemical theory explains different phenomena such as corrosion and electrophoresis[16].

In this chapter, an overview of classical redox electrochemistry will be initially provided, covering aspects of experimental methodology, electrochemical theory and electroanalytical techniques. After which bioelectrochemistry will be introduced, in which protein-film voltammetry will be covered in detail.

3.1.1 Experimental Methodology

Electrochemical processes occurring at the electrode|electrolyte interface involve electron transfer between an electrode and electroactive species in solution. These species can be interchanged between oxidation states upon applying the appropriate electrode potentials. For example, the reactions of oxidised and reduced forms of two different electroactive species (1 and 2) at separate electrodes are shown below:

$$Ox_1 + ne^- \longrightarrow Red_1 \qquad \textbf{Reaction 1} \qquad \textbf{Reduction}$$

$$Red_2 \longrightarrow Ox_2 + ne^- \qquad \textbf{Reaction 2} \qquad \textbf{Oxidation}$$

In reaction 1, the electroactive species gains electrons at the cathode and moves to a higher oxidation state, and in reaction 2, the electroactive species loses electrons at the anode and moves to a lower oxidation state. These reactions are two types

of redox reaction ('reduction' and 'oxidation'), and an electroactive species that interchanges between both is known as a redox couple.

A typical electrochemical cell is formed by these two separate electrode reactions, known as half cell reactions, and the 'electromotive force', *emf*, or cell potential required to drive these reactions is determined by the difference in chemical potential between them, as shown below:

$$emf = E_{\text{right-hand side}} - E_{\text{left-hand side}} \qquad \textbf{Equation 12}$$

where by convention the right-hand electrode (cathode) is more positive than the left-hand electrode (anode). Also, *emf* is termed E_{cell} or OCV in the case of fuel cells (see section 2.1.2).

Potential measurements are known as 'equilibrium measurements' since they are typically carried out under conditions of equilibrium (i.e. zero current flow), in order to prevent the redox reactions above (i.e. compositional changes) and provide an accurate measure of the *emf*. While current measurements are 'dynamic measurements' and rely on charge flow between electrodes, thus shifting the electrode potential away from equilibrium and initiating the redox reactions above.

Since the magnitude of the current is dictated by the amount of electrons consumed or collected by the electrode per second (i.e. the amount of species converted), then some kinetic processes will limit this process, known as 'rate-limiting processes'.

Three rate-limiting processes are typically considered:

1) Electron movement through the electrode.
2) Electron movement across the electrode|electrolyte interface.
3) Analyte movement through electrolyte.

In (1) electrodes are often chosen on the basis of their superior electronic conductivity, thus this is unlikely to be rate-limiting. In (2) the rate of interfacial electron transfer is determined by the electron transfer rate constant, k_{et}, which increases or decreases depending on the applied potential (under standard conditions). During oxidation, if an electrode potential is less positive than the thermodynamic potential of the electroactive species, then k_{et} will be small, while more positive potentials will result in faster k_{et}. In effect, non-rate limiting processes will display high current values at potentials close to the thermodynamic potential (i.e. minimal overpotential). Assuming the electrode is highly conductive and interfacial electron transfer is fast, then the rate-limiting process will be dependent on the movement of electroactive species in solution to the electrode, known as mass transport in which there are three types:

1) Migration- Movement of charged species (ions) in response to electric field.
2) Convection- Movement of electroactive species in solution mainly by mechanical stirring (e.g. hydrodynamic techniques).
3) Diffusion- Movement of electroactive species in response to concentration changes at electrodelelectrolyte interface, related to Fick's first and second laws.

Convection by stirring is the most effective method of mass transport since it provides a fast controlled flow of electroactive species towards the electrode, whereas migration and diffusion rely upon slower ionic and entropy-driven movements respectively and thus follow in order of efficiency. Convection is often employed when trying to maximise performance of a fuel cell. In analytical situations, however, the slowest mode is desired and so convection and migration are minimised by employing electrolyte solutions which are 'still' and contain an excess inert ionic salt (supporting electrolyte).

3.1.2 Equilibrium Measurements

Given that measurements of potential can only be determined under equilibrium, it is important to understand the establishment of equilibrium using the reaction below:

$$AgCl(s) + e^- \Leftrightarrow Ag(s) + Cl^-(aq) \qquad \textbf{Reaction 3}$$

This is the electrochemical reaction for the silver|silver chloride (Ag|AgCl) electrode comprised of Ag wire coated with a porous layer of AgCl immersed in potassium chloride solution, shown in Figure 23.

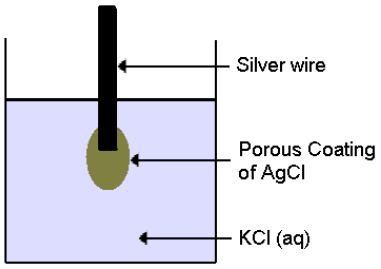

Figure 23: Schematic of Ag|AgCl electrode

Equilibrium is established at the Ag|AgCl interface, when the porous AgCl layer allows penetration of chloride ions, thus establishing a three phase boundary between all components in Reaction 3. In this case, the net transfer of electrons between the components is so small that their concentrations remain unchanged, although, a charge separation will remain at the interface (otherwise the reaction would not have occurred) and thus an electrode potential is established on the metal.

However, it is already known that the potential at a single electrode cannot be determined only the potential difference, *emf*, with respect to another electrode (as shown in Equation 12). This is a problem when only one electrode or half cell reaction is focussed on, as is often the case for most analytical studies. This rationale led to the creation of reference electrodes against which electrode potentials are universally quoted.

3.1.2.1 Reference Electrodes

A reference electrode is a device which has a constant potential and is used to calculate the potential of the electrode being measured (working electrode). The potential of the standard, or normal hydrogen electrode (S/NHE) for the hydrogen redox couple ($2H^+|H_2$) was arbitrarily defined as $E^{\Theta} = 0.0V$, at all temperatures, under standard conditions (Θ). From this reference electrode, the potentials of all single electrodes can be devised.

By convention, the potential difference, *emf*, between two (or more) redox couples is measured using a voltmeter, or any replicable device, under conditions of equilibrium (i.e. zero current) to prevent activity changes in the solution at both electrodes, thus obeying the Nernst equation, as described in the following section. Using the equation below, the electrode potential of the Fe^{2+}, Fe redox couple can be determined[218]:

$$E_{Fe^{2+},Fe} = E^{\theta}_{H+|H2} - emf \qquad \textbf{Equation 13}$$
$$= 0 - 0.714$$
$$= -0.714$$

The electrode potential is always quoted with respect to the reference used, thus $E_{Fe^{2+},Fe}$= -0.714 V vs. NHE.

In practice, however, using the NHE is highly undesirable because it involves hydrogen gas and is very difficult to operate experimentally. Therefore, this has led to the development of secondary reference electrodes by which the potentials have been standardised under given conditions against the zero potential of NHE, hence creating a universal potential scale.

The secondary reference electrode used in this thesis was the silver|silver chloride (Ag|AgCl) as shown in Reaction 3. The potential of the Ag|AgCl electrode is 0.210 V vs. NHE in 3M KCl. The relative ease of fabrication and experimental operation makes this reference electrode a preferred candidate for electrochemical measurements.

3.1.2.2 Nernst Equation

The Nernst equation relates the electrode potential, E, to the amounts of material in solution in terms of activity, *a*, as follows[218]:

$$E = E^{\theta} + \frac{RT}{nF}\ln\frac{(a_O)}{(a_R)} \qquad \textbf{Equation 14}$$

where E^{θ} is the potential for the redox couple under standard conditions.

In most cases, however, the Nernst equation is written in terms of concentration rather than activity, since activity coefficients are often unknown, and thus the formal electrode potential, $E^{o\prime}$, is often employed where products and reagents are present at unit concentration:

$$E = E^{\circ\prime} + \frac{RT}{nF}\ln\frac{[\mathrm{Ox}]}{[\mathrm{Red}]} \qquad \textbf{Equation 15}$$

Under equilibrium conditions, the concentration of oxidised and reduced species ([Ox] and [Red]) at the electrode remains the same, thus the electrode potential is equal to equilibrium potential ($E=E^{o\prime}$).

When current flows, the concentrations of species are not equal and the potential shifts from equilibrium. The difference between the electrodes is therefore:

$$E = E_2 - E_1 = E^{\circ\prime}{}_2 - E^{\circ\prime}{}_1 + \frac{RT}{nF}\ln\frac{[\mathrm{Ox}_2][\mathrm{Red}_1]}{[\mathrm{Red}_2][\mathrm{Ox}_1]} \qquad \textbf{Equation 16}$$

If $E^{o\prime}{}_1 > E^{o\prime}{}_2$, then the cell reaction will proceed spontaneously in the direction according to Equation 16 (above), and Gibbs free energy, $\Delta G^{o\prime}$ will be negative, according to the thermodynamic equation below[16]:

$$\Delta G^{\circ\prime} = -nFE^{\circ\prime} \qquad \textbf{Equation 17}$$

3.1.3 Dynamic Measurements

This is the second of the two main electrochemical situations to be considered with the first involving potential measurements at equilibrium (i.e. no current passes through the cell), explained as "equilibrium measurements" and now where current measurements are required and equilibrium is not possible "dynamic measurements".

Dynamic electrochemistry disrupts equilibrium as a result of current flow due to shifting the electrode potential away from equilibrium (i.e. polarising the electrode). This is the concept of polarisation and the magnitude of this deviation is termed the overpotential, η, as shown below[218]:

$$\eta = E_{electrode} - E_{equilibrium} \qquad \textbf{Equation 18}$$

As stated in the previous section, the potential at the working electrode, $E_{electrode}$, cannot be known, instead the potential difference is taken with respect to a secondary reference electrode having a known fixed potential. Therefore, the reference electrode is critical in determining correct overpotential values and thus an important component of a cell system.

Dynamic measurements are usually conducted using a three-electrode cell (Figure 24). The three components of the cell system are the working electrode (the electrode under investigation), counter electrode (current collector) and the reference electrode, usually abbreviated to WE, CE and RE respectively.

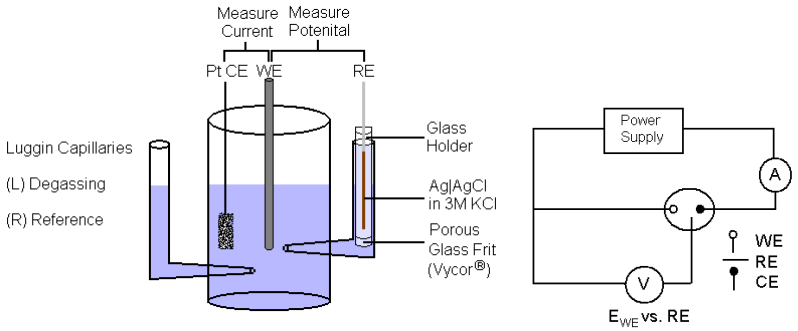

Figure 24: (Left) Schematic illustration of three-electrode electrochemical cell used for dynamic measurements. (Right) Circuit diagram where the symbols V and A represent the voltmeter and ammeter respectively[16].

In Figure 24, the potential is measured between the WE and RE, which is under zero-current flow and thus at equilibrium in order for the potential to be accurately determined. The current is measured between the WE and CE, the CE controls both potential and current since the potential is applied relative to the RE by the CE. In effect, the WE is a passenger and thus is connected to earth via a current follower (converts low current outputs into easily measured voltages).

Dynamic measurements are typically categorised into two systems; those which are under diffusion control and those which are under convection control. In diffusion controlled experiments the supporting electrolyte is usually quiescent (that is unstirred) and contains an excess of ions, thus eliminating mass transport by convection and migration respectively. In practice, however, the majority of catalytic enzyme measurements are carried out under convective control to supply fuel or oxidant, as will be discussed in section 3.1.7.2. Measurements under convective control follow two extremes[218]:

1. Movement of an electrode through an otherwise still solution (e.g. rotating disk electrode, see section 3.1.3.3).
2. Movement of solution past a stationary electrode (e.g. stirring, pump systems, flow cells and channel electrodes).

Both of these are classes of hydrodynamic electrodes, where 'hydrodynamic' simply means the movement of water, which is often the solvent of choice in electroanalytical measurements.

3.1.3.1 Diffusion Controlled Cyclic Voltammetry

The most common technique used for studying dynamic electrochemistry is cyclic voltammetry (CV). Other voltammetric techniques are available, such as linear sweep and differential pulse but these do not have the ability to look at redox species and are therefore non-reversible techniques.

In cyclic voltammetry current is measured as a function of electrode potential, where the potential is swept forward and back at a constant rate between two potential values, E1 and E2, as given in Figure 25[218] .Since the electrode potential is swept forward and back in a cyclic manner, the technique is called "cyclic voltammetry".

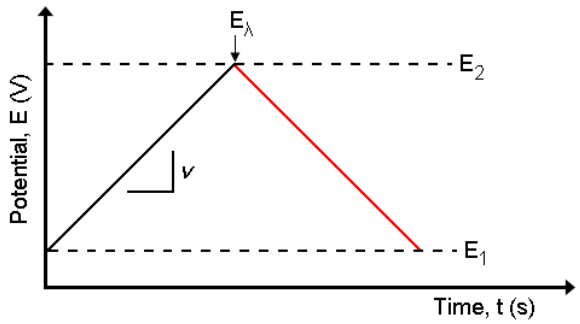

Figure 25: Potential profile for one cycle in a cyclic voltammetric experiment at scan rate, *v*. (Black) Forward scan (Red) Backward scan.

A cyclic voltammogram for the reduced form of a soluble redox species is shown in Figure 25. As the electrode potential approaches $E^{o\prime}$, current increases as the reduced species is oxidised at the electrode surface, reaching a maximum at E_{pa}. This is where the concentration of reduced species at the surface becomes zero, as a result of accumulation of oxidised species at the electrode surface, the depletion layer.

After the scan is reversed, E_λ, the current is still positive and decreasing, reduced species are still being oxidised since the electrode potential is above $E^{o\prime}$. Near $E^{o\prime}$, the oxidised species accumulated at the electrode are reduced and negative current is observed. Once the concentration at the interface approaches zero, the current falls under the same behaviour. This results in peaks of similar shape and

providing the redox couple fulfil a range of criteria as described below, the couple are only then deemed to be fully reversible (see Figure 26).

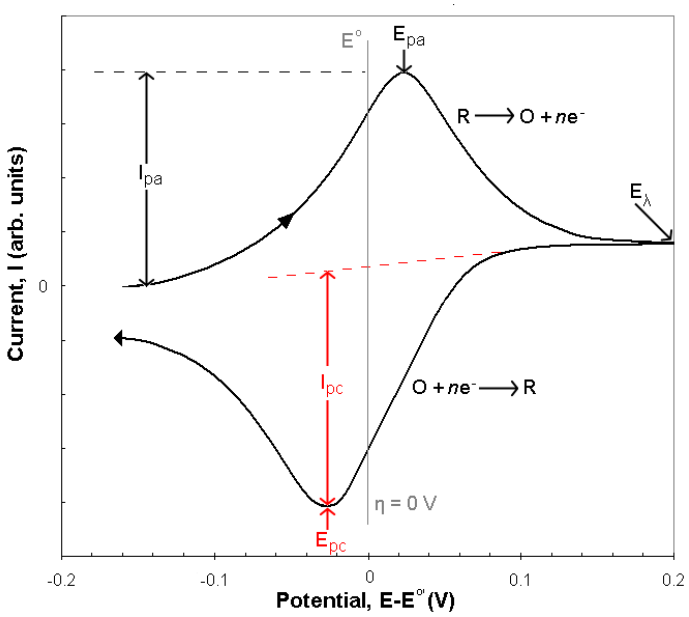

Figure 26: Example cyclic voltammogram of a redox couple displaying reversible behaviour, where solution is under diffusion control and initially contains the reduced form of the electroactive couple.

For a reversible redox couple under semi-infinite linear diffusion, that is when analyte diffusion occurs in one dimension only, perpendicular to the electrode, the peak current, I_P, is given by the Randles-Sevčik equation[218]:

$$I_p = 0.4463nFA\left(\frac{nF}{RT}\right)^{0.5} D^{0.5}v^{0.5}c_{analyte} \qquad \textbf{Equation 19}$$

A linear plot of I_P vs $v^{0.5}$ is often used as the criterion for redox species under diffusion control and included in the criteria below used for a reversible redox couple:

1. $I_{PA} = I_{PC}$
2. Peak potentials, E_{PA} and E_{PC} are independent of scan rate
3. Peak separation ($E_{PA} - E_{PC}$) is 0.059 V/n for an n-electron couple
4. I_P is proportional to $v^{0.5}$
5. $E^{o\prime} = (E_{PA}-E_{PC})/2$

Cyclic voltammetry can be used to determine various mechanistic parameters relating to electrochemical processes, in addition to the thermodynamic information usually obtained at equilibrium. For example, the peaks provide information on the redox processes, the positions provide useful thermodynamic information (e.g. formal redox potentials), the number of peaks gives a measure of the reactions involved and the shape of a CV also provides information on the faradaic contributions to the overall current (see section 3.1.5).

3.1.3.2 Diffusion Controlled Chronoamperometry

In this experiment the potential is usually stepped with time in a predetermined manner as the current is measured as a function of time or potential. These measurements are only concerned with the conversion of one redox form of the analyte by applying a potential above the formal potential of the redox couple, as shown in the oxidation reaction below:

$$\text{Red} \longrightarrow \text{Ox} + ne^- \qquad \textbf{Reaction 4}$$

As shown in Figure 27 (Top)[218], the potential of the WE is initially held more negative (E_1 = 0V vs. NHE) than the formal potential for the redox couple, $E^{o\prime}$ (above). In this case the reduced form (R) is stable and the concentration of R in the bulk solution remains unchanged. Once the potential is stepped above $E^{o\prime}$, to the second potential (E_2 = 0.5V vs. NHE), the electron transfer reaction is energetically favourable and electrons move from the electrode to the analyte.

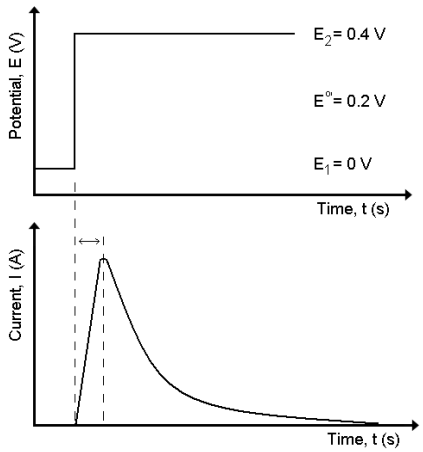

Figure 27: (Top) Potential step profile and (Bottom) Trace of current against time in response to potential step. The time between the potential step and reaching the maximum current (indicated by the arrow) is termed the "rise time" and results from electrochemical changes within the double layer (see section 3.1.5.1).

The decay in current with time after the maximum is described by the Cottrell equation[218]:

$$I_{\text{lim}} = nFAc\sqrt{\frac{D}{\pi t}} \qquad \textbf{Equation 20}$$

For this equation to apply, the current must be limiting (i.e. the potential step must be far removed from the $E^{o\prime}$, to an extreme overpotential) and thus $I_{\text{lim}} \propto c_{\text{analyte}}$. The reaction will be driven to completion at this overpotential because the concentration of R at the surface quickly becomes zero and a depletion layer forms which grows with time, as shown in Figure 28[218].

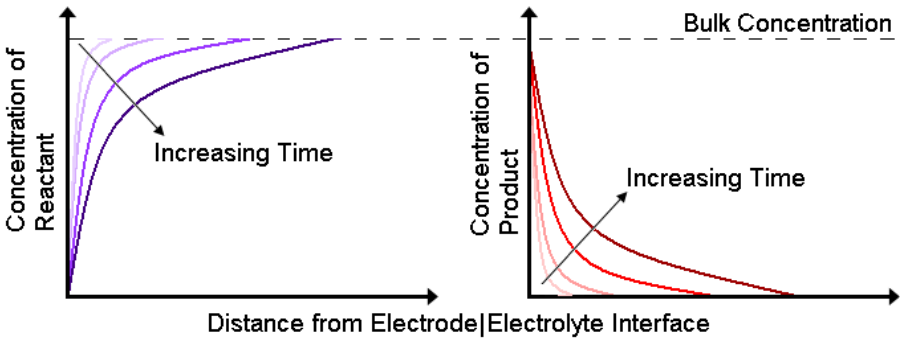

Figure 28: Concentration profile as a function of time during the chronoamperometry experiment.

3.1.3.3 Convective Control: Hydrodynamic Techniques

In the dynamic measurements as described, the principal mode of mass transport was diffusion, since convection and migration were minimised by using a still electrolyte solution with high ionic strength. Hydrodynamic techniques involve mass transport by convection, which is such a highly efficient form of mass transport that migration and diffusion are negligible. Convective electrolyte flow can occur via two extremes, as described earlier and below[218]:

1. Movement of an electrode through an otherwise still solution (e.g. rotating disk electrode)
2. Movement of solution past a stationary electrode (e.g. flow cells and channel electrodes)

In the first case, a disc electrode is immersed in electrolyte and rotated at a known frequency, ω, initiating a convective flow of solution over the disc face (flux) that can be characterised in two dimensions, the radial direction, r, and distance in solution, y, as shown below in Figure 29. This is the most commonly used technique due to the reproducible and high convective flux that can be obtained by the rotating disc electrode (RDE).

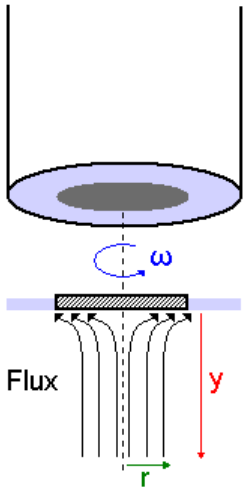

Figure 29: (Top) 3D-representation of RDE and (Bottom) 2D-representation highlighting electrolyte flow when rotated at frequency, ω.

The Levich equation[218] predicts that the limiting current is proportional to the concentration of analyte and square root of rotation frequency, ω:

$$i_{\lim} = 0.62nFAD^{2/3}v^{-1/6}\omega^{1/2}c_{analyte} \qquad \textbf{Equation 21}$$

where v is the kinematic viscosity of the solution ($cm^3\ s^{-1}$).

However, these predictions fall short at high rotation frequencies due to the convective flow changing from laminar to turbulent. The Levich plot becomes non-linear and reaches a maximum limiting current, as shown in Figure 30 (below):

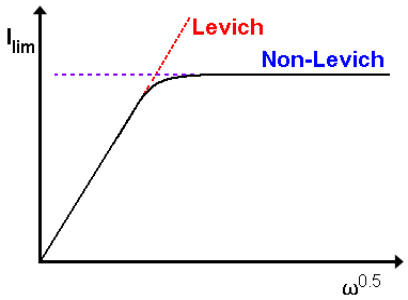

Figure 30: Example of Levich plot for RDE experiments

Other reasons for this deviation include slow electron transfer kinetics or breakdown of mass transport due to insufficient replenishment of electrolyte at infinite rotation . In addition, it is important that laminar flow is well defined by ensuring the electrode does not wobble, the counter electrode is large and does not obstruct solution flow and the disc face is well positioned in solution ensuring reproducible flow.

Furthermore, it must be noted that the Levich equation contains a diffusion coefficient, D, even though the RDE system is under convective control. This is because the viscous drag of solution over the electrode surface results in the formation of a thin layer known as the diffusion layer, through which the analyte must diffuse, characterised by a constant term, D ($cm^2\ s^{-1}$).

The thickness of the layer, δ (in cm), can be measured using the equation below[218]:

$$\delta = \frac{1.61 v^{1/6} D^{1/3}}{\omega^{1/2}} \qquad \textbf{Equation 22}$$

3.1.4 Electrode Kinetics

3.1.4.1 Tafel Kinetics

It is known experimentally that increasing the temperature, T, results in an exponential increase in the rate constant, *k*, according to the Arrhenius equation (Equation 23)[218], where A is a pre exponential factor and E_A activation energy. Similarly in electrochemistry, increasing the electrode overpotential, η, results in an increase in the rate of electron transfer, thus at constant temperature the following Tafel equation is used (Equation 24)[218]:

$$k = Ae^{-E_A/RT} \qquad \textbf{Equation 23}$$

$$I = a + b\exp\eta \qquad \textbf{Equation 24}$$

According to the Tafel equation, the plot of ln(*I*) and η should be linear, however, this is only valid over a narrow overpotential range (Figure 32). At extreme overpotentials, insufficient flux causes the current at the electrode to plateau. Conversely at very small overpotentials, the system is at equilibrium and therefore the current is zero.

3.1.4.2 Butler-Volmer Kinetics

A more accurate approach than the Tafel equation is given by the Butler-Volmer equation, which considers both the oxidation and reduction currents across all overpotentials (Equation 25)[218] and also allows determination of the electron transfer rate constant, k_{et}, from the exchange current density, I_0, which is the rate of turnover at zero overpotential (Equation 26)[218]:

$$I_{net} = I_0[e^{\left(\frac{(1-\alpha)F\eta}{RT}\right)} - e^{\left(\frac{-\alpha F\eta}{RT}\right)}] \qquad \textbf{Equation 25}$$

$$I_0 = nFAk_{et} \qquad \textbf{Equation 26}$$

As shown in Figure 32, the Butler-Volmer plot has three regions of interest:

1. At very small overpotentials, the current is small enough that the magnitude of the reverse reaction is large enough that $I_{net} = 0$.
2. At intermediate overpotentials, the system is under kinetic control; ln(I) is directly proportional to η and extrapolation of the slopes describes the electron transfer rates for the corresponding oxidation and reduction reactions (known as Tafel region).
3. At extreme (large) overpotentials, the response is linear due to insufficient flux of analyte to electrode surface, thus the system is under mass transport control.

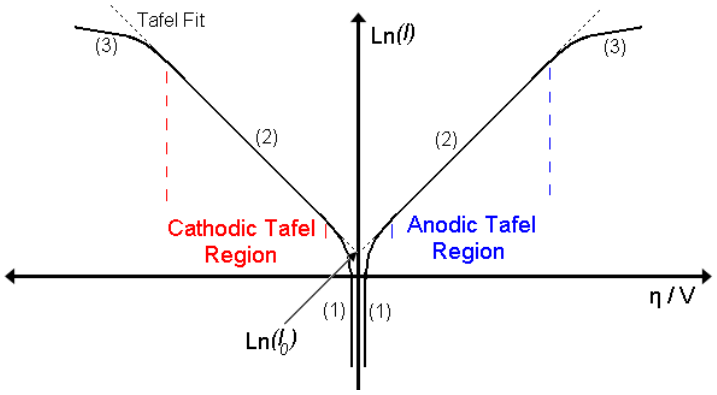

Figure 31: Example Butler-Volmer plot, showing three regions (numbered) and y-intercept corresponding to exchange the current density, (I_0).

3.1.4.3 Koutecky-Levich Kinetics

The Levich approach is concerned with limiting current, I_{lim}, under mass transport control (Equation 27)[218], whereas the Butler-Volmer approach is usually concerned with the Tafel region under kinetic control. The Koutecky-Levich equation combines both approaches and takes the following form:

$$\frac{1}{I_{non-limiting}} = \frac{1}{nFAk_{et}c_{analyte}} + \frac{1.61\nu^{1/6}}{nFAc_{analyte}D^{2/3}}\frac{1}{\omega^{1/2}} \qquad \textbf{Equation 27}$$

This equation departs from mass transport control at infinite rotation, $\omega = \infty$, the current is non-limiting and instead mass-transport limited. Therefore, the Koutecky-Levich plot of I^{-1} against $\omega^{-0.5}$ at a certain overpotential yields a straight line; the extrapolated current (i.e. where $x = 0 = \omega = \infty$) can be used to calculate the rate of electron transfer, k_{et}.

3.1.4.4 The Marcus Theory

Many theories of electrode kinetics have been constructed and some already discussed, however, it is concepts of the Marcus theory which provided the most encouraging results and therefore has been widely applied in electrochemical studies. The relative simplicity of the model and ability to predict with some accuracy the structural effects of the reactant on the kinetics of the reaction has encouraged belief in the concepts of the Marcus theory[219].

Marcus theory can be initially explained in terms of the interaction of the reactant molecule at the electrode|electrolyte interface. Two types of interaction have been described[16]:

1. Outer-sphere electrode reactions occur when the reactant is limited to the 'Outer Helmholtz Plane' (OHP) due to the presence of the solvent layer which is specifically adsorbed or coordinated to the electrode (Figure 32).
2. Inner-sphere electrode reactions occur when there is strong interaction between the reactant and electrode, such reactions involve ligands which

help to bridge the interaction of the reactant centre or ion with the electrode (Figure 32)[219]. As such the kinetics of these reactions are highly dependant on the electrode surface, such as double-layer effects, energy and distribution of electronic states in the electrode and so on.

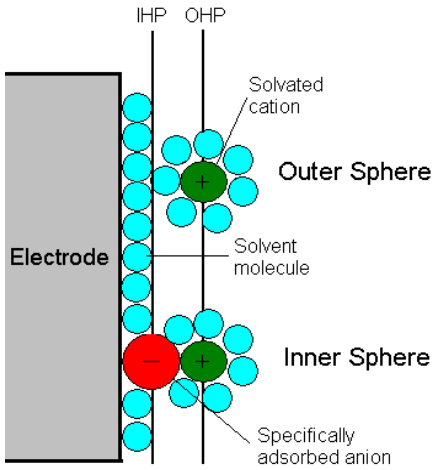

Figure 32: Schematic representation of outer sphere and inner sphere electrode reactions.

Considering that inner-sphere processes require knowledge of specific adsorption effects, the theory of outer-sphere electron transfer is more implicit and thus the discussion that follows relates to these kinds of reactions.

These concepts are typically illustrated using potential energy curves, which also can be used to help quantitatively predict the electron transfer rate constants, k^0. Figure 33 illustrates a potential energy curve going from reactants (R) to products (P) as a function of 'reaction coordinate', which in this case is the bond length and/or angle of the species[219]. For simplicity, the electron transfer process involves the one-electron reduction at the electrode surface and the crossover point, marked by dark circle, represents the transition state from reactants to products. It can be noticed that an energy barrier, ΔG^*, must be overcome for transition from the ground state reactant energy (i.e. lowest point on R curve) to products, marked by circle. This excitation energy cannot simply appear in the system (unless under irradiation through absorption of a photon), and thus the reactant must be 'thermally activated' (i.e. bond angles and lengths must be stretched and distorted along with solvation shells). Thermal activation proceeds when potential energy from the electrode causes the reactant ions to become

thermally excited, and when this excitation energy matches, ΔG^*, electron tunnelling proceeds and transition to the product occurs. After which, excitation is lost via collisions with solvent molecules and the product reaches a ground state.

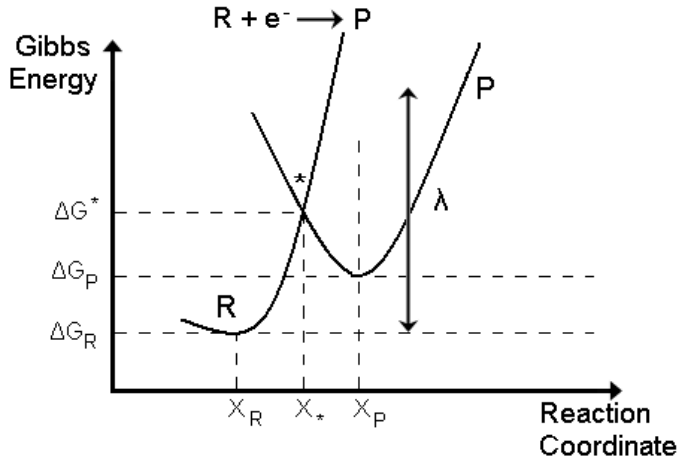

Figure 33: Gibbs energy, ΔG, as a function of reaction coordinate, X.

According to Marcus theory, the electrochemical rate constant, k_{ET}, depends on the Gibbs activation energy, ΔG^*, and can be calculated as follows[219]:

$$k_{ET} = KZ\exp(-\Delta G^* / RT) \qquad \textbf{Equation 28}$$

where K is the probability of electron-tunneling (i.e. transition probability) such that K~1 for an adiabatic process, whereas K«1 for a non-adiabatic reaction and Z is a pre-exponential term related to the collision frequency.

The probability of electron-tunneling, K, can be described using the potential energy curves shown below in Figure 34 [16]. The extent of interaction between the reactant and electrode is known as adiabaticity, such that strong interactions or adiabatic reactions, result in large splitting of the energy curves at the transition point so that the reaction takes place on the lower curve with a probability close to unity, as shown in Figure 34(left). Conversely, non-adiabatic reactions are result of small interactions (e.g. reactant and electrode are far apart), such that the energy gaps are tiny and the transfer from R to P is much less than unity, as shown in Figure 34 (right).

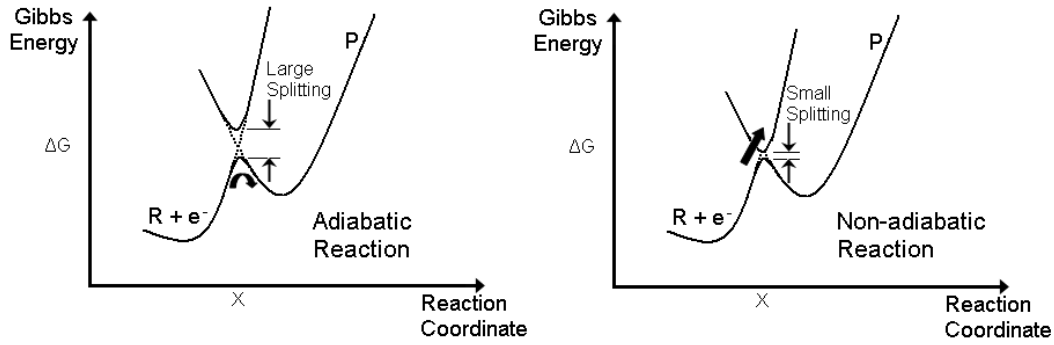

Figure 34: Representative splitting of energy curves (energy surfaces) for adiabatic (left) and non-adiabatic reactions (right).

Generally, in most electron transfer reactions the energy gap is negligible enough (even for inner sphere reactions) for adiabatic reactions to still occur and the location of the transition state can be approximated, as displayed in Figure 34. Accordingly, this allows the Gibbs energy of activation, ΔG^*, to be accurately determined[219]:

$$\Delta G^* = \frac{(\lambda + \Delta G)^2}{4\lambda} \qquad \textbf{Equation 29}$$

where ΔG^* is related to the standard Gibbs free energy, ΔG, and the reorganisation energy, λ. These are two critical parameters of the Marcus model and calculated as follows[16, 219]:

$$\lambda = \frac{1}{2} k (X_R - X_P)^2 \qquad \textbf{Equation 30}$$

where k is the force constant describing the vibrational changes at the transition point and $(X_R - X_P)$ relates to the difference in reaction coordinate (the greater the difference, the smaller k_{et} and hence higher ΔG^*).

Therefore, the reorganisation energy, λ, represents the energy to transform the molecular geometries of the reactant (λ_i) and solvent (λ_o) to those of the product state, as shown below[16]:

$$\lambda = \lambda_i + \lambda_o \qquad \textbf{Equation 31}$$

and

$$\Delta G = G_p(X = X_p) - G_R(X = X_R) = -nF\eta \quad \textbf{Equation 32}$$

where overpotential η = (E-E$^{o\prime}$) and E is the applied potential. This theoretical concept is described in section 2.1.2 where the activation overpotential, η_{act}, relates to the electrode energy (potential) required to drive these reactions (i.e the greater η_{act}, the higher ΔG^*).

In enzyme electrochemistry, the redox centres are buried within the protein shell, as such the distance between the electrode and enzyme may be considerable meaning that adiabacity has more relevance than dissolved reactants participating in a hetereogeneous reaction. Therefore, the following relation is used to predict the k_{ET} with distance from electrode, d [220]:

$$k_{ET} = k_0 \exp[-\beta(d - d_0)] \quad \textbf{Equation 33}$$

where k_0 is the electron transfer rate constant at distance of closest contact d_0 and β is typically between 8.5 – 11.5 nm^{-1}, such that k_{ET} decreases with distance, d.

This equation is useful when using self-assembled monolayers to study the distance dependence of an electroactive species at an electrode surface. Furthermore, the Marcus theory highlights the importance of effective electronic coupling between the enzyme and electrode, and is often used to demonstrate why direct electron transfer cannot be achieved for some enzymes.

3.1.5 Faradaic and Non-Faradaic Charge

Until now discussion has been focussed on faradaic charge transfer related to electron transfer across an electrode|electrolyte interface and resulted in the redox reactions given in section 3.1.1 Since the total charge passed is directly proportional to the number of chemical reactions at the interface, such reactions are governed by Faraday's laws and thus called faradaic processes[16].

Contrary to this process is non-faradaic charge transfer, in which no charge transfer reactions occur within a potential range because they are not energetically favourable (thermodynamically or kinetically). Instead, the charge arises from current transients due to surface processes such as adsorption and desorption of ions from solution, re-ordering of ions at the interface, and charging of electrode double layer.

3.1.5.1 Electrode Double Layer and Capacitance

The electrode double layer (EDL) consists of an array of ions and solvent molecules at the electrode|electrolyte interface. The two principle layers of the EDL model are named after the pioneer Hermann Helmholtz, and known as the inner Helmholtz plane (IHP) and outer Helmholtz plane (OHP). The IHP describes the layer nearest the electrode surface which is at a distance, x_1, and consists of solvent molecules (orientated dipoles) and specifically adsorbed ions which are no longer solvated. While the remaining solvated ions are limited to a distance from the electrode, x_2, and form the OHP. Outside the OHP into bulk solution the ions are randomly distributed due to thermal agitation, thus this region is called the diffuse layer.

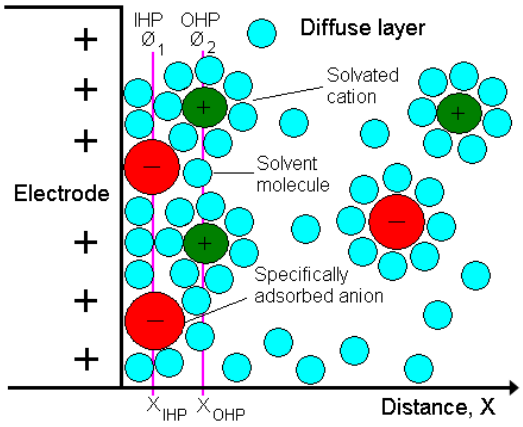

Figure 35: EDL Model for a positively polarised electrode.

During an electrochemical experiment, non-faradaic processes can directly influence the rates of electrode processes. For example, the movement of electroactive species from the bulk to the electrode surface is dependant on the thickness of the diffuse layer. The extent of the EDL or charging current depends on many factors such as the electrode, potential, adsorbate and ionic concentration.

In essence, the EDL behaves in a similar manner to a capacitor, where the total charge stored across the metal plate, q, is dependant on the potential across it, E, as shown below[16]:

$$C = \frac{q}{E} \qquad \textbf{Equation 34}$$

This finite quantity is known as the capacitance, C, and is directly proportional to the surface area of the metal plate, thus values are often expressed per unit surface area (F cm^{-2}) or per unit mass (F g^{-1}).

In an electrochemical experiment, the double layer capacitance can be accurately determined by dividing the integrated current transient with respect to time for the positive or negative potential scan (and surface area or mass of electrode)[16]:

$$C_{dl} = \frac{\int_{E_2}^{E_1} I_c dt}{(E_2 - E_1)} \qquad \textbf{Equation 35}$$

An idealised example of a porous carbon electrode displaying pure capacitance is shown in the CV below, Figure 36 (a). As the potential is swept at a constant rate between E_1 and E_2 the net charge of the electrode is balanced by ions in close vicinity of the electrode surface. In this potential range, charge-transfer reactions are not energetically favourable and hence only non-faradaic charge is observed.

A rectangular CV shape indicates ideal non-faradaic behaviour since there is no charge imbalance with applied potential. In addition, an instantaneous switch in capacitive current between $+I_c$ and $-I_c$ (i.e. short reversal time, Figure 36 (a)), indicates good pore accessibility and ion mobility. While, the magnitude of I_c provides an indication of the available electroactive area.

In the presence of a redox couple, the faradaic charge is superimposed over the non-faradaic reponse and redox peaks are shown in Figure 36 (b). However, the signal to background ratio is small, thus highlighting the effect of the double layer on charge transfer. This response should be avoided in systems such as electrochemical sensors, where high faradaic detection signals are imperative.

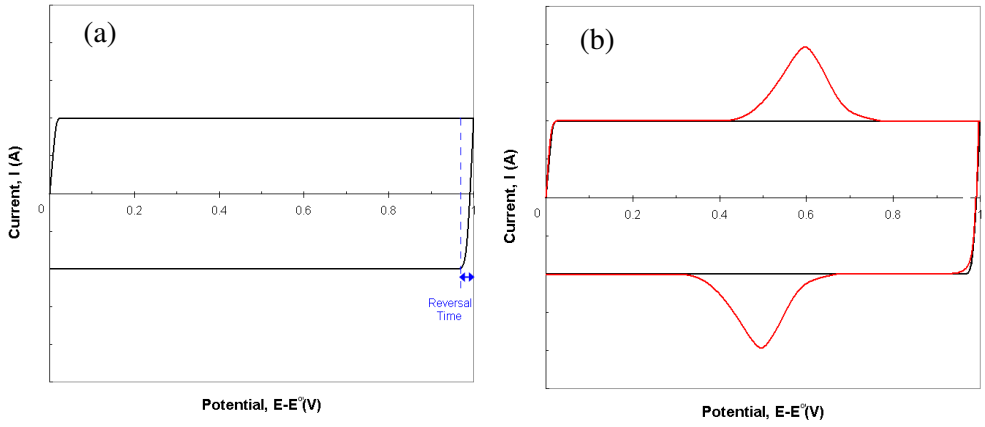

Figure 36: (a) Example of idealised non-faradaic behaviour. (b) Faradaic behaviour superimposed, where the weak signal is consequence of the double layer.

3.1.6 Effect of Electrode Porosity: Thin-Layer Behaviour

Porous electrodes not only increase the capacitance of the electrode but can also display thin-layer electrochemical effects. This behaviour is observed when the cell thickness (electrode pores) is smaller than the diffusion layer, such that mass transfer within the cell is limited and the analyte is confined to a thin-layer at the electrode surface (2-100 μm)[16]. The concentration profile expected for thin-layer behaviour is shown in Figure 37 (Right), where the concentration of analyte in the pores decreases quickly with time and is said to be under finite linear diffusion control. In contrast, the concentration profile for an electrode with cell thickness greater than the diffusion layer is shown in Figure 37 (Left), previously described in section 3.1.3.2 and is behaving under semi infinite linear diffusion.

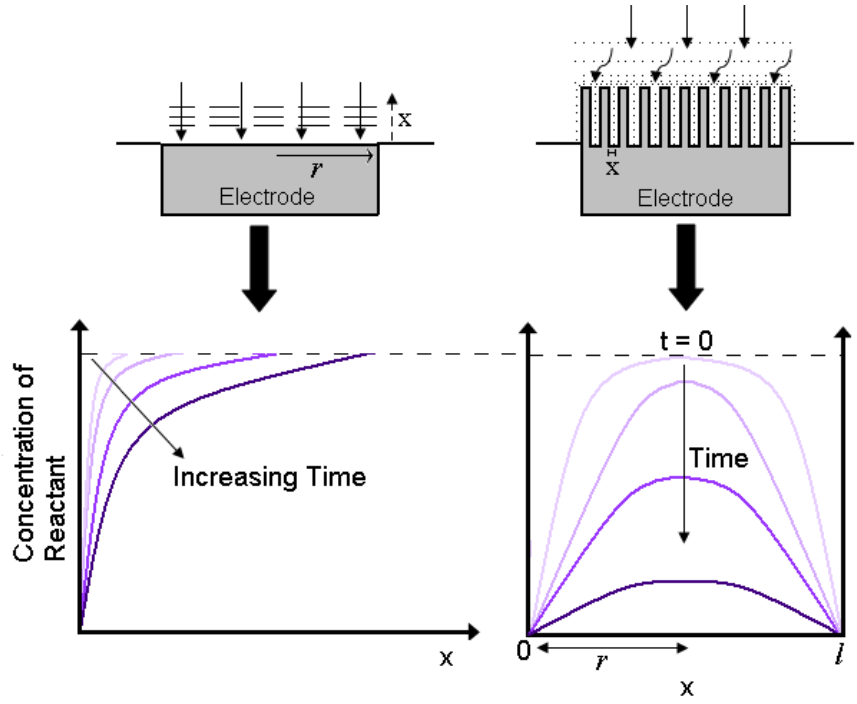

Figure 37: Schematic and corresponding concentration profile for (Left) macro-electrode displaying planar diffusion (semi infinite linear diffusion) with large diffusion layer, and (Right) micro-porous electrode displaying diffusion limited transfer of reactant, where overlapping of small diffusion layers within electrode pores results in faster depletion of reactant.

Cyclic voltammetry of a perfectly reversible redox couple undergoing thin-layer behaviour would have a peak separation of 0 V (see Figure 38), instead of 0.059/*n* V[16]. The peak current occurs at E = E$^{o\prime}$ and is given by Equation 36 below, where V is pore volume (cm^3)[16]:

$$I_p = \frac{n^2 F^2 v V C}{4RT} \qquad \textbf{Equation 36}$$

For thin-layer behaviour the peak current is directly proportional to scan rate, not $v^{0.5}$ as with planar diffusion, but the charge under the curve is independent of *v*.

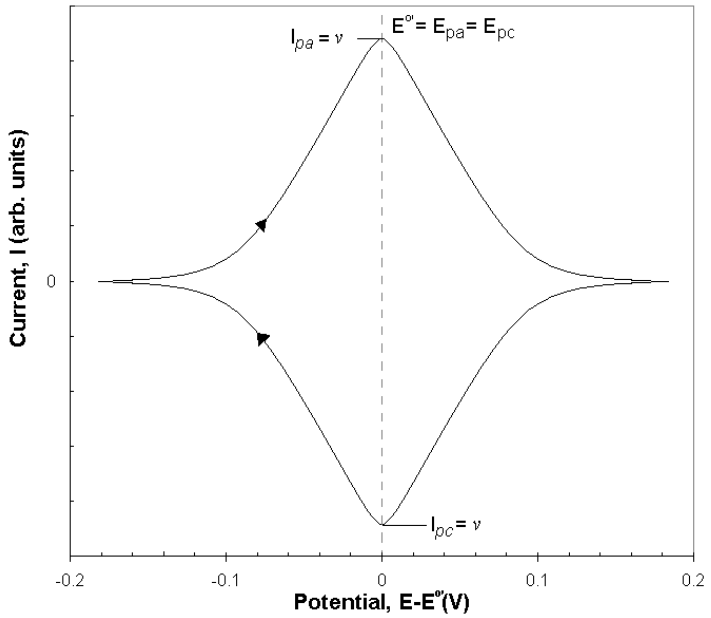

Figure 38: Example CV displaying thin-layer behaviour.

3.1.7 Voltammetry of Adsorbed Enzymes: Protein-Film Voltammetry

Previous sections described electrochemical measurements involving redox analytes under diffusive or convective control, however in this case both are eliminated and redox proteins (i.e. enzymes) are adsorbed onto an electrode surface. In fact, these enzymes are adsorbed in a configuration that allows analysis by dynamic electrochemical methods; this is known as 'protein-film voltammetry', as shown in Figure 39. These studies are often carried out using CV, by applying a potential to the electrode which is either rotating or stationary, and measuring the electron transfer between the electrode and enzyme redox centres, resulting in diagnostically useful current signals. From these signals it is possible to elucidate useful thermodynamic and kinetic information of enzymes.

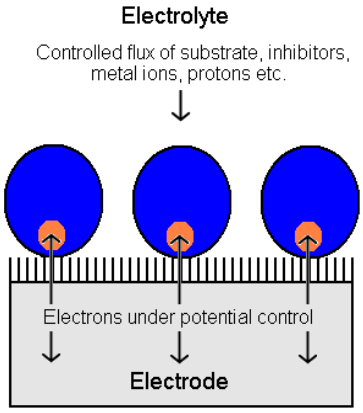

Figure 39: Representation of ideal configuration for protein-film voltammetry. The adsorbed enzyme monolayer is orientated via non-covalent functionalities on electrode surface, thus allowing direct electron transfer.

This direct communication is only possible with enzymes, that have active sites at (or close to) their exterior surface and thus can directly communicate with the electrode surface (e.g. oxidoreductases). In addition these CV measurements can be carried out under 'non-catalytic' or 'catalytic' conditions giving rise to different CV shapes or waveforms and these will be discussed in the following sections. Furthermore, the waveforms will be interpreted in terms of the enzyme processes occurring and the useful information that can be obtained.

It must be noted that each waveform discussed will be simplified in terms of reversible interfacial electron transfer (i.e. without consideration of IR effects) but will differ in the type of electron transfer coupling, as will be explained in the following sections.

3.1.7.1 Non-Catalytic Voltammetry

A 'non-catalytic' or 'non-turnover' signal is observed when the adsorbed enzyme is measured in the absence of substrate or inhibited (usually by halide ions). The CV usually displays a pair of peaks corresponding to the reduction and oxidation of the redox centre, as shown in Figure 40. The average position of these peaks corresponds to the reduction potential of the redox centre, $E^{\circ'}$, and for an ideal, reversible system the peaks are symmetrical to each other and electron transfer is Nernstian (i.e. all ET steps are fast).

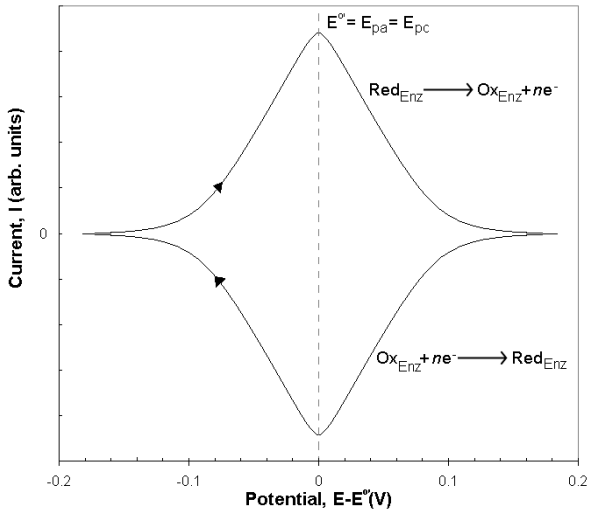

Figure 40: Example voltammogram for adsorbed enzyme displaying ideal non-catalytic behaviour.

Depending on the enzyme several signals may be apparent due to the active site and different relay centres. For example, high potential laccases, such as *Trametes hirsuta* and *Trametes versicolor*, have displayed two pairs of peak-like signals with midpoint potentials at 790 mV and 400 mV corresponding to redox transformations of the T1 and T2/T3 sites[221]. These peak current signals are often of low intensity due to low monolayer surface coverage (pmol/cm^2) and

associated electron contributions (depending on orientation), shown in the relation below[222], where peak current is proportional to surface coverage of enzyme, Γ, and to the number of electrons, n^2 :

$$i_p = \frac{n^2 F^2 A \Gamma v}{4RT} \qquad \textbf{Equation 37}$$

Furthermore, the background non-faradaic current can often mask these signals (see section 3.1.5). However, a linear plot of i_p against v often proves that the redox species are adsorbed onto the electrode.

Further detailed investigations can be carried out to probe the electron transfer efficiency between the electrode and active site and also resolve and quantify the chemical processes coupled to electron transfer (i.e. electron transfer coupled reactions)[222]. An overview of how to undertake these studies will be given below, however, the reader is directed towards the following reviews for further detailed understanding and insight into these investigations[195, 222-225].

In these investigations, the scan rate employed is sufficiently fast so that the system is said to have departed from equilibrium. Therefore, as scan rate increases, the rate of electron transfer between the electrode and enzyme becomes too fast to maintain equilibrium and the peaks deviate from their reversible Nernst peak shape. This allows investigation into the kinetics of interfacial electron transfer by varying the experimental timescale (scan rate). The simplest case can be observed for an uncoupled one-electron redox centre in Figure 41 [222], where the peaks are shown to have broadened and shifted to higher driving forces. These results are often displayed in the form of a trumpet plot where the corresponding peak potentials are plotted as a function of scan rate, on a log scale (Figure 42)[222]. As a general rule, the higher the scan rate at which peak separation occurs, the more efficient the electron transfer between electrode and enzyme.

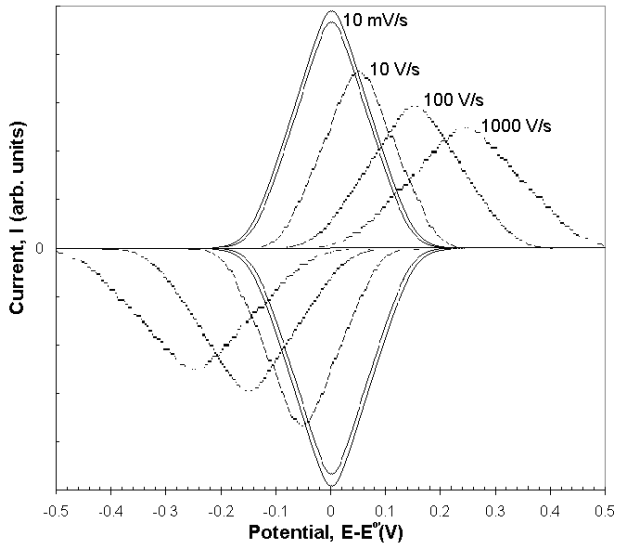

Figure 41: Example voltammograms showing effect of scan rate (from 1000 V/s to 10 mV/s) for an uncoupled one-electron redox centre.

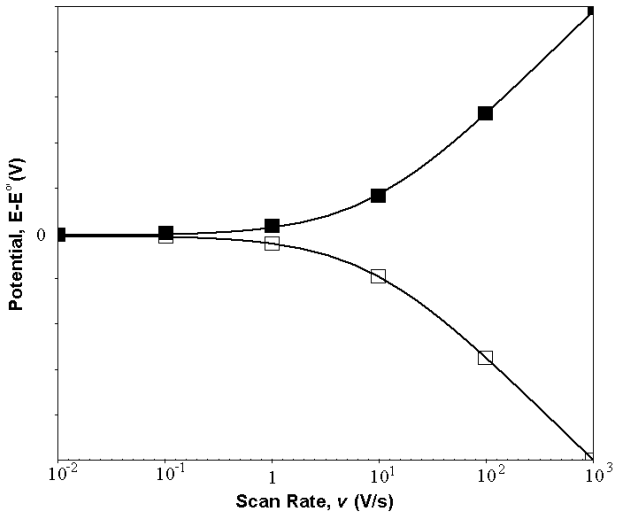

Figure 42: Corresponding trumpet plot from Figure 20, where E_{pa} (filled squares) and E_{pc} (empty squares) separate at high scan rates due to lower electron transfer efficiency.

Coupled reactions, for example, where the change in oxidation state of the enzyme is dependant on the transfer of a proton can also be electrochemically interrogated at high scan rates. Using time scales that complement the reaction event (1ms at 1000 V/s) enables the rates of (de)protonation to be measured.

In addition, these fast scan measurements can be also applied to catalytic systems described in the following section, where the catalytic cycle can be outrun

allowing for detection of transient catalytic intermediates (e.g. redox cofactors such as FAD)[225].

3.1.7.2 Catalytic Voltammetry

In the presence of substrate, the catalytic turnover of the adsorbed enzyme transforms the peak shape into a sigmoidal wave (see Figure 43) which is easily observed even at low enzyme coverage (unlike non-catalytic signals).The sigmoidal shape is because the substrate regenerates the redox state of the enzyme in a succession of catalytic cycles (i.e. electrons are no longer confined to the adsorbed protein film on the electrode)[195]. The direct relationship between catalytic current and the turnover rate provides a direct measure of the activity of the enzyme.

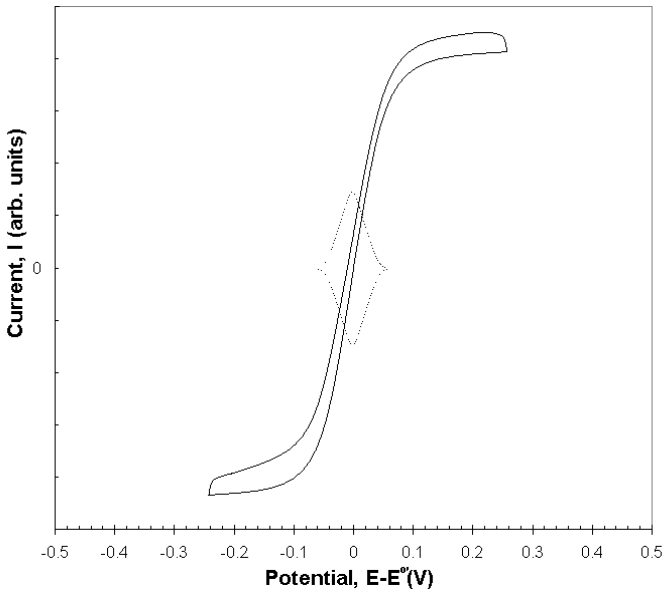

Figure 43: Example voltammogram for adsorbed enzyme showing reversible catalytic oxidation and reduction of substrate.

In catalytic voltammetry, three electrochemical situations must be considered and these will be discussed briefly below, the reader is directed to the following publications for further detailed understanding [195, 222-228]:

1. Systems under mass transport control
2. Systems under enzyme control
3. Systems under interfacial electron transfer control

The first case occurs when the rate of supply of substrate to the enzyme is much smaller than the turnover rate, and interfacial electron transfer is fast relative to product formation[226]. This limiting current due to depletion of substrate near the electrode can be demonstrated to be under mass-transport control by rotating the electrode. As shown in Figure 44, the limiting current increases with electrode rotation because the substrate is consumed more quickly by convection.

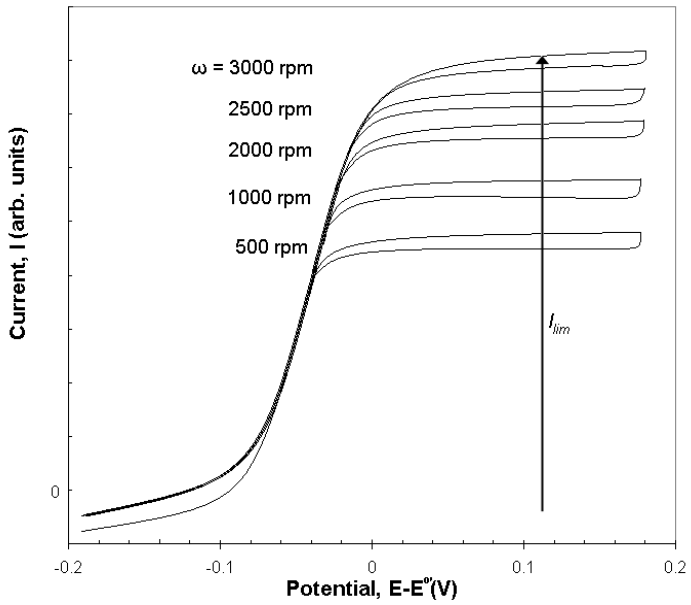

Figure 44: Example CV demonstrating the effect of electrode rotation on catalytic current

This behaviour is described by the Levich equation[218, 222], where the transport of substrate to the electrode limits the current response:

$$i_{\lim} = 0.62nFAD^{2/3}v^{-1/6}\omega^{1/2}c_{analyte} \qquad \textbf{Equation 38}$$

Given that, the $c_{analyte}$ at the electrode is equal to the enzyme turnover number, the equation can be re-written as:

$$i_{\lim cat} = nFA\Gamma \text{ x turnover number} \qquad \textbf{Equation 39}$$

thus,

$$i_{\lim cat} = nFA\Gamma \frac{k_{cat}}{1 + \frac{k_M}{[substrate]}} \qquad \textbf{Equation 40}$$

where Γ is the surface coverage of active enzyme (mol cm^{-2}), k_M is the Michaelis Menten constant (mol dm^{-3}) and k_{cat} the maximum turnover rate (s^{-1}).

However, at "infinite" rotation rate a maximum flux is reached (usually ≥3000 rpm) and the catalytic current is finite and thus controlled by the inherent properties of the enzyme (Note: higher rotation rates can be expected for enzymes that display significantly faster kinetics). The system is now said to be under enzyme control, without limitations to mass-transport or interfacial electron transfer. A Koutecky-Levich plot shown in Figure 45 illustrates this departure from mass-transport at infinite rotation rate, where limiting current is plotted against the square root of rotation rate in a reciprocal manner, following the inverse of Equations 38 and 39 above[222, 226]:

$$\frac{1}{I_{\lim(\omega)}} = \frac{1}{I_{\lim}} + \frac{1}{I_{\lim cat}} \qquad \textbf{Equation 41}$$

thus,

$$\frac{1}{I_{\lim(\omega)}} = \frac{1}{nFA\Gamma k_{cat}} + \frac{\text{constant}}{\omega^{1/2}} \qquad \textbf{Equation 42}$$

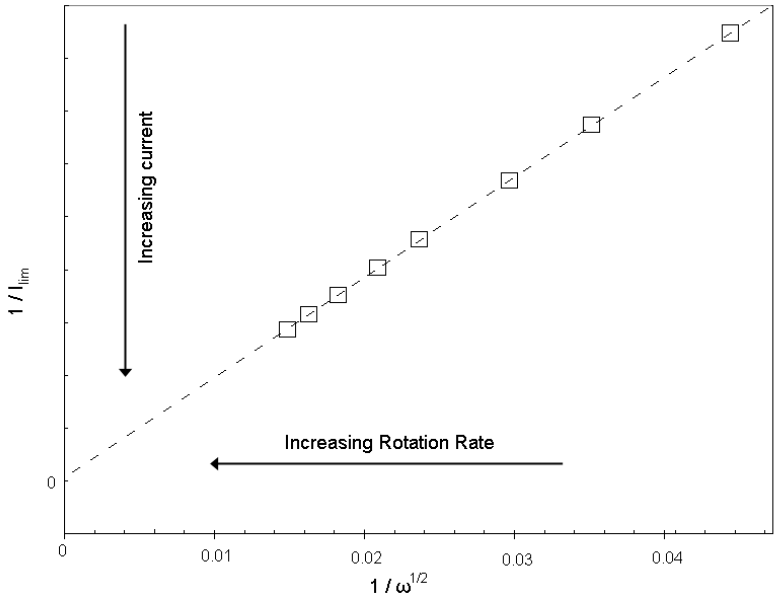

Figure 45: Example Koutecky-Levich plot

If the electroactive coverage of enzyme is known (accurately determined from non-catalytic signals), the intercept of the plot reveals the enzyme turnover number since the substrate concentration at infinite rotation is greater than the K_M (i.e. not limiting). The K_M value for the substrate can be determined electrochemically by varying the substrate concentration at infinite rotation rate (i.e. in the absence of diffusional limitations). In this case, the limiting current increases with substrate concentration in an analogous manner that applies to studies of reactions in homogenous solution (i.e. enzymatic assays), as shown in Figure 46. It can be noticed that the peak potential of the catalytic waves also shift with an increasing substrate concentration in accordance to the Nernst equation which also depends on solution pH. Once again, the Koutecky-Levich plot can be extrapolated to reveal the turnover number and then the K_M can be determined using Equation 43, shown again below [222]:

$$i_{\lim cat} = nFA\Gamma \frac{k_{cat}}{1 + \frac{k_M}{[substrate]}} \qquad \textbf{Equation 43}$$

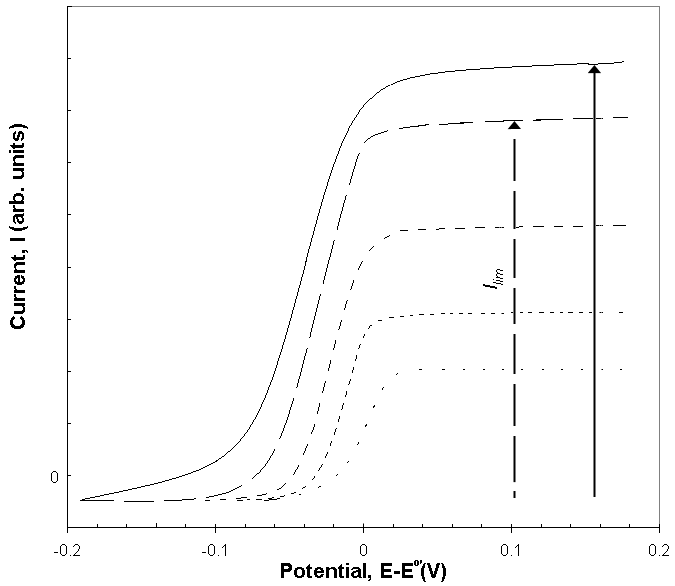

Figure 46: Example CV of the influence of substrate concentration on catalytic current.

Finally, the rate of interfacial electron transfer is dependent on the efficiency of the electronic coupling between the electrode and active site and this is best described using the Marcus model (section 3.1.4.4). The more traditionally used Butler-Volmer model does not consider the nature of the active site and associated effects on the interfacial rate constant (e.g. sluggish kinetics and high scan rates)[195]. Instead, Butler-Volmer predicts that the rate of interfacial electron transfer increases exponentially with driving force, such that at large overpotentials the rate exceeds the turnover rate of the enzyme and thus is greatly overestimated. Conversely, the Marcus theory predicts that the rate of interfacial electron transfer reaches a constant level (plateaus) when the overpotential exceeds the reorganisation energy of the reaction, as such the rate constant increases sigmoidally rather than linearly. This behaviour is characteristic of metalloenzymes which typically display poor electronic coupling and have low reorganisation energies. Marcus theory also predicts broadening of the peaks with applied potential which arises from non-ideal behaviour at the electrode surface, where different orientations of enzymes have different rate constants (i.e. small reorganisation energies discontinue at high overpotentials). However, this theory also applies to ideally orientated enzymes and therefore is limited in this regard and thus the Butler-Volmer would be the preferred model.

3.1.7.3 Catalytic Chronoamperometry

This technique is particularly useful for measuring the lifetime of the enzyme when adsorbed onto the electrode. The time dependence of catalytic currents can be sampled every 0.1 sec or even faster over long measurement periods, such as days, weeks or months, as shown in Figure 47. This allows investigation into changes in enzyme stability over different periods and on different electrode surfaces. Furthermore, this technique is particularly convenient for detecting activity changes in response to different inhibitor concentrations which can be used to resolve the kinetics of inhibition[229].

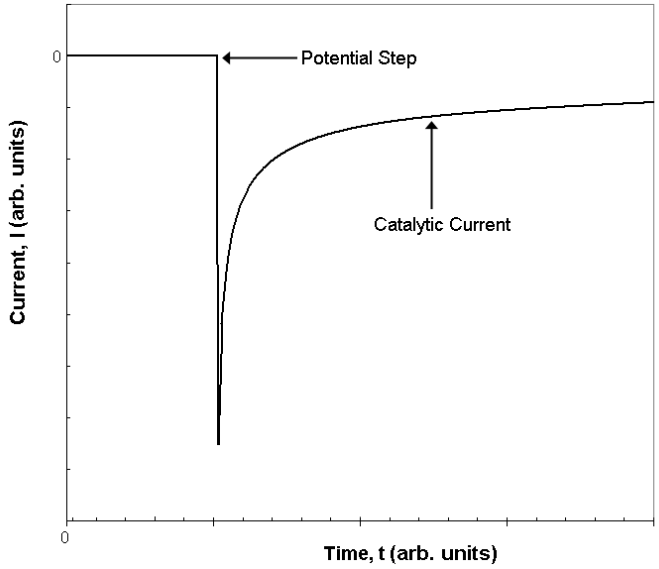

Figure 47: Example catalytic chronoamperometric graph.

3.1.8 Equipment

The majority of electroanalytical measurements were carried out on an Ivium compactstat (Ivium Tech) in the School of Materials. For the multi-electrode measurements used during extended testing (7 days), the compactstat was connected to a MultiWE32 (Ivium Tech). The rotating disk experiments were carried out in the School of Chemistry, using a EG&G PARC model 616 rotator (Princeton Applied Research, USA) in conjunction with a standard Autolab potentiostat (Eco Chemie, Netherlands).

3.2 Physical Analysis

3.2.1 Raman Spectroscopy

Raman spectroscopy is based on the inelastic scattering of monochromatic light, usually from a laser source. This inelastic scattering occurs when the frequency of photons in laser light, ν_o, changes upon interaction with a molecule. As the photon interacts with the molecule it perturbs the electric field and the molecules vibrate with a characteristic frequency, ν_m. Such molecular vibrations scatter photons under three different frequencies, defined as individual scattering processes: Stokes scattering occurs when the molecule takes a small amount of energy from the photon due to vibrational modes (phonons), thereby the photon is scattered at a lower energy (longer wavelength) (Figure 48). Anti-Stokes scattering occurs when the molecule at the time of interaction is already in the excited state, resulting in the energy of scattered photon being higher (shorter wavelength) than the incident photon (Figure 48). The resulting frequency of these scattered photons is the measured Raman shift (cm^{-1}), where Stokes are positive shifts and anti-Stokes negative shifts in energy. Usually, the Stokes shifted scatter is observed in Raman spectroscopy, which is of higher intensity, due to the anti-Stokes requirement of molecules being in a pre-vibrationally excited state. The energy of these scattered photons depends on the molecular structure and environment and therefore provides important information of the sample under investigation.

The third scattering process is known as elastic Rayleigh scattering, where there is no energy change between the incident and scattered photon (Figure 48). In fact, almost all incident photons in Raman measurements undergo this type of scattering. However, this type of signal is useless for molecular characterisation purposes and therefore filters are used to remove the signal; allowing for accurate determination of the inelastic signal.

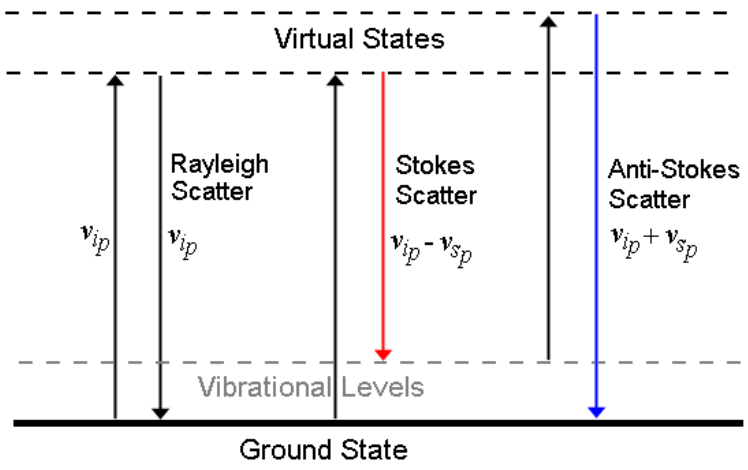

Figure 48: The three types of Raman scattering processes

The Raman shift is the energy difference between the incident and scattered photons which is represented by the arrows of different lengths in Figure 48 and calculated numerically through Equation 44:

$$Shift = \frac{1}{\lambda_{incident}} - \frac{1}{\lambda_{scattered}} \qquad \textbf{Equation 44}$$

where the change in wavelengths (λ) of the incident and scattered photons gives rise to the Raman shift in terms of wavenumber (cm^{-1}).

Raman spectroscopy is such an efficient technique for studying carbon materials because these materials contain delocalised π-electrons which can be excited easily. Therefore, carbons are always in resonance and it is these resonant features which provide information on the physical and electronic properties of these materials.

Raman measurements were carried out on Renishaw microscope with laser excitation 633 nm at power 50 % and objective x50. Spectra were collected between 3000-100 cm^{-1} over a time of 20 seconds with x5 accumulations.

3.2.2. Scanning Electron Microscopy/Energy Dispersive X-ray Analysis (EDX)

SEM imaging of carbon samples was carried out in the School of Materials, using a Philips 1000 field emission gun SEM (FEGSEM) with EDX incorporated. EDX measurements were carried out on the CNT mats at different sample regions and averaged, using an acceleration voltage of 15.0 kV. For all measurements, carbon samples were attached onto metal stubs containing adhesive carbon tabs and measured.

3.2.3 Transmission Electron Microscopy

TEM imaging of carbon samples was carried out by Yanning Li, School of Materials, using TEM CM 200. All samples were washed in 15 ml of ethanol (≥ 99.5 %, Sigma-Aldrich UK) and centrifuged at x4000 rpm for 30 minutes, this procedure was repeated twice.

The washed CNTs were then pipetted onto a holey carbon TEM grids (Agar Scientific UK) and measured.

3.2.4 Ultraviolet-Visible Light Spectroscopy (UV-Vis)

The UV-Vis spectra were obtained in the School of Materials, using a U1800 spectrophotometer. All disposable polystyrene cuvettes and quartz cuvettes had a path length of 10 mm (both purchased from Fisher Scientific UK). All enzyme activity measurements were carried out under controlled temperature conditions, using a connected water bath.

The instrument functions by measuring the intensity of light travelling through a sample (I) as a function of wavelength, and subsequently converts this to the absorbance of the sample, A, Equation 45 with accordance to the Beer-Lambert Law, Equation 46:

$$A = -Log_{10}(I / I_o) \qquad \textbf{Equation 45}$$

where I_o is the intensity of incident light.

$$A = \varepsilon bc \qquad \textbf{Equation 46}$$

where A is dimensionless, ε is the absorption (molar extinction) coefficient (mol^{-1} dm^3 cm^{-1}), c is concentration (mol^{-1} dm^3) and b is the cuvette path length (cm).

Using UV-vis it will be possible to measure the absorptivity of the samples and then determine their concentrations using Beer's Law (Equation 46). However, at relatively high concentrations Beer's law no longer functions, especially if the material is highly scattering.

3.2.5 Contact Angle Measurements

Understanding the various ways a liquid interacts with a solid surface is important in many systems of everyday life such as printing, flotation and water-repellents. When a liquid such as water is dropped onto a flat solid surface, the surface forces (surface tensions), γ, between the respective phases (solid, liquid and liquid-solid) dictate the overall shape of the droplet and thus the angle of contact at the liquid-solid interface for that system, defined as the contact angle, θ[230]:

$$\gamma_{Solid} = \gamma_{SL} + \gamma_{Liquid}\cos(\theta) \qquad \textbf{Equation 47}$$

This relation is known as Young's equation[231] and states that surfaces with higher surface tension have smaller contact angles, such as hydrophilic surfaces which attract polar molecules, while surfaces with lower surface tension have higher contact angles, such as hydrophobic surfaces which repel polar molecules.

Since the equation only takes into account perfectly flat surfaces and not roughened surfaces which cause deviation in the angle, more specific models have since been developed which are more suitable to certain systems. The two most commonly employed are the Wenzel[232] and Cassie-Baxter[233] models.

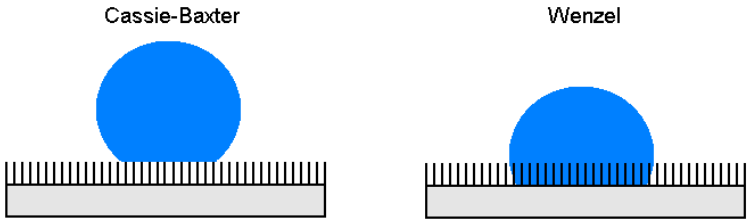

Figure 49: Schematic illustration of the Cassie-Baxter and Wenzel wetting states on aCNTs.

In the Cassie-Baxter model, the water droplet sits on top of the aCNT array leaving pockets of air between the droplet and substrate, as shown in Figure 49 The observed contact angle, θ_{CB}, is dependent on the fraction of surface in contact with the droplet, f, as given by the Cassie-Baxter equation[233, 234]:

$$\cos\theta_{CB} = f(\cos\theta + 1) - 1 \qquad \textbf{Equation 48}$$

Since CNTs can be subject to wetting by substances having surface tensions lower than 200 mN/m[235, 236]; water (γ = 72.8 mN/m) can penetrate into the arrays when driven by capillary forces. This behaviour is known as the Wenzel state (see Figure 49), and is dependant on the surface roughness, r, which is a ratio of the actual surface area over the geometric area, thus r will always be greater than 1 ($r > 1$). The effect of roughness, r, on the observed contact angle, θ_W, is given by the Wenzel equation[232]:

$$\cos\theta_W = r\cos\theta \qquad \textbf{Equation 49}$$

Where in both equations, $\cos\theta$ is related to the Young's contact angle on a flat surface of the same composition (e.g. for CNTs, graphite = 93.5 ° [237]).

Contact angle measurements were obtained using a Kruss DSA 100, School of Materials. A water droplet volume of 20 µl was used to measure the contact angles on modified aCNT samples heated at different temperatures and under air or H_2 atmospheres, see section 3.3.7.2. The water droplet was left on each treated sample for a period of 5 minutes and the contact angle averaged.

3.2.6 Epifluorescence Microscopy

Epifluorescence images of modified aCNT electrodes were taken using a Nikon digital Camera, School of Materials. Electrodes were fixed to glass slides and measured using x10 objective under a maximum exposure time of 20s in air. Samples were illuminated using a mercury lamp filtered through a FITC filter cube (excitation wavelength, λ_{ex}= 494 nm, emission wavelength, λ_{em} = 521 nm). Each aCNT electrode surface was spotted with 1 µL of the labelled laccase solution and measured once the enzyme had fully soaked into the mat (around 1-2 minutes). The effect of surface functionalisation on recorded fluorescence was measured for individually gas-treated electrodes. The experimental protocol for these measurements can be found in Section 3.3.5.

3.3 Experimental

3.3.1 Chemicals and Samples

Unless otherwise stated all chemicals were purchased from Sigma-Alrich, UK, and were certified laboratory reagent grade.

Electrolyte solutions were prepared using ultra-pure water obtained from a reverse osmosis unit (Millipore, Watford, UK) coupled to an Elga "Purelab Ultra" purification system (Veolia Water systems, Marlow, UK) to give water of resistivity >18 MΩ cm).

All glassware was cleaned thoroughly before experimental use, using ultra-pure water as stated above and a mixture of acetone (≥ 99.5 %) and ethanol (≥ 99.5 %).

Standard redox couples were potassium hexacyanoferrate(II) trihydrate (>99%), hexammine ruthenium(III) chloride (98%) and ferrocenemethanol (97%), the supporting electrolyte in these cases was KCl (Lab reagent grade, Fisher Scientific).

For the majority of electrochemical measurements, industrial grade oxygen was used (oxygen, 99.5 % purity) supplied by BOC, Guildford, UK. In some cases, electrolyte solutions were degassed with nitrogen ("Oxygen Free" nitrogen, 99.998% purity, BOC) or alternatively purged with air using a fish pump. All gases were flushed through a luggin capillary (1.5 mm diameter) situated in the bottom of the glass cell for a minimum of 15 minutes, unless otherwise stated. The gas flow rates were controlled and measured using gas specific flow meters (Caché Instrumentation Ltd), measured in units of cm^3min^{-1}.

3.3.2 Laccase voltammetry

Except where otherwise stated, the electrolyte used for all laccase voltammetry was 0.10 M sodium citrate, pH 4.5 at 25 °C (citric acid monohydrate and trisodium citrate dehydrate) this is simply referred to as 'citrate buffer'. All solutions were accurately pH corrected using a pH/ISE meter (VWR International Ltd) which was pre-calibrated using the pH 4.0 and pH 7.0 buffer standards (±0.01, 25 °C). For all laccase voltammetry, the volume of citrate buffer varied between 4-8 ml depending on the cell size. All measurements were carried out at room temperature, unless otherwise stated. In most cases, the electrodes were cycled between 0.8-0.4 V. After initial CV cycling, buffer solutions were refreshed to eliminate the effects of free enzyme on laccase voltammetry. All buffer solutions were purged for a maximum of 15 minutes and continuously bubbled at 40 cm^3 min^{-1} during measurement.

3.3.3 Enzyme Purification - Purification of laccase from *Trametes versicolor*

The laccase purification technique was enhanced over the research period as a result of direct collaboration with C.F. Blanford's research group at The University of Oxford. Preliminary purification procedures involved only a short dialysis and centrifugation, removing the majority of cell debris' but leaving a mixture of other undesired proteins found in crude commercial extracts. The end product was only moderately purified, green in colour.

Purification of the laccase obtained from Blanford's research group in Oxford involved a multi-step procedure. More advanced two-column chromatographic purification steps were used, separating out proteins based on ionic charge and hydrophobic amino acid interaction. The end product is highly purified, typically characterised by its deep blue colour. Both purification procedures are described in detail below.

3.3.3.1 Moderately purified laccase (produced in The University of Manchester)

Crude, lyophilised laccase (Fluka, >20 μmol catechol oxidised min^{-1} mg^{-1} at pH 4.5 and 25 °C) was dissolved in citrate buffer at a concentration of 50 mg ml^{-1} (50 g l^{-1}). The mixture was then placed in a pre-washed dialysis bag (15 MWCO tubing pore size) and immersed in approximately 200 ml of citrate buffer and the buffer stirred for 30 minutes at room temperature. The bag was then transferred to fresh citrate buffer and left to dialyse for up to 3 days at 4 °C, while constantly replacing the dialysate with fresh buffer every 24 hours. After dialysis, the enzyme solution leftover in the bag (~3 ml) was then removed and saturated with ammonium sulphate until precipitation. The suspension was then centrifuged at 4000 rpm for 20 minutes and the supernatant removed. The obtained precipitate was dissolved in 500 μL of citrate buffer and saturated with ammonium sulphate. The resulting suspension was then centrifuged at 4000 rpm for 20 minutes and the supernatant was discarded. A small amount (300 μL) of citrate buffer was used to dissolve the remaining precipitate and the resulting solution was then re-dialysed

in citrate buffer following the same procedure to remove any remaining salt (ammonium sulphate). After dialysis, any remaining precipitated material was removed by centrifugation at 10,260 rpm for 20 minutes. The supernatant was recovered and then stored at -80 °C.

3.3.3.2 Highly purified laccase (produced in The University of Oxford)

This time laccase (same product as above) was dissolved in 0.10 M sodium actetate buffer pH 5.5 at a concentration of 2.5 g l^{-1}. The mixture was vacuum filtered sequentially through GF/A, 0.45 µm HVLP and 0.22 µm GVWP membrane filters (Whatman). Once washed, the filtrate was ready for column chromatography carried out at 4-6 °C, the pH of all buffer solutions was determined at 5 °C. The filtrate was loaded on a Q Sepharose Fast Flow strong anion exchange resin (GE Life Sciences, ca. 1 g laccase per 10 ml resin) and eluted with 0-100 mM ammonium sulphate gradient while monitoring the absorbance at 280 nm and 610 nm. Fractions with constant A_{280}/A_{610} absorbance ratios were combined and repeatedly dialysed in 20 mM sodium acetate pH 4.7 at 4000 rpm for 15 minutes using a 30 kDa MWCO Vivaspin centrifugal dialysis tube. The dialysate was then concentrated to high ionic strength and dialysed in 1.65 M ammonium sulphate in 20 mM sodium acetate pH 4.7 for hydrophobic interaction chromotagraphy. Using a Phenyl Sepharose Fast Flow hydrophobic interaction column (GE Life Sciences) the dialysate was eluted with a 1.65-0 M ammonium sulphate gradient. The laccase eluted over the range 0.6-0.9 M ammonium sulphate. Once again, samples with a constant A_{280}/A_{610} ratio were concentrated and dialysed through a 30 kDa membrane into citrate buffer, then immediately frozen using liquid N_2 and stored at -80 °C.

3.3.4 Enzyme Purity and Concentration

After carrying out a protein purification procedure, it is essential that the overall purity of enzyme in the collected fraction is determined. Usually, this purity is assessed by two measurements; firstly the enzyme activity and secondly the total amount of protein obtained after purification. From these two properties, the percentage recovery and degree of purification can be calculated[163].

3.3.4.1 Enzyme Assays

Enzyme assays involve measuring the activity of an enzyme, by determining either the rate of product formation or substrate used during the enzyme-catalysed reaction. Several different assay methods exist for most enzymes and the method chosen is based upon consideration of the costs, equipment, reagents needed and the required level of sensitivity[238]. The assay method for laccase was chosen in accordance with the above and is described below.

3.3.4.2 ABTS Assay Method (Diammonium 2,2′-azino-bis(3-ethylbenzothiazoline-6-sulfonate)

This assay method was first introduced by Wolfenden and Wilson (1982), where laccase oxidises ABTS (Sigma-Aldrich) to form a stable cation radical. The absorbance of the cation radical was monitored at 420 nm and 25 °C, where the blue-green colour responsible was used to correlate the enzyme activity.

The reaction mixture contained of 0.89 ml of 0.1 M sodium citrate, pH 4.5, 0.1 ml of 0.5 mM ABTS (dissolved in distilled water/dH_2O) and 0.01 ml of enzyme-containing solution in a final volume of 1 ml. All assays were performed at 25 °C. Laccase activity was calculated in U/ml where 1 U is defined as the amount of enzyme required to oxidise 1 µmol of ABTS per minute.

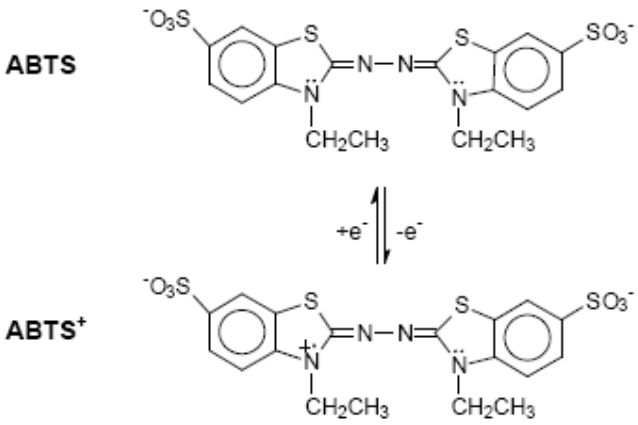

Figure 50: The typical reaction, where ABTS is oxidised to a cation radical ($ABTS^+$)

3.3.4.3 Protein Assays

The protein contents were estimated by spectrometric measurement at 610 nm. Laccase's have a characteristic absorption band at 610 nm, due to the T1 copper site which imparts the blue colour to the enzyme solutions[151, 166].

Protein concentration (mg/ml) was also measured at 595 nm using the Bio-Rad Protein Assay Kit II (Bio-rad Laboratories), based on the Bradford method[239]. The assay kit consisted of Bradford-dye reagent and bovine serum albumin (BSA) as the standard and was carried out according to the manufacturer's instructions. The BSA protein standard was used to construct a standard curve from which the protein concentration of unknown laccase samples could be determined.

3.3.4.4 Kinetic Constants of Trametes versicolor laccase

The kinetic constants of laccase were determined using the most commonly used substrate, ABTS. The rate of cation radical formation was determined by spectrometry, using reported molar extinction coeffecients (ε). The reactions were carried out at 21 °C, using substrate concentration ranges of 50 - 1000 µM. Kinetic studies were conducted and the V_{max} and K_M values were calculated using both Michaelis-Menten and Lineweaver-Burk plots.

The kinetic properties of enzymes may be characterised by measuring the rate of catalysis, V, as a function of substrate concentration [S] (at a fixed enzyme concentration, [E]). The graph that follows has a hyperbolic shape (see Figure 51), where the reaction rate (V) increases, as the substrate concentration (denoted as [S]) increases. At high [S], however, the enzyme becomes saturated with substrate and reaches V_{max}, the enzymes maximum catalytic rate.

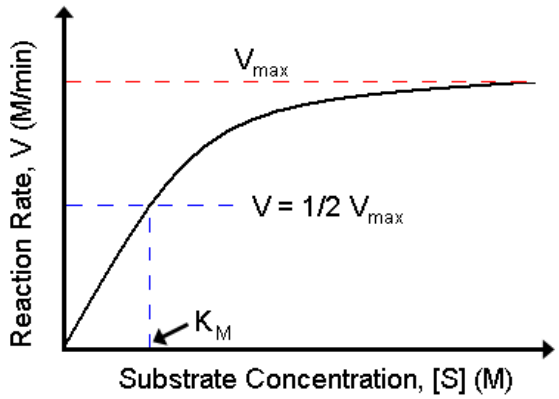

Figure 51: Curve showing the relation between the rate of an enzyme-catalysed reaction and substrate concentration. Also known as the Michaelis-Menten curve since the approach to maximum catalytic rate, V_{max}, for large [S] is explained using the Michaelis-Menten model.

A simple kinetic description of this behaviour is provided by the Michaelis-Menten model. In this model, an enzyme (E) and substrate (S) combine to form the enzyme-substrate complex (ES) which can either proceed to form the product (P) or dissociate, as shown below:

$$E + S \underset{k_{-1}}{\overset{k_1}{\longleftrightarrow}} ES \xrightarrow{k_2} E + P \qquad \textbf{Reaction 5}$$

Using this reaction, the reaction rate, V, is determined by the slowest step, k_2 (rate constant) and [ES], expressed as:

$$V = k_2[ES] \qquad \textbf{Equation 50}$$

However, since [ES] is an intermediate, it is difficult to measure because its concentration is unknown and thus must be expressed using known values such as

enzyme concentration and substrate concentration. This can be achieved using the steady state approximation which assumes both the rates of forward and reverse reactions are equal and that enzyme concentration [E] does not change over time.

The final equation is depicted below, and is known as the Michaelis-Menten equation:

$$V_o = V_{max} \frac{[S]}{[S] + K_M} \quad \textbf{Equation 51}$$

where V_{max} is the maximum catalytic rate (i.e. enzyme fully saturated with substrate) which is equal to k_2 (also known as the turnover number, k_{cat}) and the total enzyme concentration. While K_M, the Michaelis constant, describes the [S] at which the reaction rate is half its maximal and is related to the rate constants, $K_M = (k_2 + k_{-1})/k_1$. If k_2 is much smaller than k_{-1}, then $K_M = k_{-1}/k_1$ which is the dissociation constant of ES complex.

Therefore, both K_M and V_{max} are important kinetic parameters since the former describes the affinity of the enzyme for the substrate (i.e. the tightness of ES complex), while the latter describes the maximum catalytic rate of the enzyme. These two parameters can be determined from the Michaelis-Menten curve, as shown in Figure 51. Although in some cases the V_{max} value can be under estimated using the curve, instead a straight line plot is used, known as the Lineweaver-Burk plot and reciprocals of both sides of Equation 52 are taken:

$$\frac{1}{V} = \frac{K_M}{V_{max}} \frac{1}{[S]} + \frac{1}{V_{max}} \quad \textbf{Equation 52}$$
$$y = mx + c$$

Then the y-intercept (c) = $1/V_{max}$ and gradient (m) = K_M/V_{max}, thus derivations of both allow V_{max} and K_M to be calculated. Further kinetic parameters of the enzyme such as the catalytic constant, k_{cat}, ($V_{max}/[E]$) (denoted as the number of catalytic cycles per enzyme active site per minute (or second)) and catalytic efficiency, ε, (k_{cat}/K_M) were also calculated.

3.3.5 Epifluorescence Measurements

The fluorescently labelled laccase was provided by the Blanford group (Oxford University). The laccase was labelled at amino acid Lys-174, with fluorescein-5-EX, succinimidyl ester (Molecular Probes) using the company's protocol[240]. The degree of labelling was determined to be 0.6 dye molecules per laccase molecule[13]. Prior dilution of the fluorescent laccase solution was not necessary due to the densely packed nature of aCNTs significantly reducing the amount of emitted light from the labelled laccase.

3.3.6 Effect of pH

The optimum pH of the purified enzyme was studied over a pH range of 3.0 – 6.0, using increments of 0.5 pH units. The laccase activity was determined both spectrally and electrochemically, the differences between them being that the enzyme was freely suspended in solution (homogeneous electron transfer) and adsorbed onto aCNT electrode (heterogeneous electron transfer).

For the spectral measurements, the laccase activity was measured under standard ABTS assay conditions, a total of three measurements were taken at each pH for repeatability. Temperature was controlled by connecting a thermostated water bath to the UV-Vis spectrometer.

Whereas, laccase voltammetry was measured using the open cell setup by applying 1 µL pure of laccase (15 mg ml^{-1}) on the aCNT electrode (1mm x 1mm), and bubbling 40 cm^3/min of O_2 into the cell containing 5 ml of sodium citrate (pH 3.0 - 6.0) solution. All measurements were carried out room temperature (21 °C) and recorded between 0.8 - 0.2 V vs Ag/AgCl (3M) at 10 mVs^{-1}. Buffer solutions were purged for a minimum of 15 minutes prior to measurement and cycled until a stable current was reached. Fresh buffer solutions were used when re-measured at each pH to remove any unbound enzyme and hence eliminate the influence of free enzyme on the catalytic voltammetry.

3.3.7 Aligned Carbon Nanotube Electrodes

3.3.7.1 Aligned Carbon Nanotube Growth

Aligned arrays of carbon nanotubes (aCNTs) were grown in-house by the catalytic vapour deposition process (CVD). The aCNTs were synthesised on a growth substrate of oxidised silicon (silica) using a reactant solution containing toluene as the carbon source and 2.5 wt% ferrocene as the growth catalyst.

Preceding the CVD reaction, the silicon substrates (IDB Technologies Ltd, cut to 8 x 1 cm^2 square pieces) were cleaned to remove any surface contaminants. The wafers were initially sonicated in acetone (Sigma-Aldrich, 99.9 %) for 5 minutes, washed in propan-2-ol (Sigma-Aldrich, 98 %) and de-ionised water and finally dried in the oven at 60 °C. The cleaned wafers were then heated at 800 °C under air flow for 1 hr to oxidise the surface, followed by a purge with 300 ml/min argon for 15 minutes to remove the remaining gases. The CVD process was then initiated by injecting the reactant solution at a rate of 0.04 ml/min into a two-zone furnace, with zones one and two heated at 200 °C and 760 °C respectively. The solution was vaporised in zone one and then swept by an argon carrier gas (100 ml/min) to the second zone. In the second zone, aCNTs were grown on the silica (SiO_2) substrates while more entangled CNTs were formed on the surrounding quartz reaction tube. The desired reaction time was typically 4 hrs, following which the furnace was cooled under Ar flow to avoid oxidation of the nanotubes.

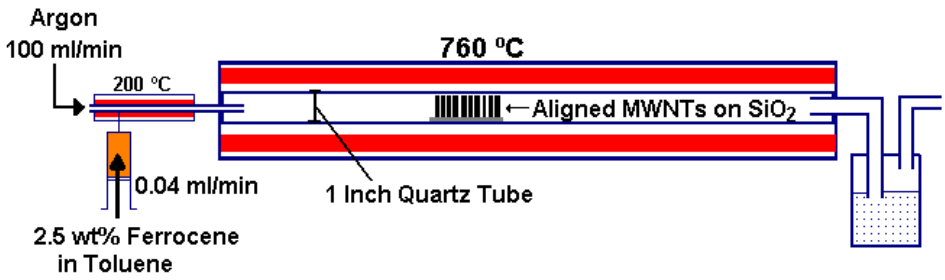

Figure 52: Schematic of CVD experimental setup and conditions.

3.3.7.2 Surface Functionalisation

The surface chemistry of the aCNTs was changed with oxidative and reductive gas treatments, providing a route for surface switch-ability. The nanotube surface was first switched from hydrophobic to hydrophilic using a quick oxidative treatment attained by heating at 400 °C under air flow (fish pump) for 10 minutes.

The nanotube surface was then switched back to hydrophobic by annealing the nanotubes in hydrogen gas. Initially, the furnace was purged with argon and heated up to 300 °C, upon which only hydrogen flowed at 600 cm^3 min^{-1}. The nanotubes were then heated up to 650 °C at a heating rate of 20 °C min^{-1} and held at this temperature for 10 minutes. After treatment, the furnace was switched off and the nanotubes were cooled to 300 °C in hydrogen at 600 cm^3 min^{-1}, before finally purging in pure argon to room temperature.

3.3.8. Patterned CNT Electrodes

3.3.8.1 Patterned CNT Growth

Growth of the aligned nanotube arrays into a micro-pattern was enabled using a gold mask. Prior to patterning, silicon substrates were cleaned and oxidised following standard procedures in section 3.3.7.1. A square 300 mesh copper TEM grid (3.05 mm diameter, Agar Scientific Ltd.) was chosen as the pattern template and this template was then placed perfectly flat onto the silica substrate surface and fixed using sellotape (Scotch). The templated surface was then gold sputter coated for 5 or 10 minutes depending on coating procedure at 3.6 – 3.8 x 10^{-1} atm, 40 mA and 0.8 – 0.9 kV (Edwards Sputter Coater S150 B). The newly patterned silica surface was then ready for CVD reaction, where the CNT arrays grew only from the silica in the pattern template under the same 4hr growth conditions (section 3.3.7.1).

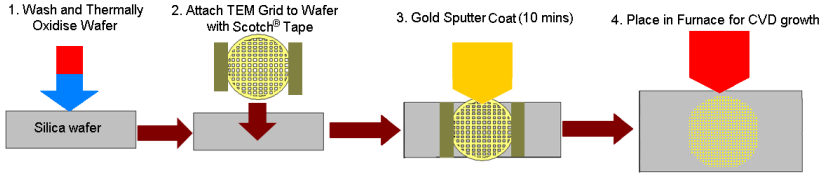

Figure 53: Outline of patterning process

3.3.9 Electrode Preparation

3.3.9.1 Working Electrodes

3.3.9.1.1 Aligned Carbon Nanotube Electrodes

Aligned nanotube electrodes were prepared by simply transferring the aligned mat from the silica substrate onto a more conductive surface. A razor blade was used to 'peel' away the nanotubes as an intact film. An electrical connection was then made by applying a thin layer of silver epoxy adhesive (RS Components, UK) to the newly exposed side of the mat and then contacting a piece of thin silver wire (Advent). To prevent contact between the silver epoxy and electrolyte solution, low viscosity epoxy was prepared (Araldite Rapid) and applied directly to the connection and surrounding CNT periphery. This thin coating provided sufficient insulation with minimal reduction in CNT porosity; pores away from connection were left open.

This electrode preparation procedure was proven to be most effective, given that various CNT configurations were investigated allowing for conductivities through the mat to be compared.

The majority of electrodes were made into 1 mm x 1 mm square dimensions since a large number of electrodes could be prepared from a single CVD reaction, allowing for improved repeatability. Exceptions were made when investigating the effect of electrode size against a set of various parameters such as enzyme response, enzyme loading etc.

3.3.9.1.2 Patterned Carbon Nanotube Electrodes

Following the CVD reaction, the micro-patterned CNT arrays remained on the silica substrate and an electrical connection was made to the side and base of the CNT pattern using silver epoxy in contact with silver wire. The connection was insulated using the epoxy procedure described above and the electrode was then ready for electrochemical measurements. However, it must be noted that some

patterned CNT arrays were thermally oxidised prior to electrical connection in order to improve enzyme adsorption into the CNT patterned arrays.

3.3.9.1.3 Glassy Carbon Electrodes

Glassy carbon electrodes (CHI 104 electrode, 3mm diameter, CH Instruments) were used as smooth planar, low surface area electrodes and also conductive electrode surfaces for accommodating randomly dispersed CNT deposits. The CNT deposits were prepared by dispersing aCNTs in ethanol (absolute 200 proof) via sonication, and then depositing droplets of suspension onto the electrode surface. The suspension was dried using a hand dryer, the mass of CNTs added could be determined by weighing the electrode before and after deposition, using a high accuracy mass balance ($\geq$ 0.01 mg, Sartorious).

3.3.9.1.4 Edge-Plane Highly Orientated Pyrolytic Graphite (Edge-HOPG)

The pyrolytic graphite edge has shown to greatly improve the electrocatalytic response of enzymes, in comparison to the basal plane[225]. As a result, the edge-plane surface was the preferred surface for electrochemical measurements and pre-treated accordingly. The pyrolytic graphite edge was abraded with sandpaper (P400 and P800, Norton Tufbak Durite), rinsed with water and then sonicated in water for 10 mins. The corresponding untreated edge was then coated in silver epoxy adhesive (RS Components) and electrically connected using a piece of silver wire (Advent Research Materials, UK). The connection was insulated as previously described.

3.3.9.1.5 Rotating Disc Electrode

Rotating disc measurements were carried out using a custom made copper (Cu) rotating disc electrode (3 mm diameter, disc circumference insulated using PTFE, total diameter 20 mm). The Cu electrode surface was modified with a thin coating of silver epoxy adhesive (RS Components) with the aCNT mat (2.5 mm x 2 mm)

vertically positioned on top. The entire base of the aCNT mat was in contact with the copper disc providing excellent conductivity through the mat; the perimeter was insulated with epoxy adhesive using previously mentioned methods.

3.3.9.2 Reference Electrodes

The reference electrode chosen was silver|silver chloride, E = 0.222 V vs. SHE, fabricated in-house. Using a silver wire connected to a 9V battery in the presence of KCl, the wire was oxidised to silver chloride and placed in a 3 mm inner diameter glass tube, sealed at one end with a Vycor frit (Scientific and Medical Products Ltd., Cheadle, UK) by heating the shrink sleeve. The glass tube was filled with 3 M KCl solution with the meniscus just below the brown silver chloride over layer; the remaining air gap was purged with argon and sealed tightly with Parafilm (Pechiney Plastic Company, Chicago, IL). The electrode was kept in 3 M KCl when not being used and it was refreshed by two-stage cleaning in dilute ammonia and dilute nitric acid (Sigma-Aldrich), the wire was then re-oxidised according to procedure above.

3.3.9.3 Counter Electrodes

The counter electrode adopted was a platinum mesh spot welded to a platinum wire support (Advent Research Materials, UK). Prior to experimental use, the electrode was cleaned from contaminants using a blue Bunsen flame. The counter electrode deliberately had a larger surface area than the working electrodes employed.

4 Laccase Purification, Kinetics and Preliminary Electrochemistry

4.1 Introduction to Laccase Purification, Kinetics and Electrochemistry

Fungal laccases are one of the most widely studied fuel cell catalysts because they reduce oxygen efficiently with minimal overpotential when adsorbed on electrode surfaces. However, in order to take advantage of these electrocatalytic properties the laccase extract has to be of sufficient purity and concentration. This high purity increases the likelihood of effective communication with the electrode and, in some cases, improves the enzymes' stability on the surface. The fungal laccase, *Trametes versicolor*, used in this thesis was purchased commercially and contained unwanted contaminating proteins and cellular material which needed removal. The initial challenge, therefore, was to develop a rapid and inexpensive method for the isolation and purification of laccase, while maintaining the biological activity and chemical integrity of the enzyme.

This chapter introduces the improvements made in purification during the course of the project through comparing the spectroscopic and electrochemical properties of two laccase extracts obtained by different purification techniques. Initial laccase purification methods were based on using more traditional procedures, such as dialysis and salt fractionation, which often resulted in products of low purity and electrochemical activity. Purification was later improved through using column chromatography in collaboration with Dr. Blanford at the University of Oxford. (Dr. Blanford has since moved to the University of Manchester.) This improved method of purification was used for all the electrochemical investigations beyond section 4.3.

Following purification, it is important to check that the enzyme is still catalytically active, since a successful purification method is judged on obtaining a high yield of pure and active enzyme. Enzyme kinetics studies were carried out by measuring reaction rates at a series of different substrate concentrations. These experiments developed a progress curve which was described using the Michaelis-Menten kinetic model and allowed important kinetic parameters to be determined.

Further kinetic studies were undertaken to investigate the effect of pH on the catalytic activity of laccase. These were carried out homogenously (in solution) and heterogeneously (on electrode), which enabled the electrocatalytic behaviour to be compared under different conditions and electron transfer environments.

Electrochemical studies were performed using PFV, whereby laccasse was directly adsorbed onto the aCNT electrode and the catalytic response measured using cyclic voltammetry. Studies have shown that laccase can directly interact with the electrode[24, 241] and thus comparisons were made between laccase-aCNT electrodes and other potential carbon electrode materials with varied topologies. Electrode performance was then evaluated based on variations in geometric areas, surface areas, length of electrodes and enzyme loading.

4.2 Kinetics and Electrochemistry

4.2.1 Results - Comparing Laccase Purification Procedures

Early attempts of purification were developed in-house using simple dialysis and centrifugation procedures which removed unwanted impurities based on differences in size and solubility (see section 3.3.3.1). Spectroscopic and electrochemical analysis found that the laccase obtained was of poor purity and low concentration, as shown later. Therefore, a second approach using two separate chromatographic columns was studied. In this case, laccase was isolated based on hydrophobicity and charge, and subsequent rigorous washing, dialysis and centrifugation steps were introduced. These purification steps resulted in laccase of high purity and improved electrochemical performance. The two batches will be referred to as partially purified and highly purified for the in-house and Oxford purified samples, respectively.

4.2.2 Physical Characterisation

4.2.2.1 UV-Vis Absorption Spectrum

As mentioned previously in section 2.3.1.3, *Trametes versicolor* laccase contains three-different copper (Cu) sites which can be identified on the basis of their spectroscopic properties. Typically, two of these copper sites (Cu) can be identified in the UV-Vis absorption spectra. The T1 Cu site has a strong absorption at around 610 nm as a result of the highly covalent bond formed with the neighbouring cysteine and gives laccase its characteristic blue colour[151]. The T2 Cu site exhibits only weak absorption in the visible region, whereas the two coppers of the T3 site are characterised by a shoulder at around 330 nm[151].

The UV-Vis spectral features of the different purified laccase extracts were compared (Figure 54). The moderately purified extract showed no peak absorption at around 610 nm but a shoulder at around 330 nm believed to be from the Type-3 site. Whilst, the highly purified laccase showed broad peak absorption at 610 nm and strong absorption at 280 nm, suggesting it was of good purity.

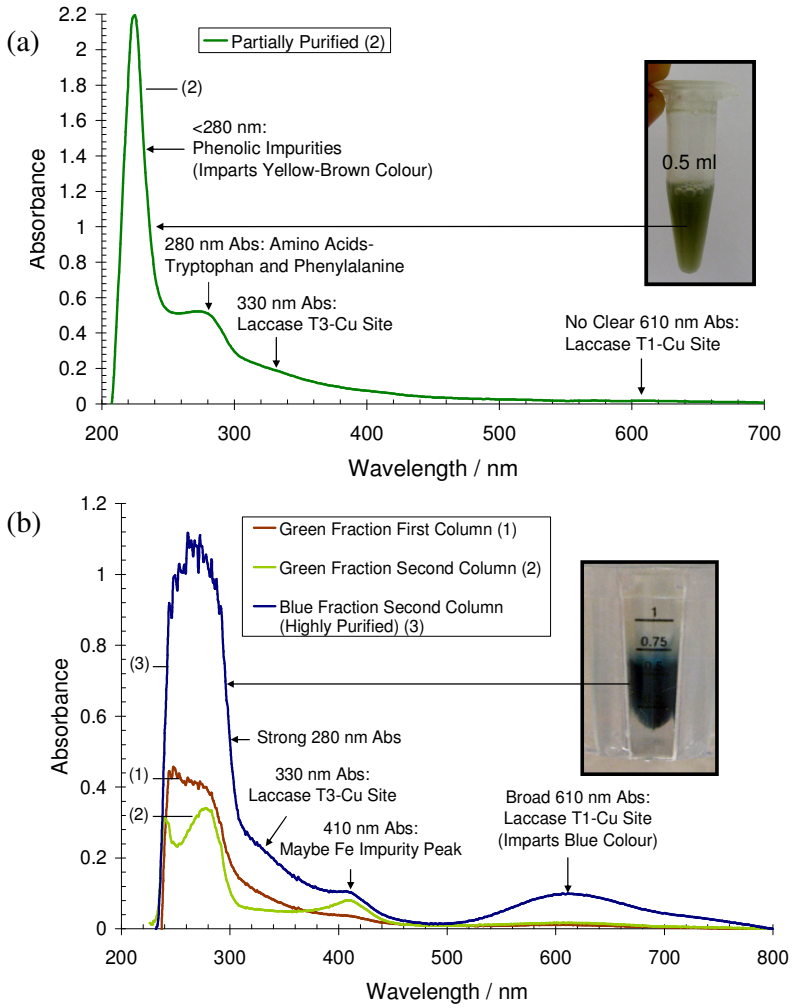

Figure 54: UV-Vis spectral analysis of *Trametes versicolor* laccase obtained by the two different purification procedures. Spectra (a) partially purified laccase extracts and (b) (1) after first chromatographic step (anion exchange), (2) second chromatographic step (hydrophobic) and (3) final highly purified extract obtained after washing, dialysis and centrifugation. Inset pictures detail final concentrated solutions of (a) partially purified laccase, brown/yellow-green colour (0.5 ml) and (b) highly purified extract (0.5 ml) with deep blue colour expected of typical Cu rich laccase extract. All spectra were measured using 1 cm pathlength and laccase solution was diluted 10-fold prior to measurement.

The low purity laccase fractions obtained after the first and second chromatographic steps had similar spectral characteristics and colour as the partially purified extract, highlighting that purity can be judged by eye.

Ideally, the concentration of the enzymes would be measured using the peak absorbance value at 610 nm and assuming a molar extinction coefficient at this wavelength of 5 x 10^3 M^{-1} cm^{-1} [242]. The concentration of the highly purified laccase extract was determined to be 200 µM or 10 mg/ml (see Figure 55).

However, the concentration of the moderately purified extract could not be calculated due to lack of absorption at 610 nm. Therefore, the Bradford Assay method[239] (see section 4.2.2.2) was also used to determine the level of protein content in the samples.

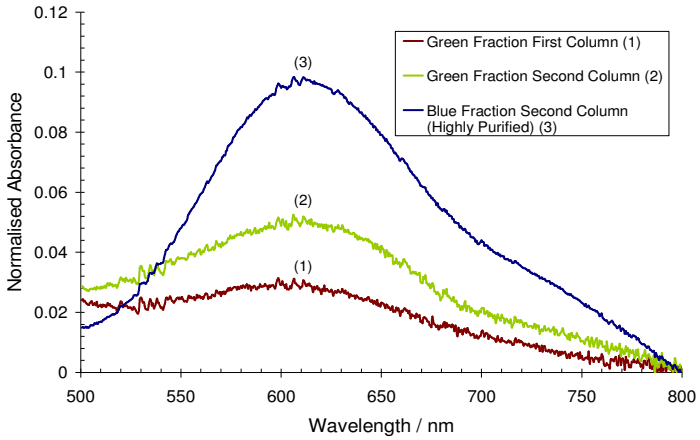

Figure 55: The 610 nm absorption peaks for T1-Cu site normalised with respect to 280 nm peaks, where (1 and 2) represent spectra of low purity laccase extracts obtained after first column and second column chromatography and (3) the final highly purified blue laccase extract.

4.2.2.2 Bradford Assay

Using the Bradford method [239], the amount of protein in the purified extracts could be determined and used as a direct measure of laccase concentration. The Bradford method is based on the colour change of the Coomassie Blue G-250 dye which changes from red-brown in its acidic solution to blue colour, as a result of protein binding. The bound form of the dye has an absorbance maxima at 595 nm, thus the concentration of laccase was related to the increase in absorbance at this wavelength.

A protein of known concentration, bovine serum albumin (BSA), was initially used to prepare a standard curve in order to relate the absorbance at 595 nm to the concentration of protein. The absorbencies of three laccase extracts were then determined and concentrations determined using the standard curve equation shown in Figure 56. Several other methods were available for determination of protein concentration, however, the Bradford method was chosen as being best

suited for this work as it was deemed to be simpler, faster and more sensitive than the other methods available. Also, Bradford was subject to less interference by common reagents and non-protein components of biological samples.

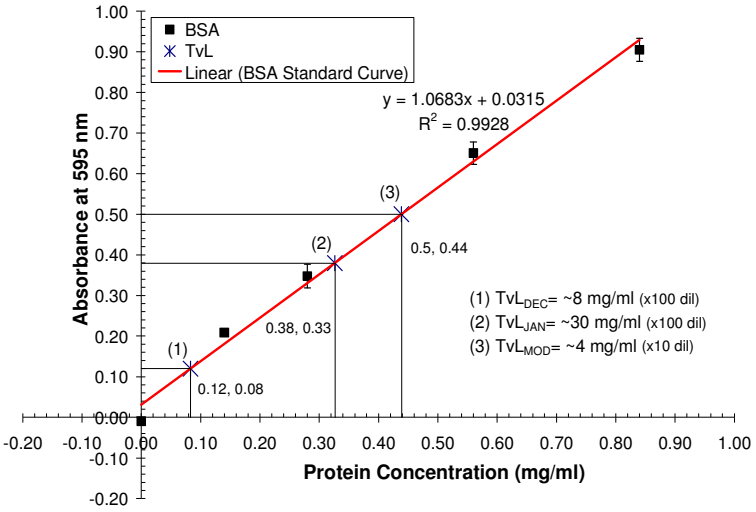

Figure 56: Bradford plot displaying the standard curve and relative absorbencies and concentrations of two highly purified laccase samples (1 and 2) where (1) represents the spectroscopically characterised sample from previous section and (3) the partially purified sample.

Overall, the protein concentrations determined from the Bradford method and UV-Vis spectroscopy were in good agreement with each other, as shown in Table 2. To evaluate the purity of each extract, absorbance ratios at 280 nm/610 nm were taken, where low ratios are indicative of highly purified extracts due to strong absorption of 610 nm peak (laccase T1-Cu site). Protein concentrations were compared to evaluate the overall yield of laccase after the adopted purification steps. It can be noticed that the purified blue laccase extract obtained by two-stage column chromatography is of higher purity and contains twice the amount of laccase compared to laccase purified by dialysis and centrifugation procedures.

	Abs Ratios	Concentrations, C (mg/ml)		
	A_{280}/A_{610}	C(280 nm)[a]	C(610 nm)[b]	C(595 nm)[c]
Moderately Purified	26	4	3	4
Green Laccase 1st Column	35	2	1	-
Green Fractions 2nd Column	20	2	2	-
Purified Blue Fractions 2nd Column	10	6	10	8

Table 2: Protein concentrations and absorbance ratios determined for each laccase extract, where [a] and [b]- calculated using extinction coefficients, $\varepsilon_{280\ nm}$ = 82000 M^{-1} cm^{-1}[177] and $\varepsilon_{610\ nm}$ = 5000 M^{-1} cm^{-1}[242], [c]- calculated using standard curve form Bradford method.

4.2.2.3 Laccase Voltammetry

The electrocatalytic properties of the two different purified laccase batches (partially and highly purified) were directly measured and compared using protein film voltammetry (PFV). This approach involved directly adsorbing the enzyme onto the electrode surface and measuring the electrocatalytic response, as detailed in Figure 57. Direct electron transfer (DET) between the enzyme and electrode was established by using aligned arrays of nanotubes in which the small size, curvature and high surface areas increased the probability of electron tunnelling across the interface.

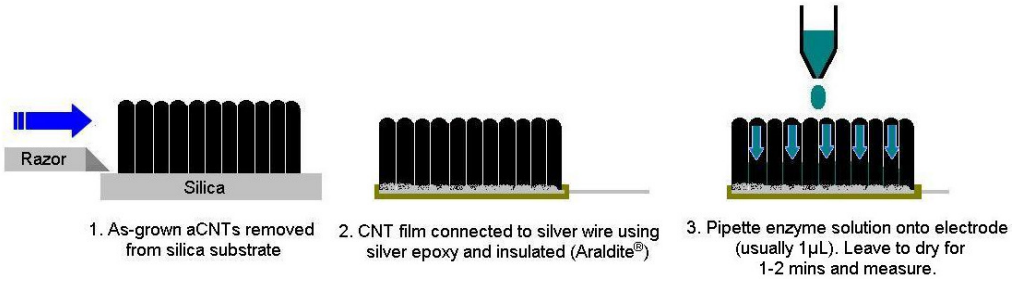

Figure 57: Schematic of the three simple steps towards fabricating the biocathode.

These aCNT electrodes are composed of a densely packed array of nanotubes (order 10^8-10^9 CNTs/cm^2), as shown in Figure 58(a), which facilitates high electroactive coverage of enzyme. Furthermore, the hierarchical organisation of this '3D' nanostructure increases the surface area, enabling fast electron transport and the uniform mesopores (2 nm<D<50 nm[243]) higher enzyme loadings and improved O_2 mass transport.

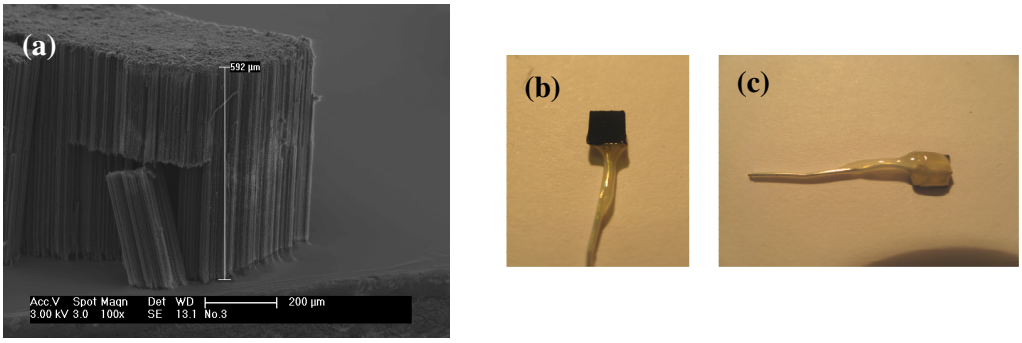

Figure 58: SEM image of aCNT array ~600 µm height (a) and representative images of aCNT electrode, where (b) top view and (c) bottom view (4 mm x 4 mm).

The electrodes used in this investigation were 1 mm x 1 mm in projected area and grown under identical conditions. The capacitances of the two electrodes were similar (1.27 F g^{-1} and 1.49 F g^{-1}), confirming that they had similar surface areas and chemistry. 20 μg of laccase was deposited as a solution onto the electrode surface and the catalytic currents measured using CV. (The concentration of the highly purified laccase solution was much higher than that of the partially purified, therefore different volumes of each were added to ensure a total loading of 20 μg enzyme was on the electrode.) Measurements were carried out in an open cell under standard cell conditions, as stated in the experimental methods (section 3.3.2).

Figure 59 presents the voltammetric waves for both laccase extracts immoblised on the aCNT electrodes in an O_2 saturated solution. The waves were stable and hence were averaged by taking the mean of 5 CV cycles. The partially purified laccase electrode displayed no observable O_2 reduction response. It is believed this poor performance was probably due to the low purity of the laccase extract which decreased the probability of electron tunnelling since the active site is less accessible. DET transfer between laccase and the nanotube relies on correct orientation on the electrode surface, so that the laccase T1-Cu active site and electrode surface are separated by no more than 8 Å[151]. The tiny peak current measured for the moderately purified extract, 0.5 μA at 0.4 V, suggests that the enzyme was probably inactive. Peak current, $I_{p,}$ is the maximum faradaic current corrected for the non-faradaic component (blank).

However, the highly purified laccase extract displayed good communication with the aCNT electrode (see (2)). The sigmoidal wave shape indicates that the O_2 substrate is regenerating the redox state of the enzyme in a succession of catalytic cycles, reaching an I_p of 19 μA at 0.45 V. The half-wave potential for O_2 reduction, $E_{Lac\ O2,}$ was +0.56 V (pH 4.5), which is in good agreement with the half wave-potential of the T1-Cu site, +0.54 V vs Ag|AgCl (pH 3.0)[177]. However, it must be noted when comparing to literature values that redox potentials can shift when measured electrochemically due to variables such as the electrode material, pH, partial pressure of oxygen in the system *etc*. Given that the redox potential for O_2 reduction is +0.75 V vs Ag|AgCl (pH 4.5) (see dotted line in Figure 59),

the cathode can be estimated to have an overpotential of around +0.2 V for the electrocatalytic conversion oxygen to water. It is believed that the electrocatalytic response was limited by the mass-transport of oxygen to the active site due to the inflection of the catalytic wave towards the plateau-like diffusion limited current. At this point it is believed the high catalytic activity of the enzyme exceeds substrate diffusion and so the current becomes rate limited. During voltammetric measurements the citrate buffer solution had to be bubbled continuously with O_2 (40 cm^3 min^{-1}) in order to achieve a stable catalytic response, thus the current was found to be related to the amount of O_2 available and under diffusion control.

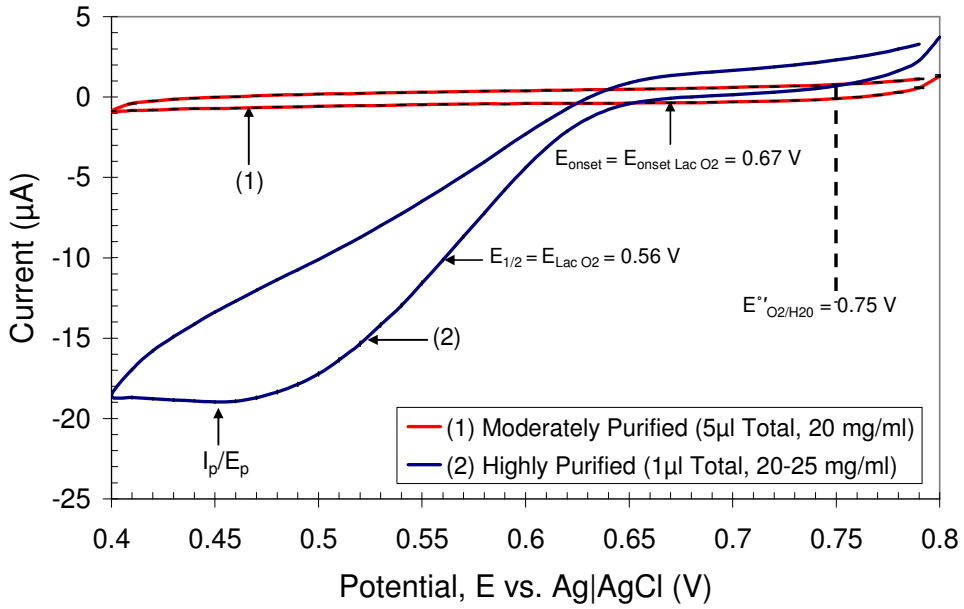

Figure 59: CVs comparing the O_2 reduction of moderately purified and highly purified laccase extracts on aCNT electrodes (1 mm x 1 mm). CV responses shown were stable over 10 cycles. Dotted line represents the redox potential for the reduction of O_2, $E^{\circ\prime}_{O2/H2O}$ = 0.75 V vs. Ag|AgCl at 25 °C, pH 4.5. Conditions: Na-Cit buffer, 0.1 M, pH 4.5, 25 °C, saturated O_2, O_2 flow rate: 40 cm^3 min^{-1}, TvL/electrode: 20 µg, scan rate: 10 mVs^{-1}.

The electrochemical response was repeated three times using different electrodes but the same purified stock solution (Figure 60). The moderately purified enzyme showed good response in just one experiment, whereas the current and onset potential were consistent with the highly purified extract. This difference was probably the increased purity increasing the probability of direct communication with the electrode.

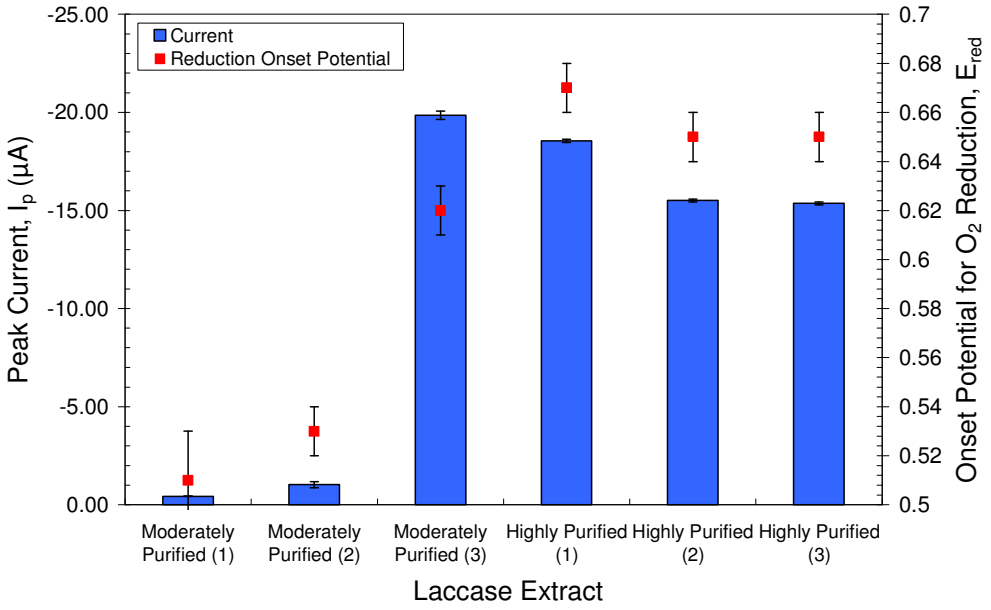

Figure 60: Comparison of current responses and reduction onset potentials between moderately purified and highly purified laccase extracts.

On the basis of the results so far, it can be concluded that laccase purified by two-stage column chromatography resulted in a final extract with the highest purity, overall yield and repeatability. Thus, this enzyme extract and purification procedure was used for the remaining experiments of the thesis.

4.3 Highly Purified Laccase

In this section, the kinetic properties of the highly purified laccase extract were determined through measuring the rate of catalysis, as a function of substrate concentration. A simple model was then used to describe this catalytic behaviour, known as the Michaelis-Menten model, and to determine important kinetic properties such as the enzyme's maximum catalytic rate, V_{max}, and its affinity for the substrate, K_M. Knowing these properties provides an indication of the enzyme's catalytic mechanism and how it will respond to changes in conditions.

4.3.1 Enzyme Kinetics

A series of enzyme assays were run at different substrate (ABTS) concentrations in order to determine the initial reaction rates, under the conditions mentioned in section 3.3.4.2. The initial reaction rate of an enzyme-catalysed reaction is usually determined by calculating the slope of the progress curve. This procedure is only valid when the curve displays truly linear behaviour within the time frame of the assay[238] (i.e. when absorbance increases at a linear rate as more and more product is formed). Therefore, preliminary studies were carried out to determine the optimal laccase concentration which catalyses ABTS at a suitable rate.

Using the initial reaction rates measured for each substrate concentration, Michaelis-Menten and Lineweaver-Burk plots were created using Origin Pro 8 curve fitting software, see Figure 61. As shown, the Michaelis-Menten plot was fitted using the Hill function[244]:

$$V = V_{\max} \frac{x^n}{k^n + x^n} \qquad \textbf{Equation 53}$$

where n is the number of cooperative sites, x is the substrate concentration [S] and k is the Michaelis constant.

For simplicity, the laccase catalysed reaction of ABTS was taken as a single-substrate reaction, thus n was fixed to n=1 during fitting and thus plotted according to the Michaelis-Menten equation (Equation 51). Since the rate of this reaction is dependant on oxygen concentration, the maximum oxygen concentration in the air saturated assay solution was estimated to be around 0.27 mM[245] (near the K_M for an enzyme catalysed O_2 reduction reaction), hence the measured catalytic rates were expected to be half the maximum.

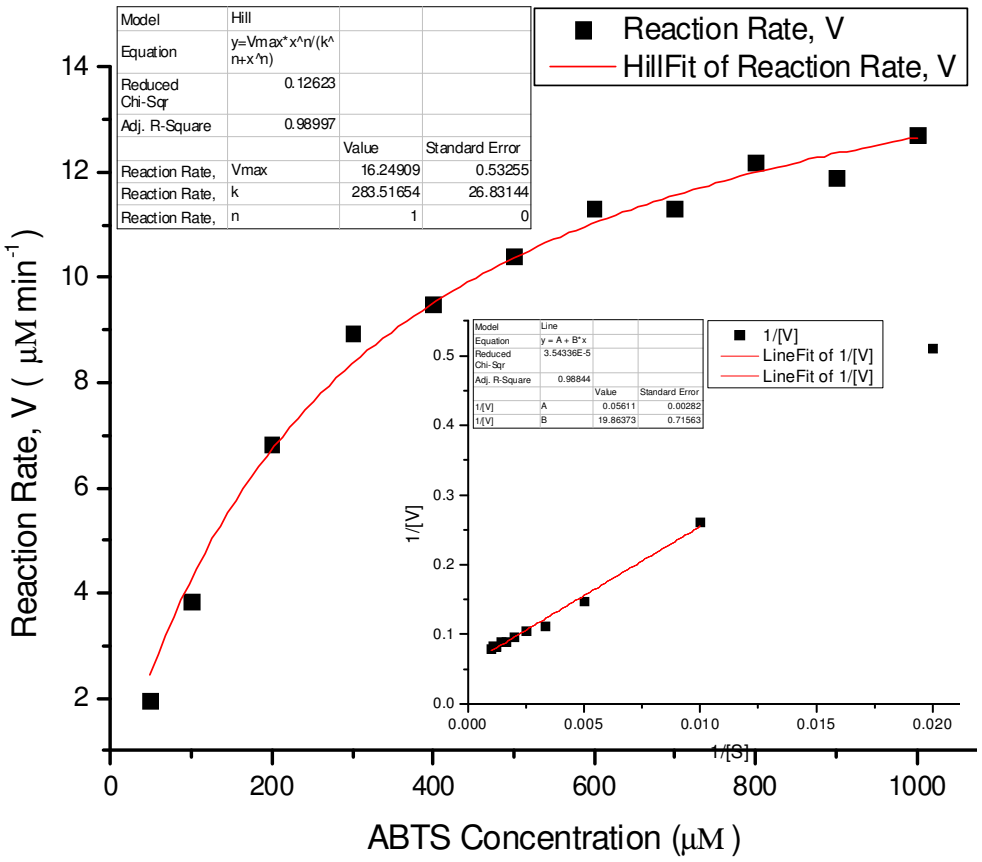

Figure 61: Michaelis-Menten kinetic plot of highly purified Trametes versicolor laccase and Lineweaver-Burk plot (inset). The plots were created using OriginPro 8 software. The V_{max} and K_M values were calculated from the Michaelis-Menten curve and derivations of the Michaelis-Menten equation.

Using the Michael-Menten curve and derivations of the Michaelis-Menten equation, the enzyme kinetic constants, V_{max} and $K_{M\ (ABTS)}$, were determined as 16.2 µM min^{-1} and 283.5 µM respectively. The curve fit was taken as the accepted plot determined suitable since the reciprocal linear plot (Lineweaver-Burk) attributed inaccuracies only at high substrate concentrations, where the data points were far apart (see Figure 61). However, the values determined from the Lineweaver-Burk plot were V_{max} = 17.8 µM/min and K_M = 354 µM, where V_{max} values were close to the Michaelis-Menten curve but the K_M values quite different.

Finally, using the calculated V_{max} and K_M values from the Michaelis-Menten curve and the laccase concentration [E] for the assays, the catalytic constant, k_{cat} (or k_2 in Reaction 5) for laccase was determined using:

$$k_{cat} = k_2 = \frac{V_{\max}}{[E]} = \frac{16.2\mu M / \min}{1.3nM} = 12461 \min^{-1} (208\, s^{-1}) \qquad \textbf{Equation 54}$$

and the catalytic efficiency of laccase was calculated as:

$$\varepsilon = \frac{k_{cat}}{K_M} = \frac{208\, s^{-1}}{283.5\, \mu M} = 5.9 \times 10^5 \ dm^3 \ mol^{-1} \ s^{-1} \qquad \textbf{Equation 55}$$

The Michaelis constant K_M and the catalytic efficiency constant k_{cat} have been measured for a large number of laccases, and great variance can be observed among them. Although once again, the variances in assay conditions must be taken into account when the catalytic constants measured in different laboratories are compared[246]. For example, varying pH, ionic strength, oxygen concentration, temperature and different protein concentrations all have a direct effect on the results. However, it is believed that the specificity for oxygen is less dependant on the enzyme source[247]. The k_{cat} values for a single laccase usually do not differ more than 2-10 fold between different substrates, which reflects the fact that the k_{cat} describes the rate of electron-transfer reactions taking place inside the enzyme after substrate binding[248].

Furthermore, it has been found that the catalytic efficiency (ε) of laccases for some reducing substrates depended linearly on the redox potential of the T1-Cu site, such that the higher the potential of the T1-Cu site the higher catalytic efficiency[181]. This highlights the distinct advantage of choosing *Trametes versicolor* as the cathode catalyst in this thesis.

Han *et al.* recently measured the K_M value for *Trametes versicolor*, laccase to be 12.8 μM and its corresponding V_{max} value, 8125.4 U mg^{-1}, using ABTS as the substrate[249]. These values were significantly better than the results obtained (285 μM and 0.18 U mg^{-1}). However, the strain used in their case had been cultivated,

specially isolated and is thus expected to be of superior purity. For reference purposes, K_M values for laccases are typically in the range 2-5000 μM and thus the sample purified was in the low end of this range, indicating favourable kinetic properties.

4.3.2 Effect of pH on Laccase Activity

Laccase activity was investigated homogenously (in solution) and heterogeneously (on electrode) over a series of pH values. These experiments allowed the pH optima under the different environments to be compared, as well as the catalytic rates.

Figure 62 shows cyclic voltammograms of laccase in oxygen-saturated solutions (1.3 mM at 25 °C) measured over pH values ranging from pH 3.0 to pH 6.0 (Na-Cit, 0.1M). Measurements were conducted by adsorbing 1 μL (30 mg/ml) of laccase onto an aCNT electrode and measuring the electrocatalytic currents starting at pH 4.5, decreasing the pH to 3.0 and then increasing the pH up to 6.0. Experiments were also started at pH 3.0 and pH 6.0, where the pH was increased and decreased respectively. In all cases, a higher electrocatalytic activity was observed at pH values < 4.5 and the optimum pH was ~ 3.5. This result is in agreement with previously published data[174, 250]. The decrease in activity (i.e. reduction in catalytic limiting-current) with increasing pH (see Figure 62) can be explained in terms of enzyme inhibition due to complex formation between the T2-Cu^{2+} oxygen substrate site and OH^-[151, 185]. Conversely, the increase in activity in the low pH region was due to the reduction in thermodynamic driving force for the O_2 reduction reaction, since the electrode works as an electron donor and the protons necessary for the oxygen reduction reaction are provided from the acidic solution.

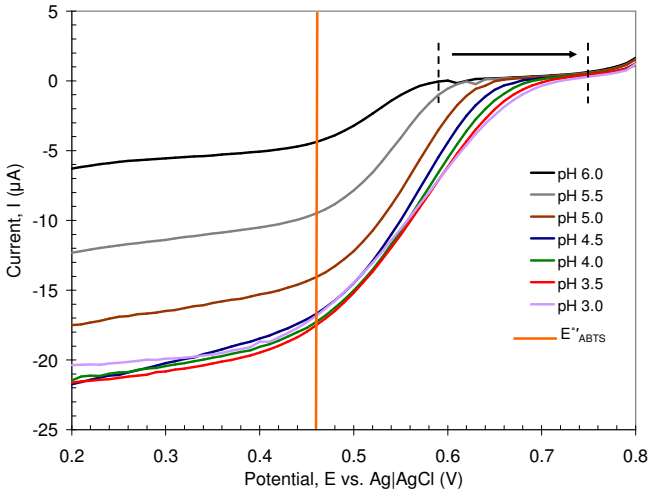

Figure 62: Voltammograms representing laccase potential-dependant O_2 reduction activity at pH values ranging from 3.0 to 6.0. Vertical line represents the potential of the electron donor ABTS which is not affected by pH. Conditions: 0.1 M Na-Cit, O_2 saturated, flow rate: 40cm^3 min^{-1}, pH 3.0-6.0, 10 mV s^{-1}, electrode batch: CVD 1 (1 mm x 1 mm).

It is clear in Figure 62 that the onset potential for catalytic reduction of O_2 shifts with decreasing pH (dotted lines), which highlights the pH dependence on the enzyme catalytic potential and diffusion of oxygen to T1-Cu site.

Solution based assays were conducted over the same pH range using the ABTS assay method described in section 3.3.4.2. Reaction rates were determined by measuring the change in absorbance at 420 nm over a one minute period and dividing by the extinction coefficient, ε_{ABTS} = 36000 M^{-1} cm^{-1}[251]. In order to compare the pH dependencies between the homogeneous and heterogenous catalytic process, the laccase activities of both processes were plotted in Figure 63. Given that ABTS is an electron donor whose potential is not affected by pH[245], the catalytic activity could be predicted by drawing a vertical line through the CV plot (see Figure 62) at the redox potential for ABTS (0.46 V vs. Ag|AgCl). Each intersection corresponds to the catalytic activity towards ABTS reduction at that pH value. Laccase activity was taken as a percentage of the maximum catalytic activity for each separate curve. This corresponded to maximal activities at pH 3.5 for both electron transfer processes.

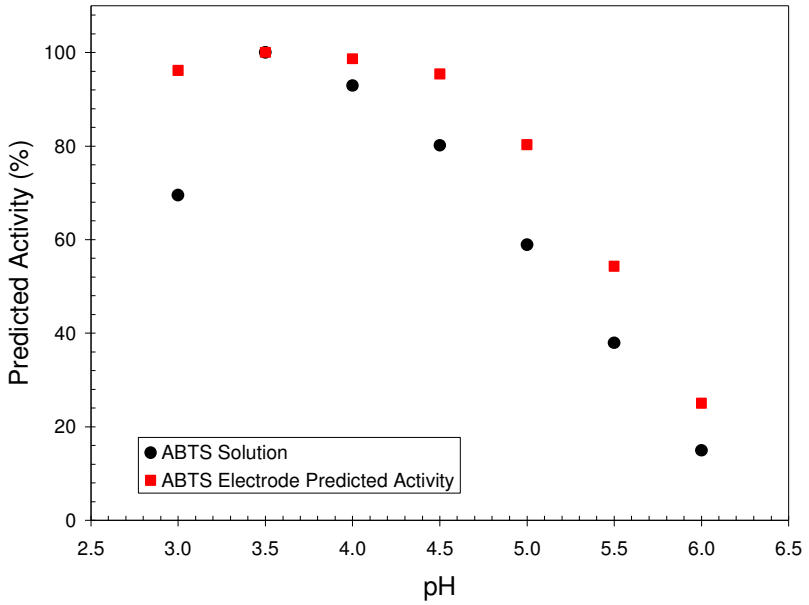

Figure 63: Comparing Laccase activity through homogenous and heterogeneous electron transfer processes. The intersection of ABTS potential line with each catalytic wave in Figure 62 was used to predict the activity for the heterogeneous electron transfer process, (note: data points at pH 3.5 overlap).

The similar behaviour observed between the curves suggests that the heterogenous electron transfer characteristics of laccases when adsorbed on nanotubes are very similar to their homogeneous properties. The only difference was the large activity loss (from 3.5 lower) observed for the homogeneous process. This result was presumably caused by a stability loss which is common at low pH values[174]. However, it has not been determined why this effect was less apparent when immobilised on the electrode and thus further detailed experiments are required to provide an informed explanation of the effect. Recent reports have suggested that phenolic functionalities at carbon surfaces can play a role in the pH-dependencies of electrocatalytic currents.

Despite laccase displaying maximum activity at pH 3.5 under both types of electron transfer, the pH used in all experiments in this thesis was chosen as pH 4.5 to maintain consistency and hence comparability between all the experiments. Thus, for all the results in this thesis, a further 5-10 % increase in current can be achieved by lowering the pH.

4.4 TvL Electrocatalytic Response - Effect of Topology

This study investigated the effect of electrode surface topology on enzyme response. Three carbon electrode materials with different surface topologies were chosen and the electrocatalytic response of laccase on each was measured and compared using PFV. The electrodes studied were all carbon-based since laccase has previously shown good adsorption and direct electrical communication on these surfaces[204, 252]. In addition, these electrode materials are considered to be attractive because they are affordable, abundant, come in many different forms and can be chemically modified in a variety of ways.

4.4.1 Glassy Carbon, Edge-HOPG and aCNTs

For the purpose of this investigation, the three carbon electrodes studied were glassy carbon (GC), the edge of highly oriented pyrolytic graphite (E-HOPG) and aligned carbon nanotube arrays (aCNTs). Figure 64 displays SEM images taken of the different electrode surfaces. It must be noted that no images of the GC electrode were obtained because the electrode was pre-mounted and did not fit in the SEM chamber. However, it is known that these electrodes can be considered as being essentially flat with low defect densities when polished using diamond and alumina-based slurries, as carried out in this investigation (see Table 3). This mechanical polishing renews the electrode surface by removing surface contaminants, thus increasing the electrode sensitivity and reproducibility when used for analytical work. This leaves a relatively smooth surface flat surface, which is similar to the basal-plane of HOPG (see Figure 64 (a)).

In contrast, the edge of the HOPG electrode displays a high surface roughness where the edges of graphite layers, typically 50-60 nm thick and around 5-10μm wide, can be seen protruding from the surface (see Figure 64(b)). A high number of these edge sites were introduced through polishing with fine abrasive sandpapers (see Table 3), subsequent rinsing and sonication in water to remove any loose graphite debris. Many reports have demonstrated that these sites provide a biocompatible environment for the enzyme which is rich in C-O functionalities,

thus facilitating electrostatic interactions and hydrogen bonds with redox enzymes and proteins[174, 204, 253]. Taking this into account, it was necessary to investigate whether protein adsorption and electron transfer was improved due to these topological features and the anisotropic nature of the graphite edge.

The final electrode investigated consisted of an array of densely packed nanotubes (Figure 64 (c)), which were typically separated by 60-80 nm and had lengths and diameters of 1.12 mm and 50-100 nm respectively (see inset). The scale of roughness on the surface will be higher than edge HOPG (E-HOPG) due to the large number of high aspect-ratio nanotubes present, as illustrated in Figure 64 (d). As such, no surface treatments were applied to the aCNT electrode.

Electrode Material	Manufactured	Topology	Resistivity Ω-m (0.5 V, DC)	Enzyme Coverage
Glassy Carbon (GCE) S.A = 7.1 x 10^{-6} m^2 Diamond Polished 1 µm and ¼ µm, 3 mm diameter	Commercially-IJ Cambria Co.	Predominantly Flat	1.9 x 10^{-4}	Poor - Enzyme Desorbs
Edge-HOPG (E-HOPG) S.A* = ~1 m^2 g^{-1} Abraded-Sandpaper P400 and P800, 3 mm x 0.5 mm	Commercially-SPI Supplies Co.	Rough - Dangling Bonds	7.7 x 10^{-3}	Low- Low Currents
Aligned CNT Film (aCNT) S.A = ~30-40 m^2 g^{-1} Removed from Si, 5 mm x 3 mm, 1.12 mm CNT length	Grown In-House	Dense Forest of CNTs	4.0 x 10^{-2}	High- High Currents

Table 3: Electrode comparison table detailing preparation steps, properties and adsorption behaviour. Surface areas (S.A) were estimated, *based on literature value [204].

The electrical resistivity of each electrode was measured by applying a potential of 0.5 V across them in D.C. mode, as shown in Table 3. The GC electrode possessed the lowest resistivity; however this electrode was commercially purchased and so may have had lower load resistance. The E-HOPG and aCNT electrodes were electrically contacted with silver epoxy and silver wire, where the presence of the epoxy and less effective contact to aCNTs resulted in the higher resistivity's observed.

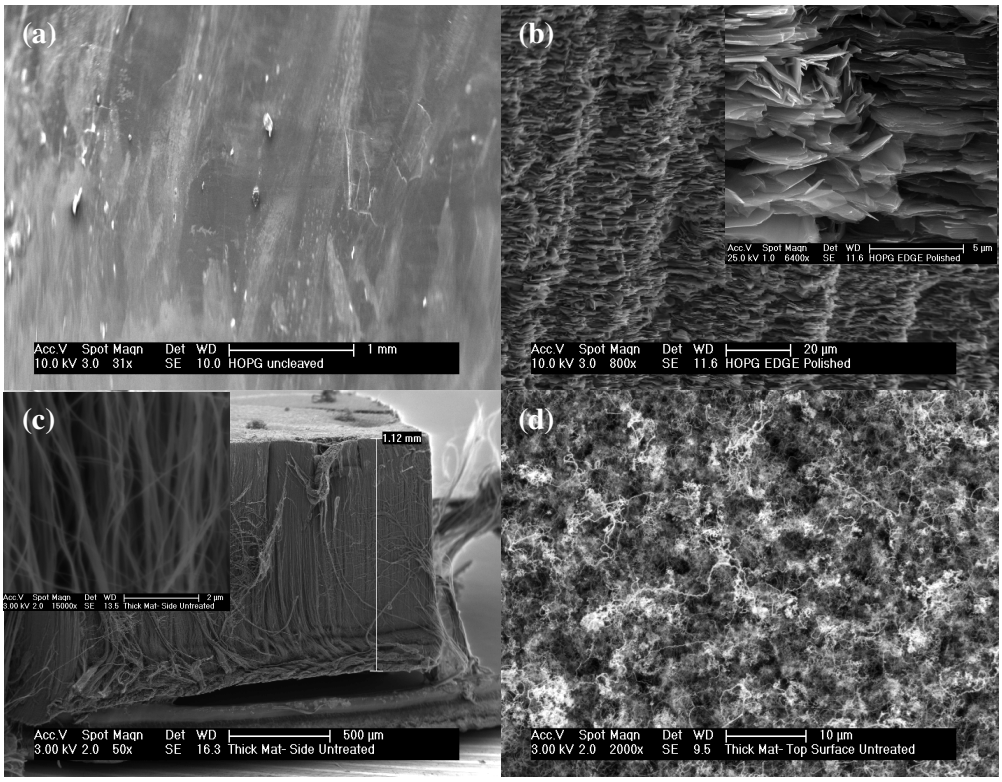

Figure 64: SEM images of (a) Basal-plane HOPG, (b) polished E-HOPG and inset (higher magnification), (c) cross-section of aCNT electrode and inset (higher magnification) and (d) top surface of aCNT electrode.

Initial CV measurements were carried out on bare electrodes (i.e. without laccase) to measure difference in the non-Faradaic signal between the electrodes as a result of different surface areas. A pair of small redox peaks can be noticed in the response from the aCNT electrode which are attributed to some silver epoxy from the electrode connection. The capacitances measured for the electrodes were GCE = 2 µF (28 µF cm^{-2}), E-HOPG = 3 µF (200 µF cm^{-2}) and aCNT = 3556 µF (~23700 µF cm^{-2}). Densities were normalised to geometric area of electrode.

Laccase voltammetry was conducted after 1 µL of laccase, (10 mg ml^{-1}), was deposited and dried on each electrode surface. It must be noted that buffer solutions were saturated with O_2 prior and during measurement. No electrocatalytic response was observed on the GCE electrode (see Figure 65 (a)), where it is assumed that the flat topology and low roughness and surface area hindered enzyme adsorption. It was possible, however, to observe DET from laccase adsorbed on E-HOPG (Figure 65(b)). The low current response and flat waveshape were comparable to those observed in the literature, where it is

believed that the reaction is not limited by oxygen depletion since there is such a low amount of electrochemically active enzyme at the surface. Finally, the aCNT electrode displayed the best electrocatalytic behaviour due to the high surface area and increased enzyme coverage obtained (see Figure 65 (c)). Current density (normalised to geometric area) values were x30 fold higher than E-HOPG electrodes due to the high coverage's obtained on these electrodes. The high catalytic activity of the enzyme resulted in a diffusion-limited current response, where substrate was being turned over faster than it reached the enzyme. Furthermore, the smaller driving force and higher reduction potential could be attributed to improvements in kinetic performance, as has been reviewed in the literature[70, 88, 219]. However, this assumption will not be made as yet and will be explained in following sections in the thesis.

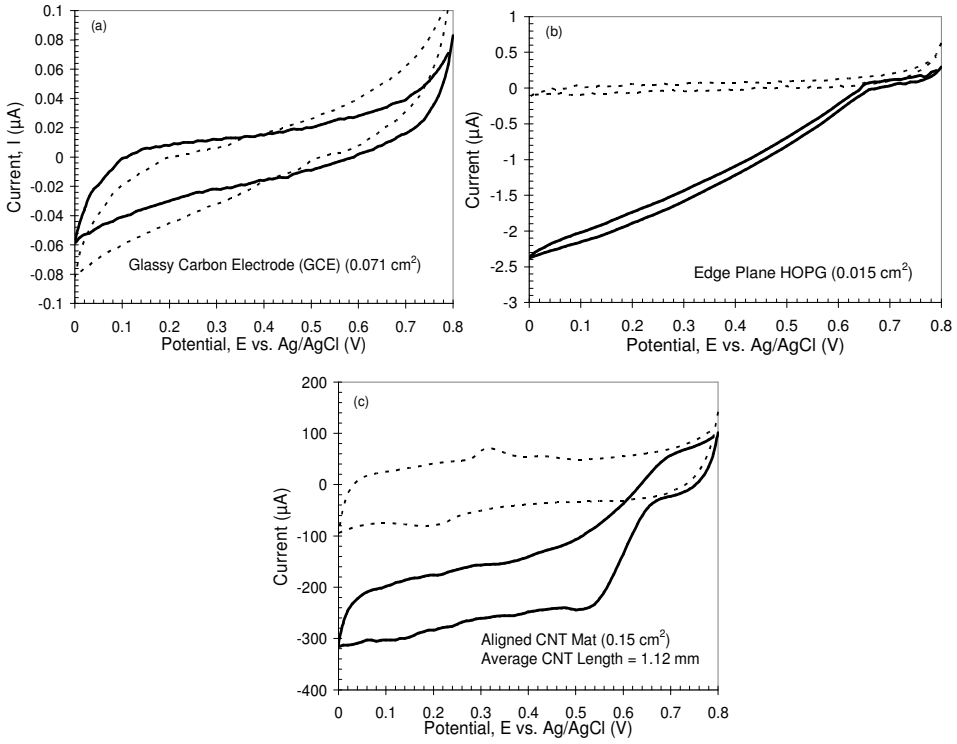

Figure 65: Laccase electrocatalytic reduction of molecular oxygen on different electrode topologies (dotted line) with no laccase (bold line) with laccase. Conditions: 0.1 M Na-Cit, pH 4.5, O_2 saturated, flow rate: 40 cm^3 min^{-1}, 10 mV/s, TvL/electrode: 10 µg averaged over 4 CV cycles.

4.5 Aligned Carbon Nanotube Electrodes (aCNTs)

On the basis of the results presented, CNTs have been shown to be the most suitable carbon electrode material for BFCs, thus the electrocatalytic response of laccase on these supports was researched for the remainder of the thesis. Electrochemical experiments were conducted using aCNT electrodes grown from three separate growth batches; referred to as CVD1, CVD2 and CVD3 throughout the thesis. These batches were grown under identical CVD conditions and hence minimal variations in structural quality and purity were expected between the batches.

4.5.1 Preliminary CVD Experiments

CVD was used to grow the nanotubes since it is cost-effective, robust and scalable, properties which are essential for commercial realisation. In addition, this technique produces highly organised aCNT arrays increasing the surface area to projected area ratio of the electrode and thus increasing the loading of catalytic enzyme. These vertically aligned arrays can be further credited for their superior adsorption properties, where the high capillary forces resulting from the porous 3D network of aligned nanotubes allows the top surface to essentially act as a 'sponge', encapsulating the enzyme and thus preventing minimal loss of enzyme.

Using the floating catalyst CVD method, aCNTs were grown directly on silica substrates, following an adapted method reported by Singh *et al.*[254] and described in section 3.3.7.11. Preliminary investigations into different growth parameters such as reaction length, reactant solution concentrations, and substrate oxide layer application and thickness enabled a good understanding of the ideal conditions required to produce robust and effective nanotube electrodes. Initial experiments produced aligned nanotubes grown using a ferrocene in toluene with a concentration of 5 wt%. This concentration was later reduced to 2.5 wt%, since similar lengths were achieved using only half the metallocene reactant concentration and fewer Fe impurities were expected from the growth procedure.

Using this concentration, the distribution in CNT lengths was subsequently determined for the reaction times of 1 hr, 2 hrs and 4 hrs, producing typical lengths of between 100-200 µm, 400-500 µm and 700-900 µm respectively. Representative SEM images are given in Figure 66 for the SiO_2 wafers grown under the different CVD reaction times. However, it was found towards the end of the project that the heating elements in the furnace had deteriorated over the last year of the thesis. This degradation meant that the furnaces hot zone gradually reduced in length over a period of several months, changing the nanotubes produced, decreasing their length profiles. This change in reaction conditions affected some of the batches of the electrodes and is discussed later in the thesis. It should be noted that all the batches concerned have been drawn to the reader's attention when discussed in this thesis.

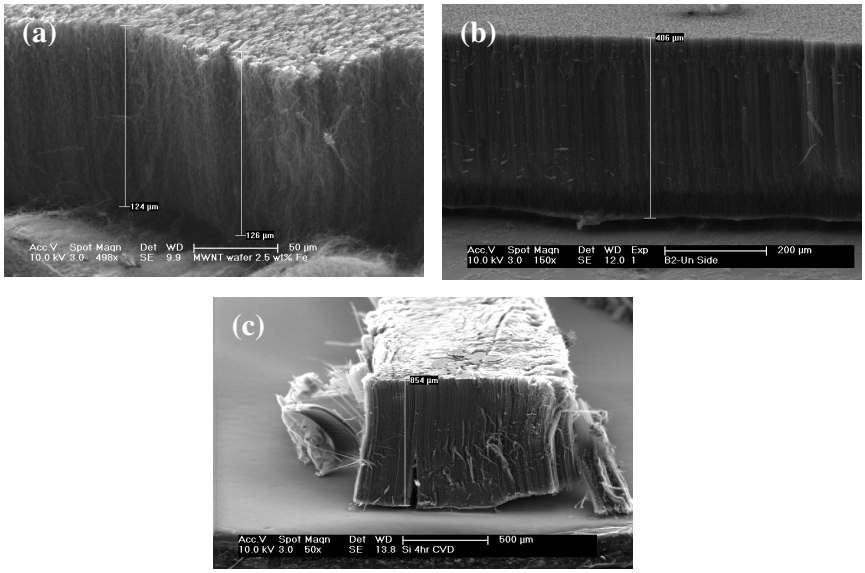

Figure 66: SEM images of a aCNTs grown for a) 1hr (~125 µm) b) 2hr (~400 µm) and c) 4hrs (~850 µm) on SiO_2 wafers.

4.5.2 Electrode Surface Area and Mass Calculations

Typically the surface area of highly porous materials is accurately measured using nitrogen gas adsorption and combined with various theories to yield the specific surface area and pore size distributions of the material. However, time constraints and equipment availability prevented such analysis on the aCNT electrodes.

As such, the surface area was estimated using a rational, although approximate, approach in which a characteristic CNT density, length and diameter was assigned to each aCNT batch based on SEM and TEM imaging. These terms were then consolidated to provide an estimate of the aCNT surface area which was subsequently used in the normalisation of current density. Using high magnification SEM images and the imaging software ImageJ (ImageJ 1.45 b) the average CNT density, diameter and length were estimated by averaging three sample areas for each aCNT growth batch. The estimated CNT diameters were primarily used as a basis for comparison against the TEM determinations. Based on these estimates the surface areas could be determined. As expected, nanotube batches with smaller diameters, longer lengths and high densities yielded larger surface areas, as shown in Table 4.

CVD Batch	Estimated Surface Area (cm^2)	Average CNT Length (mm)	Average CNT diameter (nm)	Average CNT Density (within 7 μm^2)
1	6.29	0.50 ± 0.05	70	40
2	10.37	0.70 ± 0.05	55	60
3	5.33, 9.60	0.36 ± 0.01 0.65 ± 0.04	55	60
3	22.20, 32.74	1.50 ± 0.01, 2.00 ± 0.01	55	60

Table 4: Surfaces areas, lengths, diameters and densitys determined using SEM, TEM and ImageJ software.

The mass of each nanotube was determined using the equation derived by *Peigney et al.*[255, 256], as shown below:

$$W_{MWNT} = \frac{1}{1315} \times \pi \times L \left[n d_{out} - 2 d_{s-s} \sum_{i=0}^{n-1} \right] \quad \textbf{Equation 56}$$

where L is the length of the array, n is the number of walls, d_{out} is the external diameter, $d_{s\text{-}s}$ is the inter-shell spacing (typically 0.34 nm).

This equation states the weight of any MWNT can be calculated from the surface of external and internal graphene sheets that compose it (bracketed part of equation), taking into account the surfacic weight of the graphene sheet 1/1315 m^2/g.

Combining the surface area and mass calculations, the surface area to relative mass could be determined and compared with reported values. Specific surface area values were between 25 and 33 m^2/g which was in agreement with values based on nanotubes with similar diameters and number of walls[256].

4.5.3 Preliminary Electrochemistry

4.5.3.1 Cyclic Voltammetry

Voltammetric measurements were undertaken on the aCNT electrodes to measure their electrochemical response in 0.1 M Na-Cit, pH 4.5. An initial problem was reaction of the silver (Ag) epoxy with the buffer solution, as the porous nature of the aCNT electrode allowed the buffer to react with the silver oxide. Using SEM analysis, the penetration of the Ag epoxy into the mat was determined to be 60 -80 µm from the edge of electrode. This problem was overcome by ensuring the base of the aCNT mat (nearest the connection) was sufficiently insulated. A thin layer of epoxy resin (Araldite Rapid) was applied around the base perimeter of all electrodes; this had minimal effect on diffusion into the mat and allowed the majority of the CNT to remain electrochemically active. The maximum height of the epoxy resin layer was ~100 µm (using SEM), while penetration into the mat was undetermined but assumed to be low due to the high viscosity of the resin. Note that CNT electrode lengths mentioned throughout this work do not account for the thin epoxy resin layer since only the outer CNTs were believed to be affected.

The silver redox peaks can be clearly noticed in the CV shown in Figure 67, however this illustrates an extreme case scenario. In most cases, the silver redox peaks were only present at slow scan rates (10-25 mV s^{-1}) due to diffusion effects. The redox peaks at 0.48 V and 0.58 V are believed to be oxidation of silver oxide,

while the peak at 0.35 V is the reduction of silver oxide. The insulated aCNT array displayed a featureless CV with perfectly parallel capacitive currents of equal magnitude in both scan directions, and thus the electrode is behaving well.

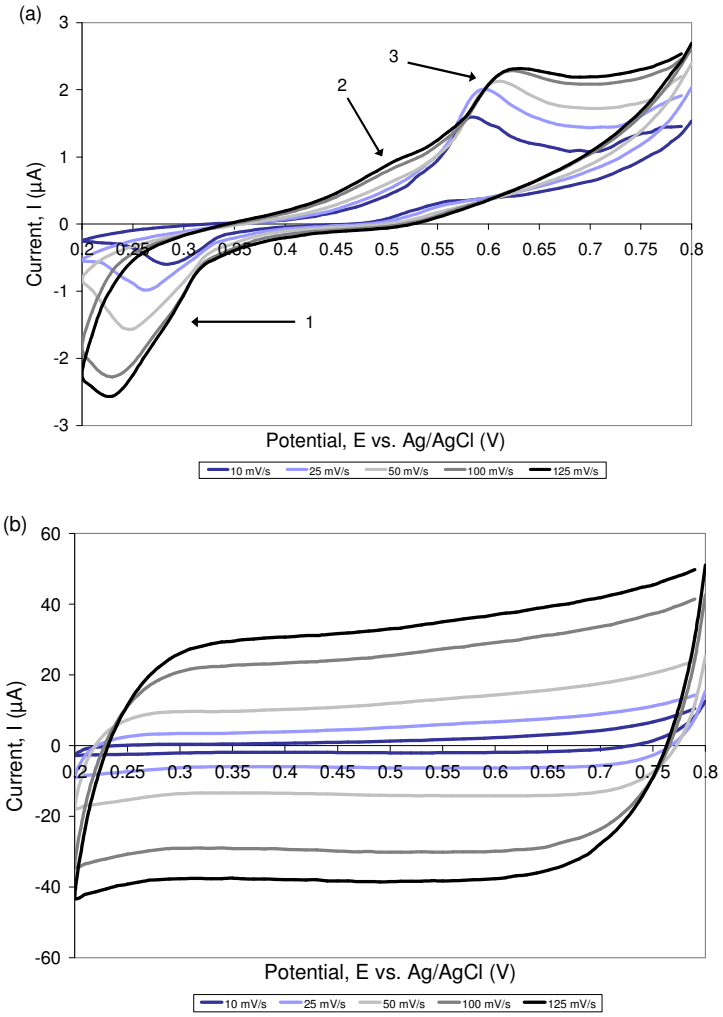

Figure 67: CVs of a) aCNT with silver epoxy exposure b) aCNT with base of mat insulated, thereby removing silver redox peaks ((a) 1-3), scan rates between 10 and 125 mV s^{-1}.

A drawback of catalytically synthesised carbon nanotubes such as those prepared by the CVD method, is the incorporation of residual metal catalyst particles (typically 3-30 %)[108] into CNT structures. In this work, the metal contaminant concerned is Fe, obtained via pyrolysis of the ferrocene precursor in the floating catalyst CVD method. These metallic impurities have shown to be electrochemically active in solutions, influencing electrochemical reactions when present within carbon nanotube electrodes. Numerous electrochemical studies

have suggested that the enhanced electroactivity of CNT-based electrodes is a direct result of the surface-bound metallic species, effectively acting as the primary catalytic site for the redox reactions involved[108]. High-resolution TEM analysis of the CNTs synthesised in this work showed that the metal contaminants were predominantly entrapped within the graphene layers, see Figure 68 below. The metal particles ranged from a few nanometers to a few tens of nanometers, with the larger particles situated inside the CNT or even on the outer surface of the CNT covered with thin layers of amorphous carbon.

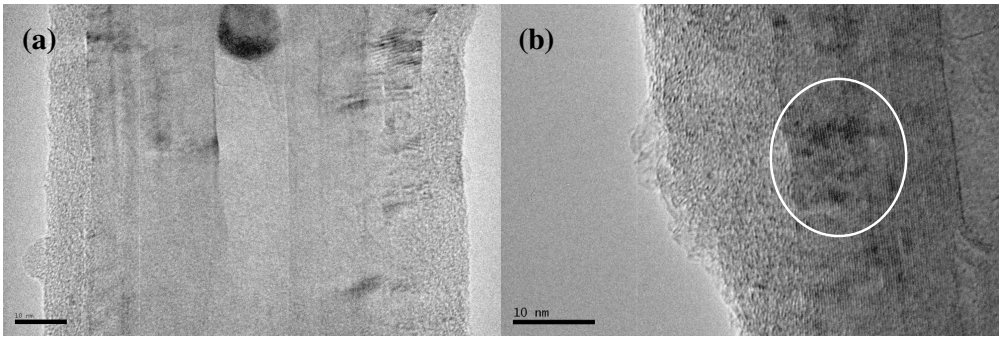

Figure 68: TEM images of Fe particles encased in (a) nanotube canal (dark particle) and (b) walls (circled).

Cyclic voltammetric measurements were carried out on the aCNT electrodes to determine the amount of Fe encased within the CNTs. Figure 69 shows representative CVs obtained from aCNT electrodes, both grown under different CVD reaction times and immersed in 0.5 M KCl. These CVs were measured by sweeping the potential negative from 0.8 V to -0.3 V and then returning to 0.8 V. The CVs confirmed the presence of redox activity corresponding to surface-bound $Fe^{II/III}$ electron transfer, previously reported by Lyon *et al*[108]. The cathodic peak (between -0.1 and -0.2 V) relates to Fe^{III} reduction and the anodic peak (between 0.1 and 0.2 V) to Fe^{II} oxidation. Interestingly, there was x 10 reduction in peak current observed with the 2 hr grown aCNT electrodes, suggesting increasing impurities with CVD growth time. Research by Lyon *et al.*, found that the nature of the coordinating anion (electrolyte) composition influences the formation and relative amounts of these Fe species[108]. Preliminary experiments carried out on these aCNT electrodes showed that the peaks from the residual iron peaks decreased in intensity after the electrodes were pre-treated by reduction in a hydrogen atmosphere.

Despite, the many techniques available to selectively remove or suppress these redox active particles, it was decided that this should be best avoided as there is limited evidence to suggest that the structural integrity of CNTs is maintained after such aggressive treatments. Instead, all voltammetric measurements were carried out on the aCNTs using a maximum potential window of 0.8 and 0 V, thus eliminating any $Fe^{II/III}$ redox behaviour, since no Fe^{II} oxidation occurs without prior reduction of Fe^{III} species.

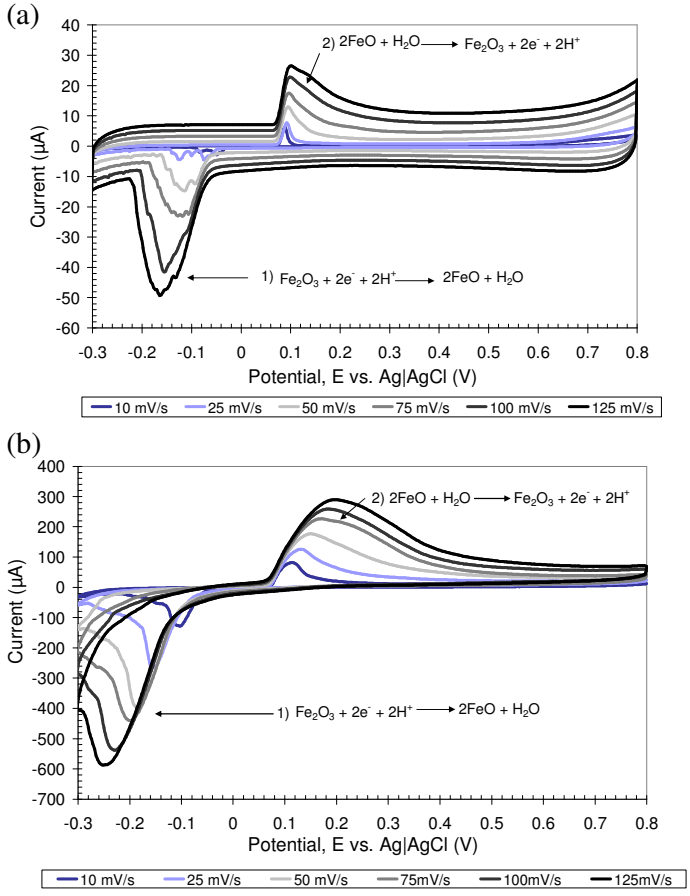

Figure 69: Cyclic Voltammetry of Fe redox activity in aCNT array grown for (a) 2 hours and (b) 4 hours.

4.5.3.2 Enzyme Adsorption onto the Electrodes

Preliminary investigations were carried out to determine the adsorption profile of enzyme into the aCNT electrode and stability under applied potentials. Epifluorescence and electrochemical measurements were conducted on these electrodes using fluorescently-tagged laccase. Laccase was labelled with the fluorophore fluorescein-5-EX, (see section 3.3.5) which fluoresces green in response to an excitation wavelength of 494 nm. In its dry state, the aCNT electrode (1 mm x 1 mm) was spotted with 1 µL of fluorescently-tagged laccase and the fluorescence measured once the enzyme had fully soaked into the mat (see section 3.2.8). The same experiment was also conducted on silica substrates with no nanotubes on them ("blank").

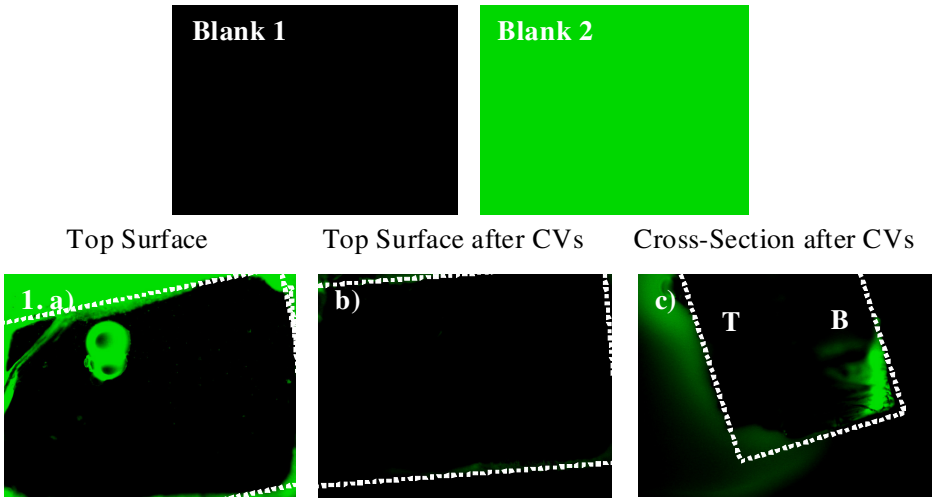

Figure 70: Epifluorescence images where: (Blank 1) aCNT electrode with no fluorescent laccase, (Blank 2) 1µL fluorescent laccase on glass slide, and (1.(a)) aCNT electrode with 1 µL fluorescent laccase added to surface before CV and (b-c) After CV. Dotted lines outline perimeter of electrode and T and B correspond to top and bottom of electrode.

The majority of enzyme was found to have soaked into the nanotube electrode (Figure 70 (a)). The high electrode porosity coupled with the capillary forces acting on the enzyme solution provoked this 'sponge-like' behaviour. The strong fluorescence outside the electrode perimeter (dotted line) is believed to have resulted from fluorescence from the sides of the electrode due to the high concentration of enzyme within the aCNT array.

After initial epifluorescence measurements (Figure 70 (a)), the electrode was placed in an electrochemical cell and the catalytic response measured within a potential window of 0.8 – 0.4 V. The electrode was cycled five times, during which no catalytic activity was observed in an oxygen saturated electrolyte (0.1 M Na-Cit, pH 4.5). It was hypothesized that the fluorophore labelling of the enzyme was responsible for the inactivation. Other reports have highlighted catalytic loss after binding of fluorophores[257, 258], where it was believed that the covalent linkage induces steric conflict with the substrate.

After electrochemical analysis, the electrode was dried with a paper towel to absorb any excess electrolyte and then re-measured. The fluorescent signal was found to be weaker from the top and sides of the electrode, possibly indicating some enzyme desorption contributing to a weaker fluorescent signal, see Figure 70 (b). In order to check the presence of the enzyme, the electrode was cut in half using a razor blade, thus revealing the adsorption profile through the mat and providing a more quantitative measure of the amount of enzyme still absorbed after potential cycling. The cross-sectional fluorescent image (Figure 70 (c)) showed an intense fluorescent signal towards the bottom of the electrode, indicating a high concentration of enzyme probably due to the strong capillary forces as mentioned earlier. Attempts were made to quantify the amount of enzyme remaining from the starting solution. However, difficulties were found in detecting the fluorescent signal using the chosen experimental equipment. In order to increase the emission signal the nanotubes were hydrated, but the fluorescent signal was still too weak to be detected. Therefore, without knowledge of the cross-sectional signal intensity before electrochemical measurement, it was difficult to surmise if any enzyme desorbed. Although it was evident that enzyme present on the top surface desorbed and the majority of enzyme appears to be situated towards the bottom of the aCNT array. In addition, it must be noted that the aCNT electrode did not collapse or lose alignment after immersion in buffer and upon drying.

For future experiments, it would be necessary to analyse the electrolyte for any enzyme activity as well as taking cross-sectional fluorescent images of identical electrodes which have undergone and not undergone electrochemical

measurement so fluorescence intensity can be directly compared and any desorption identified. Furthermore, it would be beneficial if the enzyme was also catalytically active when labelled so that that catalytic response can be correlated to the fluorescent signal.

4.6 Carbon Nanotubes- Laccase Electrochemistry

4.6.1 Effect of Carbon Nanotube Electrode Area

Electrode performance can be summarised in terms of the current response per electrode area, commonly termed as the electrode current density (A cm^{-2}). In this work, a good estimation of electrode performance was provided by measuring the laccase reduction current as a function of the aCNT electrode geometric area. These measurements not only indicated whether the current is scalable but, when normalised to the surface area, can also provide further insight into any limitations or even improvements found with respect to enzyme adsorption, electronic coupling and mass transport.

To investigate the effect of electrode area, electrodes were fabricated from the same growth batch of aCNTs (CVD 1), therefore reasonably being deemed chemically and structurally similar. A fixed 1 μL aliquot of enzyme (10 mg ml^{-1}) was applied to each electrode area (i.e. loading decreased with area): 0.01 cm^2, 0.04 cm^2, 0.09 cm^2 and 0.16 cm^2, and the reduction response measured using cyclic voltammetry, once the currents had stabilised (after 4-5 cycles) and the buffer refreshed. The CV responses for laccase O_2 reduction on each electrode are shown in Figure 71. The catalytic current scaled linearly with electrode area (for ref - Figure 77); with approximately a 20 fold increase from the smallest electrode (0.01 cm^2) to the largest (0.16 cm^2). These results suggested that more of the enzyme is electroactive due to the higher obtainable coverage and electron transfer found on larger high-surface area electrode supports. However, it can be noticed that despite higher current values the catalytic responses were still substrate-limited, as shown by the plateaus in current. The exception to this behaviour was the 0.16 cm^2 electrode (4 mm x 4 mm), where limiting current was not reached within the potential window.

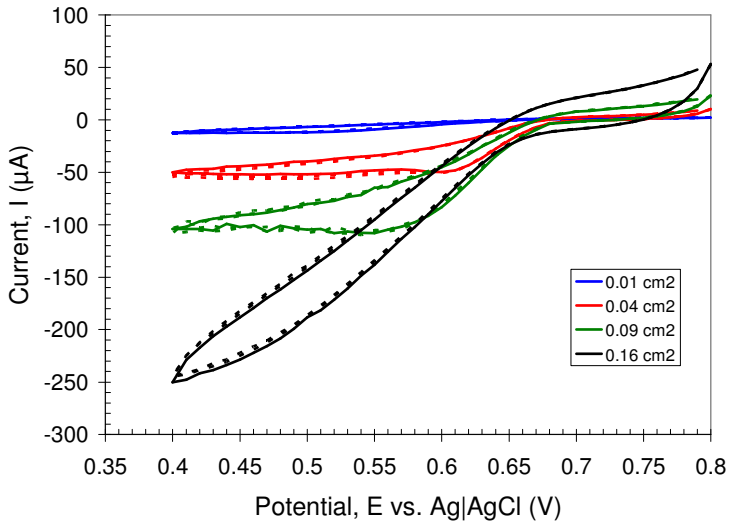

Figure 71: Effect of electrode area on laccase O_2 reduction response. Dotted lines represent scans 1-3 and bold lines scan 4. Conditions: 0.1 M Na-Cit, pH 4.5, O_2 saturated, flow rate: 40 cm^3, 10 mV/s, 20-25 °C, Laccase: 1 µL (10 mg ml^{-1}) to each electrode, electrode batch: CVD 1.

A more clear representation of this surface area effect on laccase catalytic response is shown in the scatter plot in Figure 72 (a). It can be observed that both the peak current and capacitance values scaled for each electrode. In this plot, the electrode area was taken as the projected area of the electrodes and the enzyme loading was normalised to this. The increase in catalytic current with lower loading suggests that laccase's rate was limited by substrate diffusion rather than amount of enzyme. Whilst the current did scale with geometric area ("electrode area"), the current did not scale with actual surface area ("electrode surface area") of the nanotubes on the electrode with the current ~ 2 µA cm^{-2} (Figure 72 (b)). This behaviour indicates that current response is fixed per electrode surface area since most of the enzyme is lost or inactivated due to substrate limitations and density values will remain in the low µA cm^{-2} until these limitations are overcome (i.e through rotation). Furthermore, enzyme molecules that are poorly orientated at the electrode surface and are subject to slow electron transfer rates cannot be ignored.

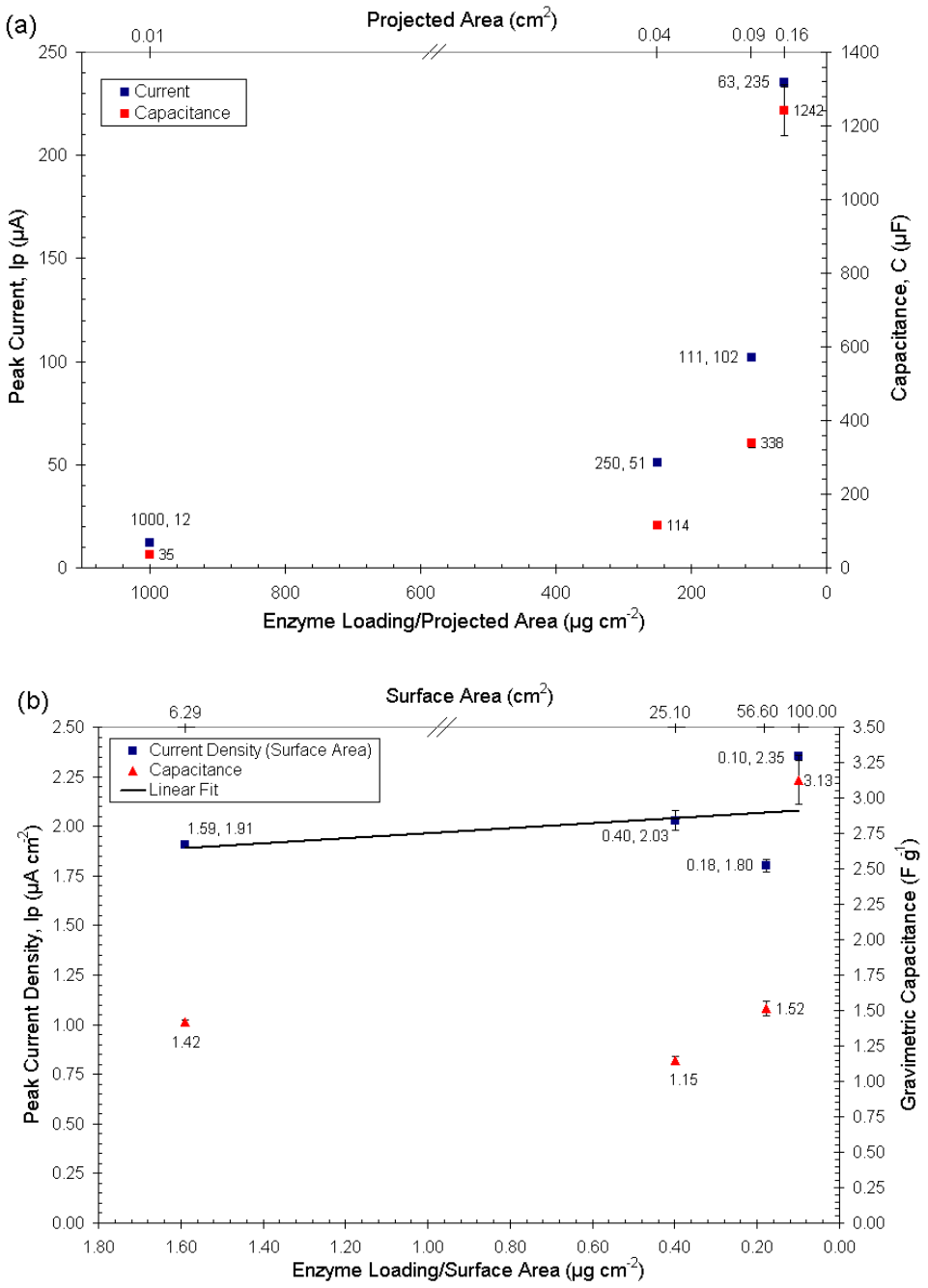

Figure 72: Effect of electrode area on laccase O_2 reduction response with fixed enzyme loading. In (a) Peak current values are maximum current values at 0.4 V and (b) Peak current density was normalised to electrode surface area and capacitances to electrode mass using method in section 4.5.2. Error bars indicate standard deviation for three CV cycles. Conditions: 0.1 M Na-Cit, pH 4.5, 10 mV s^{-1}, O_2 saturated solution, flow rate: 40 cm^3 min^{-1}, TvL: 1 µL (10 mg ml^{-1}) on each electrode, electrode batch CVD 1.

4.6.2 Effect of CNT Length

In the previous section it was demonstrated that laccase activity increases with electrode area, however, the mass transport of oxygen was shown to be rate limiting and therefore current density did not scale when normalised to the electrode surface area. It is possible that substrate transport became more rate limiting as the electrode area increased given the longer diffusion path to the enzyme which has been shown to be situated towards the bottom of the electrode. Therefore, it was necessary to investigate the effect of increasing the nanotube length for fixed electrode areas, thus maintaining the diffusion path length while increasing the electrochemically accessible area for enhanced laccase activity.

This investigation was carried out using nanotubes from the CVD 3 batch which grew to a variety of lengths. These variations in length were believed to be the cause of furnace deterioration, where the loss in temperature profile across the nanotube growth zone resulted in different growth rates as a function of position in the furnace during the CVD process. Conveniently, this nanotube growth batch was ideal for this investigation, however, it must be noted that departure from ideal CVD growth conditions can lead to higher impurity levels and defect densities within the batch.

1 μL (10 mg ml^{-1}) was applied to each electrode, thus loading per projected area was once again fixed. The aCNT electrodes chosen had a large separation in length scales between them, which allowed for changes in catalytic performance to be highlighted more clearly, thus providing good comparison between the electrodes. Buffer solutions were purged with O_2 during measurement. It must be noted that difficulties were found with the enzyme adsorbing into these electrodes, in some cases not adsorbing into the aCNT arrays at all and instead forming a film on the surface. This poor adsorption behaviour resulted in poor laccase electrocatalytic activity on these electrodes. The presence of a thick amorphous carbon layer was later evidenced upon surface analysis (section 5.2.3.1) which probably decreased electron transfer efficiency to the enzyme as well as surface stability. The electrodes which demonstrated poor adsorption behaviour were not

used in this investigation and instead only electrodes where the enzyme fully adsorbed into the aCNT array were analysed.

Figure 73 details the voltammograms measured for the aCNT electrodes with increasing lengths. The waves shown are representative of three CV scans (bold lines represent the final scan). These measurements were recorded after refreshing the buffer solution and once the currents had stabilised (typically 5-6 CV scans). It can be observed that laccase O_2-reduction response increased with increasing CNT lengths, in a similar manner to the area experiments. Although, the waveforms were shown to be slightly different with more of a residual slope at which O_2 was reduced down to around 0.48 V (compared to 0.6 V) followed by a trailing edge at more negative potential.

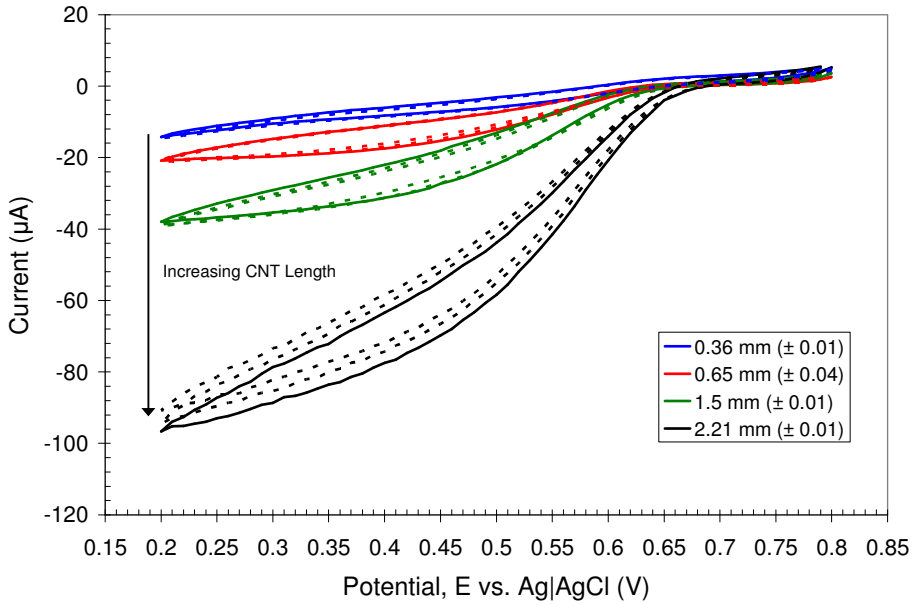

Figure 73: CVs displaying laccase O_2 reduction response with increasing nanotube lengths. Conditions: 0.1 M Na-Cit, pH 4.5, O_2 saturated solution, flow rate: 40 cm^3 min^{-1}, Laccase: 1 µL (10 mg ml^{-1} on each electrode, electrode batch: CVD 3 (1 mm x 1 mm).

This trailing edge was present on all electrodes and thus was investigated further by increasing the O_2 flow rate. This was carried out to check if slow O_2 diffusion into the array was responsible for this effect. Increasing the O_2 flow rate effectively increases the convective flow of O_2 in solution, which could improve transport into the array. However, increasing the flow rate for all electrodes had no effect on this trailing slope (Figure 74). However, the current magnitude for

the longer electrodes (1.5 and 2.21 mm) was shown to increase, thus suggesting that the catalytic rate was partly limited by substrate diffusion (see inset in 74). The shorter electrodes (0.65 and 0.36 mm) displayed a more stable current response, with maybe a small decrease at the highest flow rates possibly due to some desorption through excessive agitation of the cell solution. These results suggest that O_2 diffusion tends to be slower into arrays with long nanotube lengths (>1.00 mm). However, in Figure 75 it can be noticed that the longest nanotube array had the highest current density and the 1.5 mm array had the lowest. This disparity, although small, could suggest that different catalytic responses were observed due to variations in impurity levels across the arrays measured. The low capacitances shown for the longer electrodes suggest that these had a higher impurity level coating the nanotubes, essentially blocking electrolyte access. The high catalytic activity observed for the 2.21 mm electrode, however, can only be explained in terms of preferential adsorption on nanotubes which were not coated in impurities. The shorter electrodes had higher capacitances and these along with their current responses were shown to be well-matched to the 1 mm x 1 mm electrode used in the previous section (4.5.2) which was of siimilar length (75).

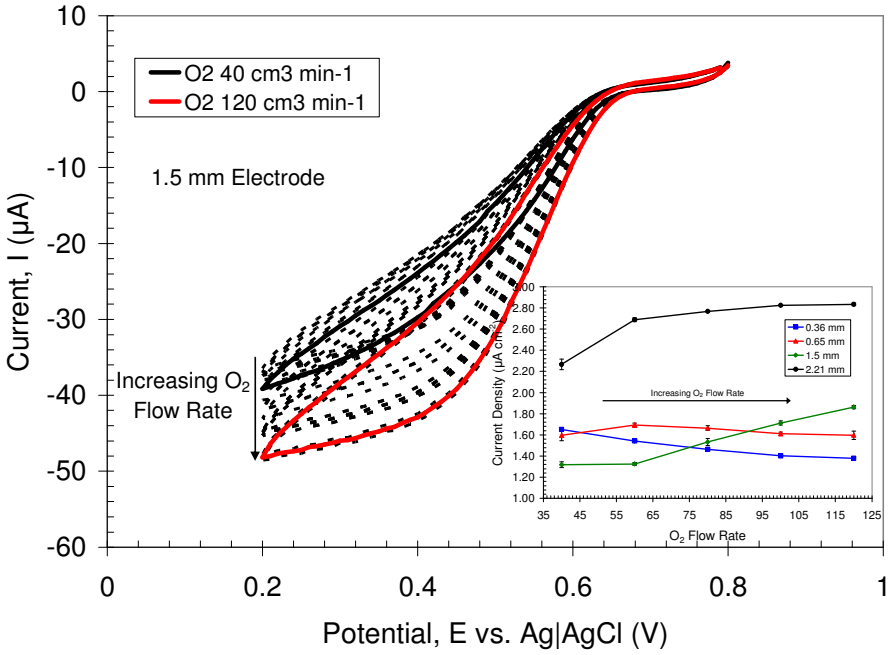

Figure 74: CV scans taken at increasing O_2 flow rates from 40-120 cm^3 min^{-1} (20 cm^3 min^{-1} increments) on 1.5 mm electrode (4 scans per flow rate). Bold black line represents first cycle at 40 cm^3 min^{-1} and last scan 120 cm^3 min^{-1}. Inset: Detailing current density vs. flow rate effect on all electrodes (density normalised to estimated surface area).

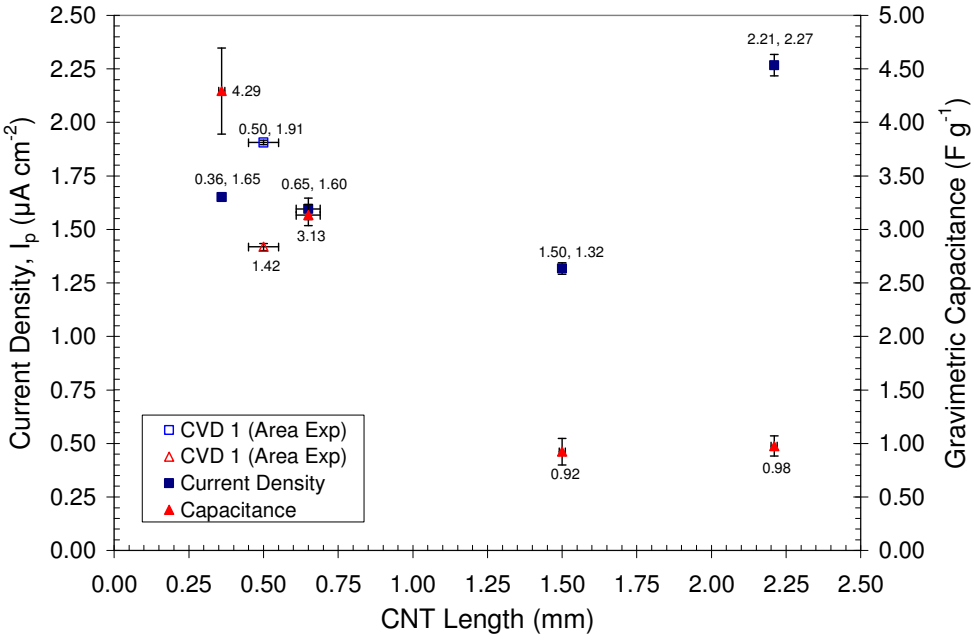

Figure 75: Scatter plot detailing current density (surface area CNTs) and capacitance (mass CNTs) versus electrodes with different CNT lengths (including electrode from area investigation for comparison). Conditions: 0.1 M Na-Cit, pH 4.5, 10 mV s^{-1}, O_2 saturated solution, flow rate: 40 cm^3 min^{-1}, Laccase: 1 µL (10 mg ml^{-1}) to each electrode, electrode batch: CVD 3 (and CVD 1).

4.6.3 Effect of Laccase Loading and Thin-Layer Behaviour

The previous sections have highlighted that laccase current response is limited by substrate diffusion rather than the loading of enzyme, since the current magnitude was shown to scale with electrode area and nanotube length, despite lower loadings in each case. Therefore, it can be said that the electrodes are in effect saturated with laccase, where the high catalytic activity of the enzyme dominates the electrode response.

Since the amount of electroactive laccase required to reach the rate-limiting current was unknown, it was necessary to determine this loading by lowering the laccase concentration on the electrode surface. The concentrated laccase solution (440 μM) was diluted to a final concentration of 1.59 μM over a series of dilution steps. It must be noted that solutions were only diluted when required in order to avoid activity and stability losses. All solutions were stored on ice prior to adsorbing on the electrode surface. Electrodes from the same nanotube growth batch (CVD 1) and with increasing geometric areas (0.01 – 0.16 cm^2) were investigated. This was to check if the current scaled with both loading and area, which would be in agreement with earlier hypotheses.

Laccase voltammetry was started upon addition of 1 μL of diluted laccase to the electrode surface and measurements were recorded in O_2 saturated solutions. The enzyme loading concentration was increased by 1.33 fold for the first six steps and 2 fold thereafter. Figure 76 details the maximum currents (taken at 0.4 V) measured for each electrode area at each loading. It can be seen that the current increases with electrode area and coverage, as demonstrated in previous results. It must be emphasised that maximum currents (not peak currents) were taken, since the smallest electrode (0.01 cm^2) did not reach a rate-limiting current value within the potential window due to lower loading, and the rate limiting currents changed at high loadings, as will be explained later. The electrode measuring 0.09 cm^2 in area was the only discrepancy to this behaviour. Reasons for this behaviour are believed to be low O_2 diffusion into the electrode as a result of a thicker than usual epoxy covering around the electrode edges. Using the results in Figure 76, the maximum coverage required on each electrode area was calculated. This

calculation assumed that all the laccase added to the electrode surface was catalytically active, which could be plausible given the constant current response and modest adsorption behaviour shown on the majority of electrodes.

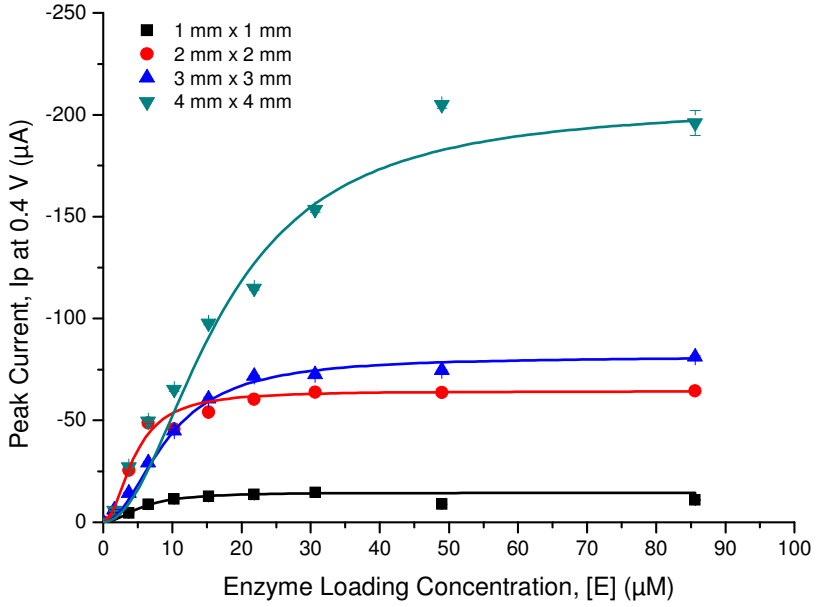

Figure 76: Effect of Enzyme loading on aCNT area. Conditions: 0.1 M, pH 4.5, O_2 saturate solution, flow rate: 40 cm^3 min^{-1}, Electrodes (CVD 1), (note: curves fitted using Hill function).

In Figure 76, it can also be noticed that the peak current started to decrease past the plateau in limiting-current. This adsorption behaviour was further investigated by taking the currents at each saturation point (plateaus in Figure 76) and comparing them to currents obtained from the effect of electrode area investigation. This provided an insight into whether the catalytic response is still maintained at higher loadings. It must be noted that the enzyme concentration in the area investigation was half since it was from a different batch; however, the total loading on the electrode was still past saturation. The results shown in Figure 77 clearly demonstrate that catalytic response is maintained at higher loadings since the peak current values observed are also identical. This catalytic stability may be maintained because the overall current is limited by substrate diffusion, thus at higher loadings more enzyme can be "lost" within the electrode without altering the current magnitude. This highlights a significant advantage of using high surface area 3D electrodes, although current responses are often worsened due to substrate-limitations, as has been demonstrated.

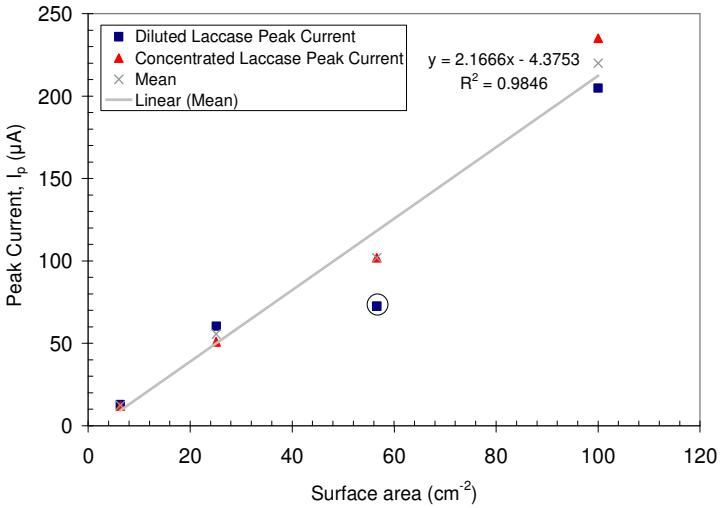

Figure 77: Peak current versus estimated electrode surface area (cm^{-2}), showing plots using concentrated laccase (area experiments) and diluted (loading experiments).

Further attention must be drawn to the catalytic behaviour which was observed during the cyclic voltammetry experiments. Figure 78 below displays the voltammograms measured for each electrode with increased loading.

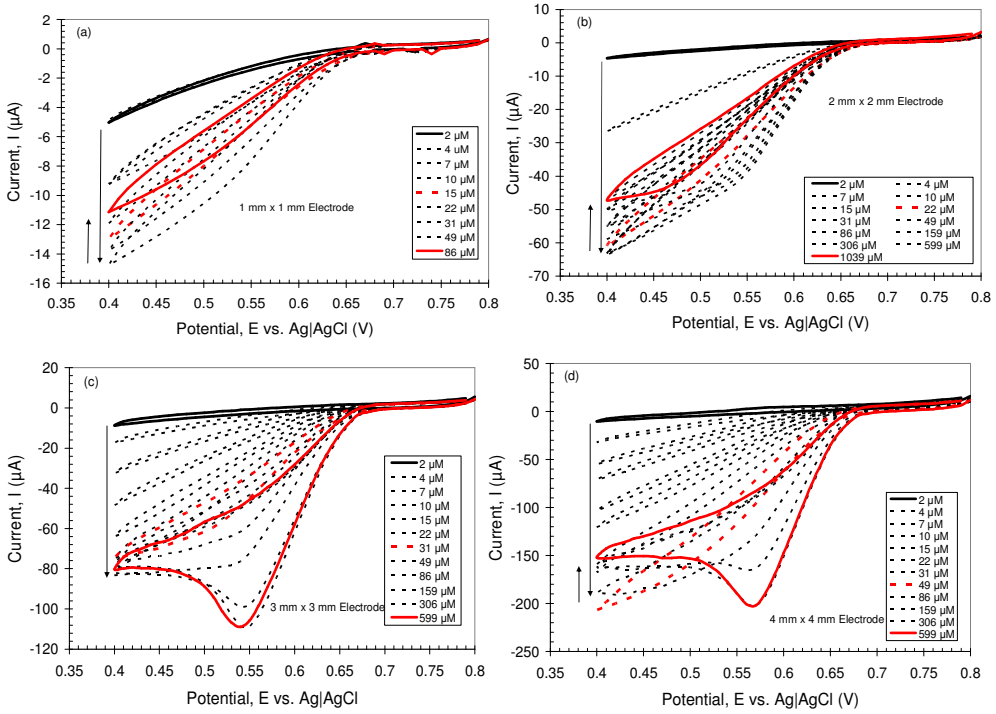

Figure 78: Cyclic voltammograms displaying CVs after each loading, where (a) 1 mm x 1mm, (b) 2 mm x 2 mm, (c) 3 mm x 3 mm (4) 4 mm x 4 mm.

Firstly, it can be noticed that the 1 mm x 1mm electrode in (a) demonstrates hysteresis commonly observed with electrodes experiencing semi-infinite linear diffusion, where the catalytic response is under diffusion control, as previously demonstrated when measuring laccase electrocatalytic response on HOPG in Figure 78 (b). The red dotted line in the figures represent the loading point where maximum current was reached, as shown in Figure 78 (i.e. where the curve plateaus) and the bold red line represents the current at maximum loading concentration. In all cases, the catalytic response at loading saturation (red dotted line) displays this hysteresis and a residual slope ((b) and (d)). This slope has been proposed to arise from enzyme molecules that are inhomogenously adsorbed at the electrode surface and are subject to slow electron transfer rates[259]. At higher loadings it can be noticed that a limiting current response is reached. This corresponds to the point where the enzyme cannot turnover any faster or substrate cannot be supplied fast enough to keep up with the high enzyme loading on the electrode. It is believed this behaviour was not observed in (a) because the loading of enzyme was not high enough (x 7-12 fold lower than maximums in (b-d)).

It is clearly evident in the CVs that the voltammetric waveform changes upon increasing the loading and electrode area. Concentrating on the potentials at maximum current (E_p) for each electrode, it can be observed that these shift toward higher potentials with electrode area and loading suggesting that electron transfer kinetics are improved as it approaches the equilibrium potential for O_2 reduction. Many reports in the literature involving the use of carbon nanotubes or porous materials have proposed that these thermodynamic shifts are enhancements in enzyme electron transfer kinetics[70, 260-263]. An alternative suggestion for this catalytic response is that it is purely a result of thin-layer cell behaviour due to the inherent porosity of the aCNT electrodes.

Thin-layer behaviour, described in section 3.1.6, occurs when the distance between the electrode pores is smaller than the diffusion layer, as such faster than expected depletion of analyte occurs. Figures (c) and (d) highlight this effect, where fast depletion of oxygen occurs at small overpotentials which is a characteristic behaviour of electrodes behaving under finite linear diffusion control. This behaviour occurs because of the longer diffusion path length to the

enzyme (from the edges) and higher electroactive coverages achieved on these electrodes, which when combined result in fast depletion of substrate. The attenuation in catalytic activity observed provides further evidence of this thin-layer behaviour since it represents the accumulation of reduced species (H_2O product) which cannot be removed from the electrode pores fast enough.

4.7 Conclusion

In summary, the aim of the work presented in this chapter was to develop a novel BFC half cell comprising of vertically aligned carbon nanotubes in contact with the fungal enzyme, *Trametes versicolor* laccase. Initial studies focussed on the purification of laccase in order to produce a highly purified and concentrated extract. This was achieved by using column chromatography in collaboration with Dr. Blanford at the University of Oxford. Kinetic and electrochemical studies revealed that the extract was of superior purity and displayed consistent catalytic activity when immobilised on nanotube electrodes.

In order to evaluate the performance of the aCNT electrodes comparisons were made to other potential carbon electrode materials. Results showed that the high surface area of the nanotubes significantly increased the loading of enzyme resulting in considerably higher current outputs.

Preliminary investigations were carried out on the aCNT electrodes to determine the enzyme adsorption profile. This was achieved using fluorescently-tagged enzyme which highlighted that most of the enzyme was situated towards the bottom of the array. This observation was attributed to the high capillary forces and ‘sponge-like’ behaviour of the porous electrodes. It is proposed that the location of the enzyme could negatively affect the electrocatalytic properties due to longer diffusion pathlengths.

Electrode performance was investigated by measuring the current response as a function of electrode area (geometric area) and nanotube length. In both cases, the current scaled linearly with area and length despite lower loadings, however, the current did not scale with surface area since low current densities were standard

across all electrodes. This behaviour indicated that catalytic activity was limited by substrate diffusion rather than loading of enzyme, since more enzyme molecules were electroactive over larger areas and lengths but turnover rates were substrate limited.

Since current was found to be limiting it was necessary to investigate the loading of enzyme on the electrode surface. The enzyme stock solution was highly diluted and the loading increased until currents were limited by substrate diffusion. Remarkably, catalytic activity was measured at very low concentrations (0.11 μM) and steadily increased with each increase in loading. This behaviour suggested good communication at the enzyme-nanotube interface and high catalytic activity. Examination of the voltammograms taken at higher enzyme loadings and geometric areas suggested improvements in enzyme kinetic behaviour due to the presence of waveforms which sharply descended (high turnover) and shifted to higher potentials. An alternative suggestion for this catalytic response is based on thin-layer cell behaviour, where the porous electrode contributes to slower diffusion and faster depletion of reactants at increased areas and loadings.

5 Laccase Electrocatalytic Response on Functionalised CNT Surfaces

5.1 Introduction to CNT Functionalisation and Enzyme Electrochemistry on Functionalised Surfaces

In the previous chapter, promising electrochemical properties were observed for the aCNT-enzyme electrodes. It was found that the high surface area of the nanotubes and the increased electroactivity of the enzymes were the most influential factors for the performance. Research has suggested that the structure, activity and stability of directly adsorbed proteins are influenced strongly by both the surface chemistry and curvature of the electrode[264]. Therefore, further improvements in the performance of the aCNT electrodes can be achieved through understanding and controlling the protein-nanomaterial interface.

The first part of this Chapter focuses on the functionalisation of the surface of the carbon nanotubes using simple gas phase chemistry and the resultant physical properties. Chemical functionalisation can have the combined effect of purifying the CNTs, in some cases improving the crystalline quality, and improving the electrochemical properties (depending on the treatment method). Purification is beneficial since residual metal particles interfere with the electrochemical performance in fuel cells, sensors etc. Ironically, the electrochemical performance is also improved through adding defect sites which may act as centres for electron transfer, changing the wettability of the electrode by the electrolyte and introducing electrochemically active surface groups[88, 93, 100, 106] .

The most destructive functionalisation methods often involve acid oxidation, whereby nanotubes (typically CVD grown tubes due to their high defect density) are often destroyed. Although many publications have reported high nanotube purities and removal of catalyst particles,[127, 128] these routes are not ideal for use since the purification times are often long, yields low and the iron content poorly determined. Gas-phase treatments can also be destructive at high temperatures and long exposure times. However, the combination of a shorter oxidative treatment, followed by annealing at graphitisation temperatures (1600-3000 °C) has recently

been demonstrated to be the most effective technique of removing amorphous carbon and catalyst impurities, while also improving the structural quality of the nanotubes[100]. Another advantage of this approach is that nanotube alignment can be preserved during functionalisation, which is required in this thesis. Therefore, a gas phase process is developed in this Chapter where oxygen groups are introduced by gas oxidation at moderate temperatures. These groups could then be exchanged to hydrophobic groups by subsequent annealing in hydrogen. The structure and architectures of the resultant nanotubes as a function of treatment temperature was studied by Raman spectroscopy, SEM and TEM.

An electrode's wettability can also be enhanced through functionalisation, whereby not only surface chemistry plays a part, but also the purification effect can assist in increasing the porosity of an electrode's structure. This approach was recently demonstrated by Li *et al.* when oxidising aCNT arrays at 450 °C for 10 hours[98]. The capacitive current doubled due to the increased density of oxygen containing groups. The heat treatment also produced a more porous electrode, as evidenced by the collapse of the treated nanotube films when removed from electrolyte solution and dried. Therefore, the wettability of treated mats in this thesis were assessed using contact angle measurements.

Finally, enzymes are considered to interact favourably at functionalised nanotube ends and electron transfer rates are usually higher between the enzymes and the functionalised sites[2]. *Trametes versicolor*, Laccase, has a unique ability in directly attaching onto carbon nanotubes through π-π stacking interactions using its large hydrophobic active site. Therefore, it is believed that the small size and high aspect ratio of the functionalised nanotubes will enable them to act as a molecular "wires" probing the enzyme's hydrophobic active site resulting in higher electron transfer rates and improved stability. The effects of the functional groups were thus studied on the stability and efficiency of the treated aCNT-laccase electrodes. In particular, studies were conducted to establish whether increased hydrophobicity to enhance general protein adsorption, non-treatment to maximise the π-π stacking or increased hydrophilicity to improve electrode wetting dominated the electrode's performance.

5.2 Results

5.2.1 Physical Properties of Short aCNT-arrays (2 hour Grown)

5.2.1.1 Contact Angle Measurements of as-grown aCNT arrays

Two batches of aCNT arrays were grown on silica wafers (1 cm x 1 cm) for a total of 2hrs using the CVD growth method, and thus assumed to be structurally and chemically identical. Static contact angle measurements of the as-grown aCNT surface were obtained from goniometric measurements, using a water droplet volume of 20 µL. Surfaces with a water contact angle > 90 ° are classed as hydrophobic, while surfaces with angles < 90 ° are classed as hydrophilic. An often unnoticed feature of aCNTs is their collapse and compression upon water contact which results in a diminishing contact angle over time[265-267] (Figure 79 (a)). Therefore, the contact angles were measured over a 5 minute period and the average angle was taken over this time (Figure 79 (b)).

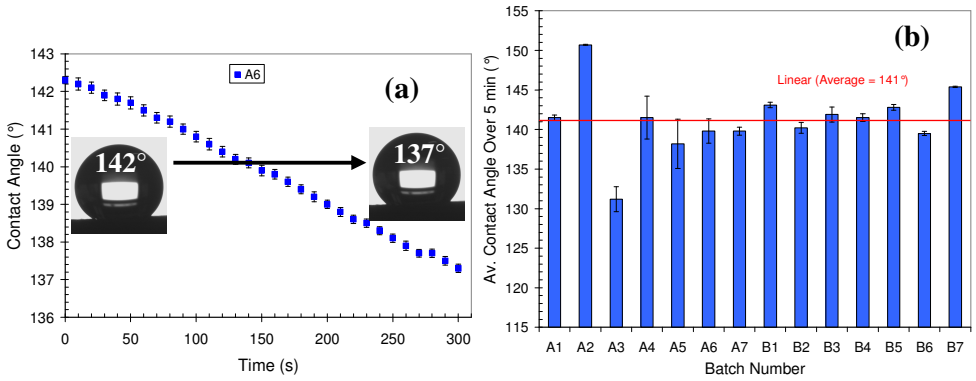

Figure 79: (a) Contact angle of water on an aCNT array over time. (b) Average contact angle over five minute period on 14 electrodes, with and A and B referring to the batch they were grown in. The error bars denote the standard deviation in the contact angle over the five minute measurement period.

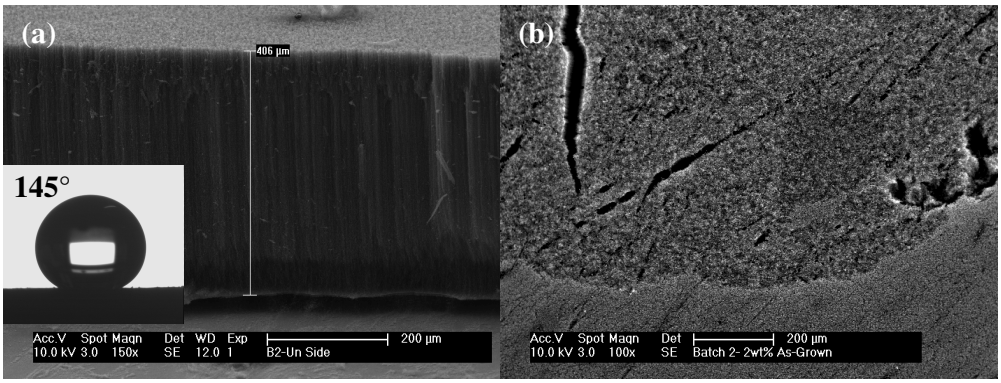

Figure 80: SEM images of aCNTs arrays from batch 2, where (a) cross-sectional image showing height of film ~400 µm with contact angle measurement (145 °) (inlet) and (b) aCNT surface after contact angle measurement and removal of water droplet illustrating surface cracking due to hydration adhesion and collapse of nanotube tips.

As stated above, recent reports investigating the wetting behaviour of aCNT films have reported a loss in droplet height and reduction in contact angle due to the collapse and compression of the aCNTs[265-267]. This behaviour has recently been explained in terms of the transition between two wetting states[265]; the Cassie state[233] and the Wenzel state[232] (see section 3.2.7). In the results shown, this transition was not observed and the samples showed minimal losses in contact angle. It is believed that aspects such as the height, density of the CNTs and also droplet volume are responsible for this behaviour, where previous reports used arrays measuring ~100 µm and droplet volumes of 40 µL. In our case, the longer and more densely packed arrays provided good strength and high surface roughness, thus preventing the collapse of the aCNT array. Figure 80 (b) shows an SEM image of the top surface of the aCNT array where a small step in the surface can be observed which is believed to be due to the collapse of the CNT tips. This behaviour explains the small reductions in contact angle over time but also illustrates the high stability of the nanotube structure. The small surface cracks displayed are believed to be a consequence of adhesion of the CNTs upon drying. Using the images in (b) and the contact angle measurement (inset, (a)), the water droplet appeared to sit on top of the aCNT array and therefore the Cassie-Baxter model can be used to describe its wetting behaviour:

$$\cos\theta_{CB} = f(\cos\theta + 1) - 1 \qquad \textbf{Equation 57}$$

Using the equation the theoretical calculation of 139° was in good agreement with the measured average contact angle of 141 °.

5.2.1.2 Thermal Treatment

The aCNT arrays were oxidised by placing them in a furnace at a fixed temperature for 10 minutes in air. In order to establish the onset temperature for oxidation to occur, the contact angle of the treated arrays was measured as a function of heat treatment temperature. This critical temperature was 350 ºC, either side of which the wetting properties were shown to drastically change from uniformly hydrophobic (< 350 ºC) to hydrophilic (> 350 ºC) (Figure 81). Based upon the work of Tran *et al.* carboxyl, hydroxyl and ketone groups are believed to be introduced onto the surface and tips of the nanotubes[130].

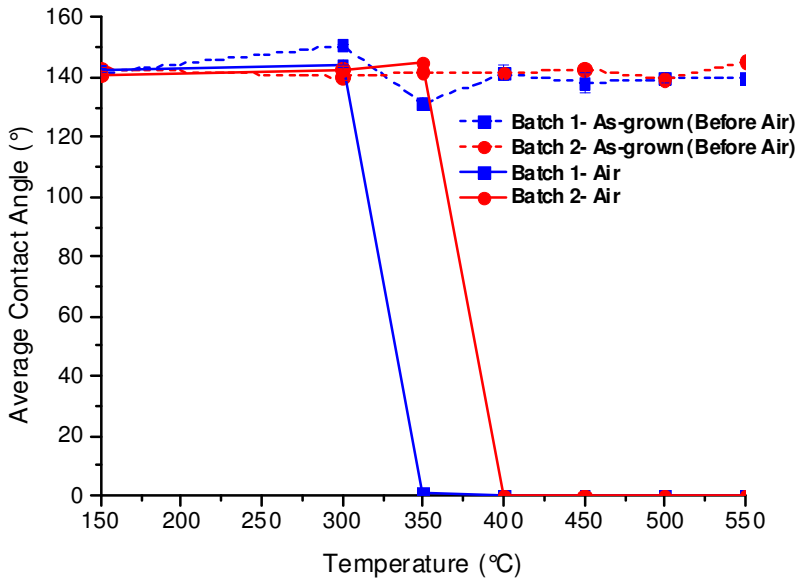

Figure 81: Thermal oxidation profile showing the effect of the contact angle on heating temperature in air (note: lines are guide to eye).

In order to reduce the CNTs so that the defects were terminated with hydrogen rather than oxygen containing groups, the oxidised aCNT arrays were heated at 650 ºC for 10 minutes in 600 ml/min of pure hydrogen. These reduced nanotubes would lose their hydrophilic capillary effect but would still have a similar degree of cleaned surface with defective sites as the original oxidised nanotubes.

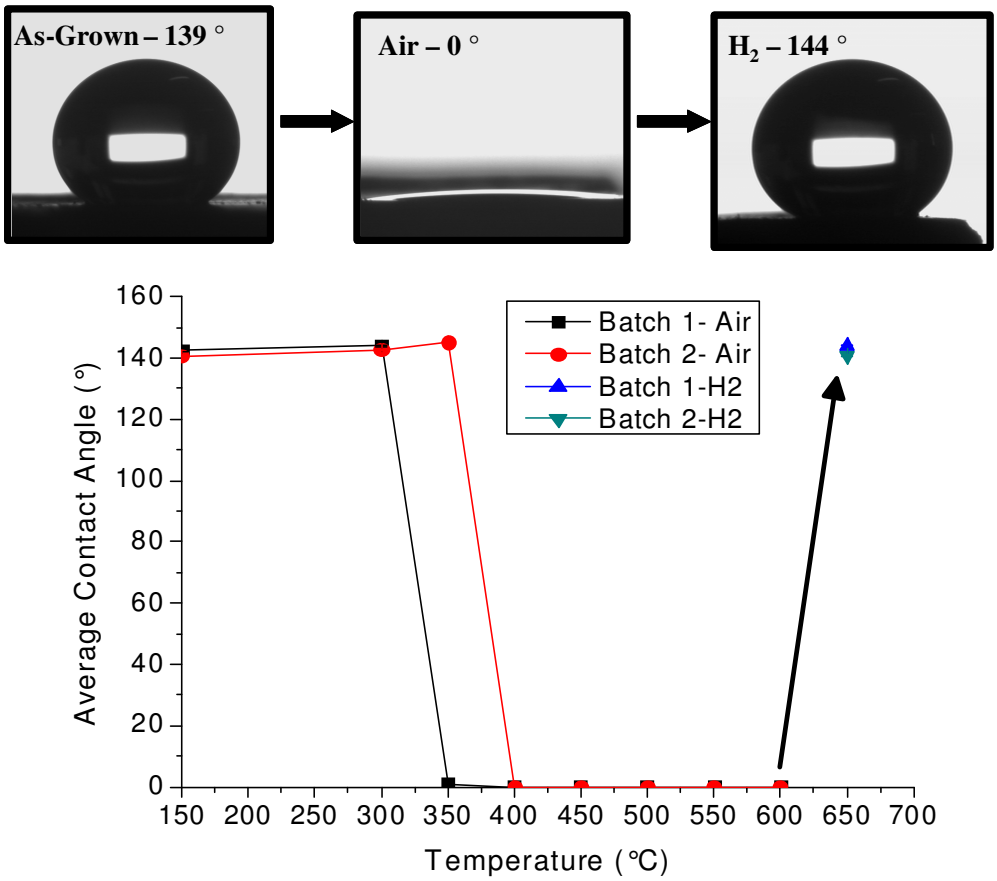

Figure 82: Effect of thermal gas treatment on the contact angle of aCNT mats. CNT surface chemistry switched from hydrophobic to hydrophilic when heated in air at ⩾ 350 ° C. Subsequent high temperature annealing of these samples in pure hydrogen at 650 ° C reversed the CNT surface chemistry back to hydrophobic (note: lines are guide to eye). Conditions: see experimental methods.

Figure 82 shows the results of the treatments on the contact angles measured over a five minute period. The two batches of aCNTs grown under the same conditions were measured with a water droplet (20 µl volume) positioned at three set positions. It can be noticed that the hydrogen treatment effectively switched the electrode surface back to hydrophobic which is believed to be the effect of hydrogen molecules reacting with the oxygen free radicals present on the nanotube surface. The removal of oxygen species leaves vacant sites, which excess hydrogen molecules can occupy, uniformly increasing the hydrophobicity across the nanotube surface. Both batches achieved comparable results with the hydrogen treatment increasing the hydrophobicity of the nanotube surfaces beyond the as-grown state. This increase in hydrophobicity suggests that there is a greater amount of C-H bonds on the nanotube surface.

In order to further understand these surface chemistry changes upon oxidative and reductive treatments, detailed analysis of these samples was subsequently carried out using various physical characterisation techniques. This will be discussed in the following section.

5.2.2 Physical Characterisation

5.2.2.1 SEM Analysis

SEM analysis was used to investigate changes in structural morphology upon treatment. Taking into account the average height of the arrays (500 μm), no significant loss (i.e. > 100 μm) was observed upon treatment (see Figure 83). More accurate measurements were later carried out by treating the same aCNT array, where once again no loss in height was revealed, as discussed later.

The surface of the arrays had a high surface roughness which has shown to influence the contact angle of the droplet. A thin contrast layer around 15 μm (circled and presented in (b)) was also discovered on the surface of all arrays as a result of charging from the electron beam.

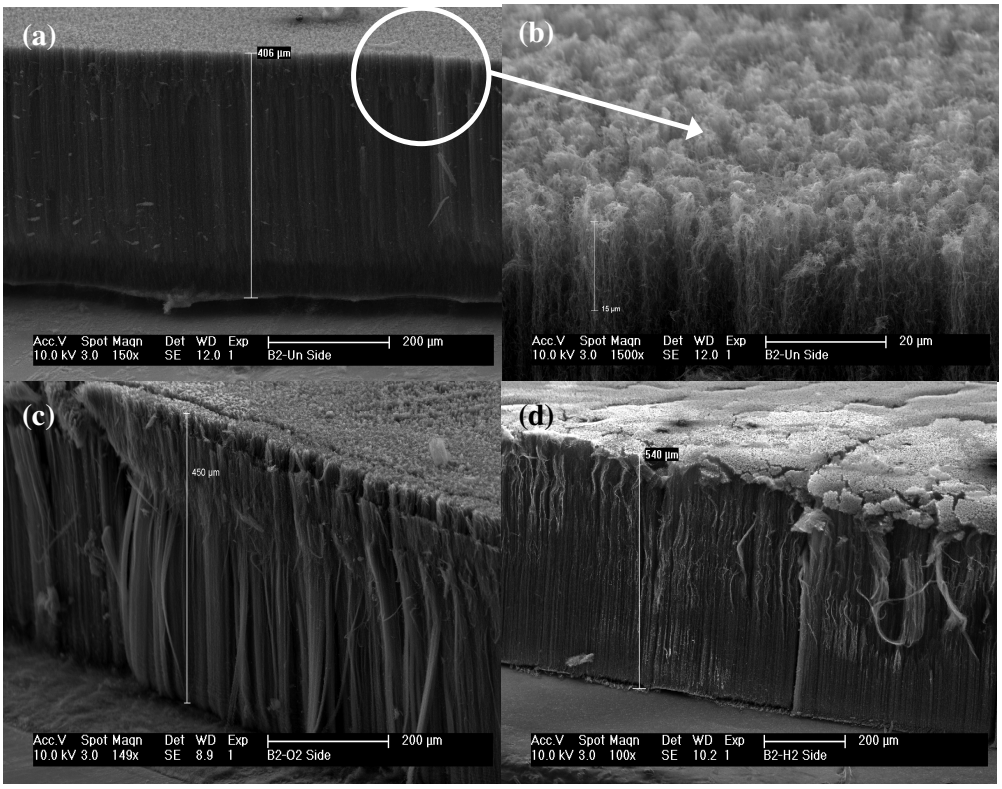

Figure 83: Cross-sectional SEM images of aCNT arrays, where (a) Untreated, (b) Top surface of (a), (c) Oxidised and (d) Oxidised and then Hydrogen treated. Each array shown was grown for 2 hrs.

Further investigation of this surface layer revealed an irregular entanglement of tubes for all samples, as shown in Figure 84 (a-c). The untreated and oxidised surfaces (a and b) contained thick irregular tubes (~100-120 nm diameter), while the oxidised and hydrogen treated surface (c) displayed thinner uniform nanotubes (~60 nm) with charged particles (circled, ~10-100 nm) situated on the tips and surface of the nanotubes (note: charging and contrast effect could mean the diameters were overestimated). This difference in appearance suggested the presence of an impurity coating (amorphous or graphitic carbon) on the untreated and oxidised nanotubes which was subsequently removed upon high temperature treatment in hydrogen revealing the charged catalyst particles.

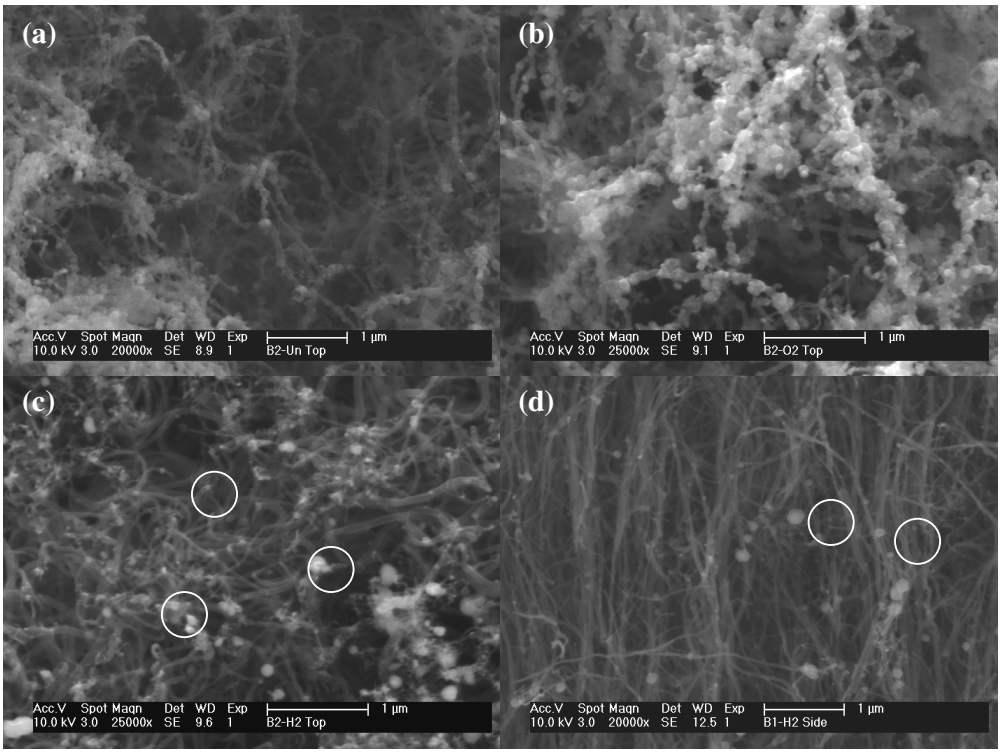

Figure 84: SEM images of the top surface of the aCNT arrays, where (a) untreated, (b) oxidised and (c) oxidised and hydrogen. While (d) side surface image of (c). Circled regions highlighting some of the iron particles exposed after hydrogen treatment.

Despite optimised growth conditions, this entangled layer has shown to be a common feature of aCNT growth[268, 269]. There is strong evidence that suggests this layer is grown on pure iron (Fe^0) catalyst particles[269]. Given that these published results were consistent with the observations above, it is believed that this layer formed due to Fe^0 from the ferrocene not interacting with the SiO_2 layer and thus the loose particles formed the seeds for tip growth and hence the thick entangled layer. Many authors claim that iron oxide (FeO) is the more active catalyst when it interacts with an oxide layer (SiO_2 or Al_2O_3)[270-272]. Recent work demonstrated that oxidised catalytic particles promote faster CNT growth without the harmful impurities[270], which may well explain the recent phenomenon of high purity ultra-long CNTs (> 1 mm) achieved with the addition of water[273] (i.e. a weak oxidiser). Future investigation into the effect of catalyst oxidation on CNT growth rate and purity would be important for the development of aCNT electrodes.

Unfortunately, without prior knowledge of the different catalytic activities, impurities such as these carbon contaminants and residual iron catalyst were inevitable during the CVD growth of MWNTs. Carbon contaminants often consist of disordered carbon or graphite nanoparticles, both of which are oxidised at lower temperatures (~ 400 °C)[274] due to their structural nature and higher surface to volume ratio. Furthermore, catalyst particles are often encapsulated within these carbon contaminants and as such, known to influence the oxidation behaviour of carbon materials because of their catalytic activity[66]. This was demonstrated when the aCNT array was completely incinerated at oxidation temperatures ≥ 600 °C, highlighting the narrow window that exists between selective oxidation of impurities and complete oxidation of the sample. High purity MWNTs have been reported to combust at temperatures around 780-790 °C[275].

The particles remaining on the CNT tips and walls (circled, (c)) are believed to be inactive Fe catalyst or iron carbide which subsequently participated in the graphitisation of amorphous carbon. These particles were also evident on the side surface of the array (circled (d)), suggesting carbon removal along the nanotube length where higher purity nanotubes were believed to be situated. Although, this could also have been a surface impurity effect and thus the interior of mat could have fewer impurities.

EDX analysis was subsequently carried out to confirm the elemental composition of the surface layer on each of the samples and support the conclusions drawn. The elements identified were carbon, iron and oxygen and the percentage weight of these elements were determined and compared between samples, as shown in Figure 85.

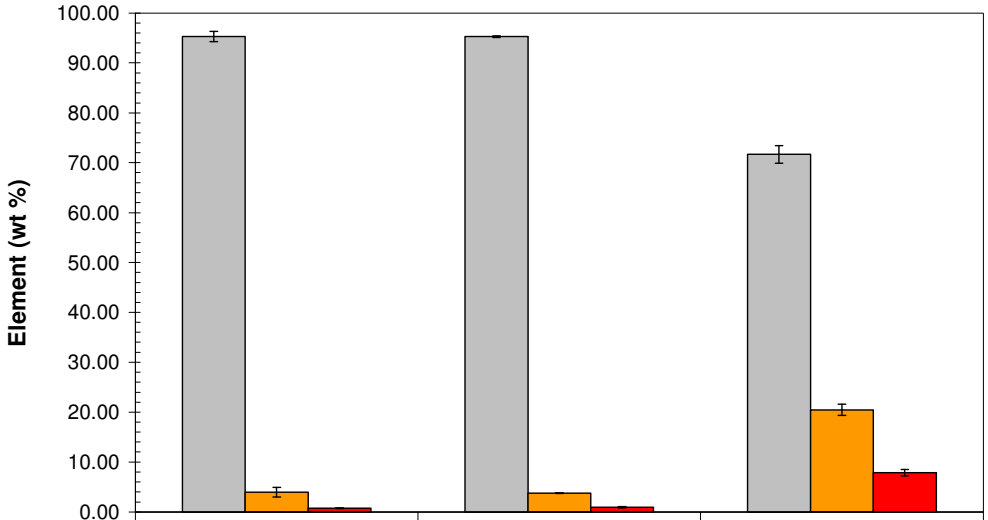

	Untreated	Oxidised	Hydrogen
Carbon	95.29	95.29	71.67
Iron	3.97	3.78	20.44
Oxygen	0.74	0.93	7.89

Figure 85: EDX-single point analysis of different treated samples (2hr), where weight percentage (wt%) of carbon, iron and oxygen was measured.

It is evident that the untreated and oxidised samples had almost identical carbon and iron compositions indicating no carbon decomposition and exposure of iron particles upon oxidation. However, only a small increase in oxygen was detected in the oxidised sample despite the surface chemistry change observed upon treatment. For the hydrogen treated sample, the carbon composition decreased by ~20 %, due to the oxidisation of carbon (Figure 84 (c and d)) which resulted in an increase in iron percentage content. Interestingly, the amount of oxygen detected also increased despite treatment in a reducing (i.e. oxygen free) atmosphere. This could be due to the non-deliberate oxidation of the exposed iron during cooling or after removal from the furnace when open to the air, which is often overlooked in the literature when evaluating the chemical state of the catalyst during CVD growth. Alternatively, it could suggest measurement inaccuracy since the ratio of iron:oxygen was similar (~3:1) in all samples. This assumption is reasonable since the iron and oxygen peaks overlap due to their similar peak energies, making the elements harder to resolve. On the other hand, the oxygen content could be directly linked to the amount of exposed iron detected (not CNTs functionalised). Further work would be necessary to confirm this using *in situ* XPS, which is a

more accurate technique for detecting surface groups and prevents the substrate from becoming exposed to the air.

5.2.2.2 TEM Analysis

TEM analysis was used to further confirm these structural changes upon treatment, as shown in Figures 86 (a-f). As expected, the surfaces of the untreated sample displayed an irregular coating, indicating the presence of an amorphous carbon layer. Approximately 70 % of the nanotubes measured had a coating with an average thickness of around 4 nm (maxima: 11 nm and minima: 1 nm), although in most cases the coating was not continuous along the length of the nanotubes measured. On the other hand, the majority of surfaces measured for the oxidised sample contained little or no amorphous carbon coating (c and d), despite SEM images and EDX analysis proving otherwise. However, as stated above, it is viable that regions away from the irregular surface layer are a lot cleaner than the top surface. Furthermore, it must be noted that all samples were pre-washed in ethanol by centrifugation prior to analysis and thus it is reasonable to suggest that some of this carbon could have been removed during this process. The dark particles in the oxidised sample represent iron catalyst impurities (av. diameter of ~3 nm). Finally, the hydrogen treated nanotubes were found to be very clean with little trace of carbon contaminants. Further evidence of iron catalyst removal with the high temperature treatment was the presence of pitted regions or holes previously occupied by the catalyst particles (circled, (e)). The volatility of iron nanoparticles has been measured to be significantly lower due to their high surface area-volume ratio, where 50 nm particles have been shown to combust at temperatures between 720 and 920 °C[276]. This suggests that diffusion or evaporation of the iron at 650 °C is practical for the 3 nm particles shown in the oxidised nanotubes.

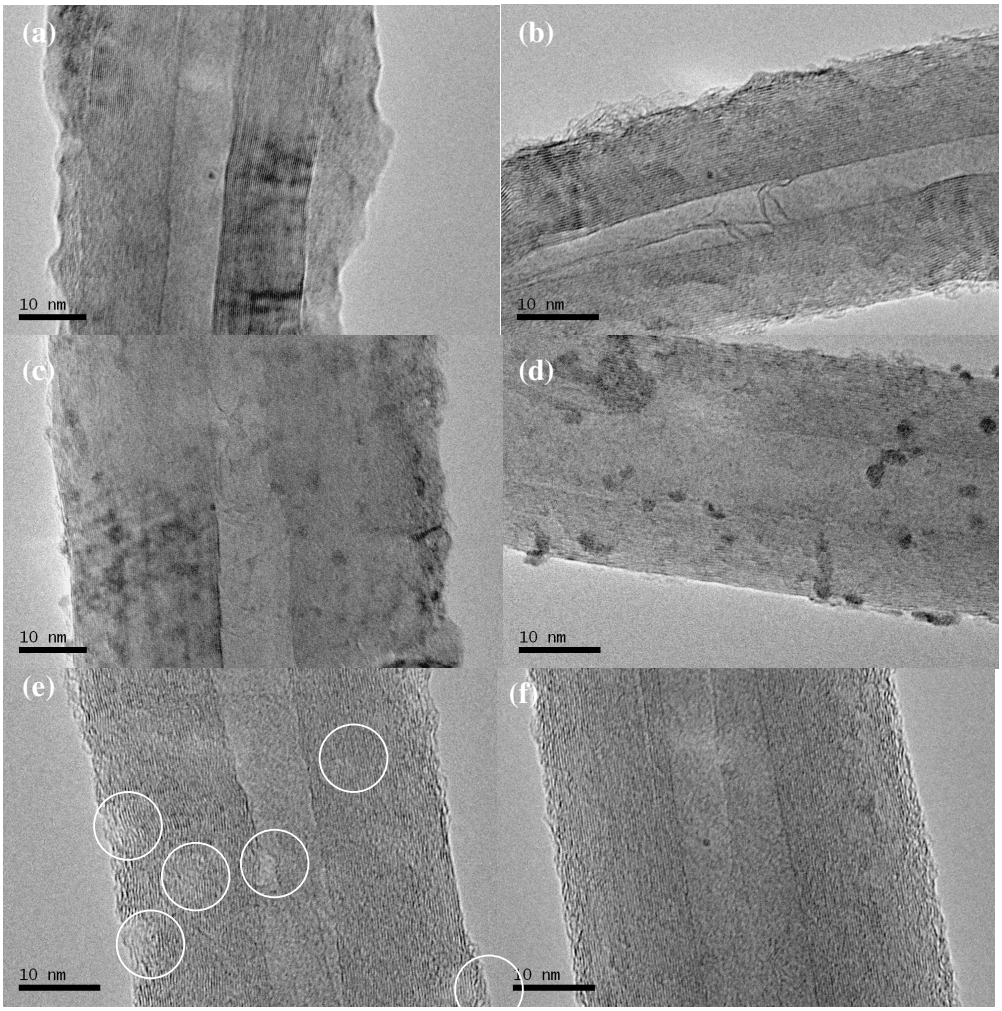

Figure 86: TEM images of 2 hr grown untreated (a and b), oxidised (c and d), hydrogen treated samples (e and f). The dark spots and regions in (a-d) are iron catalyst particles and the circles (e) illustrate holes (pitted regions) where iron particles may have been removed during high temperature hydrogen treatment.

5.2.2.3 Raman Spectroscopy

Finally, Raman spectroscopy was used to characterise the structures of the aCNT samples, where all the spectra shown are averaged measurements. Raman spectra of the top surface of each aCNT sample are shown in Figure 87. The two characteristic bands for carbon nanotubes are the D and G bands found at ~1330 cm^{-1} and ~1581 cm^{-1} respectively. The D band is attributed to disorder induced defects in the nanotube lattice and other carbon material, while the G band corresponds to the in-plane vibrations of the C-C bonds. Both the intensity and position of the D and G bands can be influenced by functionalisaton and therefore the analysis of both is crucial. The other peaks shown are the 2D peak which is an overtone of the D peak and therefore its frequency is exactly double at around 2660 cm^{-1}. The remaining low frequency RBM peak is a unique phonon mode attributed to the radial vibrations of C atoms in small diameter tubes, indicating the presence of SWNTs in all samples.

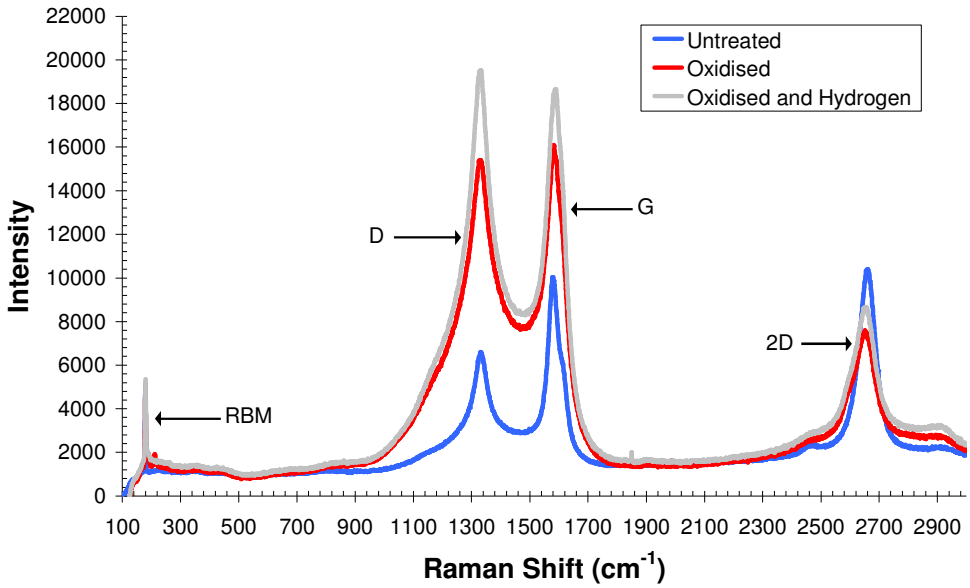

Figure 87: Raman Spectra of the top surface of each of the aCNT samples

Chemical modification of nanotubes such as oxidation and hydrogenation induces a strong D peak[277] as evidenced in the results shown in Figure 87. The oxidative treatment is believed to have been strongly oxidising towards the disordered carbon impurities, significantly increasing the amount of defects as it attacks and

expands regions of disorder (D peak). It is known that hydrogenation removes the carbon impurities thus it is hypothesised that the decrease in the G peak is attributed to removal of these impurities resulting in a small loss in crystallinity. The D peak still remains at high intensity because hydrogenation does not remove structural defects at 650 °C, instead higher 'graphitisation' temperatures (1600 - 3000 °C) and long treatments are required for improvements in crystallinity[93].

The intensity ratio of the D and G bands (I_D/I_G) can be used to estimate the disorder density (average crystal size) of the nanotube walls and thus sample purity. A low I_D/I_G relates to highly crystalline nanotubes and high I_D/I_G highly disordered nanotubes. As shown in Figure 88, the I_D/I_G ratios measured for the top surface were highest for the oxidised and hydrogen treated samples implying more defects were formed. The lowest I_D/I_G ratio was measured for the untreated sample, although fluctuations in the D-band intensity were observed in each measurement. This explains the larger error bar and suggested the influence of surface inhomogeneities as observed in the SEM images.

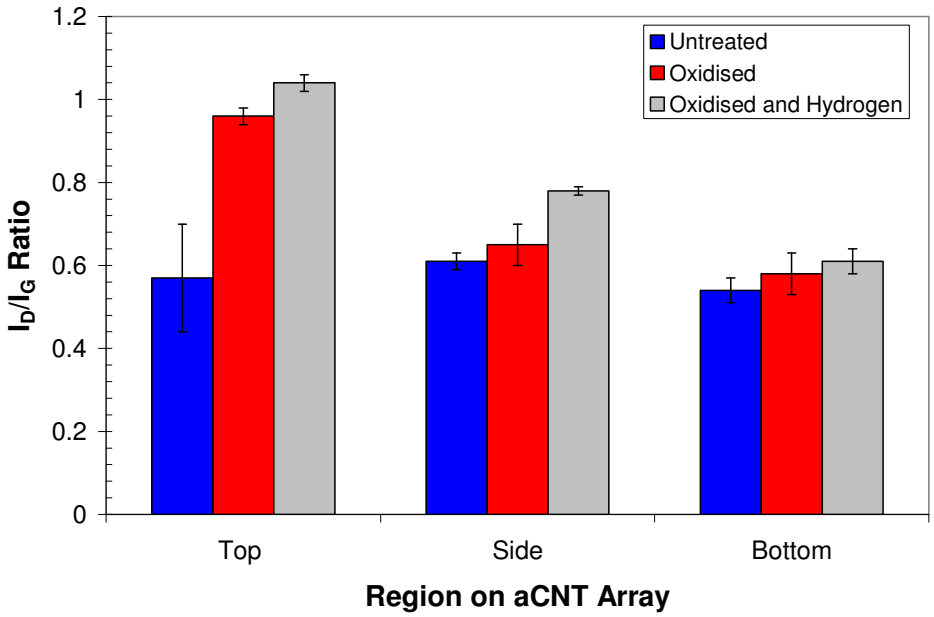

Figure 88: Comparison of ID/IG ratios of separate regions for each aCNT sample.

The G peak position is strongly influenced by functionalisation due to the strain induced on the structure and thus the resultant changes in mechanical and electrical bond strengths and physical bond distances. An upshift of the G peak

can be observed for low electron or hole doping and high hole doping[278], while a downshift is observed for high electron doping. In order to analyse the peak positions the spectra were fitted using the Lorentz function for lineshape[279], as given in the equation below and illustrated in Figure 89:

$$y = y_o + \frac{2A}{\pi}\frac{w}{4(x - x_c)^2 + w^2} \quad \textbf{Equation 58}$$

where y_o is the baseline for the x-y coordinates, x_c the peak centre, w the peak width and A the peak area.

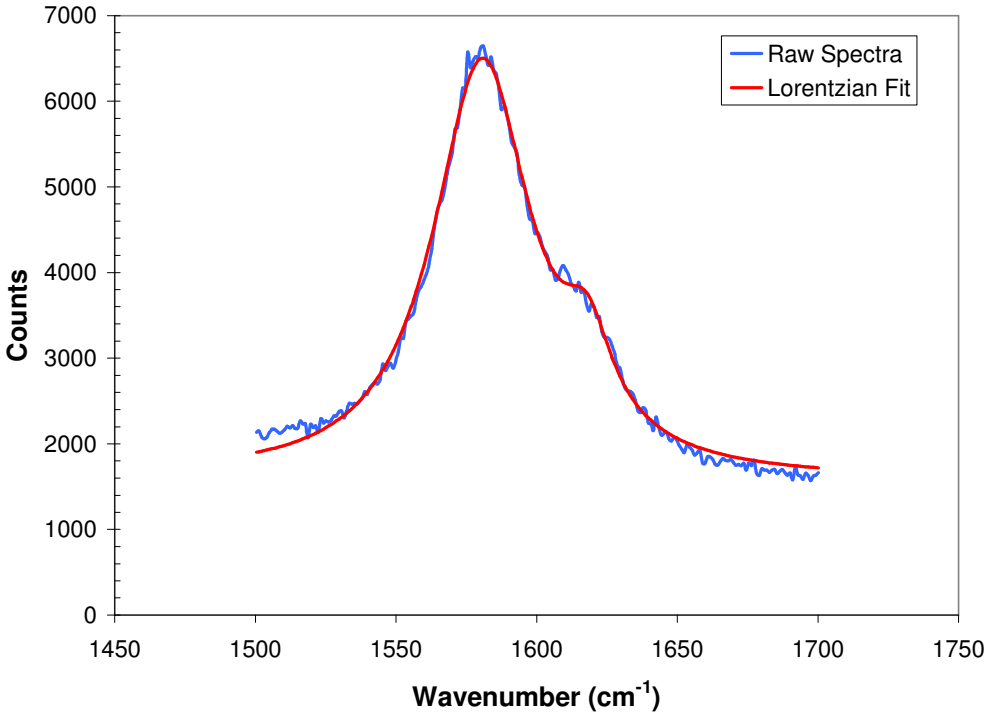

Figure 89: Example of a Lorentzian fit of two peaks to an experimental G peak with a defect induced 1610 cm^{-1} shoulder peak for an untreated aCNT sample.

The fitted G peak positions corresponding to the top surface of the different aCNT samples are shown in Table 5. All peak positions in the table are averaged for each sample and the errors associated were taken as the standard error of the mean. It can be noticed that the G band shifted to higher wavelengths in respect of the untreated sample upon oxygenation (~2 cm^{-1}). Although, it must be noted that the

associated error for the oxygenated sample was large and this was probably due in part to oxidation reactions occurring only at the most reactive sites, such as tube ends and impurity regions (i.e. regions of high defect concentration), resulting in selective functionalisation of the surface.

The hydrogenated samples presented the highest upshifts in the G band with a further increase after switching from the oxidised state (~3 cm^{-1}). The peak positions measured for the hydrogen treated sample were highly reproducible, indicating increased structural uniformity owed to the removal of the carbon contaminants, as evidenced in the SEM and TEM images.

	G Band		D Band		2D Band	
	Position (cm^{-1})	Error (cm^{-1})	Position (cm^{-1})	Error (cm^{-1})	Position (cm^{-1})	Error (cm^{-1})
Untreated	1582	0.4	1334	0.5	2661	1.33
Oxidised	1584	1.5	1328	0.8	2648	1.45
Hydrogen	1587	0.2	1328	0.5	2649	0.36

Table 5: Raman G, D, and 2D Band Positions for the measured top surface of untreated, oxidised and oxidised and hydrogen treated samples.

Furthermore, Table 5 shows the peak shifts induced for the second order D and 2D bands, where an opposite effect is observed and a downshift in peak position occurs. The oxidised samples had peak shifts of ~6 cm^{-1} and ~12 cm^{-1} in respect of the untreated sample for the D and 2D bands respectively. Interestingly, the hydrogenated sample showed no further shift in peak position, suggesting that no further defects were introduced by this treatment which is in agreement with earlier TEM analysis of the wall structure (Figure 86).

Analysis of the side surface revealed a constant D peak and a decreasing G peak intensity upon successive treatments. A lower G peak in the spectrum can be explained in terms of increased strain on the graphitic structure due to nanotube functionalisation and loss of some carbon contaminants. This is further confirmed by the reduction in 2D peak which is often found to decrease with doping and the lower intensity of the RBM mode, as a result of preferential removal of small diameter tubes. The constant D peak suggests that the nanotubes have fewer structural defects and so are less prone to oxidative attack and the lower I_D/I_G

ratios confirms that higher purity nanotubes are found underneath the disordered top surface (see Figure 90). The ratios followed the same trend as the top surface increasing with successive treatments due to changes in nanotube surface chemistry.

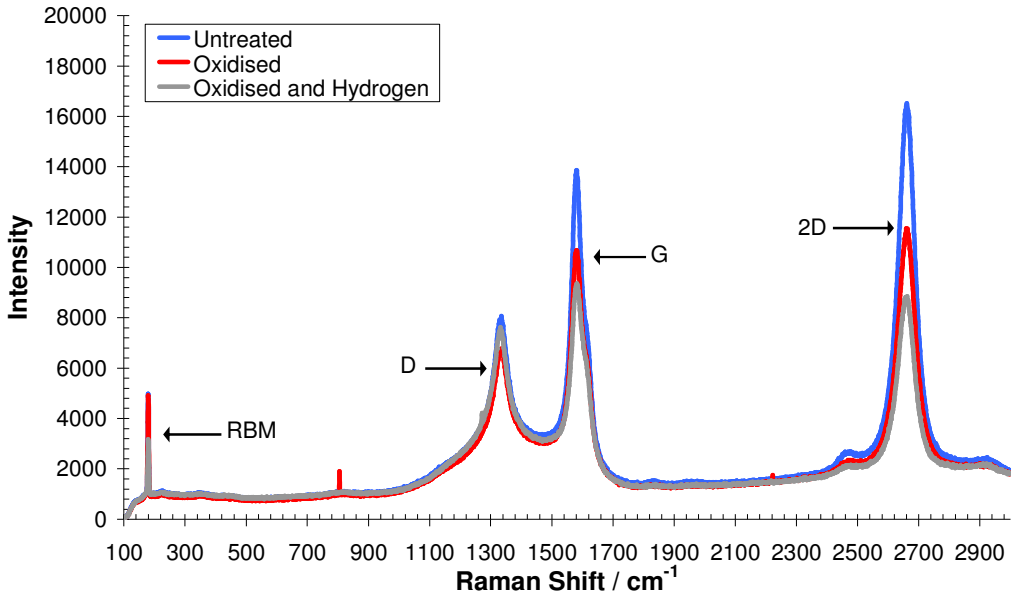

Figure 90: Raman spectra of the side surface of each of the aCNT samples.

In order to further confirm changes in nanotube functionalisation the peak positions were measured for all modes (G, D, and 2D), as shown in Table 6. The G peak position showed no upshift upon oxidation and remained fairly constant, possibly indicating a lower oxidative effect due to fewer reactive sites present on the nanotubes. The hydrogen treated sample displayed an upshift of ~3 cm^{-1}, matching the previous top surface measurements. Finally, the D and 2D bands remained constant suggesting the treatments were less destructive due to the higher purity nanotubes.

	G Band		D Band		2D Band	
	Position (cm^{-1})	Error (cm^{-1})	Position (cm^{-1})	Error (cm^{-1})	Position (cm^{-1})	Error (cm^{-1})
Untreated	1582	0.23	1334	0.23	2661	0.36
Oxidised	1581	0.41	1334	0.15	2660	0.51
Hydrogen	1585	0.37	1334	0.61	2659	0.00

Table 6: Raman G, D and 2D band positions for the measured side surface of untreated, oxidised and oxidised and hydrogen treated samples.

5.2.3 Physical Properties of Long aCNT-arrays (4 hour Grown)

Given that the samples characterised above were grown for a period of 2 hrs, it was necessary that 4hr grown samples were also characterised because these were used throughout the thesis as they were easier to handle for subsequent characterisation and electrochemical measurements. Therefore, a batch of long a-CNT were oxidised at 400 °C and subsequently reduced at 650 °C, as described above and again characterised by SEM, Raman spectroscopy and TEM.

5.2.3.1 SEM Analysis

In order to investigate for any changes in structural morphology with treatment, SEM images were taken of the same aCNT array in the as-grown (untreated), oxidised, and hydrogen treated states (see Figure 91). The height of the array showed no significant change with treatment and had an average height around 1 mm.

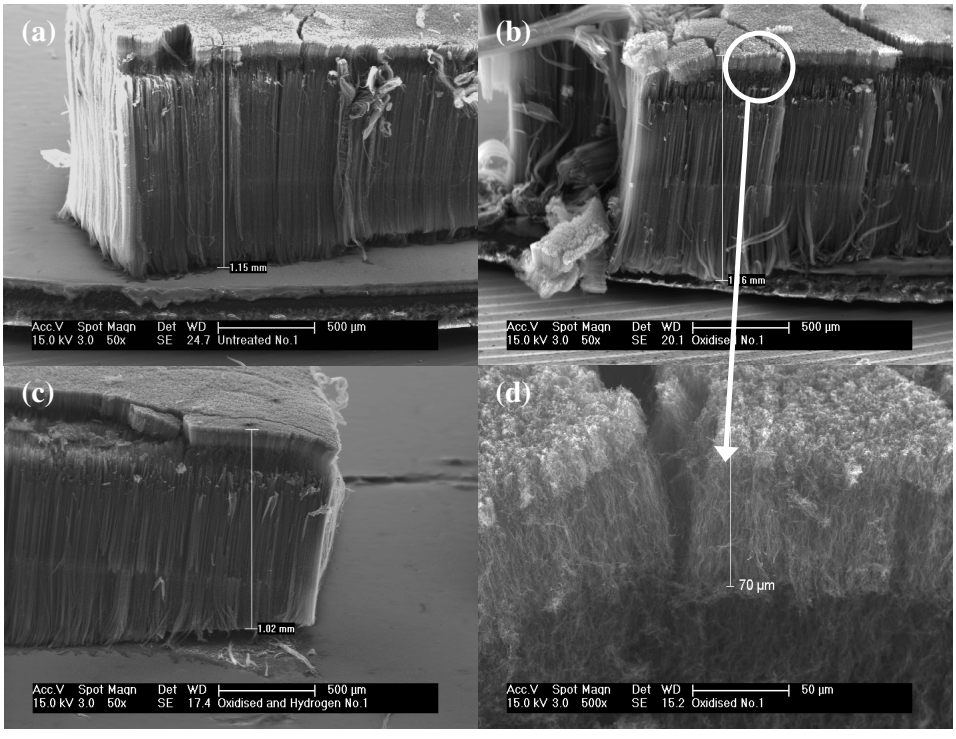

Figure 91: SEM images of (a) untreated, (b) oxidised (c) oxidised and hydrogen treated samples, (d) higher magnification of top surface of oxidised sample highlighting impurity layer.

Once again, the surface of the arrays had a contrast layer which was found to be visibly thicker than the 2 hour grown samples, ~70 μm (see (d)) suggesting a higher deposition of surface carbon contaminants with growth time.

EDX analysis was performed using mapping mode which provided a better representation of the surface chemistry effects upon treatment. Previous EDX analysis measured the elemental composition at single points on the nanotube, where peak spectra and compositional numbers were provided. In contrast, the mapping mode provides elemental distribution images of the nanotube surface within a fixed area (10.86 μm^2). However, this is a more qualitative technique. Figure 92 shows SEM images (a) of the different samples and the elemental distribution images for carbon, iron and oxygen ((b)-(d)) within the fixed imaged area.

Once again, SEM images of the top surface layer displayed an entanglement of nanotubes with irregular carbon contaminant coatings. However, in contrast to the 2 hour samples, the coatings appeared to remain after hydrogen treatment suggesting the presence of a coating with higher stability. The SEM images highlight denser regions of carbon contaminant which could explain the enhanced thermal stability.

Image analysis software was used to quantify the elements detected in terms of the total area fraction of colour displayed in the distribution images (see Figure 94). This allowed for better comparison between the samples, although more accurate quantitative analysis was later carried out using standard EDX analysis, as will be described shortly. The most notable aspects of Figure 93 are the significant increase in iron and oxygen detected in the oxidised sample compared to the untreated sample which suggests that more iron catalyst particles are exposed upon oxidation due to structural damage to the carbon coatings. Interestingly, the amount of oxygen detected was still significant after hydrogenation; the small decrease could suggest the influence of iron oxide impurities on the overall detection levels.

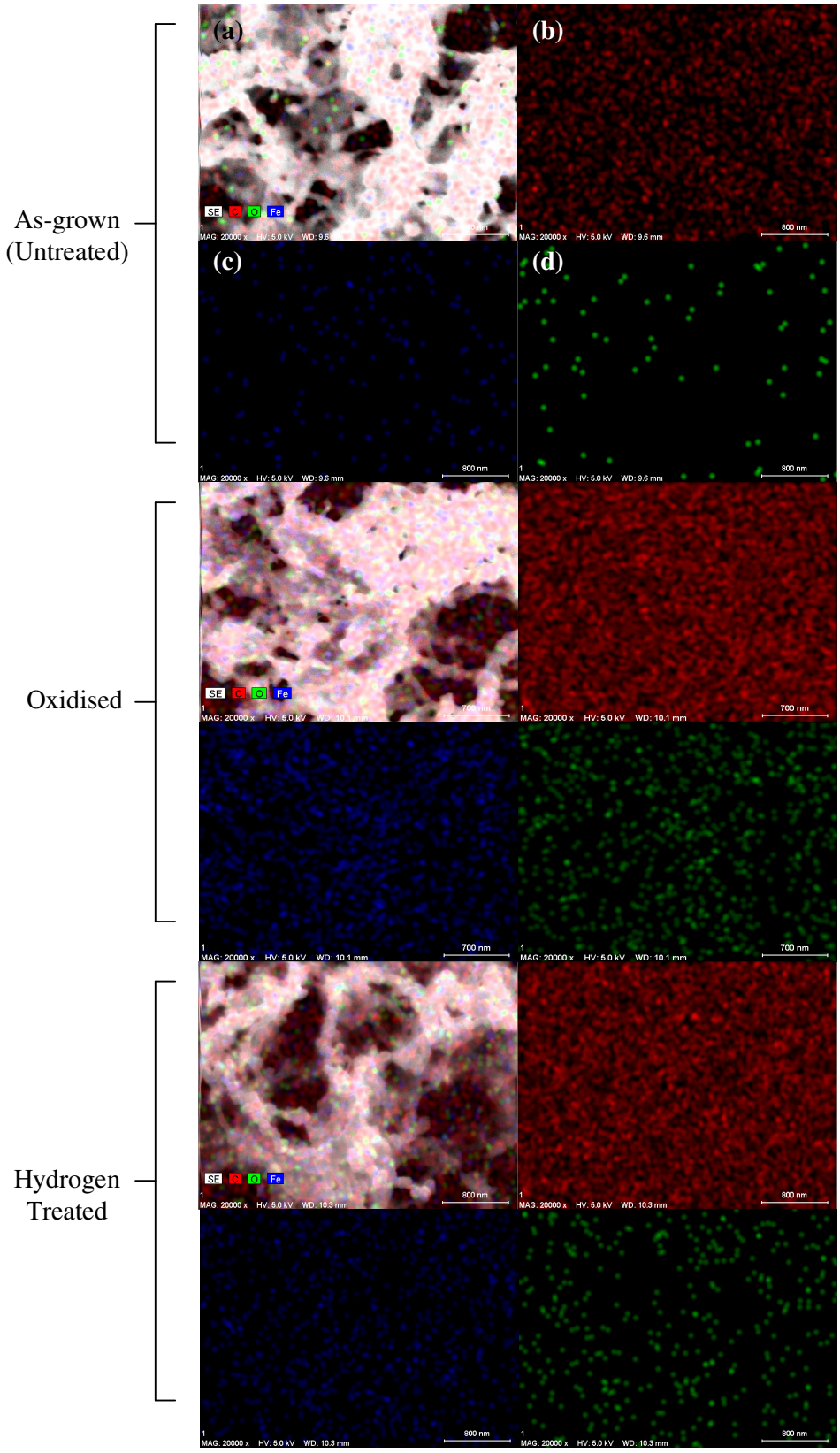

Figure 92: EDX Mapping of aCNT surfaces, red, blue, green = carbon, iron, oxygen.

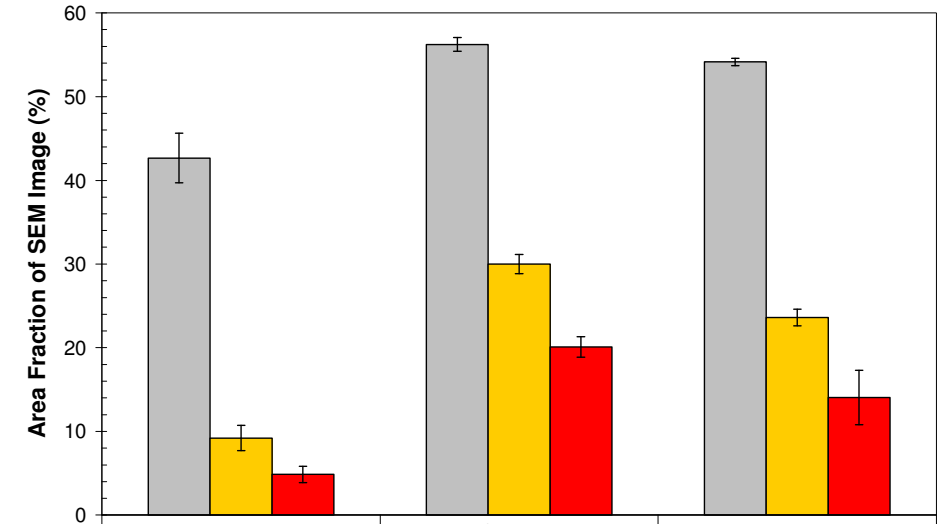

	Untreated	Oxidised	Hydrogen
Carbon	43	56	54
Iron	9	30	24
Oxygen	5	20	14

Figure 93: EDX-mapping analysis of the different treated samples. Bars represent total area fraction of elemental colour displayed in the mapping images shown in Figure 92.

Further EDX measurements of the top surface were performed using point analysis, as employed for the 2 hour grown samples. Ten single point measurements were taken per sample and the overall average of these measurements are presented in Figure 94. In agreement with the SEM images (Figure 92(a)), no differences in composition were observed between the four hour samples since no carbon contaminants were removed or iron particles exposed in the SEM images. In contrast to the 2 hour hydrogen treated sample, where a large decrease in carbon and increases in oxygen and iron contents were displayed (see Figure 85) due to purification of the surface, as illustrated in the SEM images (see Figure 84).

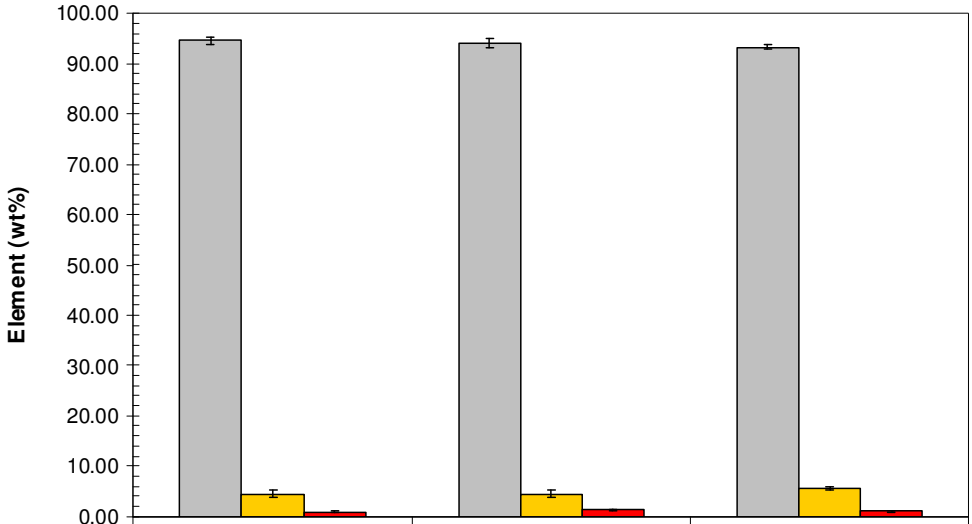

	Untreated	Oxidised	Hydrogen
Carbon	94.56	94.16	93.36
Iron	4.49	4.52	5.61
Oxygen	0.94	1.32	1.03

Figure 94: EDX-single point analysis of different treated samples, where element weight percentage (wt%) of carbon, iron and oxygen was measured.

Therefore, these results indicated that the contaminant surface layer in the four hour samples was more stable and thus it was necessary to investigate whether this impurity layer coated the underlying nanotubes by comparing the compositions through the entirety of the mat (i.e. top surface to bottom surface). The compositions are presented in Figure 95, where three measurements were taken per sample region (inset SEM image) and averaged. It must be noted that significantly more measurements would have been carried out if time limits were not placed on the microscope. Upon analysis of the results, it can be noticed that only regions 2 and 3 showed signs of purification upon oxidation and hydrogenation with decreases in carbon content and increases in iron and oxygen content. The most notable feature being the large increase in iron content for region 2 of the hydrogen treated sample, possibly indicating a thinner impurity coating below the top surface similar to the 2 hour samples. However, in some cases the amount of iron and oxygen detected in the untreated sample was higher than the oxidised and hydrogen treated samples, therefore more accurate elemental detection methods were required.

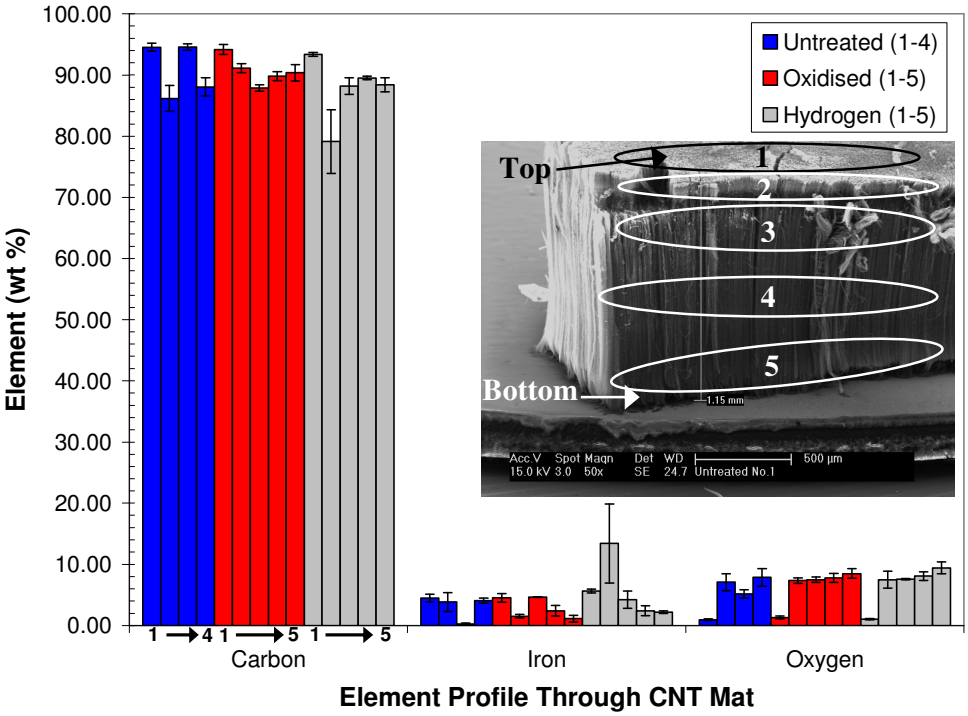

Figure 95: EDX analysis from top to bottom of untreated (blue), oxidised (red) and oxidised and hydrogen treated (grey) aCNT arrays. Numbers correspond to measurement regions, as shown in SEM image (inset).

5.2.3.2 TEM Analysis

Once again, TEM analysis was used to further confirm structural changes upon treatment, as shown in Figure 96. From the images, it is clear that the untreated nanotubes ((a) and (b)) have a contrasting appearance to the two hour samples with a thicker more uniform contaminant coating. The layered structure suggests this coating is disordered graphitic carbon and was found to vary in thickness across the samples analysed (1 -10 nm). Images of the oxidised samples revealed this graphitic layer to be less prevalent, where the coating had either almost disappeared (c) or been partially removed as shown by the loss in uniformity (d). However, the images appear to suggest that the layer is more difficult to remove due to its structured nature and thicker appearance. This is further highlighted in the images of the oxidised and hydrogen treated samples ((e) and (f)), where the layer is still coating the nanotubes and in some cases is very thick (~10 nm). These results are in agreement with those already described, since no changes in structural morphology were evidenced in the SEM images and no significant

variations in elemental detection were observed across the samples due to the presence of the stable graphitic layer coating the tubes.

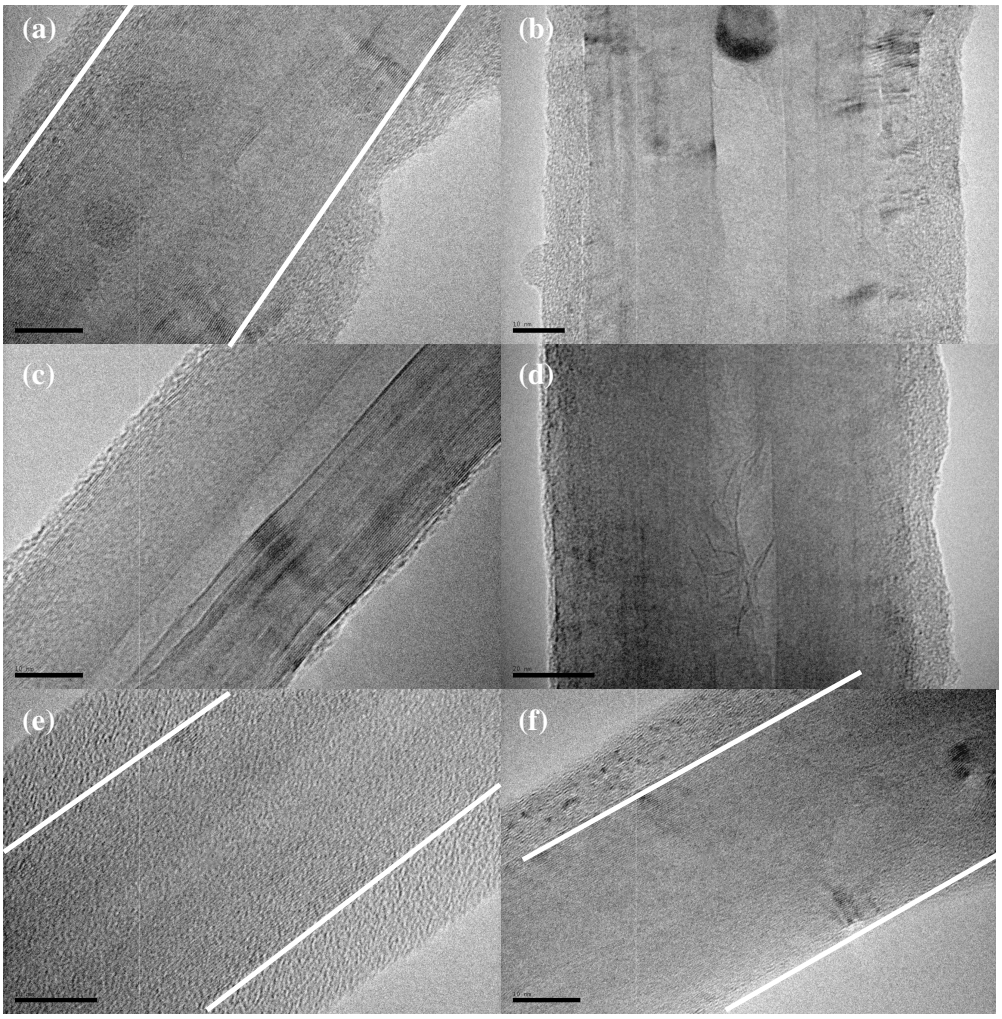

Figure 96: TEM images of 4 hour grown untreated (a and b) oxidised (c and d) and oxidised and hydrogen treated (e and f) samples. White lines are included to detail the outer walls of the nanotubes.

5.2.3.3 Raman Spectroscopy

Finally Raman spectroscopy was used to investigate the nanotube structure and surface chemistry effects by changes in the vibrational modes. Focussing on the I_D/I_G ratios, it can be noticed that no real variation was found between the samples upon treatment and all displayed high I_D/I_G ratios indicating poor sample purity (Figure 97). The high ratios were probably attributed to the thicker carbon contaminant layer, as described earlier. In fact, the ratios of the untreated samples had increased almost twofold in comparison to the two hour samples. The influence of carbon contaminants on D and G peak intensities is shown in Figure 98, where both peaks for the top surface were measured. The comparably high intensities of both peaks indicated that the majority of carbon measured is disordered material. Slightly lower ratios were found for the side surface, although no real trend was noticeable with treatments in all cases. The ratios either appeared to remain fairly constant when considering error bars, as shown in Figure 97.

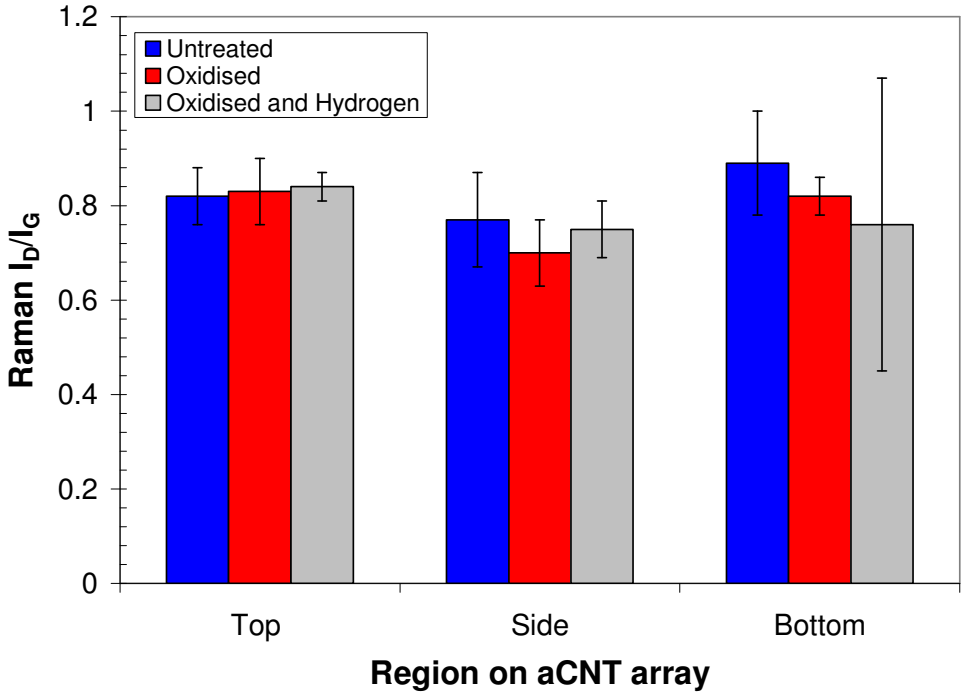

Figure 97: Comparison of ID/IG ratios of separate regions for each aCNT sample.

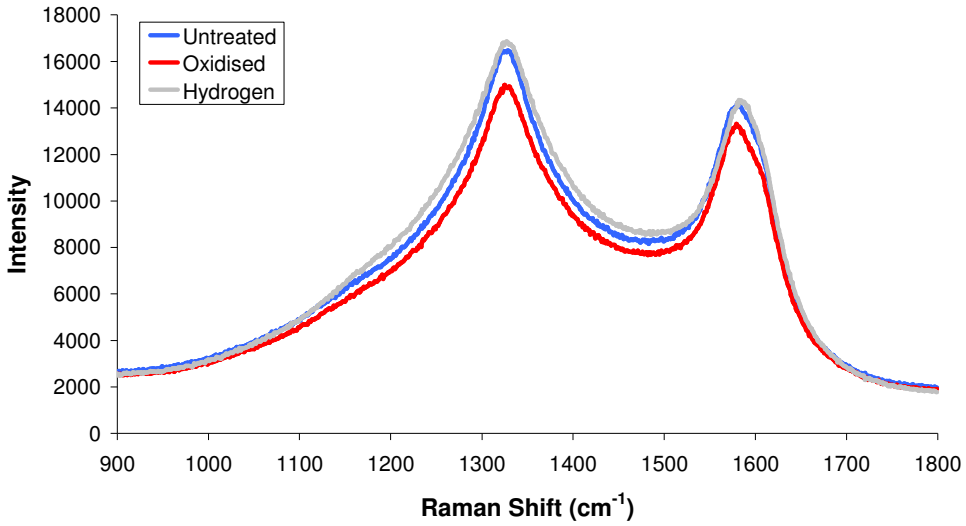

Figure 98: D and G bands of top surface for aCNT samples.

5.2.4 Electrochemical Characterisation of Long aCNT Arrays

5.2.4.1 Effect of Surface Chemistry on Capacitance

This study investigated the effect of nanotube surface chemistry on electrical double layer capacitance. aCNTs electrodes are expected to have high capacitance values due to their high specific surface areas and high mesoporosity. However, many of these properties are dependent on the structural nature and surface chemistry of the nanotubes[98]. The aCNTs investigated were chosen from the same batch (CVD 3) and therefore can be termed as being chemically identical with tubes of equivalent lengths ~700 µm, diameters ~ 55 nm, and densities ~10^6. The aCNTs were then divided into sets, where each set consisted of an (i) untreated, (ii) oxidised and (iii) oxidised and hydrogen treated electrode (all 1 mm x 1 mm). Capacitance measurements were then conducted using a multi-electrode attachment device (MultiWE32), which allowed each set of electrodes to be measured simultaneously in buffer solution. Therefore, CV experiments for each electrode set were conducted under identical cell conditions; removing experimental errors such as changes in the temperature, buffer solution and oxygen concentration which was important for subsequent laccase voltammetry experiments.

An example CV for the electrode set, E3, is shown in Figure 99, where the capacitance increased with the successive treatments. Interestingly, only a small increase in capacitance was observed for the oxidised electrode, despite the enhanced affinity between the hydrophilic electrode surface and buffer electrolyte. A recent report demonstrated twofold increments in capacitance for oxidised aCNT electrodes, although the treatment was carried out over a prolonged period in air (450 °C for 10 hrs)[98] and resulted in a high loss of amorphous carbon. The lower oxidation temperature and short treatment time used in this thesis is believed not to have been aggressive enough for removal of large amounts of amorphous carbon within the array. Evidence of this was shown by the high mechanical stability of the oxidised arrays during drying, no collapse of the structure was observed due to weakening, in contrast to the report mentioned above[98]. It is hypothesised; therefore, that the small increase in capacitance could be attributed to a low density of oxidation sites on the electrode surface which increased electrolyte interaction, although improvements in mesoporosity through removal of smaller amounts of amorphous carbon should not be dismissed. Given that the oxidised and hydrogen electrode showed the largest increase in capacitance despite the change in surface chemistry, it appears more likely that purification of the nanotubes is the most likely reason for the increase in capacitance. The high temperature treatment has shown to clean the nanotubes and therefore enhancements in mesoporosity and specific surface area are expected to have resulted in the higher capacitances.

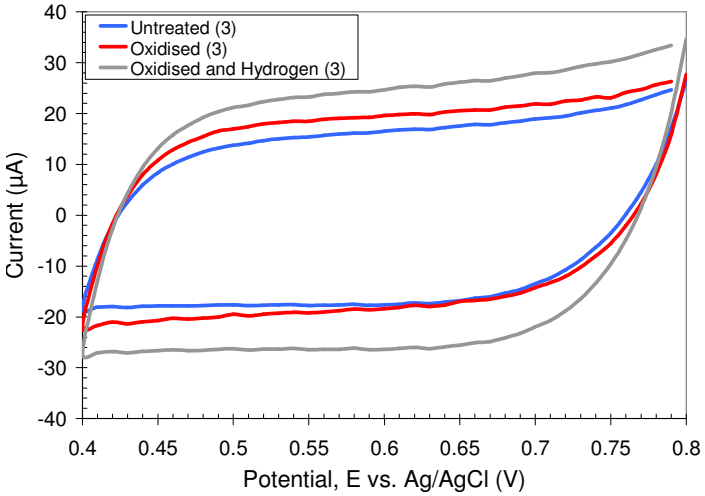

Figure 99: Capacitative currents measured for the different treated electrodes (E3).

The shape and magnitude of the CV waves can also provides an indication of the pore accessibility and available electroactive area. The rectangular CV shape indicated purely capacitive behaviour since no charge imbalance occurred with applied potential. The magnitude of the capacitive current is often determined by the available electroactive surface, which appeared to be lower than expected taking into account the large surface area of the electrode and theoretical calculations (as will be described below). Finally, the capacitive current showed no instantaneous switch when the scan direction was changed and thus took longer to reach steady current state. Usually, this is indicative of low mesoporosity and ion mobility into the electrode due to inaccessible pores as a result of amorphous carbon build-up, hydrophobicity of the electrode surface or low electrolyte concentration. Although, the latter two are most unlikely since the oxidation treatment and higher ionic concentrations (0.5 M KCl) showed no improvement.

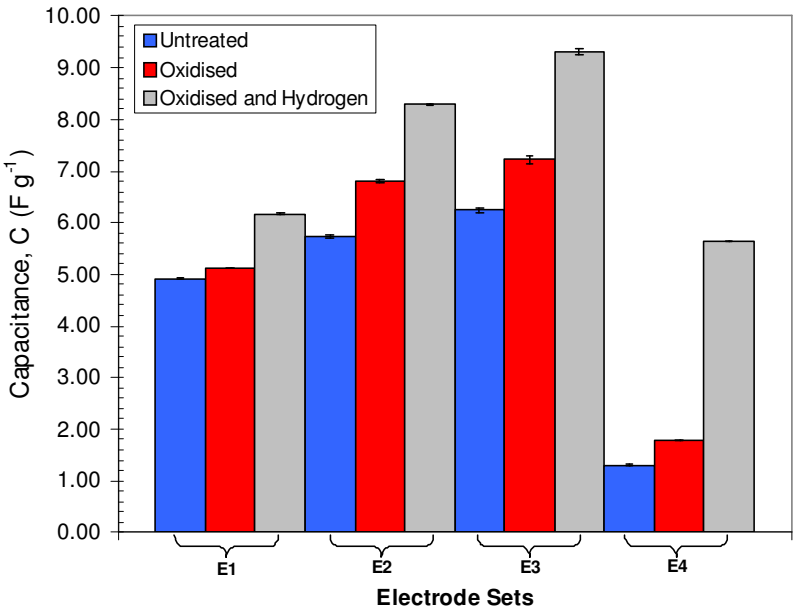

Figure 100: Effect of thermal oxidative and reductie gas treatments on the capacitance of aCNT electrodes (all 1 mm x 1 mm, CVD 2). Capacitances shown were measured at 100 mV s^{-1} and normalised to the estimated electrode mass. Conditions: 0.1 M Na-Cit, pH 4.5, 22 °C.

All electrode sets (E1-E4) showed an increase in capacitance with consecutive oxidation and hydrogen treatments (Figure 100). Capacitances were normalised to the estimated electrode mass. In respect to the untreated electrodes, the oxidation

treatment displayed increments between ~0.5-1 F g^{-1} and the reductive treatment ~1-4 F g^{-1}. Taking into account these values it was necessary to compare these with theoretical capacitance values predicted for nanotube electrodes of the same dimensions. Using the estimated surface area (33 m^2 g^{-1}) and the commonly realisable charge densities 20-50 μF cm^{-2} suggested for carbon materials[243], the theoretical capacitance was calculated to be between 6.6 and 16.5 F g^{-1}. Therefore, these calculations indicate that the capacitances measured are lower than expected, however, the oxidation and hydrogen treatments have shown to improve electrolyte accessibility and bring the capacitance nearer to expected values.

5.2.4.2 Laccase Electrochemistry

The electrocatalytic response of laccase when directly adsorbed on the treated electrodes was investigated. This direct approach was beneficial since the effect of surface chemistry and morphology could be gathered directly from the measured electrocatalytic response.

Voltammetric measurements were conducted using the multi-electrode attachment device (MultiWE32), thus all electrodes were measured under identical conditions. Buffer solutions were saturated with O_2 and continuously bubbled during cycling. Experiments were started when 1 μL of laccase (20 mg ml^{-1}) had been applied and fully adsorbed into all electrodes.

The CVs comparing the reduction responses of the treated electrodes are shown in Figure 101. The electrodes measured were taken from the batch set E3. From the results, it is clear that the oxidised and hydrogen treated electrode displayed superior electrocatalytic behaviour with x3 fold higher current densities than the untreated electrode. The waveshape for the oxidised and hydrogen electrode is suggestive of an electrode displaying superior electrokinetic behaviour, due to the faster turnover rates (steeper slope) and limiting current response at high reduction potential (~0.5 V). The oxidised electrode also displayed higher activity which suggested that the treatments must have improved the electrochemical properties of the nanotubes. To investigate this further, laccase voltammetry was

repeated on two other electrode sets in order to check if the catalytic activity increased when identical treatments were applied to the other electrode sets. The current responses (at 0.4 V) measured for all the electrode sets are shown in Figure 102. It can be noticed that the improvement in laccase activity with thermal oxidative and reductive treatments was consistent across all electrode sets. This study has highlighted that the laccase activity is highly controllable upon functionalising the nanotube surface which holds great promise in further optimising the performance of these electrode materials.

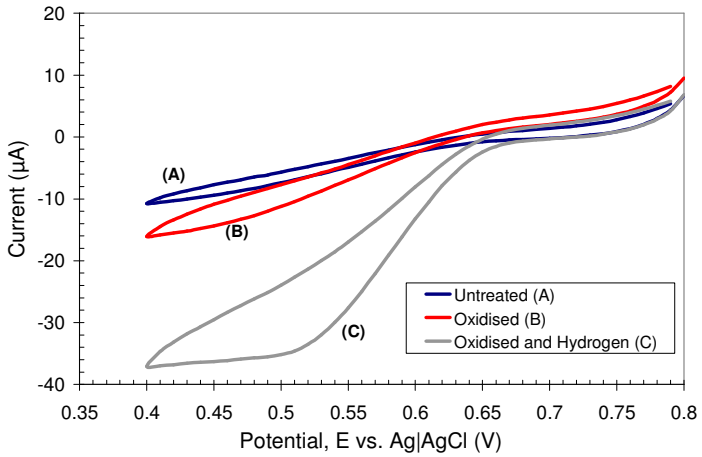

Figure 101: CV measurements showing laccase catalytic response on thermally gas modified electrodes from electrode set E3 (1 mm x 1 mm, CVD 2), where (A) untreated, (B) oxidised and (C) oxidised and hydrogen treated. Conditions: 0.1 M Na-Cit, pH 4.5, room temp, 10 mV s^{-1}, O_2 saturated solution, flow rate: 40 cm^3 min^{-1}, TvL: 1 µL of 20 mg ml^{-1} on each electrode.

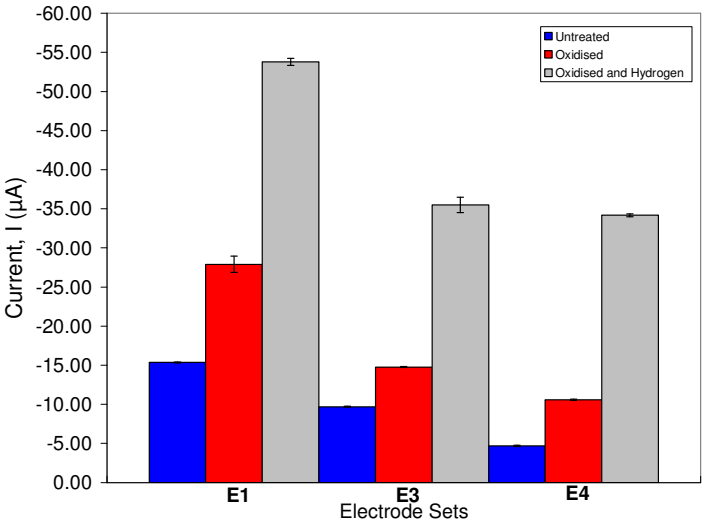

Figure 102: Effect of oxidative and reductive thermal gas treatments on the laccase electrocatalytic response when adsorbed on aCNT electrodes (all 1 mm x 1 mm, CVD 2). Currents were taken at 0.4 V. Conditions: 0.1 M Na-Cit, pH 4.5, room temp, 10 mV s^{-1}, O_2 saturated solutions, flow rate: 40 cm^3 min^{-1}.

To investigate whether enzyme stability was improved upon thermal treatment the E3 electrodes were subjected to extended testing over a seven day period. These experiments were conducted using chronoamperometry, whereby a step potential of 0.4 V (*vs.* Ag|AgCl) was applied to the electrodes and held constant over the measurement period. This potential was chosen since the current was found to be limiting at this value (see Figure 101). Once again, the multi-electrode attachment device (MultiWE32) was used so that all electrodes were measured under identical conditions. Buffer solutions were saturated with O_2 and continuously bubbled (40 cm^3 min^{-1}) during the measurement period. Figure 103 (a) shows the time dependence of catalytic currents achieved for the different treated electrodes over the seven day period. Since the cell temperature was not controlled, the oscillations in current correlate with changes in room temperature throughout the day. All plots showed a gradual in current, however it appeared that the oxidised and hydrogen treated electrode retained the highest catalytic current (6 µA) over the measurement period. It could be said that the untreated and oxidised electrodes had a total loss in current response since current values were only 0.5 µA and 1 µA and their corresponding non-faradaic contributions were in the range 0.6 – 1 µA. This improved stability and catalytic is further highlighted in Figure 103 (B) where the laccase had approximately 20 % higher activity on the oxidised and hydrogen electrode after seven days.

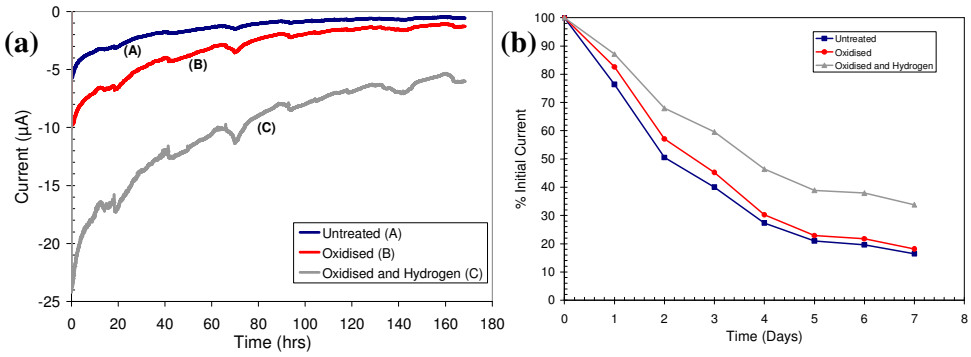

Figure 103: (a) Extended testing of laccase oxygen reduction on treated electrodes from E3 (all 1 mm x 1 mm, CVD 2), where (A) untreated, (B) oxidised and (C) oxidised and hydrogen treated. (b) Percentage current plot versus time (days) for each electrode. Conditions: 0.4 V vs. Ag|AgCl, 0.1 M, pH 4.5. Tvl: 1µL of 20 mg ml^{-1}, O_2 saturated solution, flow rate: 40 cm^3 min^{-1}, room temperature. (Note: Lines in (b) are guide to eye).

It can be concluded that the high temperature annealment in hydrogen significantly improved the catalytic activity and stability of the enzyme. Results presented have demonstrated this treatment effectively removes carbon contaminants from the nanotubes and contributes additional defects after oxidative treatment based on the higher I_D/I_G ratios. It is believed the combination of these two effects were responsible for the improved performance. The removal of contaminant material improved communication with the enzyme increasing the electroactive coverage, while the defects sites present along the tube walls and impurity surfaces and at the tube ends after oxidation and contaminant removal are believed to have improved the electron transfer kinetics. Many reports in the literature have recently shown that defects can be used as a measure of kinetic enhancement[260-263]. In addition the higher capacitances achieved with these electrodes could also play some role in the kinetic enhancement. Improving the electrode wettability could be helpful in hydrating more enzyme molecules and improving mass-transport into the array.

5.3 Conclusion

The functionalisation of carbon nanotubes was carried to investigate the changes in nanotube surface chemistry and the subsequent effects on enzyme activity and stability. This chemical functionalisation method involved gas-phase chemistry techniques whereby CNTs were subject to oxidation and reduction treatments.

Thermal oxidation and reductive treatments switched the nanotube surface chemisty from a hydrophobic to a hydrophilic state. It is believed oxidation introduced oxygen functionalities, such as carboxyl and hydroxyl groups, onto the surface and tips of the nanotubes, while subsequent reduction removed the oxygen species increasing the hydrophobicity across the nanotube surface.

Physical characterisation methods were then carried out on nanotube samples grown for 2 hours (short lengths) and 4 hours (long lengths). SEM and TEM analysis of the two hour samples revealed removal of carbon contaminant material upon reductive treatments. Raman spectroscopy was used to determine the defective nature of the treatments through measurement of the I_D/I_G. Results

highlighted the I_D/I_G ratios scaled with treatment, suggesting that both oxidative and reduction were destructive to the nanotubes. The four hour samples investigated showed to have a thicker impurity coating based on SEM and TEM analysis. This coating was approximatelty 10 nm in thickness and composed of disordered graphitic carbon and thus was more difficult to remove upon high temperature hydrogen treatment, as evidenced in the inconsistencies in the TEM images. Raman I_D/I_G ratios revealed little change with treatment which was probably due to the presence of the thicker graphitic coating.

Electrochemical studies were carried out on the four hour samples since these were used throughout the thesis. Capacitances scaled with oxidation and hydrogen treatment suggesting functionalisation upon oxidation and removal of impurities which increased electrolyte accessibility. Laccase electrochemistry showed improved laccase activity with thermal oxidative and reductive treatments and this effect was consistent across all electrode sets measured. Laccase activity was highest on the oxidised and hydrogen treated electrode. It is believed that the presence of defects and removal of carbon contaminants improved electron transfer and communication between enzyme and the nanotubes. Further studies, using chronoamperometry revealed that higher enzyme stability could be achieved when oxidising and hydrogen treating an electrode surface, this could suggest that enzymes prefer ‘cleaner’ nanotubes.

6 Laccase Electrochemistry on Patterned CNT Electrodes with Increased Pore Size for Efficient O_2 Diffusion

6.1 Introduction

Results have shown that electrode performance is limited by mass transport of oxygen to the enzyme. In this thesis, the effects of oxygen delivery and availability have been investigated and shown to influence the maximum achievable current density. The transport of oxygen at the cathode is already known to be rate-limiting due to the relatively low concentrations of oxygen (0.27 mM) and diffusion coefficients ($< 5\times10^{-5}$ cm^{-2} s^{-1}) in aqueous solutions. However, the presence of the aCNT electrode with small pores and increased thickness further restricts oxygen access and increases the diffusion length to the enzyme which is positioned towards the bottom of the array.

In order to improve the O_2 transport into the electrode it is important to address aspects of the electrode design such as CNT thickness, porosity and diameter. The micropatterning of aCNTs is an approach that can be used to solve these issues. Such patterning procedures are of interest for devices such as field emitters. In the case of electrochemical electrodes, the patterning approach can be used to increase the spacing's between aCNTs to allow for faster diffusion rates and the growth time adjusted for shorter diffusion lengths.

Patterning procedures often involve lithography techniques which are complex, time-consuming and can require expensive facilities. While non-lithography patterning techniques usually employ a patterned shadow mask allowing controlled deposition of the catalyst on the substrate surface. Fan *et al.* developed a highly controlled technique by placing a shadow mask on porous silicon substrates and using electron beam evaporation to deposit iron catalyst films (5 nm thick) on top[280]. After overnight annealing in air and subsequent growth by CVD, each of the patterned iron squares contained highly aligned 3-D blocks of nanotube arrays protruding from the substrate surface. A more simplistic approach used the sol-gel technique, whereby a silica wafer was dip-coated into a catalyst precursor solution and the TEM grid placed on top and used as a shadow mask for

growing the CNTs[281]. However, only clearly defined aCNT patterns were possible with the TEM grid remaining on substrate during growth, thus removing the grid was difficult without damaging the pattern. Despite these examples being highly effective, more simplistic approaches are possible.

The aim of this chapter is to introduce a simple and low-cost approach to micro-patterning aCNTs, which is designed to improve O_2 transport to the immobilised enzyme and hence increase the current density. Furthermore, through optimising the morphology of the aCNT arrays it would be interesting to determine the maximum obtainable cathodic current density.

6.2 Results

6.2.1 Growth of Patterned Electrodes

The patterned aCNT electrodes were produced following the reported method in section 3.3.8, and the main stages of the process are detailed in Figure 104. A square 300-mesh TEM grid was chosen as the shadow mask, where the mesh number denotes the amount of lines/inch. Gold was sputter coated on a masked silica surface, so that the area underneath the mesh bars was not coated and the square mesh holes were coated. This gold mask was then used to pattern the growth of the aCNT arrays, where the iron catalyst from the ferrocene would stick preferably to the unprotected silica surface through the formation of an iron silicide bond and remain active for nanotube growth. Whereas, the iron deposited on the gold did not remain an active catalyst. Thus the shadow-masked gold squares on the substrate provided a high density of small regularly spaced voids (55 μm x 55 μm) between the nanotubes, without causing detrimental effect on specific CNT surface area.

In Figure 105, the width of the silica CNT growth region is 25 μm while the length is continuous along the grid pattern. Therefore, considering an area of 25 μm^2, this region was sufficient to permit vertically aligned CNT growth as there was sufficient Van der Waal interaction between the nanotubes.

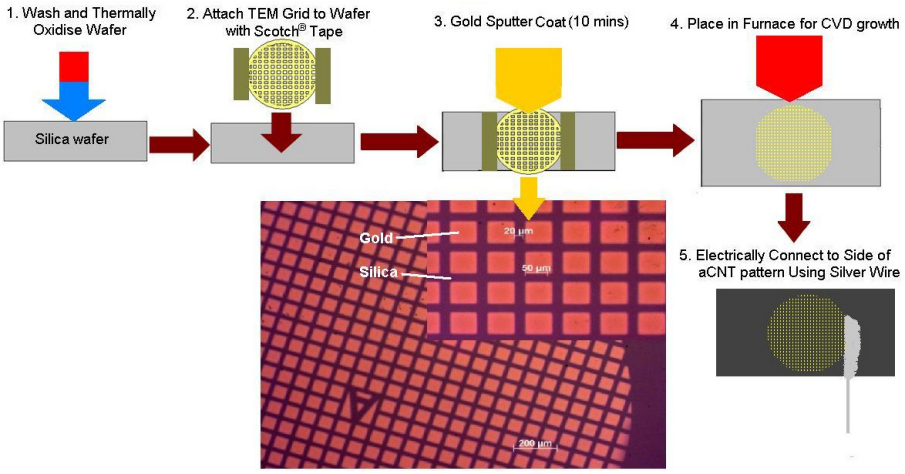

Figure 104: Five stages of aCNT patterning process. Optical microscope images of the gold patterned silica surface and higher magnification (inlet). Gold squares measure (55 µm x 55 µm) and silica channels (25 µm width). CNTs grow on silica and gold squares act as the shadow mask.

As shown in Figure 104, the patterning technique developed requires minimal preparation steps and therefore represents a simple and low-cost approach to micro-patterning aCNTs. This approach can also be used to fabricate various complex CNT patterns (e.g. aCNT mesh and tower patterns) which are difficult to synthesise by conventional lithography techniques. This can be achieved by using TEM grids with different voids and fine-tuning the parameters in the sputter coating process, as described in the following section.

6.2.2 Electrode Characterisation

Prior to CVD growth, optical microscopy was used to determine the precision and uniformity of the gold patterns on the electrode surfaces. Initial observations highlighted inconsistent gold patterns with some samples displaying good patterning with defined boundary layers, while others had imprecise deposition. These inconsistencies resulted in the formation of aCNT micro-patterns with various kinds of configurations. It was later discovered that two critical parameters needed to be met for effective gold patterning and to achieve the desired micro-pattern and these will be discussed separately as follows:

1. Flat Contact Between the Mesh Grid and Silica Surface

Since the gold atoms in the sputtering process have only moderate directionality[282], any loose contact between the TEM grid and silica substrate results in sputtering underneath the mesh bar. Figure 105 compares the SEM images of gold patterned silica substrates with tight grid contact (a) and loose grid contact (b). Immediately it can be noticed that the patterns are significantly different, where the tight contact resulted in highly resolved patterns with uniform intensity and the loose contact produced a blurry or uneven intensity pattern. Both substrates were gold sputter coated for a total of 5 minutes producing an estimated layer thickness of ~ 20 nm, based on the Kanaya and Okayama's mathematical model[283] and EDX/SEM analysis.

The CVD synthesis of nanotubes on these substrates was then directly compared, where tight contact (c) and loose contact (d) are shown in Figure 106 It is evident that the gold masked areas need to be well-defined and preserved for effective nanotube patterning.

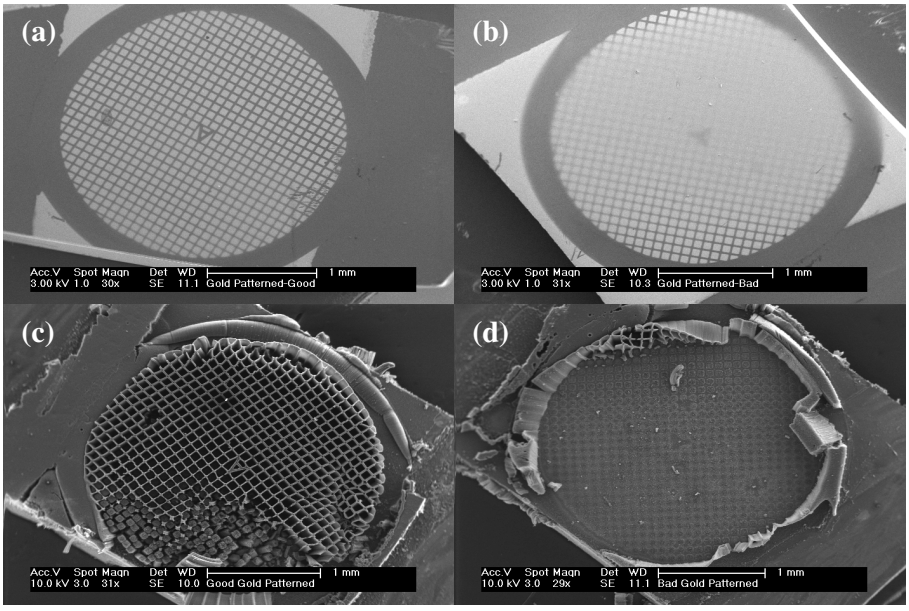

Figure 105: SEM images of gold micro-patterns (Top) and resulting nanotube micro-patterns (Bottom) formed by using 300-mesh copper TEM grids with square voids, where (a) and (c) correspond to tight grid contact and (b) and (d) loose grid contact.

Further insight into the growth process was achieved through investigating a patterned electrode similar to (c) but grown for a shorter period of time. This electrode is shown in Figure 106, where the incomplete pattern allowed the identification of nanotube growth sites and the mechanism of the growth process. The images appeared to reveal that nanotube growth initiates from the edges of the gold patterned squares, as shown in (a). This is possible since the gold step on the substrate stops iron surface migration during growth, thus leaving a higher density of catalyst sites around the edges for carbon nanotube nucleation.

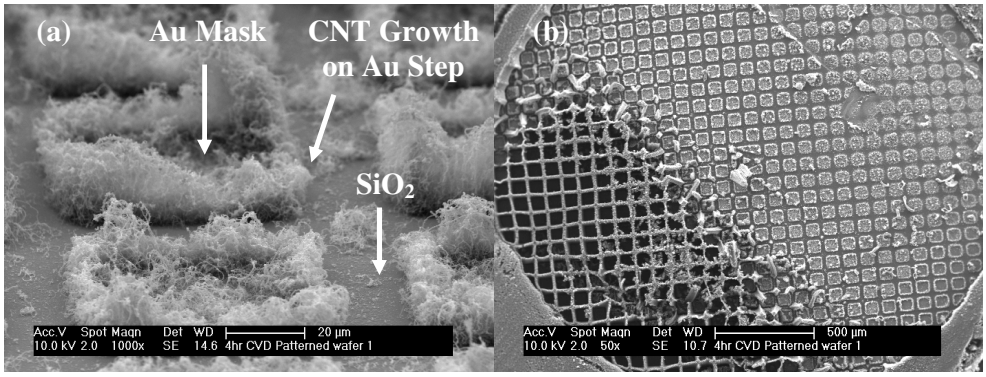

Figure 106: SEM images of (a) CNT growth at circumference of gold square and (b) lower magnification image of resulting nanotube micro-pattern.

2. Gold Layer Thickness

In some cases, aCNT growth occurred over the entirety of the gold mask squares. This was believed to be a combination of non-uniform patterning and the presence of a thin gold layer. In some cases a lift-off process was evidenced (see Figure 107) where larger gold nanoparticles appear to be lifted-off the substrate surface due to poor adhesion. This lift-off process or poor barrier thickness allowed iron catalysts to deposit on the exposed silica during growth. This adhesion problem often results in broadening of the nanoparticle size distribution due to particle coalescence by ripening and migration. Future work will improve gold adhesion by depositing an adhesion layer (e.g. titanium) [284].

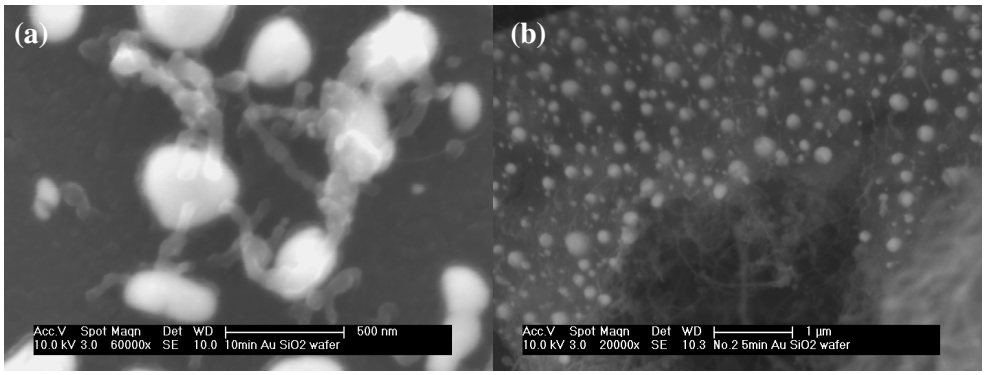

Figure 107: SEM images of CNT tip growth on coalescent particles lifted-off the substrate and (b) gold layer lifted-off the substrate.

Evidence of nanotube growth on the gold masked squares is shown in Figure 108 (a). In this image the micropattern is composed of regularly arranged nanotube towers due to penetration of the catalyst through the gold layer and favoured growth on the large area. In Figure 108 (b), a mixture of towers and grid growth can be observed due to the poor patterning which resulted in a thinner mask layer.

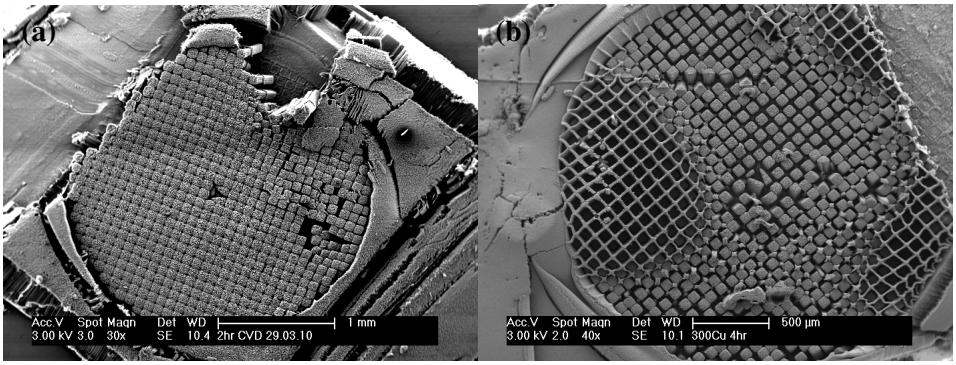

Figure 108: Images demonstrating patterned nanotube growth on (a) gold masked squares, (b) gold and silica.

6.2.3 Laccase Electrochemistry

6.2.3.1 As-Grown aCNT Micro-patterned Electrodes

Electrochemical measurements were carried out on two nanotube micro-patterned electrodes shown in Figure 109. Electrode (a) described previously, demonstrates almost ideal patterning with nanotube growth replicating the structure of the TEM grid. While electrode (b) demonstrates growth on the gold masked squares, resulting in the formation of aCNT towers after not meeting the required patterning parameters, as mentioned in the previous section.

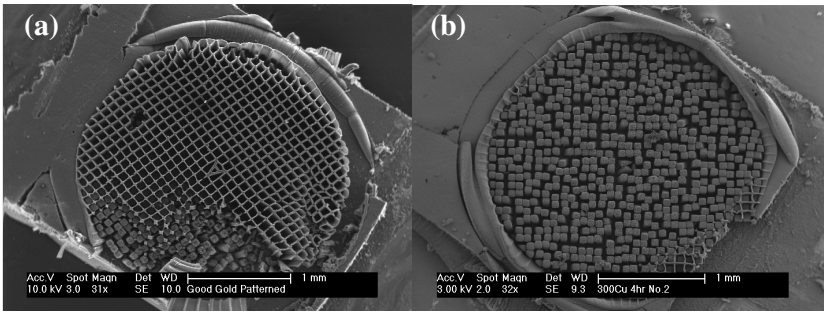

Figure 109: SEM images of aCNT micro-patterns, where (a) aCNT network replicating TEM grid micro-pattern (height- 230 µm, width- 25 µm) and (b) aCNT towers grown on gold squares (height- 170 µm and width- 55 µm). Both patterns had the same surface areas ~ 33 m^2/g.

Initial experiments were carried out in 0.1 M sodium citrate buffer (pH 4.5) solutions to determine the electrochemical capacitance of the aCNT micro-patterns. The electrochemical responses of the two electrodes are shown as the dotted lines in Figure 110. The measured capacitances for "grid" electrodes (a) and "tower" electrode (b) were 0.5 F g^{-1}. Extra peaks appeared at 0.45 V and 0.6 V and below 0.3 V in these CVs and these were attributed to the silver epoxy used for the electrical connection to the side of the aCNT pattern. Difficulties were found in insulating the silver epoxy because of the uneven nature of the patterned side connection. These features could have been avoided by using a lower viscosity insulating epoxy and a smaller potential window (0.8 - 0.4 V).

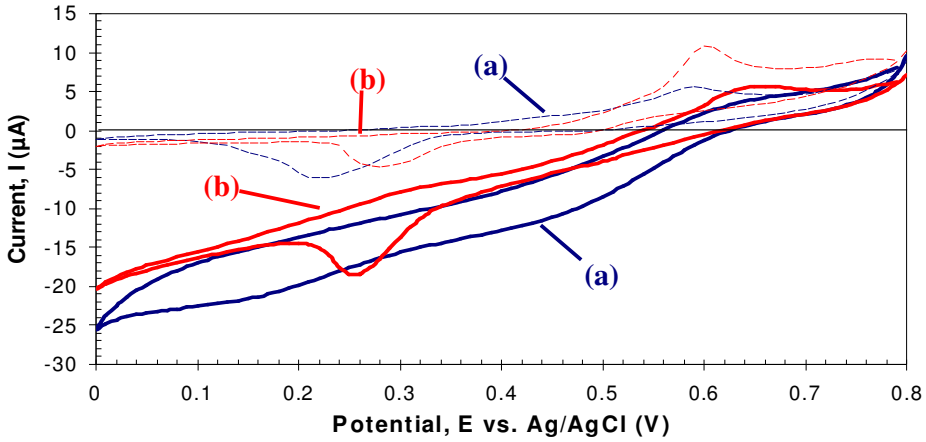

Figure 110: Cyclic Voltammetry of "grid" (a) and "tower" (b) electrodes from Figure 110, without laccase (dotted lines) and with laccase (solid lines). (Conditions: O_2 flow rate 40 cm^3/min, 10 mV/s, 0.1 M Na-Cit, pH 4.5, room temperature, TvL/electrode 30 µg).

The catalytic reduction of O_2 was then measured by the addition of 1 µL of laccase (30 mg ml^{-1}) onto the patterned surfaces. The catalytic wave was first monitored through four CV cycles at room temperature, after which the buffer solution was refreshed to remove any unbound enzyme and eliminate its influence on the catalytic voltammetry. Both electrodes were measured separately and displayed stable catalytic waves, the waves were then averaged and compared (Figure 110). Maximum current values were taken at 0.4 V because of silver oxide reduction < 0.4 V. It can be noticed that grid electrode had a higher current density of 2 µA cm^{-2} than the tower electrode 0.9 µA cm^{-2}. It is believed that the higher current density for the grid electrode resulted from a shorter O_2 diffusion path length due to a greater number of voids and less densely packed aCNT regions (55 µm spacing). Whereas the tower electrode consisted of aCNT towers with higher nanotube densities within close proximity of each other (25 µm), consequently making it difficult for O_2 to diffuse inwards reaching the enzyme. The voltammetric waveshapes of the two electrodes were also different, with more active enzyme evident in "grid" electrode due to the faster electron transfer kinetics and thus higher amplitude.

Overall, the current densities were quite disappointing, although, many problems were found with the electrodes before and during electrochemical measurement. The initial concern was the slow absorption of laccase into the electrodes, where

the higher number of spacings between the aCNTs removed the strong capillary forces. In addition, the nanotubes were found to have an irregular surface morphology attributed to an amorphous carbon coating (Figure 111), which has previously shown to hinder enzyme absorption (section 4.5.2). "Tower" electrode displayed the slowest absorption behaviour, where it took ~ 30 minutes for the enzyme to soak into the arrays due to the air pockets within the patterned spacings. Also, the electrical connection to the nanotubes was not as effective as the previous aCNT arrays and thus conductivities could have been lower. In future experiments, this will be investigated along with alternative electrode preparation techniques.

During electrochemical measurement, these patterned spacings resulted in the formation of buffer-air interfaces which appeared to restrict the wetting behaviour of the aCNTs. This could have also affected the performance of the electrode by restricting enzyme hydration. Therefore, it was necessary to investigate the effect of oxidising the patterned surface in order to improve enzyme adsorption, hydration and hydrophilicity of the electrode in buffer solution. This work is shown in the following section.

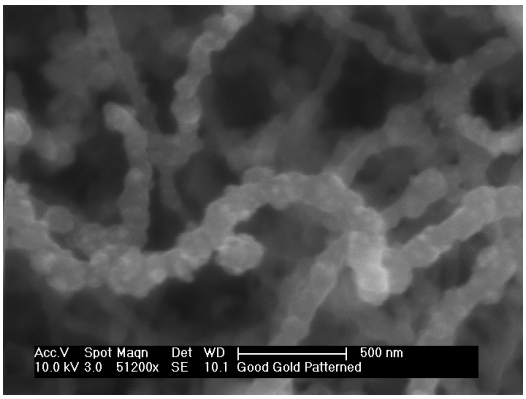

Figure 111: Carbon contaminant coatings on the patterned nanotubes.

6.2.3.2 Oxidised aCNT Micro-patterned Electrodes

6.2.3.2.1 Capacitance Measurements

This study investigated the electrochemical behaviour of patterned aCNT electrodes which had been oxidised using standard procedure. These electrodes shown in Figure 112 (a) and (b) were not ideally patterned and this resulted in the formation of nanotube towers. It is believed these aCNT towers formed due to poor adhesion of the gold particles to the substrate surface, as shown in previous SEM images (see Figure 107 (a) and (b)). Despite both electrodes displaying similar micro-patterns, it can be noticed the surfaces of the aCNT towers differed in appearance. Electrode 1 had slighter larger spacing between the aCNT towers and secondary directional growth on the tips, while electrode 2 had smaller spacing between the aCNT towers and more random-like growth towards the tips.

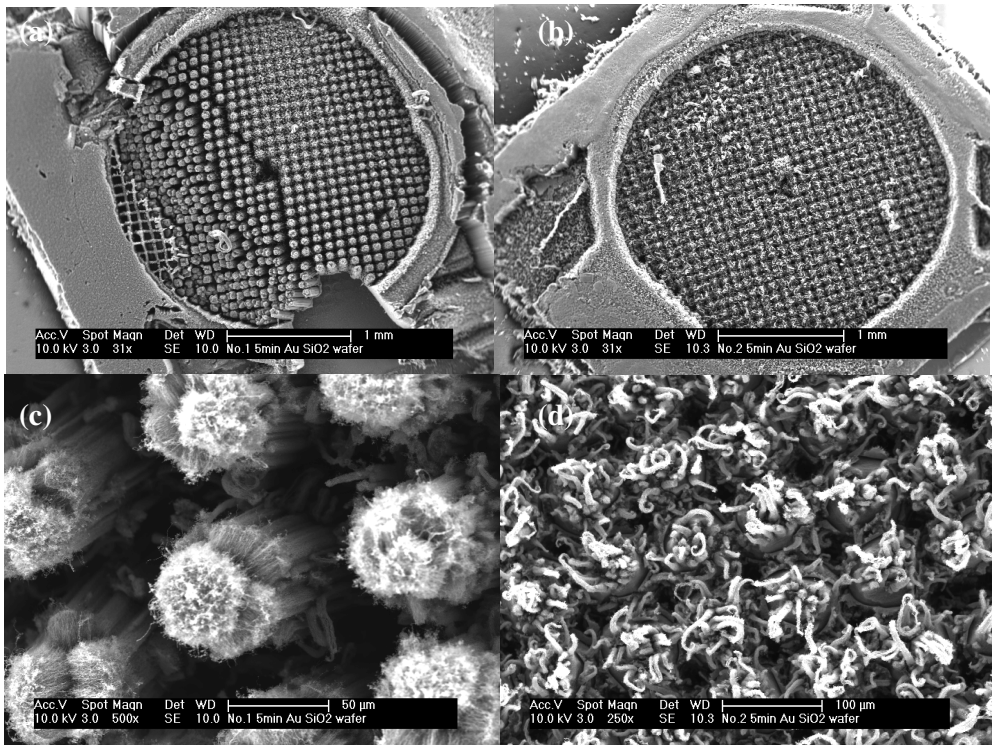

Figure 112: SEM images of oxidised, patterned aCNT towers, where (a and c) electrode 1 and (b and d) electrode (2). Additional CNT growth is shown on the surfaces of both towers due to catalytically active Au nanoparticles lifted from substrate surface. Note: the aCNT towers in electrode 1 have larger spacings than electrode 2.

Capacitance measurements were initially carried out on a gold patterned silica wafer (i.e. without CNTs), since the capacitive and catalytic responses had not been pre-determined. The capacitance wave was first monitored through 9 CV cycles at 0.01 V/s and highlighted some interesting behaviour. Figure 113 (a) details the initial voltammetric waveforms observed after 3 cycles, where the capacitive current is shown to alternate with applied potential and the amplitude and frequency of the wave increased with each cycle (see (a) and (b)). It could be speculated that this electrochemical behaviour is due to the presence of gold nanoparticles on the electrode surface. Nanoparticles like nanotubes possess unique electronic properties depending on their physical size and in this case if the metal particle size is small enough (about 20 nm)[285] then quantum size effects occur. An overview of this effect will be given below and therefore readers interested in nanoparticles are advised to consult the following literature[286-289].

The quantum size effect or more simply quantisation arises because the size of the particle is comparable to the de Broglie wavelength (i.e. wavelength of its charge carriers). The close proximity of these charge carriers results in the splitting of the outer-most valence and conduction bands into discrete quantised electronic levels, meaning that the physical properties can be controlled by the size, morphology and composition of the particles. If the electrostatic energy is larger than the thermal energy, these quantised electronic levels can give rise to single electron transfers (i.e. coulomb blockade effect). As a result, these single electron transfers shown as single electron charging peaks in Figures 114 (a) and (b) can be observed at a given temperature only if the capacitance, C_{DL}, is sufficiently small (e.g. a very small nanoparticle) and thus depends on the following equation[290]:

$$\Delta V = \frac{e}{C_{DL}} \qquad \textbf{Equation 59}$$

where e is the electron charge, ΔV is the nanoparticle potential change upon a single electron transfer from the working electrode in this study. As shown in Figure 114 (a), ΔV is the voltage spacing between the waves.

Figures 113 (a) and (b), display these single electron transfers as single electron charging peaks due to double layer charging on the gold nanoparticle electrode surface, known as quantised double layer charging, QDL. Recent reports have demonstrated this behaviour when performing voltammetry on gold nanoparticle solutions[291-294], in which the findings were developed from early understandings of the electrochemistry of metal nanoparticles by Henglein *et al.*[295] and Gratzel *et al.*[296].

In summary, all metal nanoparticles are electroactive and have a finite double layer capacitance. For example, when working down from large to smaller nanoparticles the CV curves are often featureless for larger nanoparticles (> 20 nm). However, larger current values are observed when under mass transport control, which highlights this double layer charging effect (known as bulk-continuum voltammetry). The CV curves become quantised with single-electron charging peaks if the size, and therefore capacitance, are much smaller (about 20 nm) (known as QDL). Finally, in the smallest nanoparticles a metal-molecule transition is observed where QDL voltammetric waves are separated by central larger spacing due to HOMO-LUMO gap energies (known as molecule-like voltammetry).

During QDL voltammetry of the gold patterned silica wafer, it could be noticed that the spacing between the single electron charging peaks (ΔV) decreased from cycle 1-7 at 0.01 V/s (see Figure 113 (c)). It is hypothesised that as the electrode is slowly cycled, an increasing amount of gold nanoparticles become charged due to single electron transfers from the electrode. Since only a diffuse double layer is present in the early cycling stages the peak spacings are large, and subsequently become smaller as the double layer further develops across the surface. After cycle 7, the increase in ΔV can be explained in terms of all the gold particles are charged and the double layer is formed and can no longer increase.

At higher scan rates, QDL voltammetry was less evident (see Figure 113 (d)), probably, for reasons being that the electrostatic energy was not high enough and the double layer could not be formed due to mass transport limitations at high cycling speeds. The sigmoidal wave shape could be explained in terms

hemispherical diffusion of electrolyte to the electroactive gold nanoparticles or oxidation of the gold surface.

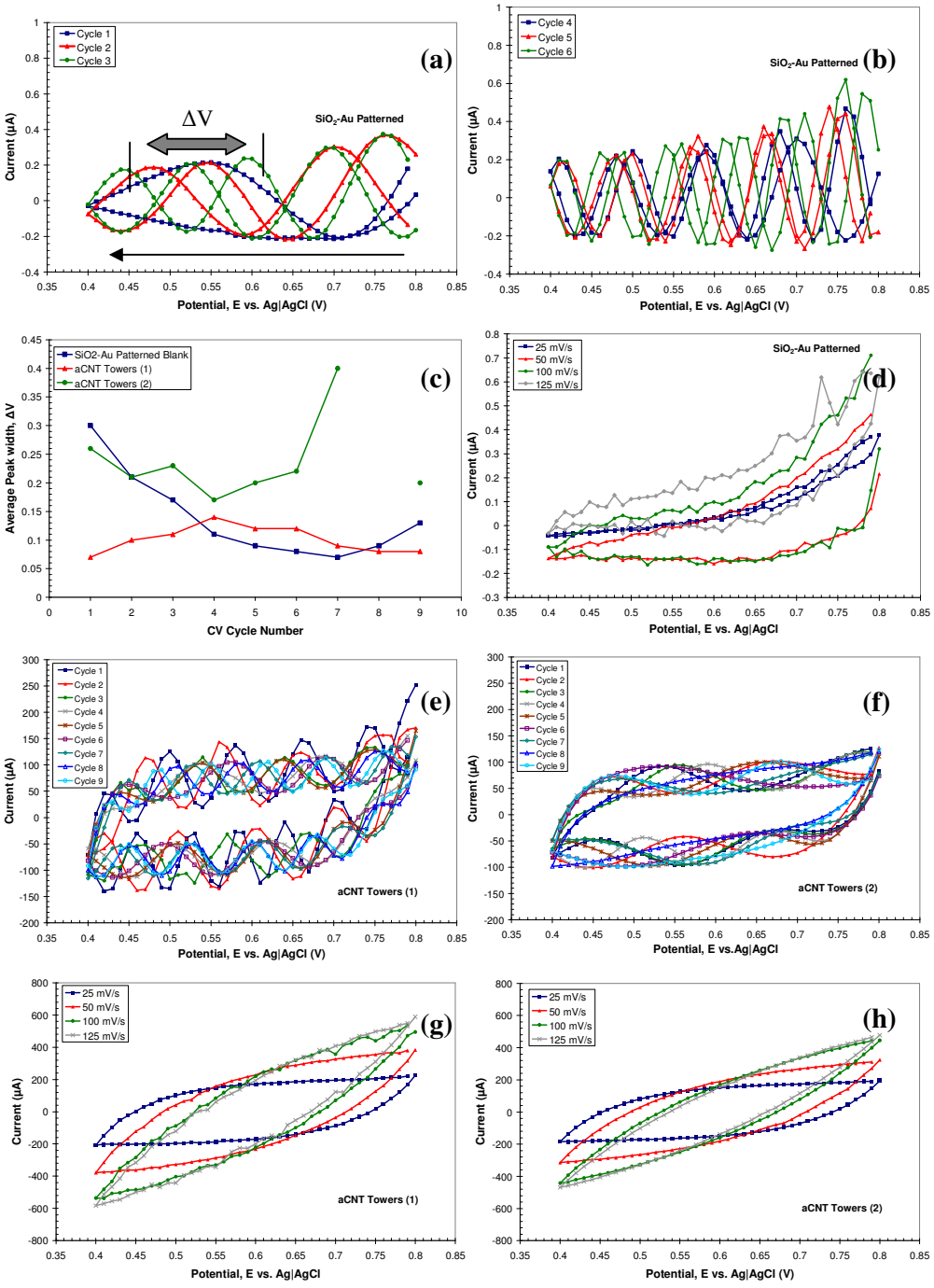

Figure 113: Voltammograms (a-b), (d-h) and graph comparing peak widths (voltage spacings) of the 10 mV/s scans (c). Cyclic Voltammograms of SiO_2-Au patterned blank displaying successive cycles measured at 10 mV/s (a,b) and scans 25, 50, 100 and 125 mV/s (d). In (c) peak widths were averaged for both forward and reverse cycles. Cyclic voltammograms of aCNT Towers (1) and aCNT Towers (2) at 10 mV/s (e,f) and higher scans (g,h). Conditions: 0.1 M Na-Cit, pH 4.5, room temperature, Scan direction 0.8-0.4 V.

Subsequent capacitance measurements were then carried out on the two aCNT tower electrodes, where QDL voltammetry was once again observed at 0.01 V/s (Figure 113 (e) and (f)). It can be noticed that the magnitude of these current peaks is much greater (~ x3 fold) due to the growth of the aCNTs on the gold nanoparticles significantly increasing double layer charging. Electrode 1 (e) displayed a greater number of single electron charging peaks compared to electrode 2 (f) and the gold patterned electrode ((a) and (b)). It is believed the smaller diffuse layer and improved pore accessibility and ion mobility resulted in this high polarisation and can be explained using the concentric sphere capacitance model as follows:

$$C_{DL} = A_{NP} \frac{\varepsilon\varepsilon_0}{r} \frac{r+d}{d} = 4\pi\varepsilon\varepsilon_0 \frac{r}{d}(r+d) \qquad \textbf{Equation 60}$$

where A_{NP} is the nanoparticle surface area, r is the radius and r + d is the radius plus ligand layer thickness (of effective dielectric constant).

This model and Equation 59, highlights that ΔV is inversely proportional to the effective dielectric constant. Given that the aCNTs are grown on the gold nanoparticles, the ΔV is inversely proportional to the nanotube double layer charging effect. Therefore, the ΔV for electrode 1 increases with each cycle because of the high polarisation and large double layer formed due to good electrolyte accessibility, as shown in Figure 113 (c). While, the ΔV for electrode 2 is sufficiently large and does not decrease as much from cycle 1-4 compared to the gold patterned electrode. Since, QDL voltammetry is controlled by mass transport rates, these results could suggest that mass transfer to electrode 2 is under finite linear diffusion control due to lower polarisation (high ΔV values) and small decrease in ΔV from cycle 1-4. At cycles 4-7, the double layer charging effect is maximised, hence ΔV increases and in fact cycle 8 displayed ideal square-like faradaic behaviour (bulk-continuum voltammetry) probably because the electrostatic energy was smaller than thermal energy, thus QDL requirements were not met.

Increasing the scan rate from 10 to 25 mV s^{-1} completely removed the QDL voltammetry behaviour for both electrodes. At higher scan rates, the capacitance decreases sharply (see Figure 114), as well as the disappearance of the rectangle shape (see Figure 113 (g) and (h)) giving a response similar to a resistor. This indicates the slow charge/discharge kinetics of the aCNTs grown on the Au nanoparticles due to this quantum size effect and the possible contribution of mass transport limitations.

It is noted that the application of this theory to the current data is speculative due to time constraints. However, further investigation of the QDL effect of gold nanoparticles on nanotubes is an interesting future project with applications in the area of transistors, oscillators, catalysis and biosensors[297]. Future experiments to study the QDL effect are discussed in section 6.4.

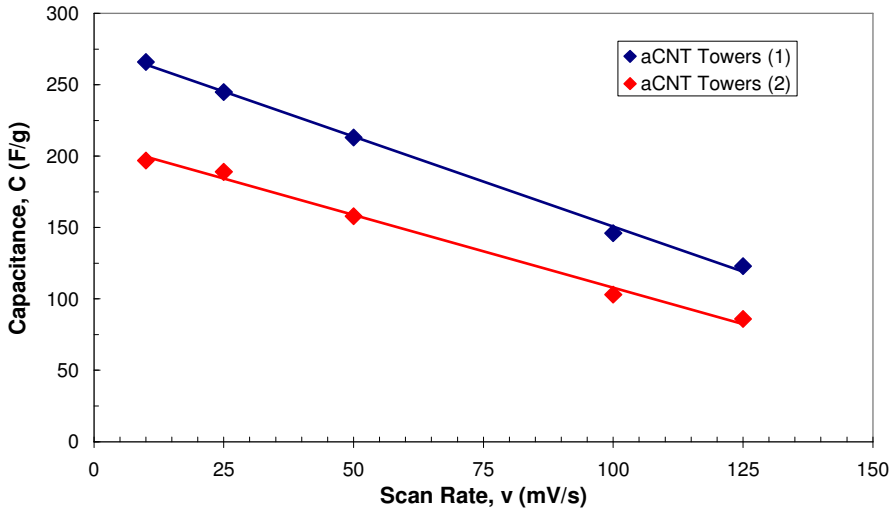

Figure 114: Capacitance change of electrodes upon increasing scan rate (note: linear fit).

6.2.3.2.2 Laccase Electrochemistry

Catalytic voltammetry was carried out on all the measured electrodes under standard closed cell conditions. A total of 0.5 μL (4 μg) was pipetted onto the electrode surface and the O_2 reduction current monitored through 5 CV scans, after which the buffer was changed and re-purged. Subsequent measurements were then recorded over 9 CV scans. The gold patterned electrode displayed no catalytic activity and poor physisorption properties despite the high surface-to-volume ratio and excellent biocompatibility of gold nanoparticles[298]. Therefore, it was concluded that gold nanoparticles do not influence laccase catalytic activity and thus their presence was ignored in the experiments remaining.

Figure 115 (a) highlights almost identical voltammetric waveshapes observed with and without laccase addition. Conversely, the aCNT tower electrodes showed an obvious reduction response with onsets occurring around ~0.6 V and reaching a maximum at ~0.4 V. As shown in Figures 115 (b) and (c), the currents recorded for both electrodes were 69 μA (1) and 64 μA (2), after subtracting the large background non-faradaic current. These CV scans were measured at 10 mV/s, while at scan rates higher than 25 mV/s, the response was not as apparent due to slow charging and discharging of the gold nanoparticles, hence resistive nature of the electrode at high scan rates (see Figure 115 (d), average of 3 CV scans). Based on the limiting current values, the current densities were calculated as 6 μA cm^{-2} (1) and 5 μA cm^{-2} (2) which were approximately 3 times larger than the previously patterned electrodes in section 6.2.3.1. This higher catalytic activity suggested that O_2 mass transport was improved by the oxidation treatment given the large increase in capacitance but still limiting. Therefore, using oxidised patterned electrodes with larger spacings between the arrays could possibly increase the current above >10 μA cm^{-2} and this will be the aim for future experiments.

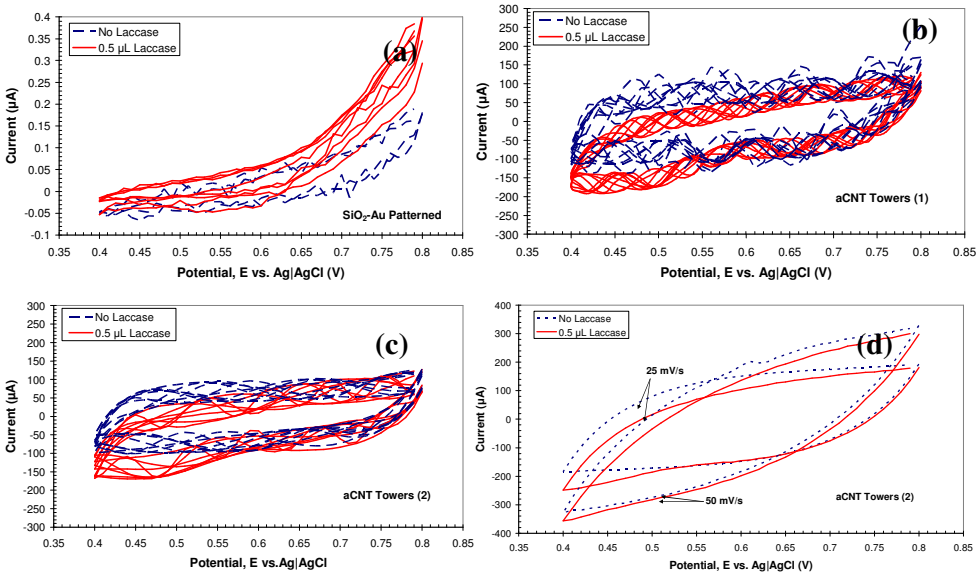

Figure 115: Voltammograms of (a) Au Blank (b) aCNT Towers (1) (c and d) aCNT Towers (2), without laccase (dotted lines, blue) and with laccase.(solid lines, red). Scan rate in (a) 25 mV/s, (b) and (c) 10 mV/s and (d) 25 mV/s and 50 mV/s. Conditions: Closed cell, 0.1 M Na-Cit, pH 4.5, O_2 saturated soln, O_2 flow rate 40 cm^3/min, TvL/electrode 4 µg.

Chronoamperometry was also conducted on the aCNT tower electrodes to investigate the current behaviour when held at constant voltage (0.45 V). Both electrodes are compared in Figure 116 and were measured using a 60 s interval time (instead of 0.2 s) to remove the high number of current oscillations, thus making the data easier to compare. It can be noticed that electrode (1) displayed the highest current output (60-80 µA) due to the improved pore accessibility. Both electrodes displayed alternating currents within a 20 µA window, indicating the charge/discharge behaviour of the nanoparticles.

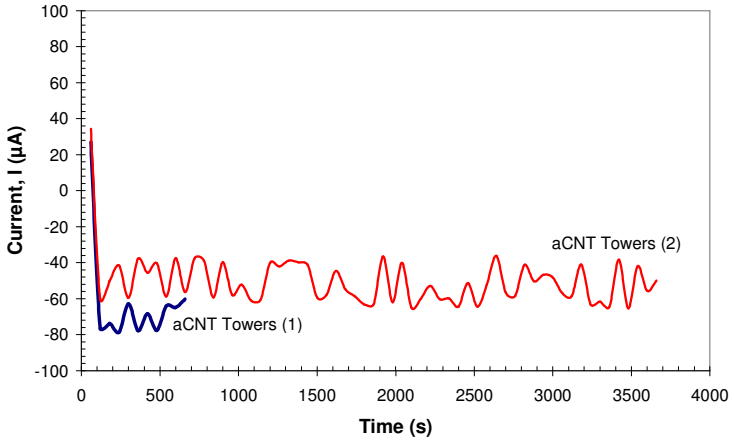

Figure 116: Chronoamperometry of aCNT towers (1) (blue) and aCNT towers (2) (red) held at 0.45 V for 600 s and 3600 s respectively. Conditions: 0.1 M Na-Cit, pH 4.5, O_2 saturated soln, O_2 flow rate 40 cm^3/min, TvL/electrode 4 µg, starting voltage 0.8 V for 60 s, measurement interval time 60 s.

6.3 Comparison of electrodes and future work

The results in this thesis can be summarised through comparing the electrocatalytic activity of laccase on all the investigated electrodes. Electrodes were compared in terms of their limiting current values taken at 0.4 V and normalised to surface area. It was considered necessary to relate the electrode performance to the surface area of the electrode for fair and accurate comparison between electrodes. In addition, the current densities taken were all measured in O_2 saturated solutions bubbled at 40 cm^3 min^{-1}, and thus under identical atmospheres.

The current densities along with the capacitances of all electrodes investigated are shown in Figure 117. It can be concluded that the oxidised micro-patterned electrode displayed the highest current response as well as the highest capacitance (x100 fold higher). It is believed the patterning procedure combined with the short oxidative treatment improved both electrolyte access and substrate diffusion to the enzyme. Intriguingly, only slightly lower current densities were achieved with the oxidised and hydrogen treated electrodes highlighting the distinct advantage of the thermal gas treatments. Given the contrasting architectures, it can be rationalised that substrate diffusion is a lot higher in the patterned electrode than the aCNT array. Therefore, in the light of recent research on carbon nanotube electrochemistry, it is hypothesised that the improvement in catalytic activity is centred on changes at the enzyme-nanotube interface. The oxidative and hydrogen treatments have previously shown to introduce higher defect densities but also have shown to clean the tubes, thus contributing to higher electron transfer rates and improved communication with the active site. It could be said that the oxidative treatment also played some role in improving the catalytic performance of the oxidised patterned electrode, in a similar manner to the oxidised aCNT array (CVD 2).

Finally, the untreated CVD 1 displayed the highest catalytic activity despite having the shortest length when compared to all the untreated non-patterned arrays. SEM analysis highlighted a slightly lower nanotube density per area which could have improved substrate transport to the enzyme. In addition, the untreated

electrode measuring 2.21 mm had a comparable density due to higher coverage of enzyme, however it was believed currents were not as high as expected due to the higher impurity content.

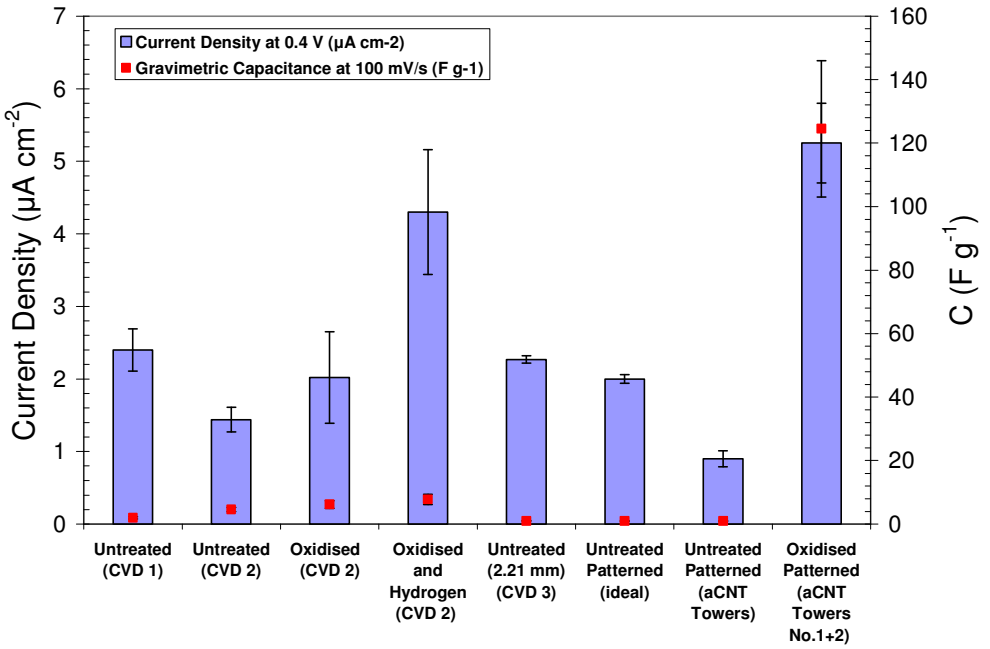

Figure 117: Comparing current densities and capacitance values obtained from all electrodes investigated in the thesis. Note: current densities and capacitances normalised to estimated electrode surface area and mass. Conditions: 0.1 M Na-Cit, pH 4.5, O_2 saturated solutions, flow rate: 40 cm^3 min^{-1}, TvL: 1 µL of 20 mg ml^{-1} (CVD 1, CVD 2) and 10 mg ml^{-1} (CVD 3, ideal, aCNT Towers) and 5 mg ml^{-1} (aCNT Towers 1+2).

6.4 Conclusion

This chapter has addressed the problem of substrate-transport into porous electrodes through the development of novel and straightforward micro-patterning procedures. Critical parameters for successful patterning have been identified and implementation of these in future analyses will allow further detailed investigation into the electrocatalytic response of laccase on these promising electrodes.

The results gathered from the small number of measurements are consistent with the hypothesis that shortening the O_2 diffusion length to the enzyme by spacing aCNT arrays allowed for faster diffusion rates and higher current densities. Future experiments will investigate different array widths, lengths and spacings between them to maximise electrode performance. In addition, thermal oxidative

treatments were shown to improve electrode performance through improving electrolyte accessibility into the arrays and increasing catalytic activity, possibly by introducing surface defects and removing some contaminant material. From all the electrodes investigated, these oxidised patterned electrodes displayed the best performance, while it must be noted not being of sufficient quality. It is understood that higher electrolyte accessibility resulted in the appearance of gold quantum-size effects and were responsible for the slow charge and discharge behaviour during cycling. However, it is not believed that these particles influenced the catalytic behaviour of laccase in anyway since no catalytic activity was observed when laccase was adsorbed on a gold patterned electrode.

It is proposed that further work should also reveal the maximum capabilities of these electrode materials in terms of total current output. Calculations have shown that current densities are x50 fold lower than maximal, but further developments in the quality of patterning and supporting electrode material, treatment methods and optimal conditions should make this target figure more reachable.

7 Future Work

7.1 Thermal Treatment

The application of thermal treatments to functionalise the nanotube surface resulted in interesting electrochemical behaviour towards enzymes, namely enhanced catalytic activity and improved stability. The reasons for this behaviour are not fully understood and this creates an opportunity for further work around the role of chemical modification of nanotubes, with a view to further improve the biocathode.

Future experiments could involve separating treatments techniques into those that are aggressive and bring about defects such as treatments at higher oxidation temperatures and for longer periods. While, those that are purely aimed at purification such as annealing at high graphitisation temperatures in inert atmospheres (e.g H_2 or Ar etc.) to improve structural quality of the nanotubes.

This would help distinguish whether the catalytic effects are primarily defect or chemistry induced or alternatively related to the purity of the nanotube.

7.2 Microarrays

The original plan for this work was to develop a simple approach to fabricating micro-patterned aCNT electrodes. This was only partly successful because the critical patterning parameters were only later realised during the study. In future experiments, it can be assured that only the desired aCNT micro-patterns will be grown since there will be a better understanding of the required patterning and CNT growth conditions. For example, the importance of the seed layer towards better gold particle adhesion has now been realised, as well as ensuring that the TEM grid lies perfectly flat on the substrate surface during sputtering and the gold layer thickness is sufficient to prevent any CNT growth.

Further improvements will also be made on the electrical connection or alternatively investigation into aCNT growth on conductive substrate supports, such as TiN-coated Copper or Inconel which have previously shown to demonstrate aCNT growth via vapour-phase catalyst delivery[299, 300]. This would significantly reduce the resistive effects and improve the electrode performance.

The micro-patterned nanotubes showed significantly improved catalytic performance when thermally oxidised. Subsequent high-temperature annealment in hydrogen was not carried out but has proven to improve laccase activity and thus will be investigated in the future. Different micro-patterns can also be explored in which precedence can be made towards patterns with short diffusion pathlengths but with high surface areas for optimal enzyme loading.

Finally, the assumed quantum-size effect observed provided some interesting electrochemistry and further investigations on these effects on different substrate surfaces would provide insight into their charge/discharge behaviour. Furthermore, it is possible that looking at different sized particles could bring about different electrochemical effects which could be interesting for various applications.

7.3 Genetically Engineered Enzymes

Finally, the purification studies performed around the enzyme laccase within this thesis have demonstrated that many steps are involved before an unimpressive yield of purified enzyme is obtained. Adding to this purification techniques are often complex, costly and time consuming.

Protein engineering is a relatively new concept that has shown great promise for the industrial-scale production of stable and active enzymes. Heterologous expression has been shown to be an encouraging method to reproduce the desired protein. This involves transferring the genes within the native host into other strains or bacteria enabling high-level protein production. Other methods such as removing structural sites for enhanced catalytic performance are currently being investigated. However, this research is still at an early stage and further understanding of the structure and biocatalytic function of enzymes is essential before industrial-scale and ground-breaking enzymes are ever realised.

8 Overall Thesis Conclusions

aCNTs have been assessed as potential electrode materials for BFC applications. The large surface areas of these nanostructures can significantly increase the enzyme loading and facilitate reaction kinetics, thus improving the power density of BFCs. Research efforts have investigated these effects through various electrochemical studies. In addition, methods of enhancing enzyme lifetime and activity have been explored through changing the surface chemistry in order to further understand and control the protein-nanomaterial interface, and developing micro-patterned electrodes to reduce mass-transport limitations.

This study investigated a BFC half cell comprising of an aCNT electrode in contact with the fungal enzyme, *Trametes versicolor* laccase. The direct adsorption of laccase onto the nanotube surface was an effective method of achieving DET with the active site. Fluorescence studies showed the aCNT arrays had 'sponge-like' properties towards enzyme solutions due to their porous structure which helped to encapsulate the enzyme.

Electrode performance was investigated by measuring the current response as a function of electrode area (geometric area) and nanotube length. In both cases, the current scaled linearly with area and length despite lower loadings, however, the current did not scale with surface area since low current densities were standard across all electrodes. This behaviour indicated that catalytic activity was limited by substrate diffusion rather than loading of enzyme, since more enzyme molecules were electroactive over larger areas and lengths but turnover rates were substrate limited.

The amount of laccase required to reach limiting conditions was investigated by increasing the loading of enzyme on the electrode surface. Catalytic activity was achieved with highly diluted enzyme stocks (x278 fold). The cathodic current increased with enzyme loading until the currents were limited by substrate diffusion. This linear behaviour demonstrated the excellent electrical communication at the nanotube-enzyme interface and the sustained catalytic activity of the enzyme when immobilised on the electrode surface. The

electrocatalytic response was also highly consistent across all electrodes, whether from the same batch or different batches with similar lengths and surface areas. Current densities obtained using these electrodes were between 1-2 μA cm^{-2}, which was higher than the previously reported CNT-Laccase cathodes, 0.001 μA cm^{-2}[241].

Upon examination of the voltammograms it was evident that with increasing electrode areas and higher enzyme loadings, the waveform shifted to higher potentials and displayed sharper reduction peaks. It is possible that this behaviour was an effect of kinetic enhancement. However, a plausible explanation for this catalytic response is the thin-layer cell behaviour found in porous electrodes[301]. It has been proposed that increasing both electrode area and loading results in longer diffusion path lengths and faster depletion of the substrate within the pore channels. The combination of these effects results in a voltammetric wave which has minimal hysteresis and apparently 'improved' kinetics. This appearance of the voltammetric wave can therefore be misleading. Therefore, the geometry of the electrode should always be taken into account before making assumptions that 'enhanced' kinetics are responsible for the apparent 'electrocatalytic' activity of nanotubes.

Enzyme activity and stability was investigated through changing the surface chemistry at the nanotube interface. Gas-phase oxidative (air) and reductive (hydrogen) treatments switched the surface chemistry from hydrophilic to hydrophobic respectively to give a range of water contact angles between 0° and 140°. Detailed SEM and TEM characterisation revealed that upon high temperature treatment in hydrogen, the nanotubes were purified by removal of contaminant material.

Raman spectroscopy showed that I_D/I_G ratios increased upon both oxidation and hydrogen treatment indicating that more defects were added to the nanotubes. Samples with high impurity levels showed no change in I_D/I_G ratios upon treatment, however it has not been determined whether this was a resonance effect from the graphitic coating on the nanotubes.

The electrochemical activity and stability of laccase on the thermally-treated electrodes was compared using voltammetry and amperometric techniques. Both oxidative and reductive treatments improved laccase activity, resulting in higher current densities. Electrodes treated in oxygen and hydrogen atmospheres displayed the highest activities (x3 fold higher than untreated electrodes) and higher enzyme stability when measured over one week.

It can be concluded that the high temperature oxidation followed by reduction of the electrodes significantly improved the catalytic activity and stability of the enzyme. The treatment effectively removed the carbon contaminants from the nanotubes and increased the number additional defects. It is believed that removal of contaminant material improved communication with the enzyme and increased electroactive coverage, whilst addition of defects sites on the nanotubes improved electron transfer kinetics. Reports in the literature have recently shown that the introduction of defects lead to kinetic enhancement[90-93]. In addition the higher capacitances achieved with these treated electrodes could also improve electrokinetics by hydrating more enzyme molecules and improving mass-transport into the array.

The most significant limitation affecting the overall performance of the BFC half cell was the diffusion of oxygen to the enzyme. The nanotube electrodes consisted of tubes positioned in close proximity to each other (60-80 nm spacing), consequently limiting O_2 diffusion to the enzyme. To overcome this problem, a growth technique was developed by depositing a patterned gold layer on the substrate in order to mask nanotube growth and increase the spacing between the nanotube arrays. There was no initial improvement in catalytic activity using these patterned electrodes due to the appearance of gas bubbles within the pores which restricted electrolyte accessibility. This problem was rectified by oxidising the electrodes, which resulting in enhanced electrode wettability, removing the bubbles and improved electrocatalytic activity. The oxidised micro-patterned electrode displayed the highest current densities in this study due to the significant improvements in mass-transport and nanotube electrochemical activity. This work points to enhanced substrate transport as an essential component for further optimisation of biocatalytic electrodes

In summary, aCNT electrodes have been demonstrated as efficient hosts for laccase immobilisation. The high surface area of these materials proved to increase the electroactive coverage of enzyme, as evidenced by the higher current outputs with electrode area and length. Laccase displayed high catalytic activity and adsorption behaviour on nanotubes since very low loadings of enzyme resulted in limited current responses. Furthermore, the ability to tailor the electrochemical properties of the nanotubes through changing their surface chemistry and morphology by gas-phase chemistry has shown to be effective in improving the electrokinetics and overall electrode performance.

However, the commercial application of nanotube electrodes is still long-term since current densities are still far removed from the target needed for practical BFC devices (10 mA cm^{-2}). The main challenge is addressing the problem of substrate diffusion which was identified and addressed during this thesis. A model patterned electrode was developed using simple patterning techniques and the improvements in performance were demonstrable. Concerted efforts towards improving gas diffusion through novel electrode designs and understanding biocatalytic function and electron transfer at the enzyme-electrode interface will undoubtedly enable more applications in the energy market.

9 References

1. Rao, A., J. Maclay, and S. Samuelsen, *Efficiency of Electrochemical Systems.* J. Power Sources, 2004. **134**(2): p. 181-184.
2. Grove, W., *Alternating H_2 and O_2 Electrodes in a 'Gas Battery'.* Philos. Mag. J. Sci., 1839. **14**: p. 127.
3. Schoenbein, C.F., *On the voltaic polarization of certain solid and fluid substances.* Phil. Mag. J. Sci., 1839. **14**: p. 43-45.
4. Carnot, N.L.S., *Réflexions sur la puissance motrice du feu et sur les machines propres à développer cette puissance*. 1824, Paris: Bachelier.
5. Yan, Y.M., et al., *Carbon-Nanotube-Based Glucose/O_2 Biofuel Cells.* Advanced Materials, 2006. **18**(19): p. 2639-2643.
6. Yahiro, A.T., S.M. Lee, and D.O. Kimble, *Enzyme Utilising Biofuel Cell Studies.* Biochim. Biophys. Acta, 1964. **88**: p. 375-383.
7. Barton, S.C., *Handbook of Fuel Cells: Fundamentals Technology and Applications: Advance in Electrocatalysis, Materials, Diagnostics and Durability: Chapter 8*, ed. W. Vielstich, H. Yokokawa, and H.A. Gasteiger. Vol. 5. 2009: John Wiley & Sons Inc. 1038.
8. Pauling, L., *Molecular Architecture and Biological Reactions.* Chem. Eng. News, 1946. **24**(10): p. 1375-1377.
9. Haldane, J.B.S., *Enzymes*. 1930: Longmans, Green, London; (reprinted by MlT Press, Cambridge, 1965).
10. Sander, R., *Compilation of Henry's Law Constants for Inorganic and Organic Species of Potential Importance in Environmental Chemistry.* 1999. **20**(1): p. 1-107.
11. Barton, S.C., *Oxygen Transport in Composite Mediated Cathode.* Electrochimica Acta, 2005. **50**(10): p. 2145-2153.
12. Gasteiger, H.A., et al., *Activity benchmarks and requirements for Pt, Pt-alloy, and non-Pt oxygen reduction catalysts for PEMFCs.* Applied Catalysis B: Environmental, 2005. **56**(1-2): p. 9-35.
13. Blanford, C.F., R.S. Heath, and F.A. Armstrong, *A Stable Electrode For High-Potential, Electrocatalytic O_2 Reduction Based on Rational Attachment of a Blue Copper Oxidase to a Graphite Surface.* Chem. Commun., 2007: p. 1710-1712.
14. Mano, N., F. Mao, and A. Heller, *A Miniature Biofuel Cell Operating in a Physiological Buffer.* J. Am. Chem. Soc., 2002. **124**(44): p. 12962-12963.
15. Moore, C.M., et al., *Improving the Environment for Immobilised Dehydrogenase Enzymes by Modifying Nafion with Tetraalkylammonium Bromides.* Biomacromolecules, 2004. **5**: p. 1241-1247.
16. Bard, A.J. and L.R. Faulkner, *Electrochemical Methods: Fundamentals and Applications*. 2nd ed. 2001: Wiley.
17. Larminie, J. and A. Dicks, *Fuel Cell Systems Explained*. 2000, Chichester, England: John Wiley & Sons, Ltd.
18. Bullen, R.A., et al., *Biofuel cells and their development.* Biosensors and Bioelectronics, 2006. **21**: p. 2015-2045.
19. Gregory, D.P., *Fuel Cells*. 1972, London: Mills and Boon Ltd.
20. Marcus, R.A., *Electron Transfer Reactions in Chemistry: Theory and Experimental (Nobel Lecture).* Angew. Chem., 1993. **32**(8): p. 1111-1121.
21. Marcus, R.A. and N. Sutin, *Electron Transfers in Chemistry and Biology.* Biochim. Biophys. Acta, 1985. **811**(3): p. 265-322.

22. Solomon, E.I., U.M. Sundaram, and T.E. Machonkin, *Multocopper Oxidases and Oxygenases.* Chem. Rev., 1996. **96**: p. 2653-2605.
23. Gray, H.B. and J.R. Winkler, *Electron Tunneling Through Proteins.* Quart. Rev. Biophys., 2003. **36**: p. 341-372.
24. Zheng, W., et al., *Direct Electrochemistry of Multi-copper Oxidases at Carbon Nanotubes Noncovalently Functionalized with Cellulose Derivatives.* Electroanalysis, 2006. **18**(6): p. 587-594.
25. Duma, R. and S.D. Minteer, *Development of Bilirubin Oxidase Cathodes for Ethanol/Oxygen Biofuel Cells.* Polym Materials: Sci Eng, 2006. **94**: p. 592-593.
26. Ivnitski, D., et al., *Glucose Oxidase Anode for Biofuel Cell Based on Direct Electron Transfer.* Electrochemistry Communications, 2006. **8**(8): p. 1204-1210.
27. Cai, C. and J. Chen, *Direct Electron Transfer of Glucose Oxidase Promoted by Carbon Nanotubes.* Anal Biochem., 2004. **332**(1): p. 75-83.
28. Chen, T., et al., *A Miniature Biofuel Cell.* J. Am. Chem. Soc, 2001. **123**: p. 8630-8631.
29. Kamitaka, Y., et al., *Fructose/dioxygen biofuel cell based on direct electron transfer-type bioelectrocatalysis.* Phys. Chem. Chem. Phys., 2007. **9**: p. 1793–1801.
30. Zhang, M., A. Smith, and W. Gorski, *Carbon nanotube-chitosan system for electrochemical sensing based on dehydrogenase enzymes.* Anal. Chem., 2004. **76**(17): p. 5045-5050.
31. Sakai, H., et al., *A High-Power Glucose/Oxygen Biofuel Cell Operating Under Quiescent Conditions.* Energy Environ. Sci., 2009. **2**: p. 133–138.
32. Arning, M.D., B.L. Treu, and S.D. Minteer, *Citric acid cycle biomimic in an ammonium salt modified nafion membrane for fuel cell applications.* Polym Mater.: Sci. Eng., 2004. **90**: p. 566-569.
33. Beilke, M.C. and S.D. Minteer, *Immobilization of Glycolysis Enzymes in Hydrophobically Modified Nafion.* Polym. Mater.: Sci. Eng., 2006. **94**: p. 556-557.
34. Teodorescu, S.G., et al. *Development of an Enzymatic Biofuel Cell Stack*. in *209th ECS Meeting Abstracts*. 2006. Denver, CO.
35. Beilke, M.C., et al., *Enzymatic Biofuel Cells*. Micro Fuel Cells: Principles and Applications, Chapter 5, ed. T.S. Zhao. 2009.
36. Mano, N., F. Mao, and A. Heller, *Characteristics of a Miniature Compartment-Less Glucose−O2 Biofuel Cell and Its Operation in a Living Plant.* J. Am. Chem. Soc., 2003. **125**(21): p. 6588 6594.
37. Lim, K.G. and G.T.R. Palmore, *Microfluidic Biofuel Cells: The Influence of Electrode Diffusion Layer on Performance.* Biosensors and Bioelectronics, 2007. **22**(6): p. 941-947.
38. Guo, Y., J.-S. Hu, and L.-J. Wan, *Nanostructured Materials for Electrochemical Energy Conversion and Storage Devices.* Adv. Materials, 2008. **20**(15): p. 2878-2887.
39. Centi, G. and S. Perathoner, *The Role of Nanostructure in Improving the Performance of Electrodes for Energy Storage and Conversion.* Eur. J. Inorg. Chem., 2009. **2009**(26): p. 3851-3878.
40. Gooding, J.J., *Nanostructuring electrodes with carbon nanotubes: A review on electrochemistry and applications for sensing.* Electrochemica Acta, 2005. **50**: p. 3049-3060.

41. Osman, M.H., A.A. Shah, and F.C. Walsh, *Recent Progress and Continuing Challenges in Bio-Fuel Cells. Part I: Enzymatic Cells.* Biosensors and Bioelectronics, 2011. **26**(7): p. 3087–3102.
42. Kim, J., H. Jia, and P. Wang, *Challenges in Biocatalysis for Enzyme-Based Biofuel Cells.* Biotechnology Advances, 2006. **24**(3): p. 296-308.
43. Ivanov, I., T. Vidaković-Koch, and K. Sundmacher, *Recent Advances in Enzymatic Fuel Cells: Experiments and Modeling.* Energies, 2010. **3**(4): p. 803-846.
44. Barton, S.C., J. Gallaway, and P. Atanassov, *Enzymatic Biofuel Cells for Implantable and Microscale Devices.* Chemical Reviews, 2004. **104**(10): p. 4867-4886.
45. Willner, B., E. Katz, and I. Willner, *Electrical Contacting of Redox Proteins by Nanotechnological Means.* Current Opinion in Biotechnology, 2006. **17**: p. 589-596.
46. Asuri, P., et al., *The Protein-Nanomaterial Interface.* Current Opinion in Biotechnology, 2006. **17**(6): p. 562-568.
47. Kwon, K.Y., et al., *Nanoscale Enzyme Reactors in Mesoporous Carbon for Improved Performance and Lifetime of Biosensors and Biofuel Cells.* Biosensors and Bioelectronics, 2010. **26**: p. 655–660.
48. Habrioux, A., et al., *Enhancement of the Performances of a Single Concentric Glucose/O_2 Biofuel Cell by Combination of Bilirubin Oxidase/Nafion Cathode and Au-Pt Anode.* Electrochem. Commun., 2009. **11**(1): p. 111–113.
49. Choi, Y.K., et al., *A Hybrid Biofuel Cell Based on Electrooxidation of Glucose using Ultra-Small Silicon Nanoparticles.* Biosens. Bioelectron., 2009. **24**(10): p. 3103–3107.
50. Deng, L., et al., *A Biofuel Cell with Enhanced Performance by Multilayer Biocatalyst Immobilized on Highly Ordered Macroporous Electrode.* Biosensors and Bioelectronics, 2008. **24**(2): p. 329-333.
51. Mano, N., et al., *A miniature biofuel cell operating at 0.78 V.* Chem. Comm., 2003.
52. Mano, N., F. Mao, and A. Heller, *A Miniature Membraneless Biofuel Cell Operating at 0.36 V under Physiological Conditions.* Journal Of The Electrochemical Society, 2003. **150**(8): p. A1136-A1138.
53. Mano, N., F. Mao, and A. Heller, *A Miniature Membrane-less Biofuel Cell Operating at +0.6V under Physiological Conditions.* ChemBioChem, 2004. **5**: p. 1703-1705.
54. Coman, V., et al., *A membrane-, mediator-, cofactor-less glucose/oxygen biofuel cell.* Phys. Chem. Chem. Phys., 2008. **10**(40): p. 6093-6096.
55. Palmore, G.T.R., et al., *A Methanol/Dioxygen Biofuel Cell that uses NAD(+)-Dependent Dehydrogenases as Catalysts: Application of an Electro-Enzymatic Method to Regenerate Nicotinamide Adenine Dinucleotide at Low Overpotentials.* J. Electroanal. Chem., 1998. **443**(1): p. 155–161.
56. Akers, N.L., C.M. Moore, and S.D. Minteer, *Development of Alcohol/O_2 Biofuel Cells using Salt-Extracted Tetrabutylammonium Bromide/Nafion Membranes to Immobilize Dehydrogenase Enzymes.* Electrochim. Acta., 2005. **50**(12): p. 2521–2525.

57. Topcagic, S. and S.D. Minteer, *Development of a Membraneless Ethanol/Oxygen Biofuel Cell.* Electrochemica Acta, 2006. **51**(11): p. 2168-2172.
58. Yan, Y.-M., et al., *An Ethanol/O_2 Biofuel Cell Based on an Electropolymerized Bilirubin Oxidase/Pt Nanoparticle Bioelectrocatalytic O_2-Reduction Cathode.* Adv. Materials, 2009. **21**(42): p. 4275-4279.
59. Arechederra, R.L. and S.D. Minteer, *Complete Oxidation of Glycerol in an Enzymatic Biofuel Cell.* Fuel Cells, 2009. **9**(1): p. 63–69.
60. Vincent, K.A., et al., *Electrocatalytic hydrogen oxidation by an enzyme at high carbon monoxide or oxygen levels.* Proc. Natl Acad. Sci. USA, 2005. **102**(47): p. 16951-16954.
61. Vincent, K.A., et al., *Electricity from Low-level H_2 in Still Air - an Ultimate Test for an Oxygen Tolerant Hydrogenase.* Chem. Commun., 2006: p. 5033-5035.
62. Iijima, S., *Helical Microtubules of Graphitic Carbon.* Nature, 1991. **354**: p. 56-58.
63. Treacy, M.M.J., T.W. Ebbesen, and J.M. Gibson, *Exceptionally High Young's Modulus Observed for Individual Carbon Nanotubes.* Nature, 1996. **381**: p. 678 - 680.
64. Yu, M.F., et al., *Tensile Loading of Ropes of Single Wall Carbon Nanotubes and their Mechanical Properties.* Phys. Rev. Lett., 2000. **84**(24): p. 5552-5555.
65. Ebbesen, T.W., et al., *Electrical Conductivity of Individual Carbon Nanotubes.* Nature, 1996. **382**: p. 54-56.
66. Harris, P.J.F., *Carbon Nanotube Science: Synthesis, Properties and Applications*. 2009: Cambridge University Press.
67. Geim, A.K. and K.S. Novoselov, *The rise of graphene.* Nature Materials, 2007. **6**(3): p. 183-191.
68. Zheng, L.X., et al., *Ultralong Single-Wall Carbon Nanotubes.* Nature Materials, 2004. **3**: p. 673-676.
69. Wang, X., et al., *Fabrication of Ultralong and Electrically Uniform Single-Walled Carbon Nanotubes on Clean Substrates.* Nano Lett., 2009. **9**(9): p. 3137-3141.
70. Dumitrescu, I., P.R. Unwin, and J.V. Macpherson, *Electrochemistry at Carbon Nanotubes: Perspective and Issues.* Chem. Commun., 2009: p. 6886-6901.
71. Callister, W.D., *Materials Science and Engineering: An Introduction*. 6th ed. 2003: John Wiley and Sons, Inc.
72. Wilder, J.W.G., et al., *Electronic Structure of Atomically Resolved Carbon Nanotubes.* Nature, 1998. **391**: p. 59-62.
73. Odom, T.W., et al., *Atomic Structure and Electronic Properties of Single-walled Carbon Nanotubes.* Nature, 1998. **391**: p. 62-64.
74. Blaze, X., et al., *Hybridisation Effects and Metallicity in Small Radius Carbon Nanotubes.* Phys Rev Lett., 1994. **72**(12): p. 1878-1881.
75. Heller, I., et al., *Electrochemistry at Single-Walled Carbon Nanotubes: The Role of Band Structure and Quantum Capacitance.* J Am Chem Soc., 2006. **128**(22): p. 7353-7359.
76. Tans, S.J., et al., *Individual Single-wall Carbon Nanotubes as Quantum Wires.* Nature, 1997. **386**: p. 474-477.

77. Ahlskog, M., et al., *Single-Electron Transistor Made of Two Crossing Multiwalled Carbon Nanotubes and its Noise Properties.* Appl. Phys. Lett., 2000. **77**(24): p. 4037-4040.
78. Dresselhaus, M.S., et al., *Raman Spectroscopy of Carbon Nanotubes.* Physics Reports, 2005.
79. Maruyama, P., *http://www.photon.t.u-tokyo.ac.jp/~maruyama/kataura/kataura.html.*, The University of Tokyo (2008) Retrieved July 2011 from.
80. Rao, A.M., et al., *Diameter-Selective Raman Scattering from Vibrational Modes in Carbon Nanotubes.* Science, 1997. **275**(5297): p. 187-191.
81. Jorio, A., et al., *Structural (n,m) Determination of Isolated Single-Wall Carbon Nanotubes by Resonant Raman Scattering.* Phys. Rev. Lett., 2001. **86**(6): p. 1118-1121.
82. Jorio, A., et al., *Characterising Carbon Nanotube Samples with Resonance Raman Scattering.* New Journal of Physics, 2003. **5**: p. 139.1-139.17.
83. Bandow, S., S. Asaka, and Y. Saito, *Effect of Van der Waals Interactions on the Raman Modes in Single Walled Carbon Nanotubes.* Phys Rev Lett., 2001. **86**(17): p. 3895-3898.
84. Kavan, L. and L. Dunsch, *Spectroelectrochemistry of Carbon Nanostructures.* ChemPhysChem., 2007. **8**(7): p. 974-998.
85. Bachilo, S.M., et al., *Structure-Assigned Optical Spectra of Single-Walled Carbon Nanotubes.* Science, 2002. **298**(5602): p. 2361-2366.
86. Kataura, H., et al., *Optical properties of single-wall carbon nanotubes.* Synthetic Metals, 1999. **103**(1-3): p. 2555-2558.
87. McCreery, R.L., *Advanced Carbon Electrode Materials for Molecular Electrochemistry.* Chem. Rev., 2008. **108**: p. 2646-2687.
88. Pumera, M., *The Electrochemistry of Carbon Nanotubes: Fundamentals and Applications.* Chem. Eur. J., 2009. **15**: p. 4970-4978.
89. Banks, C.E., et al., *Carbon Nanotubes Contain Metal Impurities Which Are Responsible for the "Electrocatalysis" Seen at Some Nanotube-Modified Electrodes.* Angew. Chem. Int. Ed., 2006. **45**: p. 2533-2537.
90. Moore, R.R., C.E. Banks, and R.G. Compton, *Basal Plane Pyrolytic Graphite Modified Electrodes: Comparison of Carbon Nanotubes and Graphite Powder as Electrocatalysts.* Anal. Chem., 2004. **76**: p. 2677-2682.
91. Banks, C.E., et al., *Investigation of Modified Basal Plane Pyrolytic Graphite Electrodes: Definitive Evidence for the Electrocatalytic Properties of the Ends of Carbon Nanotubes.* Chem. Commun., 2004: p. 1804-1805.
92. Banks, C.E., et al., *Electrocatalysis at Graphite and Carbon Nanotube Modified Electrodes: Edge-Plane Sites and Tube Ends are the Reactive Sites.* Chem. Commun., 2005: p. 829-841.
93. Holloway, A.F., et al., *The Influence of Edge-Plane Defects and Oxygen-Containing Surface Groups on the Voltammetry of Acid-treated, Annealed and "Super-annealed" Multiwalled Carbon Nanotubes.* J Solid State Electrochem, 2008. **12**: p. 1337-1348.
94. Pumera, M., T. Sasaki, and H. Iwai, *Relationship Between Carbon Nanotube Structure and Electrochemical Behavior: Heterogeneous Electron Transfer at Electrochemically Activated Carbon Nanotubes.* Chem Asian J., 2008. **3**(12): p. 2046-2055.

95. Ambrosi, A. and M. Pumera, *Nanographite Impurities Dominate Electrochemistry of Carbon Nanotubes.* Chem. Eur. J., 2010. **16**: p. 10946 -10949.
96. Jones, C.P., et al., *Use of High-Purity Metal-Catalyst-Free Multiwalled Carbon Nanotubes to Avoid Potential Experimental Misinterpretations.* Langmuir, 2007. **23**: p. 9501-9504.
97. Liu, J., et al., *Achieving Direct Electrical Connection to Glucose Oxidase Using Aligned Single Walled Carbon Nanotube Arrays.* Electroanalysis (N.Y.), 2005. **17**: p. 38-46.
98. Li, J., et al., *Novel Three-Dimensional Electrodes: Electrochemical Properties of Carbon Nanotube Ensembles.* J. Phys. Chem. B, 2002. **106**: p. 9299-9305.
99. Sánchez, S., E. Fàbregas, and M. Pumera, *Electrochemical Activation of Carbon Nanotube/Polymer Composites.* Phys. Chem. Chem. Phys., 2009. **11**: p. 182-186.
100. Holloway, A.F., et al., *Electrochemical Opening of Single-Walled Carbon Nanotubes Filled with Metal Halides and with Closed Ends.* J. Phys. Chem. C., 2008. **112**: p. 10389-10397.
101. Heller, I., et al., *Individual Single-Walled Carbon Nanotubes as Nanoelectrodes for Electrochemistry.* Nano Lett., 2005. **5**(1): p. 137-142.
102. Day, T.M., et al., *Electrochemical Templating of Metal Nanoparticles and Nanowires on Single-Walled Carbon Nanotube Networks.* J. Am. Chem. Soc., 2005. **127**(30): p. 10639-10647.
103. Wilson, N.R., et al., *Assessment of the Electrochemical Behavior of Two-Dimensional Networks of Single-Walled Carbon Nanotubes.* Anal. Chem., 2006. **78**(19): p. 7006-7015.
104. Dumitrescu, I., N.R. Wilson, and J.V. Macpherson, *Functionalizing Single-Walled Carbon Nanotube Networks: Effect on Electrical and Electrochemical Properties.* J. Phys. Chem. C., 2007. **111**: p. 12944-12953.
105. Pumera, M. and H. Iwai, *Multicomponent Metallic Impurities and Their Influence upon the Electrochemistry of Carbon Nanotubes.* J. Phys. Chem. C., 2009. **113**(11): p. 4401-4405.
106. Pumera, M. and H. Iwai, *Metallic Impurities within Residual Catalyst Metallic Nanoparticles Are in Some Cases Responsible for "Electrocatalytic" Effect of Carbon Nanotubes.* Chem Asian J., 2009. **4**(4): p. 554-560.
107. Šljukić, B., C.E. Banks, and R.G. Compton, *Iron Oxide Particles Are the Active Sites for Hydrogen Peroxide Sensing at Multiwalled Carbon Nanotube Modified Electrodes.* Nano Lett., 2006. **6**(7): p. 1556-1558.
108. Lyon, J.L. and K.J. Stevenson, *Anomalous Electrochemical Dissolution and Passivation of Iron Growth Catalysts in Carbon Nanotubes.* Langmuir, 2007. **23**: p. 11311-11318.
109. Chen, P. and R.L. McCreery, *Control of Electron Transfer Kinetics at Glassy Carbon Electrodes by Specific Surface Modification.* Anal. Chem., 1996. **68**(22): p. 3958-3965.
110. Kawaik, J., P.J. Kulesza, and Z. Galus, *A Search for Conditions Permitting Model Behavior of the Fe $(CN)_6^{3-/4-}$ System.* 1987. **226**(1-2): p. 305-314.
111. Saito, Y. and Y. Tani, *Diameters of Single-Wall Carbon Nanotubes Depending on Helium Gas Pressure in an Arc Discharge.* J. Phys. Chem. B, 2000. **104**(11): p. 2495–2499.

112. Dresselhaus, M.S., G. Dresselhaus, and K.e.a. Sugihara, *Graphite Fibers and Filaments*. 1988, Berlin: Springer-Verlag.
113. Govindaraj, A. and C.N.R. Rao, *Organometallic Precursor Route to Carbon Nanotubes.* Pure Appl. Chem., 2002. **74**(9): p. 1571-1580.
114. Baker, R.T.K., M.A. Barber, and P.S. Harris, *Nucleation and Growth of Carbon Deposits from the Nickel Catalysed Decomposition of Acetylene.* J. Catalysis, 1972. **26**(1): p. 51-62.
115. Deck, C.P. and K. Vecchio, *Prediction of Carbon Nanotube Growth Success by the Analysis of Carbon-Catalyst Binary Phase Diagrams.* Carbon, 2006. **44**(2): p. 267-275.
116. Dai, H., et al., *Controlled Chemical Routes to Nanotube Architectures, Physics, and Devices.* J. Phys. Chem. B., 1999. **103**(51): p. 11246-11255.
117. Ren, Z.F., et al., *Synthesis of Large Arrays of Well-aligned Carbon Nanotubes on Glass.* Science, 1998. **282**(5391): p. 1105-1107.
118. Bower, C., et al., *Plasma-induced Alignment of Carbon Nanotubes.* Phys. Lett., 2000. **77**(6): p. 830-833.
119. Delzeit, L., et al., *Growth of Multiwall Carbon Nanotube in an Inductively Coupled Plasma Reactor.* Appl. Phys. Lett., 2002. **91**(9): p. 6027-6033.
120. Baker, R.T.K., et al., *Formation of Filamentous Carbon from Iron Cobalt and Chromium Catalysed Decomposition of Acetylene.* J. Catalysis, 1973. **30**(1): p. 86-95.
121. Baker, R.T.K. and P.S. Harris, *The Formation of Filamentous Carbon.* Chem. Phys. Carbon, 1978. **14**: p. 83-165.
122. Chhowalla, M., et al., *Growth Process Conditions of Vertically Aligned Carbon Nanotubes Using Plasma Enhanced Chemical Vapour Deposition.* J. Appl. Phys., 2001. **90**(10): p. 5038-5317.
123. Bower, C., et al., *Nucleation and Growth of Carbon Nanotubes by Microwave Plasma Chemical Vapour Deposition.* Appl. Phys. Lett., 2000. **77**(17): p. 2767-2770.
124. Sinnott, S.B., et al., *Model of Carbon Nanotube Growth Through Chemical Vapour Deposition.* Chem. Phys. Lett., 1999. **315**: p. 25-30.
125. Amelinckx, S., et al., *A Formation Mechanism for Catalytically Grown Helix-Shaped Graphite Nanotubes.* Science, 1994. **265**(5172): p. 635-639.
126. Baker, R.T.K., G.R. Gadsby, and S. Terry, *Formation of Carbon Filaments from Catalysed Decomposition of Hydrocarbons.* Carbon, 1975. **13**: p. 245.
127. Rinzler, A.G., et al., *Large scale purification of single-wall carbon nanotubes: process, product and characterisation.* Applied Physics A Materials Science and Processing, 1998. **67**(1): p. 29-37.
128. Liu, J., et al., *Oxygen-Containing Functional Groups on Single-Wall Carbon Nanotubes: NEXAFS and Vibrational Spectroscopic Studies.* J. Am. Chem. Soc, 2001. **123**: p. 10699-10704.
129. Makris, T.D., et al., *Purification of multi-walled carbon nanotubes grown by thermal CVD on Fe-based catalyst.* Advances in Science and Technology, 2006. **48**: p. 50-54.
130. Tran, M.Q., et al., *Thermal oxidative cutting of multi-walled carbon nanotubes.* Carbon, 2007. **45**: p. 2341-2350.
131. Bismarck, A., et al., *Basic and acidic surface oxides on carbon fiber and their influence on the expected adhesion to polyamide.* Carbon, 1999. **159**(2-3): p. 341-350.

132. Andrews, R., et al., *Purification and Structural Annealing of Multiwalled Carbon Nanotubes.* Carbon, 2001. **39**(11): p. 1681-1687.
133. Bandow, S., et al., *Purification of Single-wall Carbon Nanotubes by Microfiltration.* J. Phys. Chem. B., 1997. **101**(44): p. 8839-8842.
134. Shelimov, K.B., et al., *Purification of Single-wall Nanotubes by Ultrasonically Assisted Filtration.* Chem. Phys. Lett., 1998. **282**(5-6): p. 429-434.
135. Aizawa, M. and M.S.P. Shaffer, *Silylation of Multi-walled Carbon Nanotubes.* Chem. Phys. Lett., 2003. **368**(1-2): p. 121-124.
136. Riggs, J.E., Z.X. Guo, and D.L. Carroll, *Strong Luminescence of Solubilized Carbon Nanotubes.* J. Amer. Chem. Soc., 2000. **122**(24): p. 5879-5880.
137. Tasis, D., et al., *Soluble Carbon Nanotubes.* Chemistry- A European Journal, 2003. **9**(17): p. 4000-4008.
138. Taylor, R. and D.R.M. Walton, *The Chemistry of Fullerenes.* Nature, 1993. **363**: p. 685-693.
139. Mickelson, E.T., I.W. Chiang, and J.L. Zimmerman, *Fluorination of Single-wall Carbon Nanotubes.* Chem. Phys. Lett., 1998. **296**: p. 188-194.
140. Chen, Y., et al., *Chemical Attachment of Organic Functional Groups to Single-walled Carbon Nanotube Material.* Journal of Materials Research, 1998. **13**: p. 2423-2431.
141. Holzinger, M., et al., *Functionalisation of Single-walled Carbon Nanotubes with (R-)Oxycarbonyl Nitrenes.* J. Amer. Chem. Soc., 2003. **125**(28): p. 8566-8580.
142. Banjeree, S. and S.S. Wong, *Formation of CdSe nanocrystals onto oxidized, ozonized single-walled carbon nanotube surfaces.* Chem. Comm., 2004: p. 1866-1867.
143. Blanford, C.F., et al., *Efficient Electrocatalytic Oxygen Reduction by the 'Blue Copper Oxidase, Laccase, Directly Attached to Chemically Modified Carbons.* Faraday Discuss., 2008.
144. Sosna, M., et al., *Monolayer Anthracene and Athraquinone Modified Electrodes as Platforms for Trametes hirsuta laccase Immobilisation.* Phys. Chem. Chem. Phys., 2010. **12**: p. 10018-10026.
145. Goldsmith, B.R., et al., *Conductance-Controlled Point Functionalization of Single-Walled Carbon Nanotubes.* Science, 2007. **315**(5808): p. 77-81.
146. Richard, C., et al., *Supramolecular Self-Assembly of Lipid Derivatives on Carbon Nanotubes.* Science, 2003. **300**(5620): p. 775-778.
147. Islam, M.F., et al., *High Weight Fraction Surfactant Solubilization of Single-Wall Carbon Nanotubes in Water.* Nano Lett., 2003. **3**(2): p. 269-273.
148. Kang, M., S.J. Myung, and H.-J. Jin, *Nylon 610 and Carbon Nanotube Composite by In Situ Interfacial Polymerization.* Polymer, 2006. **47**(11): p. 3961-3966.
149. Gallaway, J.W. and S.C. Barton, *Kinetics of Redox Polymer-Mediated Enzyme Electrodes.* Journal of the American Chemical Society, 2008. **130**(26): p. 8527-8536.
150. Piontek, K., M. Antorini, and T. Choinowski, *Crystal Structure of Laccase from the Fungus Trametes versicolor at 1.90-Å Resolution Containing a Full Complement of Coppers.* The Journal of Biological Chemistry, 2002. **277**(40): p. 37663-37669.

151. Solomon, E.I., U.M. Sundaram, and T.E. Machonkin, *Multicopper Oxidases and Oxygenases.* Chem. Rev., 1996. **96**: p. 2563-2606.
152. Morozova, O.V., et al., *"Blue" Laccases.* Bioelectrochemistry (Moscow), 2007. **72**(10): p. 1136-1150.
153. Yoshida, H., *Chemistry of lacquer (Urushi).* J. Chem. Soc, 1883. **43**: p. 472-486.
154. Sadhasivam, S., et al., *Production, Purification and Characterisation of Mid-Redox Potential Laccase from a Newly Isolated Trichoderma harzianum WL1.* Process Biochemistry, 2008. **43**: p. 736-742.
155. Thurston, C.F., *The Structure and Function of Fungal Laccase.* Microbiology, 1994. **140**: p. 19-26.
156. Schlosser, D., R. Grey, and W. Fritsche, *Patterns of Ligninolytic Enzymes in T. versicolor. Distribution of Extra- and Intracellular Enzyme Activities During Cultivation on Glucose, Wheat Straw and Beech Wood.* Appl. Microbiol Biotechnol, 1997. **47**: p. 412-418.
157. Valásková, V. and P. Baldrain, *Estimation of Bound and Free Fractions of Lignocellulose-Degrading Enzymes of Wood-Rotting Fungi Pleurotus ostreatus, T. versicolor and Piptoporus betulinus.* Res Microbiol., 2005. **157**(2): p. 119-124.
158. Revenker, M.S. and S.S. Lele, *Enhanced Production of Laccase Using a New Isolate of White Rot Fungus WR-1.* Process Biochemistry, 2006. **41**(3): p. 581-588.
159. Rogalski, J., et al., *Production of Laccase, Lignin Peroxidase and Manganese-Dependant Peroxidase by Various Studies of Trametes versicolor Depending on Culture Conditions.* Acta Microbiologica Polinica, 1991. **40**(3/4): p. 221-234.
160. Collins, P.J. and A.D.W. Dobson, *Regulation of Laccase Gene Transcription in Trametes versicolor.* Appl. Environ. Microbiol., 1997. **63**: p. 3444-3450.
161. Brijwani, K., A. Rigdon, and P.V. Vadlani, *Fungal Laccases: Production, Function, and Applications in Food Processing.* Enzyme Research, 2010. **2010**: p. 1-10.
162. López, M., et al., *Cell growth and Trametes versicolor laccase production in transformed Pichia pastoris cultured by solid-state or submerged fermentations.* Journal of Chemical Technology and Biotechnology, 2010. **85**(4): p. 435-440.
163. Scopes, R.K., *Protein Purification Principles and Practice*. Third Edition ed. 1994: Springer-Verlag.
164. Ranocha, P., et al., *Biochemical Characterization, Molecular Cloning and Expression of Laccases - A Divergent Gene Family - In Poplar.* Eur J Biochem., 1999. **259**(1-2): p. 485-495.
165. Woolery, G.L., et al., *X-ray Absorption Study of Rhus Laccase: Evidence For A Copper-Copper Interaction, which Disappears on Type 2 Copper Removal.* Biochemistry, 1984. **23**(15): p. 3428-3434.
166. Malmström, B.G., B. Reinhammar, and T. Vänngård, *The State of Copper in Stellacyanin and Laccase from the Laquer Tree Rhus vernicefera.* Biochim. Biophys. Acta, 1970. **205**: p. 48-57.
167. Harris, E.L.V. and S. Angal, *Protein Purification Methods: A Practical Approach*, ed. D. Rickwood and B.D. Hames. 1995: Oxford University Press.

168. Kavanagh, K., *Fungi: Biology and Applications*. 2005: John Wiley and Sons.
169. Cracknell, J.A., K.A. Vincent, and F.A. Armstrong, *Enzymes as Working or Inspirational Electrocatalysts for Fuel Cells and Electrolysis.* Chem. Rev, 2008. **108**(7): p. 2439-2461.
170. Shleev, S., et al., *Direct Electron Transfer Between Copper-Containing Proteins and Electrodes.* Biosens. Bioelectron., 2005. **20**(12): p. 2517-2554.
171. Messerschmidt, A., *Comprehensive Biological Catalysis, Chapter: Copper Metalloenzymes*, ed. M. Sinnet. Vol. 3. 1997: Academic Press Ltd. 401-426.
172. Singh, K., *Laccase*, S.a.B.M.o.T.v. laccase, Editor. 2010: University of Manchester.
173. Bertrand, T., et al., *Crystal Structure of a Four-Copper Laccase Complexed with an Arylamine: Insights into Substrate Recognition and Correlation with Kinetics.* Biochemistry, 2002. **41**(23): p. 7325-7233.
174. Shleev, S., et al., *Direct electron transfer reactions of laccases from different origins on carbon electrodes.* Bioelectrochemistry, 2005. **67**: p. 115-124.
175. Shin, W., et al., *Chemical and Spectroscopic Definition of the Peroxide-Level Intermediate in the Multicopper Oxidases: Relevance to the Catalytic Mechanism of Dioxygen Reduction to Water.* J. Am. Chem. Soc., 1996. **118**(13): p. 3202-3215.
176. Lee, S.-K., et al., *Nature of the Intermediate Formed in the Reduction of O2 to H2O at the Trinuclear Copper Cluster Active Site in Native Laccase.* J. Am. Chem. Soc., 2002. **124**(21): p. 6180-6193.
177. Reinhammer, B.R., *Oxidation-Reduction Potentials of the Electron Acceptors of Laccase and Stellacyanin.* Biochim. Biophys. Acta, 1972. **275**(2): p. 245-259.
178. Baldrian, P., *Fungal laccases-occurence and properties.* FEMS Microbiol Rev, 2006. **30**: p. 215-242.
179. Shleev, S., et al., *Direct Electron Transfer Between Copper Containing Proteins and Electrodes.* Biosensors and Bioelectronics, 2005. **20**(12): p. 2517-2554.
180. Shleev, S.V., et al., *Comparison of Physico-Chemical Characteristics of Four Laccases from Different Basidiomycetes.* Biochimie, 2004. **86**(9-10): p. 693-703.
181. Xu, F., et al., *A Study of a Series of Recombinant Fungal Laccases and Bilirubin Oxidase that Exhibit Significant Differences in Redox Potential, Substrate Specificity, and Stability.* Biochim Biophys Acta., 1996. **1292**(2): p. 303-311.
182. Schneider, P., et al., *Characterisation of Coprinus cinerus laccase.* Enzyme Microb. Tech., 1999. **25**(6): p. 502-508.
183. Enguita, F.J., et al., *Crystal Structure of a Bacterial Endospore Coat Component: A Lacasse with Enhanced Thermostability Properties.* J Biol Chem., 2003. **278**(21): p. 19416-19425.
184. Palmer, A.E., S.K. Lee, and E.I. Solomon, *Decay of the Peroxide Intermediate in Laccase: Reductive Cleavage of the O-O Bond.* J Am Chem Soc., 2001. **123**(27): p. 6591-6599.

185. Xu, F., et al., *Targeted Mutations in a Trametes villosa Laccase. Axial perturbations of the T1 copper.* J Biol Chem., 1999. **274**(18): p. 12372-12375.
186. Xu, F., et al., *Site-Directed Mutations in Fungal Laccase: Effect on Redox Potential, Activity and pH Profile.* Biochem J., 1998. **334**(Pt 1): p. 63-70.
187. Klonowska, A., et al., *Characterization of a Low Redox Potential Laccase from the Basidiomycete C30.* Eur. J. Biochem., 2002. **269**(24): p. 6119-6125.
188. Willner, I.I. and E. Katz, *Integration of Layered Redox Proteins and Conductive Supports for Bioelectronic Applications.* Angew Chem Int Ed Engl., 2000. **39**(7): p. 1180-1218.
189. Kano, K. and T. Ikeda, *Fundamentals and Practices of Mediated Bioelectrocatalysis.* Anal. Sci., 2000. **16** (10): p. 1013-1021.
190. Ikeda, T. and K. Kano, *An Electrochemical Approach to the Studies of Biological Redox Reactions and their Applications to Biosensors, Bioreactors, and Biofuel Cells.* J Biosci Bioeng., 2001. **92**(1): p. 9-18.
191. Palmisano, F., P.G. Zambonin, and D. Centonze, *Amperometric Biosensors Based on Electrosynthesised Polymeric Films.* Fresenius J Anal Chem., 2000. **366**(6-7): p. 586-601.
192. Tarasevich, M.R., *Comprehensive Treatise of Electrochemistry*, ed. S. Srinivasan, et al. Vol. 10. 1985, New York: Plenum Press.
193. Tarasevich, M.R., et al., *Electrocatalysis of a Cathodic Oxygen Reduction by Laccase.* Bioelectrochem Bioenerg., 1979. **6**(3): p. 393-403.
194. Yaropolov, A.I., et al., *Laccase. Properties, Catalytic Mechanism, and Applicability.* Appl Biochem Biotechnol, 1994. **49**(3): p. 257-280.
195. Armstrong, F.A., H.A. Heering, and J. Hirst, *Reactions of Complex Metalloproteins Studied by Protein-Film Voltammetry.* Chemical Society Reviews, 1997. **26**: p. 169-179.
196. Niki, K. and B.W. Gregory, *Electrochemistry of Redox-Active Protein Films Immobilized on Self-Assembled Monolayers of Organothiols*. Biomolecular Films. Design, Function, and Applications, ed. J.F. Rusling. 2003, New York: Marcel Dekker. 65-98.
197. Xiao, Y., et al., *"Plugging into Enzymes": Nanowiring of Redox Enzymes by a Gold Nanoparticle.* Science, 2003. **299**(5614): p. 1877-1881.
198. Davis, J.J., R.J. Coles, and H.A.O. Hill, *Protein Electrochemistry at Carbon Nanotube Electrodes.* J Electroanal. Chem., 1997. **440**(1-2): p. 279-282.
199. Gooding, J.J., et al., *Protein Electrochemistry Using Aligned Carbon Nanotubes Arrays.* J. Am. Chem. Soc, 2003. **125**: p. 9006-9007.
200. Bowden, E.F., F.M. Hawkridge, and H.N. Blount, *Electrochemical Aspects of Bioenergetics*. Comprehensive Treatise of Electrochemistry, ed. S. Srinivasan, et al. Vol. 10. 1985, New York: Plenum. 287-346.
201. Armstrong, F.A., *Probing Metalloproteins by Voltammetry*. Bioinorganic Chemistry, Structure and Bonding. Vol. 72. 1990, Berlin: Springer-Verlag. 137-221.
202. Eddowes, M.J. and H.A.O. Hill, *Novel Method for the Investigation of the Electrochemistry of Metalloproteins: Cytochrome c.* J. Chem. Soc., Chem. Commun., 1977, 1977(21): p. 771-772.
203. Armstrong, F.A., H.A.O. Hill, and N.J. Walton, *Direct Electrochemistry of Redox Proteins.* Acc. Chem. Res., 1988. **21**(11): p. 407-413.

204. Blanford, C.F. and F.A. Armstrong, *The Pyrolytic Graphite Surface as an Enzyme Substrate: Microscopic and Spectroscopic Studies.* J Solid State Electrochem, 2006. **10**(10): p. 826-832.
205. Hirst, J. and F.A. Armstrong, *Fast Scan Cyclic Voltammetry of Protein Films of Pyrolytic Graphite Edge Electrodes: Characteristics of Electron Exchange.* Anal Chem., 1998. **70**(23): p. 5062-5071.
206. Delamar, M., et al., *Covalent Modification of Carbon Surfaces by Grafting of Functionalized Aryl Radicals Produced from Electrochemical Reduction of Diazonium Salts.* J. Am. Chem. Soc., 1992. **114**(14): p. 5883-5884.
207. Allongue, P., et al., *Covalent Modification of Carbon Surfaces by Aryl Radicals Generated from the Electrochemical Reduction of Diazonium Salts.* J. Am. Chem. Soc., 1997. **119**(1): p. 201-207.
208. Shleev, S., et al., *Direct Heterogenous Electron Transfer Reactions of Trametes hirsuta Laccase at Bare and Thiol-modified Gold Electrodes.* Electroanalysis, 2006. **18**(19-20): p. 1901-1908.
209. Ramirez, P., et al., *Direct Electron Transfer from Graphite and Functionalized Gold Electrodes to T1 and T2/T3 Copper Centers of Bilirubin Oxidase.* Biochim. Biophys. Acta, 2008. **1777**(10): p. 1364-1369.
210. Gupta, G., V. Rajendran, and P. Atanassov, *Bioelectrocatalysis of Oxygen Reduction Reaction by Laccase on Gold Electrodes.* Electroanalysis, No., 2004. **16**(13-14): p. 1182-1185.
211. Klis, M., et al., *Electroreduction of Laccase Covalently Bound to rganothiol Monolayers on Gold Electrodes.* Electrochimica Acta, 2007. **52**: p. 5591-5598.
212. Chou, A., et al., *Demonstration of the Importance of Oxygenated Species at the Ends of Carbon Nanotubes for their Favourable Electrochemical Properties.* Chem. Commun., 2005: p. 842-844.
213. Gooding, J.J., et al., *The Effects of the Lengths and Orientations of Single-Walled Carbon Nanotubes on the Electrochemistry of Nanotube-Modified Electrodes.* Electrochem. Commun., 2007. **9**(7): p. 1677-1683.
214. Dagys, M., et al., *Laccase-Gold Nanoparticle Assisted Bioelectrocatalytic Reduction of Oxygen.* Electrochem. Commun., 2010. **12**(7): p. 933-935.
215. Palmore, G.T.R. and H.-H. Kim, *Electro-enzymatic reduction of dioxygen to water in the cathode compartment of a biofuel cell.* Journal of Electroanalytical Chemistry, 1999. **464**: p. 110-117.
216. Soukharev, V., N. Mano, and A. Heller, *A Four-Electron O_2-Electroreduction Biocatalyst Superior to Platinum and a Biofuel Cell Operating at 0.88 V.* J. Am. Chem. Soc., 2004. **126**(27): p. 8368-8369.
217. Christenson, A., et al., *Direct Electron Transfer between Ligninolytic Redox Enzymes and Electrodes.* Electroanalysis, 2004. **16**: p. 1074-1092.
218. Monk, P.M.S., *Fundamentals of Electroanalytical Chemistry*. 2001: Wiley.
219. Compton, R.G. and C.E. Banks, *Understanding Voltammetry*. 2007: World Scientific Publishing Co. Pte. Ltd.
220. Bartlett, P.N., *Bioelectrochemistry: Fundamentals, Experimental Techniques and Applications*. 2008: Wiley.
221. Frasconi, M., et al., *Electrochemical Evaluation of Electron Transfer Kinetics of High and Low Redox Potential Laccases on Gold Electrode Surface.* Electrochemica Acta, 2010(56): p. 817-827.

222. Leger, C., *Electrochemistry of Redox Proteins and Enzymes*. 2009, Laboratoire de Bioenergetique et Ingenerie des Proteines, CNRS, Marseille.
223. Armstrong, F.A., *Insights from Protein Film Voltammetry into Mechanisms of Complex Biological Electron-Transfer Reactions.* J. Chem. Soc., 2002: p. 661-671.
224. Leger, C. and P. Bertrand, *Direct Electrochemistry of Redox Enzymes as a Tool for Mechanistic Studies.* Chem. Rev, 2008. **108**(7): p. 2379-2438.
225. Leger, C., et al., *Enzyme Electrokinetics: Using Protein Film Voltammetry To Investigate Redox Enzymes and Their Mechanisms.* Biochemistry, 2003. **42**(29): p. 8653-8662.
226. Heering, H.A., J. Hirst, and F.A. Armstrong, *Interpreting the Catalytic Voltammetry of Electroactive Enzymes Adsorbed on Electrodes.* J. Phys. Chem. B, 1998. **102**: p. 6889-6902.
227. Pershad, H.R., et al., *Catalytic Electron Transport in Chromatium vinosum [NiFe]-Hydrogenase: Application of Voltammetry in Detecting Redox-Active Centers and Establishing That Hydrogen Oxidation Is Very Fast Even at Potentials Close to the Reversible H+/H2 Value.* Biochemistry, 1999. **38**: p. 8992-8999.
228. Scott, D.L. and E.F. Bowden, *Enzyme-Substrate Kinetics of Adsorbed Cytochrome c Peroxidase on Pyrolytic Graphite Electrodes.* Anal. Chem, 1994. **66**: p. 1217-1223.
229. Leger, C., et al., *Inhibition and Aerobic Inactivation Kinetics of Desulfovibro Fructosovorans NiFe Hydrogenases Studied by Protein-Film Voltammetry.* J. Am. Chem. Soc., 2004. **126**: p. 12162-12172.
230. Birdi, K.S., *Handbook of Surface and Colloid Chemistry*. 2nd ed. 2003: CRC Press.
231. Young, T., *An Essay on the Cohesion of Fluids.* Phil. Trans. R. Soc. Lond., 1805. **95**(1805): p. 65-87.
232. Wenzel, R.N., *Resistance of Solid Surfaces to Wetting by Water.* Ind. Eng. Chem., 1936. **28**(8): p. 988-994.
233. Cassie, A.B.D. and S. Baxter, *Wettability of Porous Surfaces.* Trans. Faraday Soc., 1944. **40**: p. 546-551.
234. Dettre, R.H. and R.E. Johnson, *Contact Angle, Wettability and Adhesion*, ed. F.M. Fowkes. Vol. 43. 1964, Washington D.C.: American Chemical Society. 112.
235. Dujardin, E., et al., *Capillarity and Wetting of Carbon Nanotubes.* Science, 1994. **265**(5180): p. 1850-1852.
236. Dujardin, E., et al., *Wetting of Single Shell Carbon Nanotubes.* Adv. Materials, 1998. **10**(17): p. 1472-1475.
237. Adamson, A.W. and A.P. Gast, *Physical Chemistry of Surfaces*. 6th ed. 1997, New York: John Wiley & Son.
238. Tipton, K.F., *Principles of Enzyme Assay and Kinetic Studies*. 2nd ed. Enzyme Assays, ed. R. Eisenthal and M.J. Danson. 2002: Oxford University Press. 1-44.
239. Bradford, M., Anal. Biochem, 1976. **72**: p. 248.
240. *Amine-reactive probes, http://probes.invitrogen.com/media/pis/mp00143.pdf, Accessed 06 July 2007.*

241. Rubenwolf, S., et al., *Carbon Electrodes for Direct Electron Transfer Type Laccase Cathodes Investigated by Current Density–Cathode Potential Behavior.* Biosensors and Bioelectronics, 2010. **26**: p. 841-845.
242. Cole, J.L., P.A. Clark, and E.I. Solomon, *Spectroscopic and Chemical Studies of the Laccase Trinuclear Copper Active Site: Geometric and Electronic Structure.* J. Am. Chem. Soc., 1990. **112**(26): p. 9534-9548.
243. Conway, B.E., *Electrochemical Supercapacitors: Scientific Fundamentals and Technological Applications*, ed. N. York. 1999: Kluwer Academic/Plenum Publishers.
244. Hill, A.V., *The Possible Effects of the Aggregation of the Molecules of Haemoglobin on its Dissociation Curves.* J Physiol, 1910. **40**(4-8): p. 1-7.
245. Rodgers, C.J., et al., *Designer Laccases: A Vogue for High-Potential Fungal Enzymes?* Trends in Biotechnology, 2009. **28**(2): p. 63-72.
246. Leonowicz, A., J. Rogalski, and A.L. Dawidowicz, *Purification and Immobilisation of the Inducible Form of Extracellular Laccase of the Fungus Trametes versicolor.* Acta Biotechnol., 1990. **10**(3): p. 261-269.
247. Kiiskinen, L.L., *Characterisation and Heterologous Production of a Novel Laccase from Melanocarpus albomyces*, in *Departement of Chemical Technology*. 2005, Helsinki University of Technology. p. 95.
248. Xu, F.e.a., *Dioxygen Reactivity of Laccase: Dependence on Laccase Source, pH and Anion Inhibition.* Appl. Biochem. Biotechnol, 2001. **95**: p. 125-133.
249. Han, M.J., H.T. Choi, and H.G. Song, *Purification and Characterisation of Laccase from the White Rot Fungus Trametes versicolor.* J.Microbiol., 2005. **43**(6): p. 555-560.
250. Yaropolov, A.I., et al., *Electrochemical properties of some copper-containing oxidases.* Bioelectrochem. Bioenerg, 1996. **40**: p. 49-57.
251. Palmieri, G., et al., *A Novel White Laccase from Pleurotus ostreatus.* J. Biol Chem., 1997. **272**(50): p. 31301-31307.
252. Zloczewska, A., et al., *Vertically Aligned Carbon Nanotube Film Electrodes for Bioelectrocatalytic Dioxygen Reduction.* Electrochimica Acta, 2011. **56**: p. 3947-3953.
253. Lee, C.-H., H.B. Gray, and F.C. Anson, *Catalysis of the Reduction of Dioxygen at Graphite Electrodes Coated with Fungal Laccase A.* J. Electroanal. Chem., 1984. **174**: p. 289-300.
254. Singh, C., et al., *Towards the Production of Large-scale Aligned Carbon Nanotubes.* Chemical Physics Letters, 2003. **372**(5-6): p. 860-865.
255. Laurent, C., E. Flahaut, and A. Peigney, *The Weight and Density of Carbon Nanotubes versus The Number of Walls and Diameter.* Carbon, 2010. **48**: p. 22989-2999.
256. Peigney, A., et al., *Specific Surface Area of Carbon Nanotubes and Bundles of Carbon Nanotubes.* Carbon, 2001. **39**: p. 507–514.
257. Gregor, M., et al., *Frequency-Domain Lifetime Fluoremetry of Double Labelled Creatine Kinase.* Physiological Research, 2003. **52**: p. 579-585.
258. Dynan, W., et al., *Understanding and Re-engineering nucleoprotein machines to cure human disease.* Nanomedicine, 2008. **3**(1): p. 93-105.
259. Armstrong, F.A., *Recent Developments in Dynamic Electrochemical Studies of Adsorbed Enzymes and Their Active Sites.* Current Opinion in Chemical Biology, 2005. **9**: p. 110-117.

260. Wang, J., et al., *Direct Electrochemistry of Cytochrome c at a Glassy Carbon Electrode Modified with Single-Wall Carbon Nanotubes.* Anal. Chem, 2002. **74**(9): p. 1993–1997.
261. Valentini, F., et al., *Carbon Nanotube Purification: Preparation and Characterization of Carbon Nanotube Paste Electrodes.* Anal. Chem., 2003. **75**(20): p. 5413-5421.
262. Wang, J., M. Musameh, and Y. Lin, *Solubilization of Carbon Nanotubes by Nafion toward the Preparation of Amperometric Biosensors.* J. Am. Chem. Soc., 2003. **125**(9): p. 2408-2409.
263. Luo, H., et al., *Investigation of the Electrochemical and Electrocatalytic Behavior of Single-Wall Carbon Nanotube Film on a Glassy Carbon Electrode.* Anal. Chem., 2001. **73**(5): p. 915-920.
264. Asuri, P., et al., *Increasing Protein Stability through Control of the Nanoscale Environment.* Langmuir, 2006. **22**: p. 5833-5836.
265. Wirth, C.T., S. Hofmann, and J. Robertson, *Surface Properties of Vertically Aligned Carbon Nanotube Arrays.* Diamond and Related Materials, 2008. **17**(7-10): p. 1518-1524.
266. Chakrapani, N., et al., *Capillarity-driven Assembly of Two-dimensional Cellular Carbon Nanotube Foams.* PNAS, 2004. **101**(12): p. 4009-4012.
267. Futaba, D.N., et al., *Shape-engineerable and Highly Densely Packed Single-walled Carbon Nanotubes and their Application as Super-capacitor Electrodes.* Nature Materials, 2006. **5**: p. 987 - 994.
268. Zhang, Q., et al., *Synchronous Growth of Vertically Aligned Carbon Nanotubes with Pristine Stress in the*
Heterogeneous Catalysis Process. J. Phys. Chem. C., 2007. **111**: p. 14638-14643.
269. Dai, X.J. and C. Skourtis, *Substrate Characteristics Beneath Self-Aligned Carbon-Nanotube Forests.* Journal of Applied Physics, 2008. **103**(124305): p. 1-5.
270. de los Arcos, T., P. Oelhafena, and D. Mathys, *The Importance of Catalyst Oxidation for the Growth of Carbon Nanotubes on Si Substrates.* Carbon, 2009. **47**: p. 1977-1982.
271. Sato, H., et al., *Effect of Catalyst Oxidation on the Growth of Carbon Nanotubes by Thermal Chemical Vapor Deposition.* J Appl Phys, 2006. **100**: p. 104321-104326.
272. Rummeli, M.H., et al., *Oxide-Driven Carbon Nanotube Growth in Supported Catalyst CVD.* J Am Chem Soc., 2007. **129**: p. 15772-15773.
273. Hata, K., et al., *Water-Assisted Highly Efficient Synthesis of Impurity-Free Single-Walled Carbon Nanotubes.* Science, 2004. **306**(5700): p. 1362-1364.
274. Dujardin, E., et al., *Purification of Single-Shell Nanotubes.* Adv. Materials, 1998. **10**(8): p. 611-613.
275. Kuznetsov, V.L.e.a., *Multi-walled carbon nanotubes with ppm level of impurities.* Phys. Status Solidi B 247. **11–12**: p. 2695–2699.
276. Beach, D.B., *Solid-State Combustion of Metallic Nanoparticles: New Possibilities for an Alternative Energy Carrier.* 2007. **129**: p. 29-32.
277. Sun, L.F.e.a., *Growth of Carbon Nanotube Arrays using the Existing Array as a Substrate and their Raman Characterization.* Chemical Physics Letters, 2001. **340**(3-4): p. 222-226.

278. Das, A., et al., *Monitoring Dopants by Raman Scattering in an Electrochemically Top-gated Graphene Transistor.* Nat Nano, 2008. **3**(4): p. 210-215.
279. Meier, R.J., *On Art and Science in Curve-fitting Vibrational Spectra.* Vibrational Spectroscopy, 2005. **39**(2): p. 266-269.
280. Fan, S., et al., *Self-Orientated Regular Arrays of Carbon Nanotubes and Their Field Emission Properties.* Science, 1999. **283**(512-514).
281. Pan, Z., et al., *Patterned growth of Vertically Aligned Carbon Nanotubes on Pre-patterned Iron/Silica Substrates Prepared by Sol-Gel and Shadow Masking.* J. Phys. Chem. B, 2003. **107**(6): p. 1338-1344.
282. Zheng, C., *Nanofabrication: Principles, Capabilities and Limits*. 2009, Boston, MA.: Springer.
283. Kanaya, K. and S. Okayama, *Penetration and Energy-loss Theory of Electrons in Solid Targets.* J. Phys. D: Appl. Phys., 1972. **5**(1): p. 43-58.
284. Williams, K.R., K. Gupta, and M. Wasilik, *Etch Rates for Micromachining Processing-Part II.* Journal of Microelectromechanical Systems, 2003. **12**(6): p. 761-778.
285. Daniel, M.C. and D. Astruc, *Gold Nanoparticles: Assembly, Supramolecular Chemistry, Quantum-Size-Related Properties, and Applications toward Biology, Catalysis, and Nanotechnology.* Chem. Rev., 2004. **104**: p. 293-346.
286. Hayat, M.A., *Colloidal Gold, Principles, Methods and Applications*. 1989, New York: Academic Press.
287. Feldheim, D.L. and J.A.F. Colby, *Metal Nanoparticles- Synthesis, Characterisation and Applications*, ed. M. Dekker. 2002: New York.
288. Schmid, G., *Clusters and Colloids: From Theory to Applications*. 1994: VCH: Weinheim.
289. Fendler, J.H., *Nanoparticles and Nanostructured Films*. 1998: Wiley-VCH: Weinheim.
290. Murray, R.W., *Nanoelectrochemistry: Metal Nanoparticles, Nanoelectrodes, and Nanopores.* Chem. Rev., 2008. **108**: p. 2688–2720.
291. Chen, S. and R.W. Murray, *Electrochemical Quantized Capacitance Charging of Surface Ensembles of Gold Nanoparticles.* J. Phys. Chem. B, 1999. **103**: p. 9996-10000.
292. Chen, S., et al., *Gold Nanoparticles of Varied Size: Transition to Molecule-like Charging.* Science, 1998. **280**: p. 2098-2101.
293. Miles, D.T. and R.W. Murray, *Dependent Quantized Double Layer Charging of Monolayer-Protected Gold Clusters.* Anal. Chem, 2003. **75**: p. 1251-1257.
294. Chen, S. and R. Pei, *Ion-Induced Rectification of Nanoparticle Quantized Capacitance Charging in Aqueous Solutions.* J. Am. Chem. Soc., 2001. **123**: p. 10607-10615.
295. Henglein, A.J., Phys. Chem., 1979. **83**: p. 2209.
296. Kiwi, J. and M. Gratzel, *Projection, Size Factors, and Reaction Dynamics of Colloidal Redox Catalysts Mediating Light Induced Hydrogen Evolution from Water.* J. Am. Chem. Soc., 1979. **101** (24): p. 7214–7217.
297. Daniel, M.C. and D. Astruc, *Gold Nanoparticles: Assembly, Supramolecular Chemistry, Quantum-Size-Related Properties, and Applications toward Biology, Catalysis, and Nanotechnology.* Chem. Rev., 2004. **104**: p. 293-346.

298. Xu, K., et al., *Recent Development of Nano-Materials Used in DNA Biosensors.* Sensors, 2009. **9**: p. 5534-5557.
299. Talapaltra, S., et al., *Direct Growth of Aligned Carbon Nanotubes on Bulk Metals.* Nature Nanotechnology, 2006. **1**: p. 112-116.
300. Garcia-Cespedes, J., et al., *Efficient Diffusion Barrier Layers For The Catalytic Growth of Carbon Nanotubes on Copper Substrates.* Carbon, 2008. **47**(3): p. 613-621.
301. Streeter, I., et al., *Cyclic Voltammetry on Electrode Surfaces Covered with Porous layers: An analysis of Electron Transfer Kinetics at Single-walled Carbon Nanotube Modified Electrodes.* Sensors and Actuators B: Chemical, 2008. **133**: p. 462-466.